

Tensor network methods for critical fermions

Quinten Mortier

August 30, 2023

Doctoral Committee

Jutho Haegeman (supervisor)
Ghent University

Nick Bultinck (co-supervisor)
University of Oxford
Ghent University

Dirk Poelman (chairman)
Ghent University

Jérôme Dubail
Université de Lorraine

Hong-Hao Tu
Technische Universität Dresden

Laurens Vanderstraeten
Ghent University

Frank Verstraete
University of Cambridge
Ghent University

English summary

In physics, the many-body problem focuses on determining the properties of a system that consists of (many) more than two particles or degrees of freedom. When we approach this problem using classical mechanics and Newton's laws, it leads to coupled partial differential equations that cannot be solved analytically for more than two particles. Therefore, we switch to numerical methods and/or effective descriptions to obtain relevant information about the global physics of the system. This method, as implemented numerically in many applications of the Monte Carlo algorithm, is highly successful and can accurately describe even macroscopic systems (with $\sim 10^{23}$ particles). However, when quantum mechanical behavior comes into play, such as in molecules or condensed matter systems, we need to solve not the classical many-body problem but its quantum mechanical equivalent. Here, the challenge becomes even greater, as the dimension of the relevant Hilbert space exponentially increases with the number of degrees of freedom.

The exponential scaling of the quantum many-body problem further necessitates the use of numerical methods. The aforementioned Monte Carlo algorithm for instance can also be employed in a quantum mechanical context, albeit with limitations. Many models, fermionic models in particular, suffer from what is known as the sign problem, rendering the quantum Monte Carlo method inapplicable. Tensor networks emerged as a worthy alternative in this regard. Originating from the field of quantum information theory, tensor network states provide a description of quantum many-body systems based on the entanglement they exhibit. Entanglement is a purely quantum mechanical phenomenon whereby the properties of two entangled partners cannot be described independently. In other words, entanglement functions as a kind of collectively shared information. It turns out that entanglement (quantified by the entanglement entropy) is limited in relevant quantum many-body states. Specifically, the entanglement entropy between a subsystem and its environment scales with the area of the boundary between them, rather than with the volume of the subsystem. This is known as the area law for entanglement entropy, and tensor networks have emerged as variational *Ansätze* that incorporate the area law through a local description, namely a tensor. These tensors are then connected (contracted) in a network, giving rise to an area law. The local nature of the tensors also enables their efficient determination using algorithms that scale polynomially with the characteristic size of the tensor, known as the bond dimension D .

Although many relevant states obey an area law for their entanglement, this is not always the case. A particular example is a metal where a multiplicative logarithmic correction to the area law occurs. In one-dimensional systems, there are also numerous models that violate the area law. These models are critical and have a conformally in-

variant low-energy behaviour, meaning that excited states follow immediately after the ground state in the energy spectrum and have a linear dispersion relation. As a result, correlation functions decay not exponentially, but polynomially in space. However, even when the area law is violated, tensor networks with their built-in area law remain useful. In fact, for one-dimensional systems, it has been demonstrated that by still employing tensor networks for problematic critical models and systematically increasing the bond dimension, one can develop a procedure called finite-entanglement scaling to make accurate predictions about the critical system. Indeed, the bond dimension controls the size of the tensors (and thus the total number of variational parameters in the *Ansatz*) but also the amount of entanglement. Although this entanglement will always be limited by the area law, we can increase the entanglement by increasing D and thus approximate the critical state.

Finite-entanglement scaling has already been applied in 1D and near critical points in 2D, but for fermionic systems with a Fermi surface (such as metals), where the violation of the area law is most pronounced, this principle has not been tested yet. Therefore, we specifically studied it in the first two research projects (see Sec. 5.4.1 and Sec. 5.4.2). However, due to the critical nature of the model and the requirement of a high bond dimension to observe entanglement scaling, the application of generic 2D tensor networks, known as Projected Entangled-Pair States (PEPS), especially their variational optimization, would be computationally extremely challenging. Therefore, we restricted to the Gaussian subclass of PEPS. "Gaussian" here refers to the fact that the two-point correlation functions determine all higher-order correlation functions, allowing for simple and exact calculations of expectation values (including the energy, necessary for optimization). In the first project, we focused primarily on the energy precision of the optimized tensor network states and discovered that it steadily increases as the bond dimension grows. By scaling up D , arbitrary precision can thus be achieved, and PEPS can still be efficiently applied to critical systems with a Fermi surface, despite the area law. In this study, we also found that the Gaussian subclass of PEPS exhibits certain parity obstructions related to their (trivial) topology. This implies that the *Ansatz* cannot provide a correct description of topologically non-trivial phases. However, the PEPS approximates the critical states exactly from these phases. Fortunately, by creatively manipulating the boundary conditions, we were able to circumvent these obstructions and demonstrate the aforementioned increase in energy precision.

In the second project, we expanded our view from energy precision towards finite-entanglement scaling. To do so, we proceed as in 1D where one can derive a power law that relates the effective correlation length of an approximative tensor network state to the utilized bond dimension by means of conformal field theory. This correlation length can then be used to establish scaling laws for various observables, including the entanglement entropy, allowing to represent results for different bond dimensions on a single curve, *i.e.* a scaling collapse. The same strategy was applied in 2D, where the methodology developed in the first research project was extended to spin- $\frac{1}{2}$ fermions with SU(2)-symmetry. Furthermore, an alternative Gaussian *Ansatz* (which was later found to be equivalent) was used. By proposing a scaling law consistent with the logarithmic violation of the area law we were able to perform a successful scaling collapse for the entanglement entropies computed using the Gaussian tensor networks. Phrased differently, it is not only conceptually

possible to approximate models with a violation of the area law using tensor networks, but this approach also systematically improves and a corresponding finite-entanglement scaling procedure can be applied as in one dimension.

To showcase the potential of tensor networks in the realm of highly critical systems, we focused our efforts on the Gaussian subclass, recognizing its limitations when it comes to interacting theories where the generic variant of tensor networks must be employed. As these generic tensor networks were originally developed for spin systems, adaptations and reformulations are required for fermionic degrees of freedom. In one dimension, the Jordan-Wigner transformation emerged as a tool to convert fermionic systems into spin systems (and vice-versa). In higher dimensions, the introduction of swap gates as functional entities allowed for the incorporation of fermionic character within tensor network diagrams. However, in line with the local description that is essential for a tensor network, our aim in the third research project (see Chapter 4) was to encode the anti-commuting nature of fermions within the tensors themselves. Therefore, we utilize the already existing \mathbb{Z}_2 -graded linear spaces, also known as super vector spaces. By further developing this formalism we demonstrated that the diagrammatic language for tensor networks can be fully adopted, albeit with the introduction of additional parity tensors. Through benchmarks utilizing various methods such as VUMPS, the excitation *Ansatz*, and the computation of correlation functions for PEPS, we illustrated the proper functionality of this fermionic variant of tensor networks.

In our fourth and final research project, we integrate all the aforementioned concepts and methods with the aim of studying Fermi surface spin liquids by using the parton construction on tensor network wave functions (see Sec. 5.4.3). Spin liquids are phases expected to contain the ground states of geometrically frustrated Mott insulators. Examples include the Heisenberg model on the kagome lattice in 2D or the pyrochlore lattice in 3D. Due to the frustrated nature of the problem, a highly degenerate ground state emerges, exhibiting intrinsic topological properties that make it potentially interesting for building fault-tolerant quantum computers. However, the frustrated nature of the problem also makes numerical approximation extremely challenging. Therefore, the parton construction has been developed as an effective description, revealing that a possible realization of spin liquids exhibits critical excitations with Fermi surface-like properties, such as polynomially decaying correlation functions and a violation of the area law. Once again, the question arises as to whether tensor networks can describe these strongly interacting states with a Fermi surface. If this is the case, they can be applied to compare their energy with other reference ground states in an attempt to qualitatively determine whether and which spin liquid forms in a physical system. Hence, our objective in this final project is to construct a PEPS that realizes a Fermi surface spin liquid. To achieve this goal, we apply the parton construction at the level of tensor network wave functions. Thus, we first optimize a Gaussian PEPS for spinful fermions with a Fermi surface, which we know is feasible based on the first two research projects. Subsequently, we transform this Gaussian PEPS into a generic variant using a SU(2)-symmetric method that we developed ourselves. Then, we apply a Gutzwiller projection to project the partons back to their corresponding spins. Finally, the resulting interacting PEPS is contracted using the methods from the third research project to calculate, among other things, correlation functions and spin structure factors that should exhibit distinct features of the underlying

Fermi surface. The initial steps in this process have already been taken successfully and are outlined in Sec. 5.4.3. The final, though most challenging, step is currently being carried out.

With the aforementioned research projects, I attempted to broaden the scope of tensor networks to critical fermionic systems. These systems are not only prevalent in nature in the form of metals, but they are also found in systems that potentially possess interesting and yet to be discovered properties, such as spin liquids. The critical behavior and the associated violation of the area law might suggest that these states are beyond the reach of tensor networks. However, we have demonstrated that this is not the case. Tensor networks can still be employed to provide accurate information about the critical states through finite-entanglement scaling. In addition to the conceptual findings, this work involved the development of many numerical algorithms for both Gaussian and generic tensor networks. As such it represents only a beginning and with it I hope to have made a valuable contribution to the field of research.

Dutch summary

In de natuurkunde richt het veeldeeltjesprobleem zich op het bepalen van de eigenschappen van een systeem dat bestaat uit (veel) meer dan twee deeltjes of vrijheidsgraden. Als we dit probleem benaderen met klassieke mechanica en de wetten van Newton, leidt dit tot gekoppelde partiële differentiaalvergelijkingen die voor meer dan twee deeltjes niet meer analytisch kunnen worden opgelost. Daarom schakelen we over op numerieke methoden en/of effectieve beschrijvingen, zodat we toch relevante informatie over de globale fysica van het systeem kunnen verkrijgen. Deze methode, zoals numeriek geïmplementeerd in vele toepassingen van het Monte Carlo algoritme, is zeer succesvol en slaagt er zelfs in macroscopische systemen (met $\sim 10^{23}$ deeltjes) nauwkeurig te beschrijven. Echter, zodra kwantummechanisch gedrag om de hoek komt kijken, zoals in moleculen of vaste stoffen, moeten we niet het klassieke veeldeeltjesprobleem, maar het kwantummechanische equivalent ervan oplossen. Hier wordt de uitdaging nog groter, aangezien de dimensie van de relevante Hilbertruimte exponentieel toeneemt naarmate het aantal vrijheidsgraden stijgt.

De exponentiële schaling van het kwantumveeldeeltjesprobleem dwingt ons er nog meer toe gebruik te maken van numerieke methoden. Zo kan het eerder genoemde Monte Carlo algoritme ook gebruikt worden in een kwantummechanische context, zij het met beperkingen. Heel wat, typisch fermionische, modellen kampen immers met wat het tekenprobleem genoemd wordt waardoor de kwantum Monte Carlo methode niet langer toepasbaar is. Met tensor netwerken trad een waardig alternatief op de voorgrond. Afkomstig uit het domein van de kwantuminformatietheorie, bieden tensor netwerk toestanden een beschrijving van kwantumveeldeeltjessystemen op basis van de verstrengeling die deze bevatten. Verstrengeling is een zuiver kwantummechanisch fenomeen waarbij de eigenschappen van twee verstrengelde partners nooit volledig afzonderlijk beschreven kunnen worden. Met andere woorden, verstrengeling fungeert als een soort collectief gedeelde informatie. Net deze verstrengeling (gekwantificeerd door de zogeheten verstrengelingsentropie) blijkt eerder beperkt in relevante kwantumveeldeeltjestoestanden. Specifiek schaalt de verstrengelingsentropie tussen een willekeurig subsysteem en zijn omgeving met de oppervlakte van het grensvlak tussen beiden, en niet met het volume van het subsysteem. Dit is de oppervlaktewet voor verstrengelingsentropie en tensor netwerken zijn ontstaan als variationele ansatze die de oppervlaktewet incorporeren door middel van een lokale beschrijving, namelijk een tensor. Deze worden dan met elkaar verbonden (gecontraheerd) in een netwerk en geven zo aanleiding tot een oppervlaktewet. Het lokale karakter van de tensoren maakt het bovendien mogelijk om ze efficiënt te bepalen met behulp van algoritmen die polynomiaal schalen met de karakteristieke grootte van de tensor, ook wel de bindingsdimensie D genoemd.

Hoewel veel relevante toestanden voldoen aan een oppervlaktewet voor hun verstengeling, is dit niet altijd het geval. Een voorbeeld hiervan is een metaal, waarbij een multiplicatieve logaritmische correctie op de oppervlaktewet optreedt. Ook in ééndimensionale systemen zijn er talloze modellen waarbij de oppervlaktewet wordt geschonden. Deze modellen zijn kritisch, wat betekent dat geëxciteerde toestanden direct volgen op de grondtoestand in het energiespectrum. Hierdoor nemen correlatielengtes niet exponentieel, maar polynomiaal af in de ruimte. Echter, zelfs wanneer de oppervlaktewet wordt geschonden, blijven tensor netwerken met hun ingebouwde oppervlaktewet nuttig. Althans, voor ééndimensionale systemen is aangetoond dat door tensor netwerken toch te gebruiken voor problematische kritische modellen en de bindingsdimensie systematisch te vergroten, men een procedure genaamd verstengelingsschaling kan ontwikkelen om nauwkeurige voorspellingen te doen over het kritische systeem. De bindingsdimensie regelt immers de grootte van de tensoren (en daarmee het totale aantal variationele parameters in de ansatz), maar zo ook de hoeveelheid verstengeling die aanwezig kan zijn in de toestand. Hoewel deze altijd beperkt zal zijn door de oppervlaktewet, kunnen we binnen deze grenzen de verstengeling laten toenemen door D te verhogen en zo de kritische toestand benaderen.

Verstengelingsschaling werd reeds toegepast in 1D en nabij kritische punten in 2D maar voor fermionische systemen met een Fermi oppervlak (zoals in metalen) waar de schending van de oppervlaktewet het meest uitgesproken is, werd dit principe nog niet getest. Bijgevolg bestudeerden we net dit in de eerste twee onderzoeksprojecten (zie Sec. 5.4.1 en Sec. 5.4.2). Echter, door de kritische aard van het model en de noodzaak aan een hoge bindingsdimensie om verstengelingsschaling waar te nemen, is de toepassing van generieke 2D tensor netwerken, Projected Entangled-Pair States (PEPS) genaamd, i.h.b. hun variationele optimalisatie, computationally extreem veeleisend. Daarom werkten we met de Gaussische subklasse van deze PEPS. “Gaussisch” verwijst hier naar het feit dat tweepuntscorrelatielengtes alle correlatielengtes van hogere orde bepalen, waardoor verwachtingswaarden (waaronder de energie, die nodig is voor de optimalisatie) eenvoudig en exact berekend kunnen worden. In een eerste stap hebben we vooral gekeken naar de energieprecisie van de geoptimaliseerde tensor netwerk toestanden. We ontdekten dat deze gestaag toeneemt naarmate de bindingsdimensie groter wordt. Door D op te schalen kan dus willekeurige precisie worden bereikt en PEPS kunnen ondanks hun oppervlaktewet dus nog steeds efficiënt toegepast worden voor kritische systemen met een Fermi-oppervlak. In deze studie vonden we ook dat de Gaussische subklasse van PEPS bepaalde pariteitsostructies heeft die verband houden met de (triviale) topologie van de toestanden. Dit zorgt ervoor dat de *Ansatz* geen correcte beschrijving kan geven van topologisch niet-triviale fasen. Laat het nu net deze fasen zijn waaruit PEPS de kritische toestanden effectief benaderen. Gelukkig konden we door creatief om te springen met de randvoorwaarden de obstructies vermijden en de eerder genoemde toename in energieprecisie alsnog aantonen.

In een tweede stap werd niet enkel de energieprecisie maar de gehele verstengelingsschaling onder de loupe genomen. In 1D kan men immers door gebruik te maken van conforme veldentheorie een machtswet afleiden die de effectieve correlatielengte van een benaderend tensor netwerk linkt aan de gebruikte bindingsdimensie. Deze correlatielengte kan dan op haar beurt gebruikt worden om schalingswetten op te stellen voor allerlei ob-

servabelen waaronder de verstrengelingsentropie. Zo kunnen resultaten voor verschillende bindingsdimensies samen op één curve voorgesteld worden, *i.e.* een zogeheten “scaling collapse”. Dezelfde strategie werd gevuld in 2D, waarbij de methodiek ontwikkeld in het eerste onderzoeksproject werd uitgebreid naar spin- $\frac{1}{2}$ fermionen met SU(2) symmetrie. Ook een andere (achteraf equivalent gebleken) Gaussische *Ansatz* werd gebruikt. Het resultaat was een coherente schaalwet en een succesvolle scaling collapse voor de verstrengelingsentropie die we berekend hebben met behulp van de Gaussische tensor netwerken. Met andere woorden, het is niet alleen principieel mogelijk om modellen met een schending van de oppervlaktewet te benaderen met behulp van tensor netwerken, maar deze benadering verbetert ook systematisch en er kan een schalingsprocedure worden toegepast die, net als in één dimensie, beschrijft hoe deze systematische verbetering verloopt.

Om de mogelijkheden van tensor netwerken in het kader van hoog-kritische systemen te demonstreren beperkten we ons tot de Gaussische subklasse. Deze schiet natuurlijk tekort voor interagerende theorieën waar de generieke variant van tensor netwerken dient toegepast te worden. In eerste instantie werden tensor netwerken ontwikkeld voor spinsystemen. Aanpassingen en/of herformuleringen voor fermionische vrijheidgraden zijn daarom noodzakelijk. Zo is er in 1D de Jordan-Wigner transformatie die fermionische systemen kan omzetten in een spinsysteem. In hogere dimensies werden “swap gates” ingevoerd als functionele entiteiten die het fermionische karakter in een tensor netwerk diagram kunnen incorporeren. Meer in lijn met de lokale beschrijving die essentieel is voor een tensor netwerk, wilden we in een derde onderzoeksproject (zie Chapter 4) de anticommuterende aard van fermionen vastleggen op het niveau van de tensoren zelf. Een manier om dit te doen is door de tensoren op te bouwen uit tweevoudig gegradeerde lineaire ruimten, ook wel supervectorruimten genoemd. We werkten dit formalisme verder uit en tonen aan dat de gelauwerde diagrammatische taal voor tensor netwerken volledig kan worden overgenomen, mits de introductie van enkele extra pariteitstensoren. Met benchmarks voor verschillend methoden zoals VUMPS, de excitatie *Ansatz* en het berekenen van correlatiefuncties voor PEPS tonen we aan dat deze fermionische variant van tensor netwerken naar behoren functioneert.

Een vierde en laatste onderzoeksproject combineert alle eerder genoemde concepten en methoden met als doel de studie van spinvloeistoffen met een Fermi oppervlak aan de hand van de parton constructie in tensor netwerk golffuncties (zie Sec. 5.4.3). Spinvloeistoffen zijn fasen waarvan wordt verwacht dat de grondtoestanden van geometrisch gefrustreerde Mott isolatoren ertoe behoren. Voorbeelden omvatten o.a. het Heisenberg model op het kagome rooster in 2D of het pyrochloor rooster in 3D. Vanwege de gefrustreerde aard van het probleem ontstaat er een sterk gedegenereerde grondtoestand die intrinsiek topologische eigenschappen vertoont, waardoor deze toestand mogelijk interessant is voor het bouwen van een fouttolerante kwantumcomputer. De gefrustreerde aard van het probleem maakt echter ook numerieke benadering uiterst uitdagend. Daarom is de parton constructie ontwikkeld als effectieve beschrijving. Uit deze constructie blijkt dat een mogelijke realisatie van spinvloeistoffen er een is met kritische excitaties die de eigenschappen van een Fermi oppervlak vertonen, zoals polynomiaal afnemende correlatiefuncties en een schending van de oppervlaktewet. Opnieuw rijst dus de vraag of tensor netwerken ook deze sterk interagerende toestanden met een Fermi-oppervlak kunnen beschrijven. Indien dit het geval is, kunnen ze worden toegepast in studies waarbij

hun energie wordt vergeleken met andere referentiegrondtoestanden om op een kwalitatieve manier te bepalen of en welke spinvloeistof zich vormt in een fysisch systeem. Ons doel in dit laatste project is dus het construeren van een PEPS die een spinvloeistof met Fermi oppervlak realiseert. Hiervoor passen we de parton constructie toe op het niveau van tensor netwerk golffuncties. We optimaliseren dus eerst een Gaussische PEPS voor spinvolle fermionen met een Fermi oppervlak, waarvan we weten dat dit mogelijk is op basis van de eerste twee onderzoeksprojecten. Vervolgens transformeren we deze Gaussische PEPS naar een generieke variant met behulp van een door onszelf ontwikkelde SU(2)-symmetrische methode. Op deze PEPS passen we vervolgens een Gutzwiller projectie toe om de partonen terug te projecteren naar hun overeenkomstige spins. De resulterende interagerende PEPS wordt uiteindelijk gecontraheerd met behulp van de methoden uit het derde onderzoeksproject om onder andere correlatiefuncties en spinstructuurfactoren te berekenen die duidelijke kenmerken moeten bevatten van het onderliggende Fermi oppervlak. De eerste stappen in dit proces zijn al succesvol gezet en worden ook toegelicht in Sec. 5.4.3. De laatste, maar meest uitdagende stap, wordt momenteel uitgevoerd.

Met de bovenvermelde onderzoeksprojecten heb ik getracht het toepassingsgebied voor tensor netwerken te verruimen naar kritische fermion systemen. Deze komen niet alleen veelvuldig voor in de natuur onder de vorm van metalen, men vindt ze ook terug in systemen die potentieel interessante en nog te ontdekken eigenschappen hebben zoals de spinvloeistoffen. Het kritische gedrag en de bijbehorende schending van de oppervlaktewet zouden kunnen suggereren dat deze systemen buiten het bereik van tensor netwerken vallen. We hebben echter aangetoond dat dit niet het geval is. Tensor netwerken kunnen nog steeds worden ingezet kunnen via verstrengelingsschaling nauwkeurige informatie bieden over de kritische toestanden. Dit onderzoek ging gepaard met het ontwikkelen van numerieke algoritmen voor zowel Gaussische als generieke tensor netwerken en vormt dus zowel conceptueel als praktisch slechts een begin. Zodoende hoop ik dan ook een waardevolle bijdrage te hebben geleverd aan het onderzoeksgebied.

Contents

Doctoral Committee	i
English summary	iii
Dutch summary	vii
1 Introduction	1
1.1 General introduction	1
1.2 Overview and structure	3
2 Key concepts	5
2.1 Quantum many-body physics	5
2.1.1 From one to many	5
2.1.2 Indistinguishable particles and second quantization	7
2.1.3 Extended quantum systems	10
2.1.4 Density operators and mixed states	12
2.2 Correlations and entanglement	14
2.3 Symmetries and phases	17
2.4 Relevant fermion systems	21
2.4.1 Quantum chemistry	21
2.4.2 Condensed matter physics	25
2.5 Tensor network states	35
3 Gaussian states	39
3.1 Definition	39
3.2 Grassmann formalism	44
3.2.1 Grassmann numbers	44
3.2.2 Gaussian states, operators and channels	46
3.2.3 Application to the lattice	48
3.3 Coherent states	53
3.4 Symmetries and phases	55
3.4.1 Global U(1) and SU(2) symmetry	56
3.4.2 CPT symmetries and the ten-fold way	58
3.4.3 Topological invariants: the Chern number	61
3.4.4 Dimensional reduction	65

4 Fermionic tensor network methods	75
4.1 Fermionic tensors	76
4.1.1 Preliminaries	76
4.1.2 Graded tensor networks	80
4.1.3 Diagrammatic notation	83
4.1.4 Tensor properties	84
4.1.5 Tensor manipulations	87
4.1.6 Tensor decompositions	89
4.2 Uniform fermionic MPS	91
4.2.1 General form	91
4.2.2 Gauge fixing	92
4.2.3 Tangent space	93
4.2.4 Fermionic VUMPS and TDVP algorithms	95
4.2.5 Quasi-particle excitations	97
4.3 Uniform fermionic PEPS	99
4.3.1 General form	99
4.3.2 Contracting fermionic PEPS	101
4.4 Applications	106
4.4.1 Excitations in the 1D Kitaev chain	106
4.4.2 Spin-charge separation in the Hubbard model	108
4.4.3 Long-range correlations in chiral superconductors	110
5 Gaussian fermionic tensor network methods	113
5.1 Definition	113
5.1.1 Kraus-Schuch formalism	113
5.1.2 Gu-Verstraete-Wen formalism	116
5.2 No-go theorem and parity obstructions	118
5.3 Reformulation as generic fTNS	120
5.3.1 Pfaffian formulas (the top-down approach)	120
5.3.2 Channel decomposition (the bottom-up approach)	121
5.4 Applications	127
5.4.1 Tensor networks can resolve Fermi surfaces	127
5.4.2 Finite entanglement scaling in 2D metals	140
5.4.3 PEPS encoding Fermi surface spin liquids	168
6 Conclusions and outlook	173
A Fermionic tangent space methods	175
A.1 Tangent-space projector for fermionic MPS	175
A.2 Vumps for fermionic MPOs	176
A.3 Vumps for a double-layer transfer matrix	178
B Parity obstructions: a proof	183

Chapter 1

Introduction

1.1 General introduction

Understanding the behavior of systems composed of many particles or degrees of freedom, known as the many-body problem, represents one of the most intriguing and relevant problems in theoretical and applied physics. However, already within the realm of classical mechanics this problem quickly becomes challenging when increasing the number of particles. Even more so in quantum mechanics where the dimension of the relevant Hilbert space scales exponentially with the number of degrees of freedom, necessitating a numerical approach. In this regard, Quantum Monte Carlo algorithms have emerged as the golden standard. However, in fermionic models they can suffer from the infamous sign problem, precluding their efficient applicability. To address this, tensor network states (TNS) were put forward as an alternative approach. Rooted in quantum information theory, tensor network states describe quantum many-body systems in a compressed way by a local tensor. As such they inherently realize an area law of entanglement scaling as observed in the majority of physically relevant (*i.e.* low-energy) quantum many-body states. However, in the case of gapless Hamiltonians, the area law is frequently violated. Two notable examples are gapless 1D systems with long-wavelength properties that can be described by conformal field theory (CFT), and systems in higher dimensions with a Fermi surface. One could therefore ask if TNS still provide a useful description in these cases. While this question was already answered in the affirmative for 1D models, 2D critical models, in particular those with a co-dimension one Fermi surface, remained unexplored. Of course approximating these highly critical states in 2D requires an elevated bond dimension (*i.e.* the dimension of the virtual, contracted indices of the tensors) as well as a stable optimization algorithm. Therefore, the generic TNS *Ansatz* will be restricted to its Gaussian submanifold, yielding Gaussian fermionic TNS (GfTNS), assuming a pivotal role in this work.

For systems violating the area law, the theory of finite-entanglement scaling describes how an area-law state (*i.e.* a TNS) best approximates the non-area-law ground state in the thermodynamic limit. A remarkable result from finite-entanglement scaling is that for 1D critical ground states described by a CFT, the finite entanglement induced by the TNS bond dimension D results in a finite correlation length, polynomially scaling with the bond dimension, $\xi \propto D^\kappa$, where κ is a universal number determined by the central

charge of the CFT. As a result, the entanglement entropy of a region of length L can be expressed in terms of a scaling function which depends only on the ratio L/D^κ . In 2D a similar analysis of the entanglement entropy of a system with a Fermi surface was not yet considered. With the GfTNS we set out to do exactly this and try to extend the finite-entanglement scaling analysis to two dimensions by showing that a similar scaling collapse is possible for the entanglement entropy of metals, *i.e.* states with a Fermi surface, despite the fact that there is no underlying CFT describing the long wavelength physics.

Evidently, the class of TNS is most interesting beyond the Gaussian submanifold where interactions can result in the realization of peculiar phases like quantum spin liquids. However, standard TNS techniques for interacting systems like Variational optimization of Uniform Matrix Product States (VUMPS) and the Time-Dependent Variational Principle (TDVP) were typically developed within the context of spin systems. For their application to fermions, one therefore needs either a reformulation of those fermions in terms of spins or an adaption of the methods to the anti-commuting nature of the degrees of freedom. In 1D, the former approach can always be followed by invoking a Jordan-Wigner transformation. Although some tentative results exist, a full-fledged and equally attractive generalization of such a transformation does not exist in higher dimensions. Hence, we are forced to explicitly integrate the fermions into our formalism. Possible routes to do so have already been proposed, e.g. by replacing the virtual degrees of freedom with Grassmann numbers or by means of swap gates, resolving leg crossings in fermionic tensor network diagrams. Though highly successful and conceptually sound these methods can become quite unwieldy (especially in higher dimensions). A more manageable alternative exists and is based on the concept of \mathbb{Z}_2 -graded linear spaces, also called super vector spaces. However, its original discussion was primarily conceptual. Therefore, we will extend the formalism toward numerical implementation by constructing fermionic TNS (in the thermodynamic limit) and considering tangent space methods like the VUMPS algorithm and the quasi-particle excitation *Ansatz*.

One of the more interesting applications of these generic fermionic tensor network could be the realization of a quantum spin liquid through the implementation of the parton construction. This method is the conventional tool for the analysis of spin liquids and embeds the spin degrees of freedom in either fermionic or bosonic operators (thus enlarging the Hilbert space). The resulting Hamiltonian is studied in a mean-field approximation and the correct parton occupation on each site (typically half-filled) is enforced by coupling the model to a gauge field. The spin liquid phases can then be classified in terms of the different deconfined phases of the resulting gauge theories. However, neither correct energy expectation values nor an idea about which particular spin liquid phase is realized by a given microscopic Hamiltonian can be determined via this method. What the mean-field Hamiltonian in the parton construction does provide, are trial states which can be used to calculate variational energies. Indeed, we can solve the mean-field model, yielding a Gaussian state and remove the erroneous (non-half-filled) parts of the wavefunction by means of a so-called Gutzwiller projection. Together with a variational Monte Carlo method, this approach can then be utilized to energetically compare trial states corresponding to different types of spin liquid states for a given microscopic Hamiltonian. Interestingly, these parton constructions on the level of wavefunctions can also be

performed with TNS and were recently demonstrated to be able to encode critical Dirac spin liquids. At the end of this work, we aim to extend these techniques to investigate Fermi surface spin liquids.

1.2 Overview and structure

As this work is situated on the crossroads of multiple branches of (mainly theoretical) physics, notably condensed matter physics and quantum information theory, it combines diverse notions from these fields. This necessitates a comprehensive discussion that can be found in Chapter 2. We also introduce the relevant (critical) effective fermion models as well as the tensor network *Ansätze* employed to investigate them. The Gaussian restriction of the latter plays a pivotal role in this work. Therefore general Gaussian states are extensively described in Chapter 3. We begin by presenting both bosonic and fermionic Gaussian states, swiftly narrowing our attention to the latter. We examine two potential definitions and their implementation on the lattice. Furthermore, we explore the existence of topological phases for these Gaussian states summarized in the periodic table for topological superconductors and insulators. Having introduced Gaussian states, Chapter 4 shifts our focus to tensor network states. Leveraging the formalism of \mathbb{Z}_2 -graded Hilbert spaces and their tensor products, we demonstrate how tensor networks can be adapted to accommodate fermions. The celebrated diagrammatic notation is revisited and modified for fermions, and well-established algorithms such as VUMPS and TDVP are reformulated accordingly. We proceed to benchmark these methods using interesting models like chiral superconductor and the 1D Hubbard model as test cases. Chapter 5 combines the notion of Gaussian states and tensor network states, resulting in the development of Gaussian fermionic tensor network states (GfTNS). In line with Chapter 3 we propose two generally equivalent definitions, explore numerical optimization techniques for these states, and investigate their topological properties. Additionally, we explore methods to reinterpret GfTNS as regular fermionic tensor network states. In the latter part of this Chapter we apply the GfTNS formalism to demonstrate the applicability of (G)fTNS to systems with a Fermi surface, thereby discovering a finite-entanglement scaling procedure for 2D metals. Building upon these findings, we pursue a final research project centered around the parton construction for spin liquids within the framework of tensor network states, with the ultimate aim of realizing a Fermi surface spin liquid. Conclusions and an outlook for future research directions are provided in Chapter 6.

Chapter 2

Key concepts

In this Chapter we explore some important basic notions that will play a significant role in the subsequent Sections. We begin by introducing quantum many-body physics and its problematic scaling. Within this framework, the concept of entanglement, originating from quantum information theory, will be indispensable as the scaling of entanglement in many relevant states of quantum many-body systems follows an area law. However, this area law can also be violated. Especially in fermion systems, critical points at the transition between phases can display strong violations. Therefore, this dissertation will predominantly be occupied with the question if tensor networks, inherently incorporating the area law of entanglement entropy, are still useful (numerical) tools when applied to relevant, critical fermion systems.

2.1 Quantum many-body physics

The quantum many-body problem describes the behavior of multiple particles (or bodies) subject to the laws of quantum mechanics. As such it is crucial for explaining phenomena in condensed matter physics and quantum chemistry and advancing areas such as quantum computation. In the following Sections we provide an introduction to the problem and its exponential scaling, discuss symmetry constraints in case of indistinguishable particles together with the method of second quantization and explore the setting of extended quantum systems such as lattices that will play a major role throughout this work. Finally, we also introduce the important concepts of density operators and mixed states establishing the link with statistical mechanics.

2.1.1 From one to many

To introduce the quantum many-body problem, we start from non-relativistic, single-particle quantum mechanics governed by the following axioms as found in many standard works [1, 2, 3]:

- The state of a single-particle quantum system is fully described by a normalized vector $|\psi\rangle$ living in a Hilbert space \mathcal{H} .
- Physical observables A correspond to self-adjoint operators acting on the vectors in this Hilbert space, *i.e.* $A \in \mathcal{L}(\mathcal{H})$ and $A = A^\dagger$.

- When performing a measurement of an observable A , the state $|\psi\rangle$ will collapse onto one of the eigenstates $|\lambda_i\rangle$ of A , yielding the corresponding eigenvalue λ_i as the outcome. The probability hereof is given by the norm squared of the overlap, $|\langle\lambda_i|\psi\rangle|^2$. As a result, the expectation value of an observable A for the state $|\psi\rangle$ is given by $\langle\psi|A|\psi\rangle$.
- The time evolution of a state $|\psi(t)\rangle$ is governed by the Schrödinger equation

$$i\frac{\partial}{\partial t}|\psi(t)\rangle = H|\psi(t)\rangle \quad (2.1)$$

where H is the Hamiltonian, the observable corresponding to the energy of the system. When H is time-independent, this yields $|\psi(t)\rangle = e^{-iHt}|\psi(0)\rangle$ with $e^{-iHt} = \sum_n e^{-iE_nt}|E_n\rangle\langle E_n|$. *I.e.* time evolution is fully characterized by the eigenvectors $|E_n\rangle$ of H obtained from the time-independent Schrödinger equation,

$$H|E_n\rangle = E_n|E_n\rangle. \quad (2.2)$$

The eigenvector(s) with the lowest energy is (are) called the groundstate(s).

A typical example in 1D considers a single particle with position X and momentum P , satisfying the canonical commutation relation, $[X, P] = i$. A complete eigenbasis for the former is $\{|x\rangle \mid \forall x \in \mathbb{R}\}$ so that it can be expressed as $X = \int dx|x\rangle x\langle x|$. Sometimes, the integral and basis states are dropped, saying that X is represented by x in configuration space. The momentum operator reads $P = \int dx|x\rangle (-i\frac{\partial}{\partial x})\langle x|$ (or thus $-i\frac{\partial}{\partial x}$ in configuration space). Indeed, this satisfies the canonical commutation relation, which can be checked by applying a random state $|\psi\rangle$ to XP and PX and expressing the overlap $\langle x|\psi\rangle$ by its so-called wavefunction $\psi(x)$. A free particle with mass m would then yield the time-independent $H = \frac{P^2}{2m}$. As a result, momentum eigenstates $\{|p\rangle \mid \forall p \in \mathbb{R}\}$ with wavefunction $\frac{1}{\sqrt{2\pi}}e^{ipx}$ diagonalize the Hamiltonian with $E = \frac{p^2}{2m}$ and the expectation values of P serving as labels characterizing the eigenstates, *i.e.* with p as a quantum number. These are all invariant in their momentum under time-evolution. The stationary particle, with $p = 0$, is the lowest in energy and thus corresponds to the ground state.

Another, even simpler, example considers a single qubit, *i.e.* a spin- $\frac{1}{2}$ particle, fixed in space. Suppose this qubit experiences a magnetic field h , directed in the z direction. The relevant operators then are S^a ($a = x, y, z$), describing the particle's intrinsic angular momentum and forming a two-dimensional representation of the Lie algebra $\mathfrak{su}(2)$ due to the canonical commutation relations $[S^a, S^b] = i\epsilon^{abc}S^c$. As a result, we can put $S^a = \frac{1}{2}\sigma^a$ where σ^a are the Pauli matrices

$$\sigma^x = \begin{pmatrix} 0 & 1 \\ 1 & 0 \end{pmatrix} \quad \sigma^y = \begin{pmatrix} 0 & -i \\ i & 0 \end{pmatrix} \quad \sigma^z = \begin{pmatrix} 1 & 0 \\ 0 & -1 \end{pmatrix} \quad (2.3)$$

and the Hilbert space is given by $\mathcal{H} = \mathbb{C}^2$. The Hamiltonian for this system is $H = -\mathbf{h} \cdot \mathbf{S}$, resulting in the energy eigenstates $|\uparrow\rangle = (1 \ 0)^\dagger$ and $|\downarrow\rangle = (0 \ 1)^\dagger$ with energy $-h$, respectively, h where the former corresponds to the ground state.

The extension from one- to many-body quantum mechanics proceeds by taking tensor products. Consider for instance two qubits with different but fixed positions \mathbf{r}_1 and \mathbf{r}_2 .

The Hilbert space containing the state vectors then is $\mathcal{H}^{(2)} = \mathcal{H} \otimes \mathcal{H}$, with for instance $|\uparrow\rangle_1 \otimes |\downarrow\rangle_2$ describing a state with the spin at position \mathbf{r}_1 (\mathbf{r}_2) in an up (down) state. Similarly, a state of two free particles with momenta p_1 and p_2 as in the first example would be $|p_1, p_2\rangle = |p_1\rangle \otimes |p_2\rangle$. An immediate consequence is the exponential scaling of the size of the composite Hilbert space, $\mathcal{H}^{(N)}$, in the number of particles, N , with $\dim(\mathcal{H}^{(N)}) = \dim(\mathcal{H})^N$. This *exponential wall* is the main cause of the complexity of the quantum many-body problem. As such, every method in this dissertation can be considered as a way of avoiding it and/or tearing it down.

2.1.2 Indistinguishable particles and second quantization

In the previous Section, the absence of motional degrees of freedom in the qubits allowed to distinguish them based on their fixed positions. This stands in stark contrast to the free-moving particles, which were completely indistinguishable. Indeed, the Hamiltonian governing a system of indistinguishable particles should be invariant under a permutation P_σ ($\sigma \in S_N$) of these particles¹. Consequently, one could attribute a quantum number to each energy eigenstate, labeling the irreducible representation (irrep) by which it transforms. While these eigenstates can generally transform non-trivially, measurements must remain unaffected by permutation of particle labels, leading to wave functions that can only transform according to one-dimensional representations of the permutation group. The two 1D irreps are the trivial irrep, $\Gamma_+(\sigma) = 1$, applicable to bosonic systems, and the sign representation, $\Gamma_-(\sigma) = \epsilon_\sigma$ (the Levi-Civita symbol), corresponding to fermionic systems. The spin-statistics theorem formalizes this argument in 3 + 1 (or more) space-time dimensions [4]. However, in non-relativistic quantum mechanics, as employed here, or in lower dimensions, fermionic or bosonic particle statistics has to be postulated or considered as a phenomenological input. For instance, the Planck law of black body radiation illustrates the motivation for applying bosonic statistics to photons, while the stability of matter is a consequence of Pauli's exclusion principle, leading to the adoption of Fermi statistics for electrons.

Let us reconsider the example of two free-moving particles. By imposing either a fully symmetric or anti-symmetric structure on the composite state, we can express it as

$$|p_1, p_2\rangle = \frac{1}{\sqrt{2}} (|p_1\rangle |p_2\rangle \pm |p_2\rangle |p_1\rangle) \quad (2.4)$$

where we omitted the tensor product symbols. More generally, the Hilbert space for a bosonic (fermionic) N -particle system is given by $\mathcal{H}^{(N)} = S_\pm \mathcal{H}^{\otimes N}$ where S_\pm is the operator responsible for the (anti-)symmetrization. If we consider a basis of the single-particle Hilbert space, $\{|i\rangle\}$ with i labeling the modes, a basis for the N -particle Hilbert space becomes

$$S_\pm (|i_1\rangle |i_2\rangle \dots |i_N\rangle) = \frac{1}{\sqrt{N!}} \sum_{\sigma \in S_N} \Gamma_\pm(\sigma) |i_{\sigma(1)}\rangle |i_{\sigma(2)}\rangle \dots |i_{\sigma(N)}\rangle , \quad (2.5)$$

i.e. (anti-)symmetrized versions of single particle mode product states. For fermions this leads to the famous Slater determinant where the overlap between two states can be

¹While introduced as a symmetry here, this constraint is actually stronger, *i.e.* a superselection rule.

expressed as

$$\langle j_N | \dots \langle j_1 | S_-^\dagger S_- | i_1 \rangle \dots | i_N \rangle = \begin{vmatrix} \langle j_1 | i_1 \rangle & \langle j_1 | i_2 \rangle & \dots & \langle j_1 | i_N \rangle \\ \langle j_2 | i_1 \rangle & \langle j_2 | i_2 \rangle & \dots & \langle j_2 | i_N \rangle \\ \vdots & \vdots & \ddots & \vdots \\ \langle j_N | i_1 \rangle & \langle j_N | i_2 \rangle & \dots & \langle j_N | i_N \rangle \end{vmatrix}. \quad (2.6)$$

A fermionic many-body state with two particles occupying the same mode hence yields zero: the *Pauli exclusion principle*. For bosons on the other hand, the symmetrization yields a permanent with the overlap between two N -boson states given by

$$\langle j_N | \dots \langle j_1 | S_+^\dagger S_+ | i_1 \rangle \dots | i_N \rangle = \sum_{\sigma \in S_N} \langle j_1 | i_{\sigma(1)} \rangle \langle j_1 | i_{\sigma(2)} \rangle \dots \langle j_1 | i_{\sigma(N)} \rangle. \quad (2.7)$$

This formula is identical to the fermionic case, but now with a permanent instead of a determinant, leading to the infamous boson sampling problem [5].

The particle-centered description of many-body physics discussed up to now is widely used, e.g. expanding molecular wavefunctions as (linear combinations of) Slater determinants (see Sec. 2.4.1). However, in doing so, one fixes the particle number N and can thus not describe states where the particle number fluctuates as for instance happens in superconducting states. In this regard, an alternative, mode-centered perspective would be preferred. This approach is more widely known as *second quantization* [6] and starts from the construction of the so called Fock space, $\mathcal{F}(\mathcal{H})$ [7], a direct sum of the N -particle Hilbert space for all natural N ,

$$\mathcal{F}(\mathcal{H}) = \bigoplus_{N=0}^{+\infty} \mathcal{H}^{(N)} = \bigoplus_{N=0}^{+\infty} S_\pm \mathcal{H}^{\otimes N}. \quad (2.8)$$

By definition, states with a definite but different particle number are orthogonal. Note that states without particles also appear in this sum. The unit vector $|\Omega\rangle$ (also denoted by $|0\rangle$) in this 1D subspace is the vacuum. Within the Fock space, one can introduce operators that transform between different particle numbers, e.g. a creator a_i^\dagger that adds a particle in mode i to the states, thus increasing the total particle number by 1. Expressing the inner product between them, one can show that every (anti-)symmetrized many-body state can then be written as

$$S_\eta |i_1\rangle |i_2\rangle \dots |i_N\rangle = a_{i_1}^\dagger a_{i_2}^\dagger \dots a_{i_N}^\dagger |\Omega\rangle \quad (2.9)$$

when

$$\begin{aligned} [a_i^\dagger, a_j^\dagger] &= 0 & [a_i, a_j^\dagger] &= \langle i | j \rangle & \text{if } \eta = +1 \\ \{a_i^\dagger, a_j^\dagger\} &= 0 & \{a_i, a_j^\dagger\} &= \langle i | j \rangle & \text{if } \eta = -1 \end{aligned} \quad (2.10)$$

These are the well-known canonical (anti-)commutation relations for bosonic (fermionic) creation operators and their duals, the annihilation operators. An immediate consequence is that $a_i |\Omega\rangle = 0 \forall i$, providing a direct characterization of the vacuum in terms of the annihilation operators. The key ingredient in the switch to second quantization now

comes down to describing/labeling states by their occupation of the various modes rather than by the mode each particle occupies. *I.e.* orthonormal Fock space basis states are expressed as

$$|n_1, n_2, \dots\rangle = \frac{1}{\sqrt{n_1! n_2! \dots}} a_1^{\dagger n_1} a_2^{\dagger n_2} \dots |\Omega\rangle \quad (2.11)$$

where $n_i \in \mathbb{N}$ ($\in \{0, 1\}$) denotes the occupation of mode i for bosons (fermions). The action of the creation and annihilation operators on these basis states yields

$$\begin{aligned} a_i |n_1, n_2, \dots, n_i, \dots\rangle &= \eta^{n_1+n_2+\dots+n_{i-1}} \sqrt{n_i} |n_1, n_2, \dots, n_i - 1, \dots\rangle \\ a_i^\dagger |n_1, n_2, \dots, n_i, \dots\rangle &= \eta^{n_1+n_2+\dots+n_{i-1}} \sqrt{1 + \eta n_i} |n_1, n_2, \dots, n_i + 1, \dots\rangle. \end{aligned} \quad (2.12)$$

We can also introduce the particle number operator in a certain mode, $a_i^\dagger a_i$, as well as the total particle number,

$$N = \sum_i a_i^\dagger a_i. \quad (2.13)$$

Note that both are diagonal in the second-quantized basis states of Eq. (2.11). The total particle number is also invariant under an orthonormal basis change of single particle modes, $\{|i\rangle\} \rightarrow \{|i'\rangle\}$. Indeed, performing this basis change, the creator and annihilators transform as

$$a_{i'}^\dagger = \sum_i \langle i | i' \rangle a_i^\dagger \quad \text{and} \quad a_{i'} = \sum_i \langle i' | i \rangle a_i \quad (2.14)$$

so that $N = \sum_i a_i^\dagger a_i = \sum_i \sum_{i', j'} \langle i' | i \rangle a_{i'}^\dagger \langle i | j' \rangle a_{j'} = \sum_{i', j'} a_{i'}^\dagger a_{j'}$ due to completeness. Other relevant operators we will encounter are the particle number conserving, one-body operators. Consider therefore an operator $O^{(1)}$ acting in $\mathcal{H}^{(1)}$ so that it can be expanded as $O^{(1)} = \langle i | O^{(1)} | j \rangle |i\rangle \langle j|$. Application of this $O^{(1)}$ on every particle in an N -particle state yields

$$\begin{aligned} O(|i_1\rangle_1 |i_2\rangle_2 \dots |i_N\rangle_N) &= \sum_{n=1}^N O_n^{(1)} (|i_1\rangle_1 |i_2\rangle_2 \dots |i_N\rangle_N) \\ &= \sum_{n=1}^N \langle j_n | O_n^{(1)} | i_n \rangle (|i_1\rangle_1 |i_2\rangle_2 \dots |j_n\rangle_n \dots |i_N\rangle_N) \end{aligned} \quad (2.15)$$

Using Eq. (2.9) in combination with linearity, one proves that the same result is obtained for any Fock space state by application of

$$O = \sum_{i,j} \langle i | O^{(1)} | j \rangle a_i^\dagger a_j. \quad (2.16)$$

Similarly, a Fock space representation of two-particle operators, $V^{(2)} \in \mathcal{H}^{(2)}$, applied on every couple of particles, is given by

$$\begin{aligned} V &= \sum_{i \leq j} \sum_{k \leq l} \langle i, j | V^{(2)} | k, l \rangle a_i^\dagger a_j^\dagger a_l a_k \\ &= \frac{1}{4} \sum_{i,j,k,l} \langle i, j | V^{(2)} | k, l \rangle a_i^\dagger a_j^\dagger a_l a_k. \end{aligned} \quad (2.17)$$

Finally, we will encounter particle number violating operators of the form

$$C = \sum_{i,j} C_{i,j} a_i^\dagger a_j^\dagger + h.c., \quad (2.18)$$

also called pairing operators, in the context of superconductivity.

2.1.3 Extended quantum systems

Throughout this work and more generally throughout condensed matter physics, the single-particle modes one encounters will typically be localized on a lattice (see Sec. 2.4.2). If the unit cell of this d -dimensional lattice is spanned by the vectors $\{\mathbf{a}_1, \mathbf{a}_2, \dots, \mathbf{a}_d\}$, vertices can be labeled by $\mathbf{R} = \sum_{i=1}^d n_i \mathbf{a}_i$ where $n_i \in \mathbb{Z}$ in the case of an infinite lattice. Finite lattices where $n_i = 0, \dots, N_i$ (and the total number of lattice sites $N_s = \prod_{i=1}^d N_i < \infty$) will be considered as well. There, the Fock space for the complete lattice can be constructed in two equivalent ways. Either one starts from a local single-particle Hilbert space \mathcal{H} at site \mathbf{r} (with basis $\{|i\rangle_{\mathbf{R}}\}$), builds a local Fock space $\mathcal{F}(\mathcal{H})$ from this and defines the Fock space for the complete lattice as $(\mathcal{F}(\mathcal{H}))^{\otimes N_s}$. Alternatively, one first defines a single-particle Hilbert space for the complete lattice \mathcal{H}' (with $\{|i, \mathbf{R}\rangle\}$ as a possible basis) and builds the global Fock space on top of this, *i.e.* $\mathcal{F}(\mathcal{H}')$. Assuming either a finite dimension of \mathcal{H} (e.g. in the case of spins, fermions or bosons with a fixed maximal modal occupation, the so-called hard-core bosons) or a countable infinite dimension (e.g. in the case of common bosons), it is straightforward to show that both constructions are unitarily equivalent since $\mathcal{H}' \cong \mathcal{H}^{\otimes N_s}$. The relevant creation and annihilation operators will be denoted by $a_{\mathbf{R},i}^\dagger$ and $a_{\mathbf{R},i}$, thus allowing for an additional, local label like a spin index.

For lattices of infinite size, *i.e.* lattices in the so-called *thermodynamic limit*, things become more difficult as taking the N_s -fold tensor product of a Hilbert space is not properly defined when $N_s = +\infty$. Therefore, a more abstract but mathematically more sound construction of many-body quantum mechanics starts from the C^* -algebra spanned by the operators defining a theory [8]. The self-adjoint elements in this algebra correspond to observables and can be represented as operators acting on a Hilbert space \mathcal{H} by invoking the Gelfand-Naimark-Segal (GNS) construction [9, 10]. The main advantage is that infinite tensor products of C^* -algebras are formally defined so that the resulting Hilbert space is defined as well. However, the GNS mapping from the C^* -algebra to the representation on \mathcal{H} makes use of a selected vector $|\Psi\rangle \in \mathcal{H}$, typically the ground state of the Hamiltonian under consideration. Consequently, the Hilbert space representation depends on this vector. For a finite number of degrees of freedom all these representations are unitarily equivalent to the standard picture considered before. When an infinite number of degrees of freedom is present on the other hand, different choices for $|\Psi\rangle$ can yield different, completely disjoint $\mathcal{H}^{|\Psi\rangle}$. Therefore, we will always assume that the ground state was used for the GNS construction and work in the resulting Hilbert space. An extra complication arises when the ground state space is degenerate. Then, one can construct multiple Hilbert spaces $\mathcal{H}^{|\Psi\rangle}$ for a set $\{|\Psi\rangle\}$ spanning the ground state space and use the direct sum of all these disjoint spaces as a *total* Hilbert space \mathcal{H} . Based on this, we will always assume the existence of a total Hilbert space onto which the operators defining the theory (and thus also the Hamiltonian) can be represented, even in the case of an extended system with an infinite number of degrees of freedom. Doing so, we will

not go into the specifics of how this space came about but rather take a pragmatic approach and focus on exploiting the advantages of the infinite nature of the system. For instance, a macroscopically large system that is fully translation invariant in the bulk but nevertheless contains a boundary (as does every realistic system), will typically be modeled as infinitely large to maximally exploit the translation invariance.

Matters become even more complicated when moving to extended systems where the positional label becomes continuous, *i.e.* when considering field theories. As these are not the main topic of this dissertation and we only touch upon them sporadically, we will take an even more pragmatic approach here and just assume that some Fock space can be constructed onto which the field operators, $\psi_\sigma(\mathbf{r})$ (*i.e.* the continuous variants of the discrete annihilation operators, $a_{\mathbf{r},\sigma}$), act in their standard way with

$$\begin{aligned}\psi_\sigma^\dagger(\mathbf{r})\psi_\tau^\dagger(\mathbf{s}) &= \eta\psi_\tau^\dagger(\mathbf{s})\psi_\sigma^\dagger(\mathbf{r}) \\ \psi_\sigma(\mathbf{r})\psi_\tau^\dagger(\mathbf{s}) &= \delta_{\sigma,\tau}\delta(\mathbf{r}-\mathbf{s}) + \eta\psi_\tau^\dagger(\mathbf{s})\psi_\sigma^\dagger(\mathbf{r})\end{aligned}\tag{2.19}$$

and $\eta = +1(-1)$ for bosonic (fermionic) fields. The second quantized form of the Hamiltonian can then be expressed in terms of these field operators. Also alternative single particle modes can be utilized. E.g. for the example we started this Chapter with, we can build creation operators for momentum p by making use of the single-particle modes,

$$\psi^\dagger(p) = \int dx \frac{1}{\sqrt{2\pi}} e^{ipx} \psi^\dagger(x),\tag{2.20}$$

i.e. by Fourier transforming. Due to completeness, these operators also satisfy the canonical (anti-)commutation relations, generally yielding

$$\begin{aligned}\psi_\sigma^\dagger(\mathbf{p})\psi_\tau^\dagger(\mathbf{q}) &= \eta\psi_\tau^\dagger(\mathbf{q})\psi_\sigma^\dagger(\mathbf{p}) \\ \psi_\sigma(\mathbf{p})\psi_\tau^\dagger(\mathbf{q}) &= \delta_{\sigma,\tau}\delta(\mathbf{p}-\mathbf{q}) + \eta\psi_\tau^\dagger(\mathbf{q})\psi_\sigma^\dagger(\mathbf{p})\end{aligned}\tag{2.21}$$

in d dimensions. The exemplary Hamiltonian,

$$H = \frac{P^2}{2m} = \int dp \frac{p^2}{2m} |p\rangle \langle p|,\tag{2.22}$$

can hence be reformulated in second quantization as

$$\begin{aligned}H &= \int dp \frac{p^2}{2m} \psi^\dagger(p)\psi(p) \\ &= \int dx \psi^\dagger(x) \left(\frac{-1}{2m} \frac{\partial^2}{\partial x^2} \right) \psi(x) \\ &= \int dx \frac{1}{2m} \frac{\partial\psi^\dagger}{\partial x}(x) \frac{\partial\psi}{\partial x}(x).\end{aligned}\tag{2.23}$$

As a part of our practical approach, technical difficulties related to double infinite nature of the positional labels (*i.e.* there is neither an ultraviolet, nor an infrared cut-off) like the corresponding orthogonality catastrophes [11, 12] will not be considered in this work.

A crucial quantity in extended quantum systems is the (excitation) *gap*. This is the energy difference between the ground state and the first excited state, in the thermodynamic limit. The latter is important as the ground state could be near degenerate on a finite lattice with low-lying energy levels in a small window that closes when taking the $N_s \rightarrow +\infty$ limit. The gap is then obtained as the difference between this degenerate ground state and the first excited state. When the (possibly degenerate) ground state is immediately followed by a continuum of excited states, the gap disappears and we obtain a *gapless* or *critical* model.

2.1.4 Density operators and mixed states

C^* -algebras were introduced as a means to define quantum mechanics in a more rigorous way. While we do not necessarily worry about the accompanying technicalities, these algebras demonstrated the central importance of operators. For this reason, but also more generally, it pays to rephrase the postulates of quantum mechanics in terms of operators, ρ , acting on a Hilbert space, \mathcal{H} , rather than (solely) in terms of vectors $|\psi\rangle$ living in this Hilbert space. The rephrased axioms read:

- The state of a quantum system is characterized by a positive operator, ρ , acting on a Hilbert space \mathcal{H} and having a trace equal to 1. These operators are called density operators.
- Systems are combined by taking tensor products of the corresponding Hilbert spaces. In the case of indistinguishable components, the resulting space has to be (anti-)symmetrized in the case of bosons (fermions) with (half-)integer spin.
- Physical observables, A , correspond to self-adjoint operators acting on the Hilbert space, *i.e.* $A \in \mathcal{L}(\mathcal{H})$ and $A = A^\dagger$.
- When performing a measurement of an observable A , the state ρ will collapse onto (the projector on) one of the eigenstates $|\lambda_i\rangle$ of A , yielding the corresponding eigenvalue λ_i as the measurement outcome. The probability hereof is given by Born's rule $P(\lambda_i) = \text{tr}(\rho |\lambda_i\rangle \langle \lambda_i|)$. As a result, the expectation value of A for the state ρ is given by $\text{tr}(\rho A)$.
- Time evolution of a state $\rho(t)$ is governed by unitary operators, $U(t) = e^{-iHt}$, with H the Hamiltonian, e.g. evolving from $\rho(0)$ to $\rho(t)$, one has

$$\rho(t) = U(t)\rho(0)U^\dagger(t). \quad (2.24)$$

Note that we added the tensor product structure for many-body quantum mechanics and the (anti-)symmetry constraint for indistinguishable particles as an additional postulate. The case of a state characterized by a vector $|\psi\rangle$, *i.e.* a so-called *pure state*, fits nicely into this formalism by associating them with $\rho = |\psi\rangle \langle \psi|$. Indeed, the original formulation of the postulates follows from the updated one if this density operator is inserted. More importantly, this redefinition of a state is broader and also allows for what we call *mixed states*. An interesting example of such a mixed state is

$$\rho = \frac{1}{Z} e^{-\beta H}, \quad (2.25)$$

representing a canonical ensemble of states for a system with Hamiltonian H in contact with a heat bath at temperature T and $\beta = \frac{1}{T}$. Note that the normalization factor $Z = \text{tr}(e^{-\beta H})$ exactly corresponds to the partition function. Furthermore, (the projector on) every eigenstate of H with energy E_i appears in ρ together with a Boltzmann weight $Z^{-1} e^{-\beta E_i}$. At zero temperature ρ will hence reduce to the ground state space projector and minimize the energy expectation value $\langle E \rangle = \text{tr}(\rho H)$. At higher temperatures, on the other hand, the canonical ensemble of states will rather minimize the (Helmholtz) free energy,

$$\langle F \rangle = \langle E \rangle - T \langle S \rangle = \text{tr}(\rho H) + T \text{tr}(\rho \ln \rho) \quad (2.26)$$

where $\langle S \rangle = -\text{tr}(\rho \ln \rho)$ is the Von Neumann entropy. One can equally well consider the grand canonical ensemble

$$\rho = \frac{1}{Z} e^{-\beta(H-\mu N)}, \quad (2.27)$$

for a system at temperature T in contact with a particle reservoir at chemical potential μ . Here, N is the total particle number operator (Eq. (2.13)) while Z corresponds to the grand-canonical partition function. This ρ minimizes the Landau free energy,

$$\langle \Phi \rangle = \langle E \rangle - \mu \langle N \rangle - T \langle S \rangle = \text{tr}(\rho H) - \mu \text{tr}(\rho N) + T \text{tr}(\rho \ln \rho). \quad (2.28)$$

As a basic example, the (spinless) free boson/fermion gas generalizes Eq. (2.23) to 3D with for the single-particle modes the plane waves, $\psi_{\mathbf{p}}(\mathbf{r}) = \langle \mathbf{p} | \mathbf{r} \rangle = \frac{e^{i\mathbf{p}\cdot\mathbf{r}}}{(2\pi)^{\frac{d}{2}}}$, so that

$$H = \int d\mathbf{p} \frac{\mathbf{p}^2}{2m} \psi^{\dagger}(\mathbf{p}) \psi(\mathbf{p}) = \int d\mathbf{p} e(\mathbf{p}) \psi^{\dagger}(\mathbf{p}) \psi(\mathbf{p}), \quad (2.29)$$

where $e(\mathbf{p})$ is the single-particle dispersion relation. The mixed state corresponding to the grand-canonical ensemble hence is

$$\rho = \frac{1}{Z} \exp \left(\int d\mathbf{p} (e(\mathbf{p}) - \mu) \psi^{\dagger}(\mathbf{p}) \psi(\mathbf{p}) \right) \quad (2.30)$$

and for the partition function we obtain

$$Z = \prod_{\mathbf{p}} \left(1 - \eta e^{-\beta(e(\mathbf{p}) - \mu)} \right)^{-\eta}, \quad (2.31)$$

where again $\eta = +1(-1)$ for bosons (fermions). As a result, the modal occupation reads

$$\langle n_{\mathbf{p}} \rangle = \langle \psi^{\dagger}(\mathbf{p}) \psi(\mathbf{p}) \rangle = \left(e^{\beta(e(\mathbf{p}) - \mu)} - \eta \right)^{-1}, \quad (2.32)$$

i.e. the Bose-Einstein (Fermi-Dirac) distribution. We will mostly consider low or zero temperatures as quantum effects are more pronounced and not watered down by thermal fluctuations. For the Bose gas, $T = 0$ implies that when $\mu > 0$, all bosons will populate the same $\mathbf{p} = 0$ state, yielding an infinite particle density: a Bose-Einstein condensate (BEC) forms [13, 14]. As an infinite particle number is not physical, it is more common to study the BEC in the canonical ensemble with a fixed particle number N . Furthermore, integration of repulsive (Van der Waals) interactions, can prevent all of the bosons to condense, thus stabilizing the condensate with a finite filling fraction. For fermions, on

the other hand, the Pauli exclusion principle makes sure that $\langle n_{\mathbf{p}} \rangle \leq 1$. Consequently, the grand canonical ensemble makes more sense now and as H always appears together with $-\mu N$, the latter is typically regarded as an integral part of the Hamiltonian. μ then serves as a parameter regulating the particle density. Indeed, the Fermi gas at $T = 0$ occupies (vacates) all modes where $e(\mathbf{p}) < e_F (> e_F)$ with $e_F = \mu(T = 0)$ the so-called Fermi level. In this way, one obtains a discrete jump in $\langle n_{\mathbf{p}} \rangle$ at the Fermi momentum $|\mathbf{p}| = p_F = \sqrt{2m e_F}$. This is called a *Fermi surface*.

Having extended the definition of states to positive operators, $\rho \in \mathcal{L}(\mathcal{H})$, we now turn to maps between states, e.g. describing time evolution. Obviously, we would like these so-called superoperators or channels, $\mathcal{E} : \mathcal{L}(\mathcal{H}) \rightarrow \mathcal{L}(\mathcal{H})$ to be linear. Additionally, normalization of ρ should imply the same to be true for $\mathcal{E}(\rho)$, *i.e.* the channel has to be trace-preserving. Finally, also positivity of ρ should be retained. Surprisingly, requiring the latter for \mathcal{E} alone is insufficient as the tensor product of two such positive maps no longer has to be positive. Therefore, the positivity constraint is replaced by complete positivity, meaning that $\text{id}_R \otimes \mathcal{E}$ is positive as a channel $\mathcal{L}(\mathcal{H}_R \otimes \mathcal{H}) \rightarrow \mathcal{L}(\mathcal{H}_R \otimes \mathcal{H})$ for each auxiliary Hilbert space \mathcal{H}_R with id_R the identity channel on this space. Physical channels between states thus correspond to completely positive and trace-preserving (CPTP) maps [15]. For these CPTP maps, the Kraus representation theorem [16] states the following:

For any CPTP $\mathcal{E} : \mathcal{L}(\mathcal{H}) \rightarrow \mathcal{L}(\mathcal{H})$ there exists a family of Kraus operators $M_l \in \mathcal{L}(\mathcal{H})$ ($l = 1, \dots, r$ with $r \leq \dim(\mathcal{H})^2$) such that

$$\mathcal{E}(X) = \sum_l M_l X M_l^\dagger \quad (2.33)$$

and $\sum_l M_l M_l^\dagger = \mathbb{1}$. Conversely, any mapping of this form is CPTP. Furthermore, different sets of Kraus operators are linked by a unitary transformation.

The case of a unitary transformation of pure states hence fits nicely in the framework of CPTP maps as this unitary can be seen as the single Kraus operator representing its corresponding \mathcal{E} . The freedom in the choice of Kraus operators now comes down to a single arbitrary phase.

2.2 Correlations and entanglement

One the most striking features setting quantum systems apart from their classical analogues is *entanglement*. Upon its discovery by Schrödinger in 1935 [17] the notion of entanglement was highly debated with Nobel laureates Bohr and Einstein as prominent advocates pro and contra. Together with Podolsky and Rosen, the latter wrote a well-known paper that based on the concepts of locality (no instantaneous (“spooky”) action at a distance) and realism (things can exist without the need for them to be observed) judged quantum mechanics to be incomplete and in need of hidden variables [18]. Based on Bohm’s reinterpretation of the Einstein-Podolsky-Rosen (EPR) paradox in terms of spin measurements on pairs of entangled electrons [19], Bell came up with a similar reinterpretation but saw that in contrast to the EPR and Bohm variant, his version could not be explained by any local hidden-variable theory [20]. His proof hereof was based on

inequalities expressing a constraint on the amount of correlation that can exist between two entangled partners when mediated by a local hidden-variable theory. Counterexamples (realized in experiments that were awarded last year's Nobel prize [21, 22]) show that these Bell inequalities can indeed be exceeded by entangled quantum states and thus that quantum mechanics cannot be a local hidden-variable theory as Einstein wished.

To translate this short historical overview to the quantum mechanical axioms proposed in the previous Section, we consider a bipartite system composed of the disjoint systems A and B with \mathcal{H}^A and \mathcal{H}^B as their respective Hilbert spaces. To the subsystems we assign two bounded operators each, A_0, A_1 and B_0, B_1 , all having the eigenvalues ± 1 . Within this basic setup, the Bell inequality can be rephrased as the Clauser-Horne-Shimony-Holt (CHSH) inequality [23], stating that for any state

$$C(\rho) = \langle A_0 B_0 \rangle + \langle A_0 B_1 \rangle + \langle A_1 B_0 \rangle - \langle A_1 B_1 \rangle \leq 2. \quad (2.34)$$

As a simple counterexample, let A and B be qubits and $A_0 = \sigma^x$, $A_1 = \sigma^y$ and $B_0 = \sigma^y$, $B_1 = \sigma^z$, then the (pure) singlet state $|\psi\rangle = \frac{1}{\sqrt{2}}(|\uparrow\rangle_A |\downarrow\rangle_B - |\downarrow\rangle_A |\uparrow\rangle_B)$ yields $C(|\psi\rangle \langle \psi|) = 2\sqrt{2}$. Hence, quantum mechanics can violate the classical Bell bounds. The essential feature of these non-classical or entangled states is that their density operator cannot be written as

$$\rho = \sum_k p_k \rho_k^A \otimes \rho_k^B \quad (2.35)$$

where $\{\rho_k^A\}$ ($\{\rho_k^B\}$) are density operators on the A (B) subsystem so that $p_k \geq 0$ and $\sum_k p_k = 1$ because of positivity, respectively, normalization. In a general setting, a state with this decomposition is called separable. Hence, the singlet state is not separable but entangled. This negative and binary definition of entangled states ("not a separable state") led to the search for a positive and more gradual/non-binary formulation. For mixed states this search is still going. For pure states, on the other hand, the entanglement spectrum and entanglement entropy provide the solution. To define these entanglement measures, consider a general bipartite and pure state,

$$|\psi\rangle = \sum_{ij} c_{ij} |i\rangle_A |j\rangle_B, \quad (2.36)$$

where $\{|i\rangle_A\}$ and $\{|i\rangle_B\}$ are bases for \mathcal{H}^A and \mathcal{H}^B . We can perform a singular-value decomposition, $c_{ij} = U_{ik} \lambda_k V_{jk}$ with λ_k ($k = 1, \dots, D$ and $D = \text{rank}(c)$) the singular values, yielding

$$|\psi\rangle = \sum_k \lambda_k |\phi_k^A\rangle_A |\phi_k^B\rangle_B, \quad (2.37)$$

also called a Schmidt decomposition, where $|\phi_k^A\rangle_A = U_{ik} |i\rangle_A$ and $|\phi_k^B\rangle_B = V_{jk} |j\rangle_B$ both constitute orthonormal sets. This makes the difference between an entangled and a separable pure state very visible. Indeed, for the latter only a single $\lambda_k \neq 0$ while for an entangled state multiple non-zero λ_k appear with $\sum_k \lambda_k^2 = 1$ because of normalization. For this reason $\{\lambda_k^2\}$ is called the *entanglement spectrum*. Since it can be interpreted as a classical probability distribution, we can associate a Shannon entropy [24] with it, the *entanglement entropy*,

$$S^{A,B} = - \sum_k \lambda_k^2 \ln \lambda_k^2, \quad (2.38)$$

serving as measure of how entangled $|\psi\rangle$ is w.r.t. the subdivision in A and B . Note that restrictions of this state to both subsystems can be described by

$$\begin{aligned}\rho^A &= \text{tr}_B(|\psi\rangle\langle\psi|) = \sum_k \lambda_k^2 |\phi_k^A\rangle_A \langle\phi_k^A|_A , \\ \rho^B &= \text{tr}_A(|\psi\rangle\langle\psi|) = \sum_k \lambda_k^2 |\phi_k^B\rangle_B \langle\phi_k^B|_B ,\end{aligned}\quad (2.39)$$

the so-called reduced density operators (or matrices). For an entangled state these are mixed and their Von Neumann entropies, $S(\rho^A) = S(\rho^B)$, exactly corresponds to the entanglement entropy.

Direct inspection of its definition shows that the entanglement entropy is maximized when the entanglement spectrum is uniform, $\lambda_k^2 = \frac{1}{D}$ where $D = \min(\dim(\mathcal{H}^A), \dim(\mathcal{H}^B))$, yielding $S = \ln D$. These maximally entangled states also maximally violate the Bell inequalities. Indeed, for the CHSH case Cirel'son showed that the correct bound is $C(\rho) \leq 2\sqrt{2}$, exactly the value for the maximally entangled singlet state [25]. Another important feature of entanglement is its monogamy: when S is maximal between subsystem A and B , having an equally large Hilbert space, there can be no entanglement between these systems and any other partner [26, 27, 28]. For the Von Neumann entropy one has the strong sub-additivity property [29],

$$S(\rho^{A\cup B}) + S(\rho^{A\cap B}) \leq S(\rho^A) + S(\rho^B), \quad (2.40)$$

so that for two disjoint systems the mutual information, defined by

$$I(A, B) = S(\rho^A) + S(\rho^B) - S(\rho^{A\cup B}), \quad (2.41)$$

is restricted between 0 and $2S^{A,B}$ (the value in case of a pure $\rho^{A\cup B}$). This mutual information limits the correlations that can exist between the A and B subsystem [30],

$$(\Gamma_{A,B})^2 \leq 2|O^A|^2|O^B|^2 I(A, B), \quad (2.42)$$

where the norms are spectral norms and

$$\Gamma_{A,B} = \langle O^A O^B \rangle - \langle O^A \rangle \langle O^B \rangle \quad (2.43)$$

is the connected two-point correlation function between O^A and O^B in $\rho^{A\cup B}$. The latter term is called the disconnected part of $\Gamma_{A,B}$.

In the context of C^* -algebras, Hilbert spaces are constructed from a complete set of operators (e.g. a set of creation and annihilation operators). Based on these, one can define the (connected) correlation matrix between two systems in a certain state as the collection of all (connected) two-point correlation functions pertaining these operator sets. In extended systems, it can be generalized to each pair of local Hilbert spaces, yielding

$$\Gamma_{\mathbf{x},\mathbf{y}}^{ij} = \langle O_{\mathbf{x},i} O_{\mathbf{y},j} \rangle - \langle O_{\mathbf{x},i} \rangle \langle O_{\mathbf{y},j} \rangle . \quad (2.44)$$

We can utilize this real-space correlation matrix to define a correlation length, ξ , where

$$\xi^{-1} = \lim_{|\mathbf{x}-\mathbf{y}| \rightarrow +\infty} \max_{ij} \left(-\frac{\log |\Gamma_{\mathbf{x},\mathbf{y}}^{ij}|}{|\mathbf{x}-\mathbf{y}|} \right), \quad (2.45)$$

though many variations are possible (and applied in this work). An overarching property is that ξ is finite only when $\Gamma_{\mathbf{x}\mathbf{y}}^{ij}$ decays at least exponentially with the separation $|\mathbf{x} - \mathbf{y}|$. Hastings proved that this always happens for unique ground states of gapped Hamiltonians [31, 32]. When the gap closes (in the next Section we will see that this typically occurs at (second-order) phase transitions), the ground state correlations decay polynomially in correspondence with an infinite correlation length. As such, ground state correlation lengths behave similarly as the inverse of the excitation gap, which indeed sets a length scale. Based on this observation, the terms “gap(less)” and “(non-)critical” are used for both (ground) states and (parent) Hamiltonians. We also remark that the correlation matrix is the defining quantity of Gaussian states, a property called *Wick’s theorem* [33]. We will heavily use these Gaussian states throughout this work and therefore treat them in more detail in the following Chapter.

In the preceding paragraphs, we introduced entanglement and its standard measure for pure states, the entanglement entropy. Through the mutual information, we established a link between correlations and entanglement. These correlations are typically limited in gapped systems due to a finite correlation length, suggesting a restricted entanglement content. Indeed, since the early 2000s, it has become increasingly clear that ground states of local and gapped Hamiltonians have a specific entanglement structure: the leading term in the entanglement entropy between a subregion and its complement scales with the area of its boundary [34, 35]. This is the *area law* of entanglement. While rigorously demonstrated in 1D [36], there is currently no proof for higher dimensions, although numerous instances support its validity (e.g. exemplified by successful applications of the PEPS *Ansatz* (see also Sec. 2.5)) [37, 38, 39, 40]. Apart from the leading contribution, sub-leading terms have also been examined and found to contain markers of topological behavior (see Sec. 2.4.2) [41, 42, 43, 44, 45]. For gapless Hamiltonians correlations decay slower, allowing the area law to be violated. Two notable examples are gapless 1D systems with long-wavelength properties that can be described by conformal field theory (CFT), and critical, fermionic systems with a co-dimension one Fermi surface in 2D (or higher). In the former, the entanglement of a subregion with linear size L scales logarithmically [46, 47, 48] and in the latter it scales as $S \sim L^{d-1} \log L$, with d the spatial dimension [49, 50, 51, 52]. In the final Section of this Chapter we will introduce Tensor Network States (TNS) like Matrix Product States (MPS) and Projected Entangled-Pair States (PEPS). They thank their versatile applicability to a built-in area law of entanglement making them extremely suited for the description of gapped states. However, does this mean that they become useless for gapless states? On the contrary. By describing how an area-law state (*i.e.* a TNS) best approximates the non-area-law ground state, scaling procedures can be devised to extract very precise results for the critical state [53, 54]. Variations of this method have been applied in both 1D [55] and 2D [56, 57, 58, 59] but were not yet used for systems with a Fermi systems. In Sec. 5.4.2 we show that this is indeed possible.

2.3 Symmetries and phases

The notion of different phases of matter is a very tangible one as the materials we experience everyday can roughly be organized in three classes: solids, liquids and gases,

each exhibiting distinct but universal characteristics. Although conceptually tangible, it was only in the latter half of the previous century that the appropriate physical tools to comprehend these phases and the transitions between them were developed. To do so, symmetry has proven to be indispensable. We introduce the concept of a symmetry starting from a (symmetry) group, G , that can be either discrete or continuous. Wigner proved that with each $g \in G$ there corresponds a symmetry transformation that can be represented by an (anti-)unitary operator, $U(g)$, on the Hilbert space of the system under consideration [60]. We then say that a Hamiltonian is symmetric under G when $[H, U(g)] = 0 \forall g \in G$. This immediately implies that H can be block-diagonalized according to the irreducible representations (irreps) of G . Simple examples of symmetries related to space-time structure include translation and rotation symmetry or even more general Lorentz invariance. Additionally, internal symmetries can be considered. These correspond to transformations that act only within local Hilbert spaces. One then distinguishes between global symmetries, performing identical symmetry transformations at each position and gauge transformations where this is not the case. As an example of the former we consider a chain of immobile qubits where a global \mathbb{Z}_2 symmetry can be represented on the local Hilbert spaces by $U(g) = \mathbb{1}$ when $g = 0$ and $U(g) = \sigma^x$ when $g = 1$. For a spin polarized in the $\pm z$ direction it has the effect of flipping it. Within the context of Gaussian states and free Hamiltonians (see Chapter 3 and 5), it will be useful to restrict to symmetries that retain the quadratic structure of H . The resulting canonical transformations then map creation and annihilation operators to linear combinations thereof that preserve the (anti-)commutation relations. E.g. one can define a general particle-hole transformation for a set of fermions with creators $\{a_i^\dagger\}$ to be represented by a unitary operator, U , so that $Ua_iU^{-1} = U_{ij}^C a_j^\dagger$ where the scalars U_{ij}^C constitute a unitary matrix.

In the thermodynamic limit, global symmetries can manifest themselves in two different ways. Either the ground state is unique and transforms under a 1D, typically trivial, representation of the symmetry group, yielding a fully symmetric ground state, or there is a higher-dimensional ground state space, transforming according to a higher-dimensional representation, *i.e.* in a non-trivial way. The former case is called the Wigner-Weyl realization. The latter is the Nambu-Goldstone realization and displays *spontaneous symmetry breaking* [61]. A simple model, showcasing both, is the 1D transverse-field Ising model,

$$H = -J \sum_i \sigma_i^z \sigma_{i+1}^z - h \sum_i \sigma_i^x, \quad (2.46)$$

i.e. a spin- $\frac{1}{2}$ chain where i labels the sites. The first term with $J > 0$ will try to align spins with their neighbors in the z -direction while the second wants to align them with an external field h in the positive x -direction. The latter happens when $h \gg J$ and yields a single ground state with a Wigner-Weyl realization of the \mathbb{Z}_2 spin-flip symmetry of H . When the external field is very weak, on the other hand, the spins will align in the $\pm z$ direction but have the two options, all up or all down. The \mathbb{Z}_2 symmetry is thus spontaneously broken with a 2D ground state space, a Nambu-Goldstone realization. One can distinguish between both phases using the magnetization, σ_z , a so-called local order parameter whose expectation value vanishes in the symmetric phase but becomes non-zero everywhere in the symmetry-broken phase. At some intermediate field (the exact value in 1D simply is $h = J$), one expects an abrupt transition between both. Indeed,

the ground state degeneracy, being an integer, cannot change smoothly. In contrast, the ground state energy, $E_0 = \lim_{\beta \rightarrow +\infty} \text{tr}(He^{-\beta H})$, has to be continuous when adiabatically changing the parameters in H . For its derivatives, on the other hand, this does not apply. Consequently, a *first-order phase transition* is defined as a phase transition where the first derivative of E_0 is discontinuous. In quantum ground states, these transitions correspond to level crossings. The energy gap does not close and observable quantities such as an order parameter or the correlation length change discontinuously. Alternatively, E_0 's first derivative can be continuous across the phase transition with a higher-order derivative (typically the second-order corresponding to a susceptibility) diverging there. These are the *continuous phase transitions*. Due to their smooth nature, the order parameter and excitation gap approach zero in a continuous manner. The model thus becomes critical with an infinite correlation length in order to “forget” about the microscopic structure in a certain phase, thereby allowing it to continuously transition into another. This paradigm for the classification of phases, based on symmetry (groups) and spontaneous symmetry breaking, was christened the Landau-Ginzburg-Wilson theory [62, 63, 64, 65]. It is highly successful in describing phase transitions in thermodynamics where for instance freezing a disordered liquid can be seen as a spontaneous breaking of translational and rotational symmetries to go to an ordered solid. Quantum phase transitions, triggered by quantum instead of thermal fluctuations can be analyzed as well, e.g. the transverse-field Ising model. Other examples include superconductivity (see Sec. 2.4.2) and Bose-Einstein condensation where particle number symmetry is broken and superfluids form. We also mention some important theorems considering spontaneous symmetry breaking that we will make use of in the following Sections. Goldstone’s theorem [66, 67]:

When a continuous symmetry is spontaneously broken, this results in massless, bosonic excitations, *Nambu-Goldstone bosons* [68]. If the symmetry group G is a Lie group with Lie algebra \mathfrak{g} is broken down to S with Lie algebra \mathfrak{s} , the number of Goldstone modes is given by $\dim \mathfrak{g} - \dim \mathfrak{s}$.

In 1D quantum systems, these Nambu-Goldstone bosons are typically not observed. The reason for this is Coleman’s theorem [69]:

Continuous symmetries corresponding to an order parameter that does not commute with the Hamiltonian cannot be broken in one-dimensional quantum systems at zero temperature.

This is in fact the quantum version of the Mermin-Wagner-Hohenberg theorem in statistical mechanics [70, 71]. The ratio behind both is that the Nambu-Goldstone bosons that correspond to such a symmetry breaking will restore the symmetry by strongly contributing to quantum (thermal) fluctuations in 1D (2D). We will collectively refer to these theorems as the Mermin-Wagner-Hohenberg-Coleman (MWHC) theorem.

Starting from the 1970s people began discovering phase transitions that fell outside of the scope of the Landau-Ginzburg-Wilson paradigm [72, 73]. The most prominent example is the discovery of the integer quantum Hall effect in 1980 which resides in a phase that does not break any symmetry (and thus has no non-zero order parameter)

but has universal properties, robust against perturbations, that strongly contrast with the trivial phase [74]. The transverse Hall conductance, for instance, is quantized and an edge current runs along the boundary of the sample [75]. These properties were experimentally observed as well as the even more exotic fractional quantum Hall effect [76]. The quasi-particle excitations in the latter behave as neither boson nor fermions, therefore called anyons, and pick up more arbitrary phases upon interchange [77]. Within the context of high- T_c superconductivity, Anderson introduced Resonating Valence Bond (RVB) states around the same time [78]. As we will discuss in Sec. 2.4.2 these too can realize anyonic excitations and play an important role in the study of spin liquids. The characteristic feature of all these phases is that they are not characterized in a local way (by a local order parameter) but more in global way related to topology. Therefore they are called *topological phases of matter*. A classification of these phases can no longer be based on groups (alone) and one has to go to category theory for a more complete, though mathematically more daunting, description [79]. In the context of free models interesting progress was made quite fast and inspired by the discovery of (spin quantum Hall) topological insulator [80] and ($p + ip$) superconductor [81]. Indeed, based on the global (anti-)unitary symmetries that can exist in free models, ten possible symmetry classes can be discerned [82, 83]. These can be attributed integer bulk topological invariants depending on the spatial dimension. As the invariants cannot vary smoothly in function of the parameters of the Hamiltonian, they are robust against perturbations and classify the possible phases. The most well-known example of such a topological invariant is the Chern number, an integer proven to be proportional to the Hall conductance via the TKNN formula [84] and thus explaining the experimentally observed Hall plateaus in the integer quantum Hall effect. Via the bulk-edge correspondence, this Chern number is also linked to the number of edge modes. Surprisingly, these are gapless (while the bulk is gapped) and move in a certain direction thus offering an explanation for the chiral edge current in the quantum Hall effect. In Chapter 3 we will zoom in more on this full classification, also called the periodic table of topological insulators and superconductors. Especially the Chern number will play an important role as it is intimately linked with parity obstructions that we encountered during tensor network simulations.

Of course the classification in terms of free models is not enough. Indeed, examples exist where interactions induce new topological states [85]. Different free phases can also collapse onto each other upon the reintroduction of interactions. In the 1D BDI class for instance, interactions reduce the free \mathbb{Z} -type topological invariant to a \mathbb{Z}_8 -type [86, 87]. This result was obtained using MPS, shown encompass a complete classification of the possible phases based on the concept of group cohomology [88], also for fermions [89]. Another important caveat is that the invariants in the periodic table can only exist in combination with the required symmetries. For instance removing parity (and thus also chiral) symmetry in the 1D BDI class, the \mathbb{Z} -type topological invariant completely disappears and only a trivial phase remains possible. These topological phases are therefore called *symmetry-protected topological phases* (SPT). Next to these SPTs there also exist topological phases that do not need (any) symmetries to exist. We say that they have *intrinsic topological order*. As an example we will see Kitaev's toric code [90] in the next Section. Though complex, these phases have attracted a lot of interest due to their potential application in the quest for a fault-tolerant topological quantum computer.

2.4 Relevant fermion systems

The main focus of this dissertation is on fermionic, quantum many-body systems, in particular those exhibiting critical behavior. In the upcoming Sections, we elaborate on the significance of the models under investigation by showing where they appear in nature, specifically within the domains of quantum chemistry and condensed matter physics. It is important to note that (critical) fermionic systems also manifest themselves in other areas such as quantum field theory. However, our attention remains directed towards the aforementioned topics and even within this restricted scope our coverage is far from exhaustive, but rather serves as an introductory discussion.

2.4.1 Quantum chemistry

Quantum chemistry is the field of research occupying itself with the study of atoms, ions, molecules and reactions between those. These molecular systems are composed of positively charged atomic nuclei, surrounded by an often fixed number of electrons. To solve them, quantum chemistry typically takes an *ab initio* approach, *i.e.* it does not use experimental input and is solely based on first principles, possibly aided by a handful of additional approximations. A first simplification of this kind is the restriction to time-independent, non-relativistic quantum mechanics based on the axioms in Sec. 2.1.4. One can then use the time-independent Schrödinger equation (with for the electrons spin- $\frac{1}{2}$ degrees of freedom and fermionic particle statistics) instead of the more general Dirac equation [91]. For light atoms this is a good approximation, but for other systems relativistic effects like the spin-orbit coupling play an important role. Fortunately, these can still be taken into account in an approximate way by adding terms to the otherwise exact, non-relativistic molecular Hamiltonian [92]. Its first-quantized form in configuration space reads

$$\begin{aligned} H = & - \sum_i \frac{1}{2} \nabla_i^2 - \sum_A \frac{1}{2M_A} \nabla_A^2 \\ & + \frac{1}{2} \sum_{A \neq B} \frac{Z_A Z_B}{|\mathbf{r}_A - \mathbf{r}_B|} - \sum_{i,A} \frac{Z_A}{|\mathbf{r}_A - \mathbf{r}_i|} + \frac{1}{2} \sum_{i \neq j} \frac{1}{|\mathbf{r}_i - \mathbf{r}_j|}. \end{aligned} \quad (2.47)$$

Here, the terms in the first line corresponds to the kinetic energy of the electrons, labeled by i , and the nuclei, labeled by A and with mass m_A and charge Z_A . Coulomb interactions are collected in the second line, respectively between nuclei, between nuclei and electrons and between the electrons. Note the signs, taking into account the attractive/repulsive nature of the interaction. Furthermore, the sums contain a fixed amount of terms and thus a definite particle number in line with first quantization. We labeled the electronic and nuclear contributions to the molecular Hamiltonian separately as their dynamics differ quite a lot. Indeed, due to the heavier mass of the nuclei, these can be considered quasi-static in space when compared to the much lighter electrons. As a result, the electronic and nuclear problem can be separated. This is the well-known Born-Oppenheimer approximation [93]: we can consider the nuclei in Eq. (2.47) to be clamped and solve the electronic problem with the nuclear configuration, $\{\mathbf{r}_A\}$, regarded as a parameter.

Eq. (2.47) hence simplifies to the electronic Hamiltonian,

$$H(\{\mathbf{r}_A\}) = - \sum_i \frac{1}{2} \nabla_i^2 + \sum_i U(\{\mathbf{r}_A\}, \mathbf{r}_i) + \frac{1}{2} \sum_{i \neq j} V(\mathbf{r}_i, \mathbf{r}_j) \quad (2.48)$$

where we subtracted the constant, purely nuclear contribution,

$$E_0(\{\mathbf{r}_A\}) = \frac{1}{2} \sum_{A \neq B} \frac{Z_A Z_B}{|\mathbf{r}_A - \mathbf{r}_B|}, \quad (2.49)$$

where

$$U(\{\mathbf{r}_A\}, \mathbf{r}_i) = - \sum_A \frac{Z_A}{|\mathbf{r}_A - \mathbf{r}_i|} \quad (2.50)$$

acts as an external potential experienced by each of the electrons and where the two-body term,

$$V(\mathbf{r}_i, \mathbf{r}_j) = V(\mathbf{r}_i - \mathbf{r}_j) = \frac{1}{|\mathbf{r}_i - \mathbf{r}_j|}, \quad (2.51)$$

describes electron-electron interactions, the main source of complexity in the quantum chemistry problem. Solving the electronic Hamiltonian for a N -particle wavefunction

$$\psi(\mathbf{r}_1, \sigma_1, \dots, \mathbf{r}_N, \sigma_N) = \langle \mathbf{r}_N, \sigma_N | \dots \langle \mathbf{r}_1, \sigma_1 | \psi \rangle \quad (2.52)$$

where σ labels spin indices, the resulting eigenenergies depend on the nuclear configuration and form the so-called potential energy surfaces. They can in turn be used as potential energy terms for the nuclear problem that is typically treated in a classical way. Furthermore, the Born-Oppenheimer approximation only holds up as long as the potential energy surfaces are well separated. We formulated the molecular Hamiltonians in first quantization in a continuous configuration space. A formulation in second quantization will thus comprise field operators. Indeed, applying the concepts of the previous Sections and dropping the $\{\mathbf{r}_A\}$ parameters, one obtains

$$\begin{aligned} H = & \int d\mathbf{r} \sum_{\sigma} \left(\frac{1}{2} \nabla \psi_{\sigma}^{\dagger}(\mathbf{r}) \cdot \nabla \psi_{\sigma}(\mathbf{r}) + U(\mathbf{r}) \psi_{\sigma}^{\dagger}(\mathbf{r}) \psi_{\sigma}(\mathbf{r}) \right) \\ & + \frac{1}{2} \int d\mathbf{r} d\mathbf{r}' V(\mathbf{r}, \mathbf{r}') \sum_{\sigma, \tau} \psi_{\sigma}^{\dagger}(\mathbf{r}) \psi_{\tau}^{\dagger}(\mathbf{r}') \psi_{\tau}(\mathbf{r}') \psi_{\sigma}(\mathbf{r}). \end{aligned} \quad (2.53)$$

Though thoroughly simplified, the electronic Hamiltonian still remains quite unwieldy and requires the solution of a partial differential equation in configuration space to obtain the ground (and excited) state(s). Only for very simple systems such as the hydrogen-like atoms a closed solution exists [94]. More complicated molecular systems require a numerical strategy. In this respect, traditional methods like the finite-element or finite-difference method have been surpassed in popularity by an approximation of the N -particle wavefunction with a (finite superposition of) Slater determinant(s) built up by single-particle modes, $\{\phi_m(\mathbf{r}, \sigma)\}$, also called molecular orbitals. Each of these modes can be used to construct a corresponding creation operator,

$$a_m^{\dagger} = \int d\mathbf{r} \sum_{\sigma=\{\uparrow, \downarrow\}} \phi_m(\mathbf{r}, \sigma) \psi_{\sigma}^{\dagger}(\mathbf{r}). \quad (2.54)$$

We typically assume $\phi_m(\mathbf{r}, \sigma)$ has factorized spin and spatial dependence, which furthermore reduced to e.g. $\phi_{2i-1}(\mathbf{r}, \sigma) = \phi_i(\mathbf{r})\delta_{\sigma,\uparrow}$ and $\phi_{2i}(\mathbf{r}, \sigma) = \phi_i(\mathbf{r})\delta_{\sigma,\downarrow}$. In terms of new creation operators

$$a_{i,\sigma}^\dagger = \int d\mathbf{r} \phi_i(\mathbf{r}) \psi_\sigma^\dagger(\mathbf{r}). \quad (2.55)$$

the second quantized electronic Hamiltonian can be approximated by

$$H = \sum_{i,j} t_{ij} \sum_{\sigma} a_{i,\sigma}^\dagger a_{j,\sigma} + \frac{1}{2} \sum_{i,j,k,l} V_{ijkl} \sum_{\sigma,\tau} a_{i,\sigma}^\dagger a_{j,\tau}^\dagger a_{l,\tau} a_{k,\sigma}. \quad (2.56)$$

where

$$t_{ij} = \int d\mathbf{r} \overline{\phi_i}(\mathbf{r}) \left(-\frac{1}{2} \nabla^2 - \sum_A \frac{Z_A}{|\mathbf{r}_A - \mathbf{r}|} \right) \phi_j(\mathbf{r}). \quad (2.57)$$

Furthermore, it is often assumed that, in the ground state, every spatial orbital is occupied by both spin flavors (also referred to as a closed-shell *Ansatz*). Unrestricted (and open-shell) *Ansätze* are also possible and sometimes even necessary (e.g. in case of an odd number of electrons), and then t_{ij} can also depend on the spin labels. Under the same restricted assumption,

$$V_{ijkl} = \int d\mathbf{r} d\mathbf{r}' \overline{\phi_i}(\mathbf{r}) \overline{\phi_j}(\mathbf{r}') \frac{1}{|\mathbf{r} - \mathbf{r}'|} \phi_k(\mathbf{r}') \phi_l(\mathbf{r}) \quad (2.58)$$

collects the two-body terms. The energy expectation value $\langle \psi | H | \psi \rangle$ of a Slater determinant $|\psi\rangle$ (playing an important role in the Hartree-Fock method discussed below) will contain the same integrals but as the bra and ket vectors are the same, only t_{ii} , V_{ijji} and V_{ijij} will appear. The former then combines the kinetic energy and Coulomb interaction with the nuclei of molecular mode i . V_{ijji} yields the Coulomb interaction between the i th and j th molecular orbital. Finally, V_{ijij} is the exchange contribution which has no classical interpretation and only appears between $\phi_i(\mathbf{r}, \sigma)$ and $\phi_j(\mathbf{r}, \tau)$ when their spins align. In this case it typically gives a negative energy contribution. Exchange thus favors aligned spins, leading to Hund's rule for the occupation of atomic (and molecular orbitals). To conclude, we repeat that Eq. (2.56) is indeed an approximation as we utilized only a finite number of $\phi_i(\mathbf{r}, \sigma)$ that do not span a complete basis.

The question now remains how to obtain the molecular orbitals. The most well-known technique to do so is the Hartree-Fock method [95, 96, 97, 98]. Here the wavefunction is approximated by a single Slater determinant. As mentioned before, energy evaluation then contains a Coulomb and exchange contribution, both describing a part of the electron-electron interaction in a mean-field way. Hence, the Hartree-Fock method is classified as mean-field method. Applying the variational principle w.r.t. to this mean-field energy, one obtains the Hartree-Fock equations for the single-particle modes. To solve these, the molecular orbitals are in turn approximated by an expansion in atomic orbital-like basis functions centered around the different atoms of the system. Two prevalent types of orbitals are the Slater-type orbitals (STO) [99] and Gaussian-type orbitals (GTO) [100]. The radial part of the former resembles the cusp behavior ($\sim \exp(-\alpha r)$) observed in the exact solution of the hydrogen atom and from experimental data on more involved molecular systems. GTOs approximate this cusp with a Gaussian profile

($\sim \exp(-\alpha r^2)$). Though less physical, they are typically preferred over the STOs as the evaluation of the resulting one- and two-body integrals can be done analytically [101]. In the end, the variational problem boils down to a generalized eigenvalue problem that is solved via a self-consistent loop. As Hartree-Fock is a mean field method, correlations are taken into account only weakly. Therefore, so-called post-Hartree-Fock methods like Configuration Interaction (CI) [102] and Coupled-Cluster (CC) [103] were devised. These build on the Hartree-Fock orbitals but go beyond the approximation of the wavefunction as a single Slater determinant to introduce more correlation. Of course, these methods only function well when the Hartree-Fock orbitals were already a good approximation, *i.e.* when the Hartree-Fock approximation of the ground state has an energy well separated from other Slater determinants, aptly called single-reference. Another category of methods, called multi-reference, has to be utilized when the Hartree-Fock approximation of the ground state is near degenerate. An example is the Density Matrix Renormalization Group (DMRG) [104] for chemical systems (see also Sec. 2.5).

A crucially different technique for solving molecular systems, called Density Functional Theory (DFT), is not based on an approximation of the many-body wavefunction, $\psi(\mathbf{r}_1, \sigma_1, \dots, \mathbf{r}_N, \sigma_N)$, but rather on the total electron density,

$$\rho(\mathbf{r}) = \int d\mathbf{r}_1 \dots d\mathbf{r}_N \sum_{\sigma_1, \dots, \sigma_N} \left(\sum_{i=1}^N \delta(\mathbf{r} - \mathbf{r}_i) \right) |\psi(\mathbf{r}_1, \sigma_1, \dots, \mathbf{r}_N, \sigma_N)|^2 \geq 0. \quad (2.59)$$

Indeed, Hohenberg and Kohn proved that the energy is a unique functional $E[\rho(\mathbf{r})]$ of the electron density and that its minimum is realized only for the true ground-state density [105]. As a result, one could imagine a variational procedure to determine this ground-state $\rho(\mathbf{r})$ by minimizing $E[\rho(\mathbf{r})]$. However, while the exact form of the functional is straightforward to determine for the kinetic energy contribution, the part corresponding to the electron-electron interactions, especially the part related to the correlations (thus containing the exchange contribution), is not known. Therefore, one picks an approximate exchange-correlation functional from the plethora that exists [106] and then utilizes the variational principle on the approximate $E[\rho(\mathbf{r})]$. Note that this free choice allows DFT to contain much more correlations than the mean-field Hartree-Fock method. The question now remains how to expand the electron density in basis functions. In most algorithms, this done by equating it to the electron density generated by a single Slater determinant. Indeed, Kohn and Sham proved that each $\rho(\mathbf{r})$ can be represented in this way [107]. The single-particle particle modes in this Slater determinant are called Kohn-Sham orbitals and can again be expanded in GTOs/STOs. However, these are not the same orbitals as in the Hartree-Fock methods. Stronger even, they do not even have to resemble them. The only thing they need to do is yield an approximately correct density function. Nevertheless, one can again approximate the second quantized form of the electronic Hamiltonian as in Eq. (2.56) but now with creation/annihilation operators corresponding to the Kohn-Sham orbitals.

We conclude that the quantum chemistry problem in a non-relativistic and time-independent setting can be simplified to the electronic Hamiltonian in Eq. (2.48) or Eq. (2.53) by invoking the Born-Oppenheimer approximation. Subsequently, one can either approximate the many-body electronic wavefunction or the total electron density

by Hartree-Fock-like methods, respectively, Density Functional Theory. The output of these methods generally consists of single-particle modes (molecular/Kohn-Sham orbitals) that can be attributed a creation and annihilation operator thus approximating the full electronic Hamiltonian by Eq. (2.56). The majority of the molecules surrounding us are hence described by this effective, second-quantized, fermionic Hamiltonian, underlining its relevance.

2.4.2 Condensed matter physics

In the preceding Section, we derived the electronic Hamiltonian for the study of molecular systems confined in space. However Eq. (2.48) and Eq. (2.53) also apply in the context of condensed matter physics. Roughly following the outline of [108] we will show that these equations lead to a well-known effective description, the celebrated *Hubbard model*. Different possible phases will be discussed like the *Mott insulator* and *quantum spin liquids*. Furthermore we explain how the *BCS mechanism* can yield additional superconducting terms. In the end, all of this rationalizes our interest in these model throughout the subsequent Chapters.

In a solid, the nuclei typically form a macroscopically large lattice, thus generating a periodic potential in the bulk, experienced by the electrons. Modeling this system as infinitely large, the external potential function is fully periodic, $U(\mathbf{r} + \mathbf{R}) = U(\mathbf{r})$, with $\mathbf{R} = \sum_{i=1}^d n_i \mathbf{a}_i$ ($n_i \in \mathbb{Z}$) again an arbitrary lattice vector. Initially, we will neglect the electron-electron interactions so that we can invoke Bloch's theorem [109] for the resulting free, single-particle problem. We thus decompose the spatial wavefunction as

$$\psi_{\mathbf{k}}(\mathbf{r}) = e^{i\mathbf{k}\cdot\mathbf{r}} u_{\mathbf{k}}(\mathbf{r}), \quad (2.60)$$

i.e. a Bloch wave where $u_{\mathbf{k}}(\mathbf{r} + \mathbf{R}) = u_{\mathbf{k}}(\mathbf{r})$ and \mathbf{k} is a continuous momentum label. Alternatively, one could have realized the periodic $U(\mathbf{r})$ in a finite lattice with (anti-)periodic boundary conditions, i.e. for $n_i = 0, \dots, N_i < \infty$ and $\psi(\mathbf{r} + N_i \mathbf{a}_i) = (-)\psi(\mathbf{r})$ so that $\mathbf{k} = \frac{1}{N_i} (x_i (+\frac{1}{2})) \mathbf{b}_i$ with \mathbf{b}_i the reciprocal lattice vectors characterized by $\mathbf{a}_i \cdot \mathbf{b}_j = 2\pi\delta_{ij}$ and $x_i \in \mathbb{Z}$. In all three cases, the Schrödinger equation can be rewritten as

$$\left(\frac{1}{2m} (-i\nabla + \mathbf{k})^2 + U(\mathbf{r}) \right) u_{\mathbf{k}}(\mathbf{r}) = e_{\mathbf{k}} u_{\mathbf{k}}(\mathbf{r}). \quad (2.61)$$

Due to the periodicity of $u_{\mathbf{k}}(\mathbf{r})$, this can be regarded as a spatially confined problem with a (finite) set of discrete eigenvalues $\{e_{\mathbf{k},j}\}$ for each \mathbf{k} . Furthermore, \mathbf{k} appears only as a parameter in this equation. Therefore, we can assume each of the energy levels to vary smoothly with \mathbf{k} and refer to them as energy bands. Finally, Eq. (2.61) is fully \mathbf{k} -periodic in the sense that adding an arbitrary reciprocal lattice vector to \mathbf{k} does not change the equation. Hence, the same applies for the energy bands and one only needs to consider the \mathbf{k} -points in the first Brillouin zone (BZ) (typically chosen as the Wigner-Seitz cell [110] of the reciprocal lattice). Moving to a many-body perspective, we thus obtain

$$H = \int d\mathbf{k} e_{\mathbf{k},j} \psi_{j,\sigma}^\dagger(\mathbf{k}) \psi_{j,\sigma}(\mathbf{k}) \quad (2.62)$$

with

$$\psi_{j,\sigma}^\dagger(\mathbf{k}) = \int d\mathbf{r} \psi_{\mathbf{k},j}(\mathbf{r}) \psi_\sigma^\dagger(\mathbf{r}) = \int d\mathbf{r} e^{i\mathbf{k}\cdot\mathbf{r}} u_{\mathbf{k},j}(\mathbf{r}) \psi_\sigma^\dagger(\mathbf{r}). \quad (2.63)$$

As a result, the physics in the (grand-)canonical ensemble is quite similar to the Fermi gas but now with different bands, $\{e_{\mathbf{k},j}\}$, whose relative position to the Fermi level defines the material's behavior. Indeed, when e_F is located right within a band (the conduction band), there is a co-dimension one Fermi surface in \mathbf{k} -space and excitations require only a small (in the thermodynamic limit, infinitesimal) amount of energy. Using linear response theory, one can show that this gapless behavior causes a current to flow when an external electric field is applied [111]: the material is a metal. When the Fermi level is located between two well-separated bands (above the valence band and below the conduction band), excitation requires a lot of energy so that the material becomes insulating. For small gaps one obtains a semiconductor. In Sec. 2.2 we saw that ground states of models with a Fermi surface contain more entanglement than their gapped counterparts. As TNS have an inherent area law and thus a limited entanglement content, it was unclear if TNS can approximate metallic properties. In Sec. 5.4.2 we show this is indeed possible (in a certain scaling limit).

The Bloch wavefunctions are \mathbf{k} -periodic. Therefore, we can represent them as a Fourier series,

$$\psi_{\mathbf{k},j}(\mathbf{r}) = \frac{1}{|\text{BZ}|^{\frac{1}{2}}} \sum_{\mathbf{R}} e^{i\mathbf{k}\cdot\mathbf{R}} \psi_{\mathbf{R},j}(\mathbf{r}), \quad (2.64)$$

with

$$\psi_{\mathbf{R},j}(\mathbf{r}) = \frac{1}{|\text{BZ}|^{\frac{1}{2}}} \int_{\text{BZ}} d\mathbf{k} e^{-i\mathbf{k}\cdot\mathbf{R}} \psi_{\mathbf{k},j}(\mathbf{r}) = \frac{1}{|\text{BZ}|^{\frac{1}{2}}} \int_{\text{BZ}} d\mathbf{k} e^{i\mathbf{k}\cdot(\mathbf{r}-\mathbf{R})} u_{\mathbf{k},j}(\mathbf{r}), \quad (2.65)$$

the so-called Wannier orbitals and $|\text{BZ}|$ the volume of the first Brillouin zone. These orbitals satisfy $\psi_{\mathbf{R},j}(\mathbf{r} + \mathbf{R}') = \psi_{\mathbf{R}+\mathbf{R}',j}(\mathbf{r})$ and are orthogonal as they are unitary transformed versions of orthogonal eigenvectors. Furthermore, they should reduce to the atomic orbitals (up to some small oscillations to keep them orthogonal) in the atomic limit, *i.e.* the limit where the separation between the nuclei/ions becomes very large. Away from this limit, one can still localize the Wannier orbitals by replacing $u_{j,\mathbf{k}}(\mathbf{r}) \rightarrow U_{jl}(\mathbf{k})u_{l,\mathbf{k}}(\mathbf{r})$ with $U_{jl}(\mathbf{k})$ unitary. This additional freedom can then be used to exponentially localize the Wannier modes, for instance by numerically minimizing their spread functional [112]. In 1D this is always possible, whereas in 2D, this is only possible in case of a trivial Chern number [113]. Also in higher dimensions restrictions exist. Following an analogous path as for the molecular/Kohn-Sham orbitals in the preceding Section, we can define

$$a_{\mathbf{R},j,\sigma}^\dagger = \int d\mathbf{r} \psi_{\mathbf{R},j}(\mathbf{r}) \psi_\sigma^\dagger(\mathbf{r}) \quad (2.66)$$

so that the Hamiltonian in second quantization can be rephrased as

$$H = \sum_{\mathbf{R},\mathbf{R}'} \sum_{i,j} \sum_{\sigma} t_{\mathbf{R},i,\mathbf{R}',j} a_{\mathbf{R},i,\sigma}^\dagger a_{\mathbf{R}',j,\sigma}. \quad (2.67)$$

When successfully localized,

$$t_{\mathbf{R},i,\mathbf{R}',j} = t_{\mathbf{R}-\mathbf{R}',i,j} = \int d\mathbf{r} \overline{\psi_{\mathbf{R},i}(\mathbf{r})} \psi_{\mathbf{R}',j}(\mathbf{r}) \quad (2.68)$$

decays very fast with the internuclear separation so that in many cases one can restrict to nearest neighbors. Further approximating these nearest-neighbor terms to be equal in

magnitude and to only be non-zero when $i = j$, one obtains the class of tight-binding models [114]. An interesting example is encountered on a 2D hexagonal lattice, effectively describing a graphene layer [115]. There, the dispersion consists out of two bands touching in two isolated points with a linear Dirac cone around them, thus realizing a semi-metal. In contrast to co-dimension one Fermi surfaces, Dirac cones do not violate the area law of entanglement as their Widom factor vanishes [50]. However, the possibility of (strong) subleading corrections does exist. Therefore, we checked and confirmed that also Dirac cones pose no difficulty to TNS simulations (see Sec. 5.4.2).

The classification of solid matter in metals, insulators and semi-conductors from the previous paragraph only applies when we can safely disregard interactions. However, for many metals the qualitative behavior seems to be very similar, even if typical interaction strengths $\sim \langle r \rangle^{-1}$ (the average inter-electronic distance) become comparable to band diagram energy scales. This can be explained by Landau's Fermi liquid theory [116, 117], which treats the interactions as perturbations on top of the free theory (for instance using time-ordered Green's functions and/or Feynman diagrams [118]). By adiabatically turning on the interactions, many qualitative features stay the same, e.g. the modal occupation displaying a sharp (though not integer) jump at the Fermi momentum, thus yielding conduction and metallic behavior. The charge carriers are quasi-particles that still resemble electrons, *i.e.* they have the same spin and charge, but have renormalized dynamical properties, e.g. a higher effective mass. As such, Fermi liquid theory fits nicely in the framework of the Renormalization Group (RG) [119]. Though highly successful, the theory also has its limitations and cannot explain non-perturbative effects. Going deeper into the periodic table of elements, for instance, transition metals and rare earth compounds with atoms having d and f valence orbitals, tend to display more exotic quantum effects, resulting in the non-Fermi liquids or strange metals. An important example is the Mott-insulator, discussed below in the context of the Hubbard model. Another strange metal is obtained by reducing the spatial dimension to one, where the sharp jump in modal occupation completely disappears. Fermi liquid theory no longer provides a correct effective description and should be replaced by Tomonaga-Luttinger liquid theory based on the concept of bosonization [120, 121, 122]. Herein the quasi-particles display spin-charge separation and either carry only spin or only charge. In Chapter 4 we will target excitations of this kind with fermionic TNS and witness spin-charge separation take place.

To study the effects of interactions beyond Fermi Liquid theory, it is useful to reconsider the second quantized Hamiltonian obtained for (nearly) free electrons in lattices (Eq. (2.67)). One could reuse the free Wannier orbitals in an interacting context and obtain

$$\begin{aligned} H = & \sum_{\mathbf{R}, \mathbf{R}'} \sum_{i,j} \sum_{\sigma} t_{\mathbf{R}, i, \mathbf{R}', j} a_{\mathbf{R}, i, \sigma}^\dagger a_{\mathbf{R}', j, \sigma} \\ & + \sum_{\substack{\mathbf{R}, \mathbf{R}' \\ \mathbf{R}'', \mathbf{R}'''}} \sum_{i,j} \sum_{k,l} \sum_{\sigma, \tau} V_{\mathbf{R}, i, \mathbf{R}', j, \mathbf{R}'', k, \mathbf{R}''', l} a_{\mathbf{R}, i, \sigma}^\dagger a_{\mathbf{R}', j, \tau}^\dagger a_{\mathbf{R}''', l, \tau} a_{\mathbf{R}'', k, \sigma}. \end{aligned} \quad (2.69)$$

where

$$V_{\mathbf{R},i,\mathbf{R}',j,\mathbf{R}'',k,\mathbf{R}''',l} = \frac{1}{2} \int d\mathbf{r} d\mathbf{r}' \overline{\psi_{\mathbf{R},i}(\mathbf{r})} \overline{\psi_{\mathbf{R}',j}(\mathbf{r}')} V(\mathbf{r} - \mathbf{r}') \psi_{\mathbf{R}'',k}(\mathbf{r}) \psi_{\mathbf{R}''',l}(\mathbf{r}'). \quad (2.70)$$

It is worth noting the resemblance between this Hamiltonian and Eq. (2.56), with the only difference being the inclusion of the positional index in t and V . Given the complexity of this Hamiltonian, our objective is to minimize the number of terms involved as much as possible. E.g. locality of the Wannier modes allows to only consider nearest-neighbors (though sometimes further terms are necessary for a correct effective description). Another simplification makes use that the relevant physics is situated within the conduction (and valence) band(s). Consequently, the influence of more tightly bound electrons below the valence band can be absorbed into the nuclear potential $U(\mathbf{r})$, thereby replacing the Coulomb interaction with a screened Yukawa potential. Doing so, the number of band indices in Eq. (2.69) reduces significantly and in many instances even a single band suffices. However, it is essential to ensure that these bound electrons do not significantly impact the more relevant bands. While oftentimes a fair assumption, this is not the case in some strongly correlated systems, for instance containing f -electron metals like the cuprates [123]. There, a more reliable strategy is to already incorporate some degree of correlation in the energy bands (and thus Wannier modes) by employing lattice-based extensions of quantum chemistry methods like post-Hartree-Fock and DFT. The resulting energy bands offer a more precise picture and one can safely restrict to the bands in the vicinity of the Fermi level, yielding an effective model with only a small number of bands, a process referred to as downfolding. From a qualitative point of view, on the other hand, we can employ a similar approach as in the tight-binding method and restrict the V terms to nearest neighbors, all with the same V . Also limiting us to a single band, the possible interaction terms reduce to:

- $\mathbf{R} = \mathbf{R}''$ neighbors $\mathbf{R}' = \mathbf{R}'''$ so that

$$V_{\mathbf{R},\mathbf{R}',\mathbf{R},\mathbf{R}'} = \frac{1}{2} \int d\mathbf{r} d\mathbf{r}' |\psi_{\mathbf{R}}(\mathbf{r})|^2 V(\mathbf{r} - \mathbf{r}') |\psi_{\mathbf{R}'}(\mathbf{r}')|^2 = V, \quad (2.71)$$

yielding the classical Coulomb/Yukawa interaction but now on the level of neighboring Wannier modes. In second quantization we obtain

$$V \sum_{\langle \mathbf{R}, \mathbf{R}' \rangle} \sum_{\sigma, \tau} a_{\mathbf{R}, \sigma}^\dagger a_{\mathbf{R}', \tau}^\dagger a_{\mathbf{R}', \tau} a_{\mathbf{R}, \sigma} = V \sum_{\langle \mathbf{R}, \mathbf{R}' \rangle} \sum_{\sigma} n_{\mathbf{R}} n_{\mathbf{R}'} \quad (2.72)$$

with $n_{\mathbf{R}} = \sum_{\sigma} n_{\mathbf{R}, \sigma} = \sum_{\sigma} a_{\mathbf{R}, \sigma}^\dagger a_{\mathbf{R}, \sigma}$ the total number operator for the Wannier orbital at \mathbf{R} . This term avoids the population of neighboring sites, denoted by $\langle \mathbf{R}, \mathbf{R}' \rangle$.

- $\mathbf{R} = \mathbf{R}'''$ neighbors $\mathbf{R}' = \mathbf{R}''$ so that

$$\begin{aligned} V_{\mathbf{R},\mathbf{R}',\mathbf{R}',\mathbf{R}} &= \frac{1}{2} \int d\mathbf{r} d\mathbf{r}' \overline{\psi_{\mathbf{R}}(\mathbf{r})} \overline{\psi_{\mathbf{R}'}(\mathbf{r}')} V(\mathbf{r} - \mathbf{r}') \psi_{\mathbf{R}'}(\mathbf{r}) \psi_{\mathbf{R}}(\mathbf{r}') \\ &= \frac{1}{2} \int d\mathbf{r} d\mathbf{r}' \overline{\psi_{\mathbf{R}}(\mathbf{r})} \overline{\psi_{\mathbf{R}'}(\mathbf{r})} V(\mathbf{r} - \mathbf{r}') \psi_{\mathbf{R}}(\mathbf{r}') \overline{\psi_{\mathbf{R}'}(\mathbf{r}')} = J_F. \end{aligned} \quad (2.73)$$

This is again the exchange interaction resulting from the fermionic particle statistics. Note that $J_F > 0$ due to the repulsive nature of $V(\mathbf{r} - \mathbf{r}')$. As a result, we can use the spin operator,

$$\mathbf{S}_{\mathbf{R}} = a_{\mathbf{R},\alpha}^\dagger \left(\frac{1}{2} \boldsymbol{\sigma}_{\alpha\beta} \right) a_{\mathbf{R},\beta}, \quad (2.74)$$

to rewrite

$$J_F \sum_{\langle \mathbf{R}, \mathbf{R}' \rangle} \sum_{\sigma, \tau} a_{\mathbf{R},\sigma}^\dagger a_{\mathbf{R}',\tau}^\dagger a_{\mathbf{R},\tau} a_{\mathbf{R}',\sigma} = -2J_F \sum_{\langle \mathbf{R}, \mathbf{R}' \rangle} \left(\mathbf{S}_{\mathbf{R}} \cdot \mathbf{S}_{\mathbf{R}'} + \frac{1}{4} n_{\mathbf{R}} n_{\mathbf{R}'} \right), \quad (2.75)$$

once again showing that the exchange interaction tends to align spins, *i.e.* a ferromagnetic coupling.

- $\mathbf{R} = \mathbf{R}' = \mathbf{R}'' = \mathbf{R}'''$ so that

$$V_{\mathbf{R}, \mathbf{R}, \mathbf{R}, \mathbf{R}} = \frac{1}{2} \int d\mathbf{r} d\mathbf{r}' |\psi_{\mathbf{R}}(\mathbf{r})|^2 V(\mathbf{r} - \mathbf{r}') |\psi_{\mathbf{R}}(\mathbf{r}')|^2 = \frac{U}{2}. \quad (2.76)$$

The second-quantized Hamiltonian contribution then becomes

$$\frac{U}{2} \sum_{\mathbf{R}} \sum_{\sigma, \tau} a_{\mathbf{R},\sigma}^\dagger a_{\mathbf{R},\tau}^\dagger a_{\mathbf{R},\tau} a_{\mathbf{R},\sigma} = U \sum_{\mathbf{R}} n_{\mathbf{R},\uparrow} n_{\mathbf{R},\downarrow}. \quad (2.77)$$

This is the Hubbard interaction, an on-site Coulomb repulsion between two electrons in the same spatial Wannier mode but with orthogonal spin.

In the atomic limit, the high degree of localization of the Wannier orbitals strongly reduces the relative strength of the ferromagnetic terms w.r.t. to the Hubbard term. Indeed, the former only contain off-diagonal products of Wannier functions. A similar reasoning applies for the Coulomb terms, at least when the nuclear/ionic potential decays fast enough. In the case of poor screening, neglecting it may not be accurate and the Coulomb term can realize charge density waves [124]. However, if we assume enough screening, we arrive at

$$H = -t \sum_{\langle i,j \rangle} \sum_{\sigma} a_{i,\sigma}^\dagger a_{j,\sigma} + U \sum_i n_{i,\uparrow} n_{i,\downarrow}. \quad (2.78)$$

where the i and j labels are now used to denote neighboring positions. This is the famous *Hubbard model* (independently formulated by Hubbard [125], Gutzwiller [126] and Kanamori [127]). In 1D it can be solved analytically using the concept of integrability. Application of the Bethe *Ansatz* [128] for instance results in the aforementioned spin-charge separation for the quasi-particle excitations yielding spinons (with a definite spin but no charge) and (anti-)holons (with a definite charge but no spin) [129]. For higher dimensions, the Bethe *Ansatz* cannot be used and also Quantum Monte Carlo methods are not applicable due to the sign problem [130]. However, some general tendencies can be distinguished in the (limits of) certain parameter regimes, *i.e.* in function of the dimensionless interaction strength U/t and particle density n . In the dilute limit $n \ll 1$ one expects the scarce charge carriers to move around near freely, yielding a metallic behavior. The same happens when we completely turn off the interaction and recover the free model with a Fermi surface. For $U/t \gg 1$, on the other hand, double occupancy is

energetically unfavorable and as a result electrons become jammed at fixed positions for half-filling: the material realizes an insulator and the charged excitations become gapped. Note however that the insulation in this so-called *Mott insulator* is a consequence of strong correlations instead of band structure. For the intermediate regimes, the nature of the ground state remains controversial due to multiple competing states with comparable energy. On a 2D square lattice with $U/t = 10$ and $n = \frac{7}{8}$, for instance, it was unclear if the material organized in stripes breaking translation invariance [131, 132] or if it realized non-zero pairing term expectations values, thus breaking the U(1) particle number symmetry and signaling (high- T_c) superconductive behavior [133, 134]. Many studies with as many methods have been performed and only recently consensus seems to build towards the stripe phase [135, 39] (observed in experiments [136, 137, 138]). Considering finite temperatures, further interaction ranges, or different geometries (in the sense of spatial dimensions, unit cells, nuclear positions within these, boundary conditions, ...), the myriad of possible phases only grows. Instances of ferromagnetism, anti-ferromagnetism, charge-density waves, superconductivity, spin liquids have all been reported. We will come back on the latter two but first return to the Hubbard Hamiltonian.

The Hubbard Hamiltonian was derived as a consequence of the Schrödinger equations in strongly-correlated condensed matter under some (in many cases reasonable) assumptions. It can be simplified further by making additional approximations. In the atomic limit ($U \gg t$), for instance, a perturbative treatment of the hopping terms w.r.t. to the Hubbard term results in the $t - J$ model [139],

$$H = V_S^\dagger \left(-t \sum_{\langle i,j \rangle, \sigma} a_{i,\sigma}^\dagger a_{j,\sigma} - \frac{J}{4} \sum_{\substack{\langle i,j \rangle \\ \langle i,k \rangle}} (a_{k,\uparrow}^\dagger a_{i,\downarrow}^\dagger - a_{k,\downarrow}^\dagger a_{i,\uparrow}^\dagger)(a_{i,\downarrow} a_{j,\uparrow} - a_{i,\uparrow} a_{j,\downarrow}) \right) V_S \quad (2.79)$$

Here, $J = 4t^2/U$ and V_S is a projector onto the subspace of states that does not contain any doubly occupied sites. For the J term two cases can be discerned. Either $k = j$ and it removes two particles at neighboring sites to create them again, thus remaining in subspace of non-double occupancy when $n = 1$. For general $n \leq 1$ (the $n > 1$ part of the phase diagram follows from particle-hole symmetry), we obtain

$$\frac{J}{4} \sum_{\langle i,j \rangle} (a_{j,\uparrow}^\dagger a_{i,\downarrow}^\dagger - a_{j,\downarrow}^\dagger a_{i,\uparrow}^\dagger)(a_{i,\downarrow} a_{j,\uparrow} - a_{i,\uparrow} a_{j,\downarrow}) = \frac{J}{2} \sum_{\langle i,j \rangle} \left(\mathbf{S}_i \cdot \mathbf{S}_j - \frac{1}{4} n_i n_j \right). \quad (2.80)$$

When $k \neq j$ on the other hand, the J term takes a particle from site j to site k possible creating a doubly occupied site there. As a result, this term typically neglected. In the Mott insulator at half-filling this treatment is exact and the Hubbard model simply reduces to

$$H = \frac{J}{2} \sum_{\langle i,j \rangle} \mathbf{S}_i \cdot \mathbf{S}_j \quad (2.81)$$

as the hopping term is also projected away. This is the anti-ferromagnetic (AFM) Heisenberg Hamiltonian, retaining only the spin degrees of freedom as all the kinetics is frozen out. On a bipartite lattice, classical intuition point towards a ground state where neighboring spin polarizations alternate, often called Néel order. In Eq. (2.75) we also found a

ferromagnetic (FM) Heisenberg interaction. Both models have been studied extensively, also in the presence of an external magnetic field and for anisotropic materials where the coupling strength differs in the different spatial directions. This gives rise to the isotropic XXX ($J_x = J_y = J_z = J$) or standard Heisenberg model, the uniaxial XXZ ($J_x = J_y \neq J_z$) model and the fully anisotropic XYZ ($J_x \neq J_y \neq J_z$) model. Also different spins, S , have been considered, so that the isotropic model is $SO(3)$ ($SU(2)$) symmetric for (half-)integer S . This symmetry gets broken down to subgroups like $O(2)$, $U(1)$ and \mathbb{Z}_2 when adding anisotropy. As an extreme case we retrieve the Ising model from Eq. (2.46).

In the previous paragraphs superconductivity could be realized by spontaneously breaking the $U(1)$ particle number symmetry in the Hubbard Hamiltonian down to \mathbb{Z}_2 . The expectation values of the pairing terms, which could be used as local order parameters, become non-zero so that the phase transition fits nicely in the Landau-Ginzburg-Wilson paradigm. However, we will also examine models that already contain particle-number-violating terms in their Hamiltonian due to the *BCS mechanism* [140, 141]. To understand this, one should consider phonons, *i.e.* vibrational modes of the nuclear degrees of freedom (similar to the standard quantum harmonic oscillator). Via a virtual process these bosons can assist the valence electrons to form pairs, the famous *Cooper pairs* [142]. These bosonic charge carriers are responsible for superconductive behavior such as the Meissner effect [143] and the London equations [144]. A detailed examination of the microscopic origin of Cooper pair formation would take us too far but requires the addition of the phonon modes to the (approximate) band Hamiltonian combined with an interaction term between the phonons and electrons. Applying a mean-field approximation, one obtains effective superconducting pairing terms. Indeed, the band electrons can interchange particles with the reservoir of Cooper pairs resulting in particle number fluctuations. Exactly these pairing terms supplement hopping and a chemical potential in the 1D Kitaev chain model [145],

$$H = - \sum_i \left(t a_i^\dagger a_{i+1} + h.c. \right) - \mu \sum_i a_i^\dagger a_i - \sum_i \left(\Delta a_i^\dagger a_{i+1}^\dagger + h.c. \right). \quad (2.82)$$

Going to Fourier space, this free and translation invariant model can easily be solved exactly (see Chapter 3 for more details), yielding a single-particle dispersion relation

$$e(k) = (2t \cos(k) - \mu)^2 + (2\Delta \sin(k))^2. \quad (2.83)$$

Critical lines in the phase diagram thus lie at $\mu = \pm 2t$ and at $\Delta = 0$ when $|\mu| < 2t$. The phases can be analyzed according to the periodic table of topological insulators and superconductors, classifying the model as BDI in 1D and thus having a \mathbb{Z} -type topological invariant. For $|\mu| > 2t$, this variant is zero and the system is in a trivial phase with the ground state reducing to a product state when $\Delta = 0$ and all momentum modes filled (empty) when $\mu > 2t$ ($\mu < -2t$). For $\Delta \neq 0$ and $|\mu| < 2t$, on the other hand, the system is in a topological phase with the winding number $|\nu| = 1$ as a topological invariant (see Chapter 3). When considering a finite chain, the corresponding gapless edge modes are isolated Majoranas, located at the ends of the wire. This topologically protected, Majorana edge modes are the main reason why Kitaev introduced the model. Indeed, together these modes carry one qubit of topologically protected data making them an

interesting platform for quantum computation. We will also examine the 2D analogue of the Kitaev chain,

$$H = - \sum_{\mathbf{n}} \left(t_1 a_{\mathbf{n}}^\dagger a_{\mathbf{n}\rightarrow} + t_2 a_{\mathbf{n}}^\dagger a_{\mathbf{n}\uparrow} + h.c. \right) - \mu \sum_{\mathbf{n}} a_{\mathbf{n}}^\dagger a_{\mathbf{n}} - \sum_{\mathbf{n}} \left(\Delta_1 a_{\mathbf{n}}^\dagger a_{\mathbf{n}\rightarrow}^\dagger + \Delta_2 a_{\mathbf{n}}^\dagger a_{\mathbf{n}\uparrow}^\dagger + h.c. \right) \quad (2.84)$$

where $\mathbf{n}_{\rightarrow(\uparrow)}$ corresponds to the nearest neighbor of site \mathbf{n} on the right (upper) side in a square lattice. Note that we allowed for anisotropy, which is necessary to open a gap. Indeed, simply setting $\Delta_1 = \Delta_2 = \Delta$ the model remains gapless for all Δ (the Fermi surface reduces to a couple of Dirac points) whereas for $\Delta_1 = -i\Delta_2 = \Delta$ one obtains

$$e(\mathbf{k}) = (2t(\cos(k_x) + \cos(k_y)) - \mu)^2 + (2\Delta \sin(k_x))^2 + (2\Delta \sin(k_y))^2 \quad (2.85)$$

for the dispersion relation, which does open gaps. Taking $t > 0$, for instance, gapped trivial phases are found when $|\mu| > 4t$. For $0 < \mu < 4t$, one obtains a chiral phase with a topological Chern number invariant, $C = -1$, whereas $-4t < \mu < 0$ yields $C = +1$. Critical lines lie in between and at analogous places as for the 1D Kitaev chain. For $\Delta = 0$ and $-4t < \mu < 4t$ the model exhibits a 1D Fermi surface. The factor preceding the $a_{\mathbf{k}}^\dagger a_{-\mathbf{k}}^\dagger$ pairing term in Fourier space is $\Delta(\mathbf{k}) = -2i(\Delta \sin(k_x) + i\Delta \sin(k_y))$, reducing to $-2i\Delta(k_x + ik_y)$ near the zone center. Therefore the model is also called the $p+ip$ or p -wave superconductor. Analogously, one can define a d -wave superconductor where $\Delta(\mathbf{k}) \sim k_x^2 - k_y^2$. s -wave superconductors also exist but require spinful fermions.

In addition to (high- T_c) superconductivity, the Hubbard model was also conjectured to contain topological spin liquid phases. To introduce these, we first consider the Mott insulator on a triangular lattice. Due to the non-bipartite geometry, building a Néel state is impossible, a feature called geometric frustration. Instead, classical intuition now points towards a spin polarization pattern under 120° angles to minimize the energy. Interestingly, this induces some additional degeneracy when compared to the bipartite case. In the latter, SU(2) spin rotation symmetry is broken as the system chooses a polarization direction to realize the Néel order in [146]. Infinitely many ground states exist and are mutually related by a rotation of the polarization axis. The resulting Goldstone bosons are magnons and correspond to spin waves [147, 148]. For the 120° degree order on the triangular lattice, a similar reasoning can be followed but now the geometric frustration leads to an additional degeneracy. Indeed, having picked a polarization axis on one site (and thus having broken SU(2)), we can select a neighbor and still have two possibilities for an appropriate polarization there (*i.e.* rotate by $\pm 120^\circ$). Once this choice is made, though, all other polarizations are fixed. For triangular lattices, this extra degeneracy does not invalidate the spin wave analysis and gapless magnons [149] exist on top of the degenerate SU(2) broken ground space [150]. For the Kagome lattice in 2D and the pyrochlore lattice in 3D, on the other hand, the number of possibilities to attach spin polarizations to the neighboring sites does not simply increase with a fixed factor but rather increases exponentially with the system size. This extensive degeneracy hints towards fluctuations that are so strong that they can recover the SU(2) symmetry in the true ground state as happens in 1D (in line with the MWHC theorem). The resulting phase is called a *quantum spin liquid*. Indeed, materials in this phase are Mott insulators

so that only spin degrees remain. In addition they retain all relevant symmetries ($SU(2)$ and translation invariance) just like a standard liquid.

The exact nature of the ground (and excited) state(s) for the Heisenberg model on the Kagome and pyrochlore lattices remains unresolved to this day. Exploring these ground states to gain a deeper understanding of spin liquids thus requires an alternative. Let us first reexamine the 1D case. There the MWHC theorem precludes long-range, Néel order that breaks the continuous $SU(2)$ symmetry. However, for half-integer spins also a unique, gapped ground state is impossible due to the Lieb-Schultz-Mattis-Oshikawa-Hastings (LSMOH) theorem. Originally discovered by Lieb, Schultz and Mattis [151] and extended by Oshikawa [152] and Hastings [153], this theorem can be loosely summarized as follows:

In a translation invariant quantum many-body system with a conserved particle number, a finite excitation gap is possible only if the particle number per unit cell of the ground state is an integer.

This applies for fermions and bosons alike but can also be translated to spins by utilizing the Holstein-Primakoff transformation [154]. A conservation of particle number then corresponds to a conserved total magnetization, $\sum_i S_i^z$. On the other hand, the particle number per spin is given by $S - m$ with m the average magnetization per spin. An AFM Heisenberg chain with half-integer spins and single-site unit cell, retaining its $SU(2)$ so that $\langle S_i^z \rangle = 0$ thus necessarily closes the gap as the particle number equals S which is not an integer. This is exactly observed when utilizing the Bethe *Ansatz*. However, a second possibility to satisfy both theorems exists. By breaking the translation invariance down to a two-site unit cell, the particle number per unit cell becomes $2S$ and a gap can be sustained. This combination of constraints is for instance realized in the ground state of the Majumdar-Ghosh model [155] (a special case of the $J_1 - J_2$ model that adds next-nearest-neighbor interactions to the Heisenberg model) where neighboring spins form singlets and excitations correspond to domain walls carrying an unpaired spin, *spinons*. Following our list of desiderata for a spin liquid, the latter state does not qualify. Indeed, translation invariance is broken so that the result is not a liquid. However, one could build a superposition of both symmetry broken ground states to restore the symmetry (though still not realizing a true “liquid” as long-range order remains). We now apply the same concepts in higher dimensions. There, the MWHC theorem does not guarantee the continuous symmetries to be unbroken. However, if we impose it as a requirement for spin liquids, the LSMOH theorem again results in either a gapless spin liquid or a gapped spin liquid with a ground state degeneracy (on the torus). When no symmetries are broken, the latter can only have a topological origin. Here, the resonating valence bond states pop up again. Originally suggested by Anderson as ground states for the AFM triangular Heisenberg model [78] and later proposed again by him within the context of superconductivity [156, 157], RVB states served neither of these purposes. However, they are the paradigmatic example of spin liquid states. RVB states are the higher-dimensional generalizations of the Majumdar-Ghosh ground state with a configuration of spin singlets covering the complete lattice. As such these states break translation and rotation symmetries and are often referred to as RVB crystals. A superposition of

many (or all) RVB states is able to restore these symmetries, realizing an RVB liquid. For a spin liquid ground state, the idea then is that the Heisenberg interactions will select a subset of RVB states that are transformed into each other and that these together span the ground state space. Excitations on top of an RVB crystal correspond to uncoupled pairs of spins. Creating these from the RVB state and further separating them will change other singlets thus resulting in an attractive potential between both spins. In an RVB liquid on the other hand this is not the case due to the lack of long-range order. The spinon quasi-particles become *deconfined* and can move freely.

A popular strategy to classify (the excitations in) these challenging spin liquid phases is to express the Heisenberg spin degrees of freedom (again) in terms of either bosons (Schwinger bosons) or fermions (Abrikosov or, more condescendingly, slave fermions), defined by

$$\mathbf{S}_i = \frac{1}{2} a_{i,\alpha}^\dagger \boldsymbol{\sigma}_{\alpha\beta} a_{i,\beta} \quad (2.86)$$

in the case of $S = \frac{1}{2}$ and with the extra constraint that $\langle a_{i,\alpha}^\dagger a_{i,\alpha} \rangle = 1$. Together, these methods are referred to as parton constructions since the spin entails only a part of the bosons/fermions. The naive hope is that these partons, though introduced purely formally, will realize true quasi-particles. While being uncontrolled, this strategy has been demonstrated to work, e.g. in context of the Kitaev honeycomb model [158]. Having introduced the partons, the next step consists of solving the parton model. This is typically done in a mean-field way and self-consistent with the local particle number constraints. The resulting effective free boson/fermion Hamiltonian will always have an emergent, global \mathbb{Z}_2 symmetry as only quadratic combinations of operators appear. Sometimes the emergent symmetry is even larger and a U(1) group is observed. These symmetries are not accidental but rather a direct consequence of the parton description. In particular, we see from Eq. (2.86) that the physical spin operators are invariant under U(1) transformations of the partons. This implies that the symmetry is a direct consequence of the redundant parameterization of the local Hilbert space. The physical theory should therefore be invariant under these local symmetries, *i.e.* they should correspond to a gauge symmetry of the effective theory. To enforce this, the free model is supplemented with gauge fields on the edges between lattice sites. The parton construction thus results in an effective Hamiltonian with quadratic matter fields coupled to a gauge field. Analyzing the excitations of such generally strongly-interacting gauge theories is a rich and complicated problem [159]. A particularly interesting example is the bosonic construction with an emergent \mathbb{Z}_2 symmetry on the square lattice. If the resulting \mathbb{Z}_2 gauge theory is in its deconfined phase, the effective Hamiltonian can reduce to a pure gauge theory appearing to be Kitaev's toric code [90]. For gapless spin liquids, the fermionic construction is typically preferred as bosons are unstable to condensation when the gap closes. Both \mathbb{Z}_2 and U(1) realizations have been examined. For the latter, a pure gauge field can be obtained again (at least in 3D or higher), now corresponding to gapless photons decoupled from the gapped matter field. A strong coupling is also possible and yields either a Dirac-type band touching and thus Dirac spinons or a Dirac spin liquid [160, 161]. Alternatively, the critical Abrikosov fermions can yield a spinon Fermi surface or Fermi surface spin liquid [162, 163]. Especially the latter will be considered in this work as again the ability of PEPS to capture these states is/was debated due to their inherent violations of the area law of entanglement. We refer to Sec. 5.4.3 in this regard.

2.5 Tensor network states

We began this Chapter by introducing the quantum many-body problem and found the relevant Hilbert space to scale exponentially in the number of particles. Already for relatively small systems (~ 40 particles), this precludes an exact diagonalization of the Hamiltonian to determine the ground state. Even just sampling all basis states quickly becomes intractable. Fortunately, the area law of entanglement learns that we do not need all of these states. Indeed, physically relevant states like the ground state and low-lying excitations obey the area law and instead of considering the full Hilbert space we can thus restrict to this smaller subset. Tensor Network States like MPS and PEPS do exactly this [164].

The standard example of a TNS is the Matrix Product State (MPS) [165],

$$|\psi\rangle = \text{---} \circlearrowleft \text{---} \circlearrowleft \text{---} \circlearrowleft \text{---} = \text{---} \square \text{---} \square \text{---} \square \text{---} \quad (2.87)$$

This type of TNS is based on the ground state of the 1D AKLT model [166]. As such, it associates to each physical site (vertical lines), two virtual degrees of freedom (white circles) that are maximally entangled with their neighbor (depicted by the wiggly lines). These maximally entangled pairs are locally projected onto the physical level (grey circles). Equivalent and more common is the MPS representation on the right. To elucidate this diagrammatic notation, we focus on a single block and identify

$$l \xrightarrow{\square A} r = A_{lr}^p \quad (2.88)$$

where A_{lr}^p is an element of a complex rank-three tensor. The dimensions of its constituent Hilbert spaces are D for the lower indices and d for the upper index. With each of the spaces we thus associate a leg and filling in an index on all of these legs we obtain the corresponding tensor element. The d -dimensional space is chosen to correspond to the local, physical Hilbert space while the horizontal legs, correspond to the virtual spaces. The so called bond dimension, D , determines the number of free parameters in the *Ansatz*. Furthermore, contraction of tensor indices is depicted by connecting legs so that for the MPS,

$$\begin{aligned} |\psi\rangle &= \dots \xrightarrow{\square A[1]} \xrightarrow{\square A[2]} \xrightarrow{\square A[3]} \dots \\ &= \sum_{p_i} (\dots A[1]^{p_1} A[2]^{p_2} A[3]^{p_3} \dots) (\dots |p_1\rangle |p_2\rangle |p_3\rangle \dots) . \end{aligned} \quad (2.89)$$

Each of its coefficients w.r.t. the local, physical bases thus corresponds to a product of matrices, hence the name matrix product states. Note that the number of variables in an MPS only increases polynomially with the system size instead of exponentially. One could reduce this further by imposing translation invariance and setting $A[i] = A$. A single tensor then determines the complete state. Moreover, global symmetries like SU(2)

can be imposed on the local tensors so that the full formalism is not only numerically tractable, it is also symmetry-compatible and systematically scalable by increasing D . In Chapter 4 we will show that the system can also incorporate fermionic degrees of freedom.

To determine the local tensors in an MPS, e.g. to approximate the ground state of a certain Hamiltonian, one can apply the variational principle. In fact, the immense success of DMRG was later understood as a particular variational method within the MPS manifold [167, 168]. Apart from optimization, numerous algorithms have been proposed for MPS to extract expectation values, to do time-evolution, to incorporate excitations, ... [169, 170, 171] We do not introduce all of these methods here but many will be revisited in Chapter 4. Typically, the gauge freedom in MPS, *i.e.* the fact that a transformation,

$$\xrightarrow{\quad A \quad} \xrightarrow{\quad X^- \quad} \boxed{A} \xrightarrow{\quad X \quad} , \quad (2.90)$$

does not alter $|\psi\rangle$, is maximally exploited to write the state in a canonical form. Based on this canonical form, it is straightforward to prove that correlations decay exponentially, thus mimicking those of unique ground states of local, gapped Hamiltonians. As a result, it did not come as a surprise that the latter can always be represented by an MPS [172]. Indeed, due to their structure the maximal amount of entanglement between a region and its complement is bounded by the entanglement mediated by the virtual legs. As this space has dimension D , the entanglement entropy of a finite region is bounded by a constant, $2 \log D$, thus realizing an area law and exponentially decaying correlations. Yet another theoretical result is the fundamental theorem of MPS stating that any two translation-invariant (and normalized) MPS, equal as a complete state, have tensors related by a gauge transform [88, 173]. An important additional condition (though it may be relaxed) is that the MPS are injective. However, when it applies, it is exactly this theorem that underlies the aforementioned cohomology-based classification of 1D phases.

The MPS was introduced as a local projection from virtual, maximally entangled pairs to the physical level. In this spirit Projected Entangled-Pair States (PEPS) [174, 175] were introduced as their higher-dimensional analogues. The construction is again equivalent to a contraction of local tensors but now with c virtual legs where c is the coordination number of the lattice under consideration. As a result we obtain

$$|\psi\rangle = \begin{array}{c} \text{Diagram of a 4-qubit state } |\psi\rangle \text{ consisting of four horizontal lines representing qubits. Each qubit is represented by a gray square box with two wires extending from its top and bottom. The four qubits are connected sequentially from left to right.} \\ \text{Figure 2.91} \end{array} \quad (2.91)$$

for a 2D square lattice with closed boundary conditions. Although they are based on similar ideas, MPS and PEPS display both numerical and conceptual differences. A canonical form, for instance, cannot be derived for PEPS. Therefore, PEPS can only be contracted in an approximate way. Together with the increase of variables due to the higher number of virtual legs, this complicates the numerical use. This is the main reason why a

large part of this dissertation is dedicated to the Gaussian submanifold of PEPS (see Chapter 5) where contractions can be performed exactly and at higher bond dimensions. This in turn allows to examine properties of PEPS that could not be verified with the generic Ansatz. The go-to example is the description of a state with a Fermi surface (see Sec. 5.4.1). The bond dimensions necessary to demonstrate the ability of PEPS to approximate these states, *i.e.* to show that their precision steadily improves as a function of D , are near unattainable for generic PEPS, even for state of the art PEPS optimization algorithms. Moreover, the high degree of criticality could destabilize them. On the more conceptual side, PEPS can realize both exponential and algebraic correlations [176, 177]. Furthermore, gauge transformations do not have to be identical in different directions. An equally powerful fundamental theorem also does not exist for PEPS so that there is no full-fledged generalization of the classification of phases [178].

As a final example of TNS we mention the Multiscale Entanglement Renormalization Ansatz (MERA) [179]. In contrast to MPS and PEPS, this TNS does not simply mimic the lattice geometry but rather consists of multiple alternating layers,

$$|\psi\rangle = \begin{array}{c} \text{Diagram showing a tensor network structure for MERA, consisting of layers of disentanglers (dark squares) and scalers (light triangles). The network starts with two top legs and branches down through several layers of tensors.} \\ , \end{array} \quad (2.92)$$

where we only drew a limited part but the diagram should be continued horizontally and, possibly, higher upward. The darker squares are unitary tensors (as linear transformations from the bottom to the top legs) and called disentanglers while the lighter triangles are isometries called scalers. The latter compress two legs to a single leg which can be interpreted as a scaling transformation, blurring out the information of the original finer lattice to a more coarse grid. Indeed, subsequent layers can be regarded as renormalization steps to different length scales. However, if only scaling transformations were present, the MERA (essentially reduced to a tree renormalization scheme) would accumulate small-scale correlations and entanglement in the tensors in the coarse layers. For this reason, the MERA tensor network combines scalers with disentanglers, aiming to remove local correlations in the lattice before the scaling transformations are applied. As such MERA is able to (approximately) describe scale-invariant behavior in critical states and it can realize infinite correlation lengths when infinitely continued in the emergent scaling dimension. However, this work contributes to the notion that MPS and PEPS, even with a finite correlation length, can still be used to describe critical models in some scaling regime. In a way, it thus undermines the *raison d'être* for MERA which will therefore not be considered further.

Chapter 3

Gaussian states

Gaussian states appear in many different fields of research ranging from high energy physics over quantum information theory and quantum optics to condensed matter physics [180, 181, 182, 183, 184, 185]. Consequently, they have been assigned a myriad of different definitions and names (quadratic states, free states, vacua, (squeezed) coherent states, generalized Slater determinants, ground states of free Hamiltonians, ...). While these definitions often focus on specific application, they share an overarching property: Wick's theorem [33]. Already introduced in the previous Chapter, this theorem essentially says that all information about the state is contained in its (one- and) two-point correlation functions. As such, Gaussian states allow for an analytical treatment of properties that are hard to access for more generic states (e.g. entanglement entropies). Exactly this quality will be exploited in Chapter 5. Furthermore, they can be used as a testing ground for certain methods or constructions and serve as the basis for successful perturbative methods like Feynman diagrams, the Bardeen–Cooper–Schrieffer theory [140, 141] and the Hartree-Fock method [95, 96, 97, 98].

3.1 Definition

For the definition of a Gaussian state we will loosely follow [183] so that both bosons and fermions are covered. We thus start by defining a set of n bosonic (fermionic) creation operators, $\{a_i^\dagger\}$ ($i = 1, \dots, n$), that together with their adjoints satisfy canonical (anti-)commutation relations,

$$\begin{aligned} [a_i, a_j^\dagger] &= \delta_{ij} & [a_i^\dagger, a_j^\dagger] &= 0 && \text{(bosons)} \\ \{a_i, a_j^\dagger\} &= \delta_{ij} & \{a_i^\dagger, a_j^\dagger\} &= 0 && \text{(fermions)} \end{aligned} . \quad (3.1)$$

In the bosonic case, these can be used to define Hermitian phase space (or quadrature) operators,

$$\begin{aligned} x_i &= \frac{1}{\sqrt{2}} (a_i^\dagger + a_i) & a_i^\dagger &= \frac{1}{2}(c_i - ic_{2i}) \\ p_i &= \frac{i}{\sqrt{2}} (a_i^\dagger - a_i) & a_i &= \frac{1}{2}(c_i + ic_{2i}) \end{aligned} . \quad (3.2)$$

Indeed, the (x_i, p_i) can be interpreted as single-particle position and conjugate momentum operators as in the quantum harmonic oscillator. We will organize them in a single

vector $c = (x_1, x_2, \dots, x_n, p_1, p_2, \dots, p_n)^T$. Analogously, we can define Hermitian Majorana operators for fermions,

$$\begin{aligned} c_i &= a_i^\dagger + a_i & a_i^\dagger &= \frac{1}{2}(c_i + ic_{2i}) \\ c_{2i} &= -i(a_i^\dagger - a_i) & a_i &= \frac{1}{2}(c_i - ic_{2i}) \end{aligned} \quad . \quad (3.3)$$

The (anti-)commutation relations then read

$$\begin{aligned} [c_i, c_j] &= i\Omega_{ij} \quad \text{with} \quad \Omega = \begin{pmatrix} 0 & \mathbb{1} \\ -\mathbb{1} & 0 \end{pmatrix} \quad (\text{bosons}) \\ \{c_i, c_j\} &= G_{ij} \quad \text{with} \quad G = 2 \begin{pmatrix} \mathbb{1} & 0 \\ 0 & \mathbb{1} \end{pmatrix} \quad (\text{fermions}) \end{aligned} \quad , \quad (3.4)$$

where Ω is symplectic while G is symmetric and positive definite and where the factor 2 in the fermionic case is due to the chosen normalization for the Majoranas. A canonical transformation is defined as an invertible linear transformation, M , that applied to c leaves Ω (G) unchanged. For bosons (fermions) this requires $M \in \mathrm{Sp}(2N, \mathbb{R})$ ($M \in O(2N)$). Now consider a general state, $|\psi\rangle$, and its one- and two-point correlation functions,

$$\begin{aligned} z_i &= \langle\psi|c_i|\psi\rangle \\ C_{ij} &= \langle\psi|(c_i - z_i)(c_j - z_j)|\psi\rangle = \langle\psi|c_i c_j|\psi\rangle - z_i z_j . \end{aligned} \quad (3.5)$$

We can decompose the latter in a symmetric and anti-symmetric part,

$$\begin{aligned} \frac{1}{2}G_{ij} &= \frac{1}{2}(C_{ij} + C_{ji}) \\ C_{ij} = \frac{1}{2}(G_{ij} + i\Omega_{ij}) \quad \text{where} \quad \frac{i}{2}\Omega_{ij} &= \frac{1}{2}(C_{ij} - C_{ji}) \\ &= \frac{1}{2}\langle\psi|[c_i, c_j]|\psi\rangle \end{aligned} \quad . \quad (3.6)$$

The utilized symbols were not chosen by coincidence as the anti-symmetric part of C_{ij} is indeed completely determined by the commutation relations for bosons. On the other hand, the symmetric part is determined by the anti-commutation relations for fermions. All the remaining information thus resides in z and G_{ij} , respectively, Ω_{ij} . In [183] Kähler structures, (G, Ω, J) , are defined as a combination of two bilinear maps, G and Ω , and one linear map, J , acting on a $2N$ -dimensional real linear space, $V \cong \mathbb{R}^{2N}$ where

- G is an metric, *i.e.* G defines an inner product and is thus symmetric and positive definite. Its representation w.r.t. to an orthonormal basis is G_{ij} with inverse g_{ij} .
- Ω is a symplectic form, *i.e.* Ω is anti-symmetric and non-degenerate. Its basis representation is Ω_{ij} with inverse ω_{ij} .
- J is a complex structure so that $J^2 = -\mathbb{1}$. Its basis representation is J_{ij} .

Furthermore, there is a compatibility equation,

$$J_{ij} = -G_{ik}\omega_{kj} \quad \iff \quad J_{ij} = \Omega_{ik}g_{kj} . \quad (3.7)$$

Hence, one can freely pick two of the three structures, solve the third from Eq. (3.7) and require the respective constraints. Promoting the Ω_{ij} (G_{ij}) matrix for bosonic (fermionic) states to a bilinear form with as Ω_{ij} (G_{ij}) the defining basis representation, the symplectic (metric) Kähler structure is already fixed. Pure Gaussian states are then defined as those states that complement this canonical structure with the non-canonical part in C_{ij} to form a consistent Kähler triplet, (G, Ω, J) . For bosons, $\Omega_{ij} = -\omega_{ij}$ is canonical so that all two-point information is contained in G_{ij} , which is symmetric and positive definite by construction. Furthermore, $J_{ij} = -G_{ik}\omega_{kj} = G_{ik}\Omega_{kj}$ is determined by the compatibility condition so that its complex structure requires $J^2 = G\Omega G\Omega = -\mathbb{1}$ for the corresponding matrices. An interesting sub-class are those states where $z = 0$ and $\langle x_i p_j \rangle = 0$ so that only the real and symmetric $\langle x_i x_j \rangle = X_{ij}$ and $\langle p_i p_j \rangle = P_{ij}$ remain in C_{ij} . For G and J we obtain

$$G = 2 \begin{pmatrix} X & 0 \\ 0 & P \end{pmatrix} \quad \Rightarrow \quad J = G\Omega = 2 \begin{pmatrix} 0 & X \\ -P & 0 \end{pmatrix} \quad (3.8)$$

so that the pure state is Gaussian when $XP = PX = \frac{1}{4}\mathbb{1}$. Analogously, $G = 2\mathbb{1}$ and $g = \frac{1}{2}\mathbb{1}$ are canonical for fermions so that $J = -2\omega = \frac{1}{2}\Omega$ yields a Gaussian state when $\Omega^2 = -4\mathbb{1}$. One can also prove that z always has to be zero in line with fermionic super-selection. This unified definition of Gaussian states in terms of Kähler structures is not only mathematically pleasing, it also encompasses the correct physical behavior as one can rigorously prove Wick's theorem [183]:

The m -point correlation function of a pure Gaussian state,

$$C_{i_1 i_2 \dots i_m}^m = \langle \psi | (c_{i_1} - z_{i_1})(c_{i_2} - z_{i_2}) \dots (c_{i_m} - z_{i_m}) | \psi \rangle \quad (3.9)$$

can always be expressed in terms of its two-point correlation functions with $C^{2m+1} = 0$ for odd-point correlations while for even products of operators

$$C_{i_1 i_2 \dots i_{2m}}^{2m} = \frac{1}{2^m m!} \sum_{\sigma \in S_{2m}} |\sigma| C_{i_{\sigma(1)}, i_{\sigma(2)}} \dots C_{i_{\sigma(2n-1)}, i_{\sigma(2m)}} \quad (3.10)$$

where $|\sigma| = 1$ for bosons while $|\sigma| = \text{sgn}(\sigma)$ for fermions.

To show that this definition also captures coherent states (discussed in more detail in Sec. 3.3), we consider a simple example of single-mode, bosonic, squeezed state. *I.e.* we only have a single bosonic creation operator, a^\dagger and from its vacuum we build a state by applying the unitary squeezing operator,

$$\begin{aligned} S(\zeta) &= e^{\frac{1}{2}\bar{\zeta}a^2 - \frac{1}{2}\zeta a^\dagger 2} \\ &= e^{-\frac{1}{2}e^{i\theta} \tanh(\rho)a^{\dagger 2}} e^{-\ln \cosh(\rho)(a^\dagger a + \frac{1}{2})} e^{\frac{1}{2}e^{i\theta} \tanh(\rho)a^2}, \end{aligned} \quad (3.11)$$

where $\zeta = \rho e^{i\theta}$ is a complex number and $S(\zeta)^\dagger = S(-\zeta)$. Utilizing the Baker-Campbell-Hausdorff formula,

$$e^X Y e^{-X} = Y + [X, Y] + \frac{1}{2!} [X, [X, Y]] + \frac{1}{3!} [X, [X, [X, Y]]] + \dots, \quad (3.12)$$

one obtains

$$\begin{aligned} S^\dagger(\zeta)aS(\zeta) &= a \cosh(\rho) - a^\dagger e^{i\theta} \sinh(\rho) \\ S^\dagger(\zeta)a^\dagger S(\zeta) &= a^\dagger \cosh(\rho) - ae^{-i\theta} \sinh(\rho) \end{aligned} \quad (3.13)$$

or equivalently

$$\begin{aligned} S^\dagger(\zeta)xS(\zeta) &= (\cosh(\rho) - \sinh(\rho) \cos(\theta))x - \sinh(\rho) \sin(\theta)p \\ S^\dagger(\zeta)pS(\zeta) &= -\sinh(\rho) \sin(\theta)x + (\cosh(\rho) + \sinh(\rho) \cos(\theta))p \end{aligned} \quad (3.14)$$

so that $S^\dagger(\zeta)cS(\zeta) = A(\zeta)c$ where the entries of the matrix $A(\zeta)$ can be read off from Eq. (3.14). For the squeezed state,

$$|\zeta\rangle = S(\zeta)|0\rangle = \frac{1}{\sqrt{\cosh(\rho)}} \sum_{n=0}^{+\infty} (-e^{i\theta} \tanh(\rho))^n \frac{\sqrt{2n!}}{2^n n!} |2n\rangle, \quad (3.15)$$

we then obtain

$$\begin{aligned} z_i &= \langle \zeta | c_i | \zeta \rangle = A_{ij} \langle 0 | c_j | 0 \rangle = 0 \\ C_{ij} &= \langle \zeta | c_i c_j | \zeta \rangle = A_{ik} \langle 0 | c_k c_l | 0 \rangle A_{lj}^T. \end{aligned} \quad (3.16)$$

Using that the two-points correlations for the vacuum ($\zeta = 0$) yield

$$C(0) = \frac{1}{2} \begin{pmatrix} 1 & i \\ -i & 1 \end{pmatrix}, \quad (3.17)$$

this results in

$$\begin{aligned} G &= \begin{pmatrix} \cosh(2\rho) + \cos(\theta) \sinh(2\rho) & \sin(\theta) \sinh(2\rho) \\ \sin(\theta) \sinh(2\rho) & \cosh(2\rho) - \cos(\theta) \sinh(2\rho) \end{pmatrix} \\ J = G\Omega &= \begin{pmatrix} -\sin(\theta) \sinh(2\rho) & \cos(\theta) \sinh(2\rho) + \cosh(2\rho) \\ \cos(\theta) \sinh(2\rho) - \cosh(2\rho) & \sin(\theta) \sinh(2\rho) \end{pmatrix}, \end{aligned} \quad (3.18)$$

where indeed $J^2 = -\mathbb{1}$ so that (G, Ω, J) is a Kähler structure.

We also note that canonical transformations can be used to bring the non-canonical part of C in a standard form. For bosons, Williamson's theorem [186] guarantees the existence of a symplectic transformation M so that

$$G = M \begin{pmatrix} \Lambda & 0 \\ 0 & \Lambda \end{pmatrix} M^T \quad (3.19)$$

where Λ is diagonal with positive diagonal entries, $\{\lambda_i\}$, the symplectic eigenvalues. Using the symplectic nature of M it is straightforward to show that

$$J = M \begin{pmatrix} \Lambda & 0 \\ 0 & \Lambda \end{pmatrix} \Omega M^T = M \begin{pmatrix} 0 & \Lambda \\ -\Lambda & 0 \end{pmatrix} M^T \quad (3.20)$$

such that all symplectic eigenvalues are equal to one as J is a complex structure. Similarly a Schur decomposition can be utilized in the fermionic case to rewrite

$$\Omega = 2M \begin{pmatrix} 0 & \Lambda \\ -\Lambda & 0 \end{pmatrix} M^T \quad (3.21)$$

where M is orthogonal and where generally $\lambda_i = \pm 1$ so that $J^2 = -\mathbb{1}$. However, we can use M to make all $\lambda_i = 1$.

Our current definition of Gaussian states only covers pure states. A mixed state is called Gaussian if and only if there exist a Hermitian quadratic operator,

$$\begin{aligned} H &= (c_a - z_a)Q_{ab}(c_b - z_b) + q && (\text{bosons}) \\ H &= ic_a Q_{ab} c_b + q && (\text{fermions}), \end{aligned} \quad (3.22)$$

such that $\rho = e^{-H}$. For bosons one additionally requires the already Hermitian Q to be positive definite while for fermions the Hermitian requirement makes Q real and anti-symmetric. The current form is very reminiscent of the thermal state in Eq. (2.25). Indeed, rescaling H with a β prefactor and using q for normalization, mixed Gaussian states could simply be defined as thermal states of quadratic Hamiltonians. For bosons the positive definite nature of Q then implies the energy spectrum to be bound from below. Based on Eq. (3.22) we can compute the one- and two-point functions

$$\begin{aligned} z_i &= \text{tr}(\rho c_i) \\ C_{ij} &= \text{tr}(\rho(c_i - z_i)(c_j - z_j)), \end{aligned} \quad (3.23)$$

where the displacement in the bosonic definition indeed corresponds to the one-point function. For general m -point correlation functions one can again prove Wick's theorem and decomposing

$$C_{ij} = \frac{1}{2}(G_{ij} + i\Omega_{ij}), \quad (3.24)$$

we again obtain a canonical part and a part characterizing the state. However, defining J by $-G\omega$ (Ωg) for bosons (fermions), one does not obtain a complex structure, *i.e.* $J^2 \neq 1$ and (G, Ω, J) does not form a Kähler triplet. To make this more explicit we bring Q in standard form by applying a canonical transformation. Indeed, for bosons Q is positive definite so that

$$Q = M \begin{pmatrix} B & \\ & B \end{pmatrix} M^T \quad (3.25)$$

with M symplectic, B diagonal and its entries $\beta_i \geq 0$ (again referring to thermal states) due to Williamson's theorem. Analogously, Schur decomposition can be utilized for fermions to write

$$Q = M \begin{pmatrix} B & \\ -B & \end{pmatrix} M^T \quad (3.26)$$

with M orthogonal and chosen so that $\beta_i \geq 0$. In the new basis, the non-canonical part of the two-point correlation functions is easily calculated,

$$\begin{aligned} G &= \begin{pmatrix} \coth B & \\ & \coth B \end{pmatrix} && (\text{bosons}) \\ \Omega &= 2 \begin{pmatrix} & \tanh 2B \\ -\tanh 2B & \end{pmatrix} && (\text{fermions}). \end{aligned} \quad (3.27)$$

This shows that the symplectic eigenvalues of G are always greater than or equal to one (with the latter applying for pure states) while for fermions $\Omega\Omega^T \leq 4$. Recovering pure states is only possible by taking the limit $\beta_i \rightarrow +\infty$ making J a complex structure again.

This does not come as a surprise. Indeed, by defining a mixed Gaussian state, ρ , as an exponential, we required it to be full rank and thus not to reduce to a pure state projector. Only by taking a limit this becomes possible. In the following Section we show that at least for fermions, this technicality can be resolved by working with Grassmann variables.

3.2 Grassmann formalism

In the previous Section, Gaussian states were defined for both bosons and fermions but pure and mixed states required a separate definition. Utilizing Grassmann variables, we will establish a unified framework for fermions based on the standard work of Bravyi [184].

3.2.1 Grassmann numbers

Since our focus is on fermions, there is no need to distinguish between the x and p components in c and we reorder it as follows,

$$\begin{aligned} c_{2i-1} &= a_i^\dagger + a_i & a_i^\dagger &= \frac{1}{2}(c_{2i-1} + ic_{2i}) \\ c_{2i} &= -i(a_i^\dagger - a_i) & a_i &= \frac{1}{2}(c_{2i-1} - ic_{2i}) \end{aligned} \quad (3.28)$$

An arbitrary operator can be written as

$$Z = \alpha + \sum_{p=1}^{2n} \sum_{1 \leq a_1 < \dots < a_p \leq 2n} \alpha_{a_1, \dots, a_p} c_{a_1} \dots c_{a_p} \quad (3.29)$$

with $\alpha = 2^{-n} \text{tr}(Z)$. Indeed, the canonical anti-commutation relations make sure that monomials with repeating factors will always reduce to a lower degree. As a result, there is a maximal monomial that contains every Majorana operator just once. The corresponding algebraic structure is called a Clifford algebra and every operator Z thus belongs to the Clifford algebra \mathcal{C}_{2n} . If only terms with an even (odd) number of factors appear in Eq. (3.29) we call Z even (odd). A specific example of an even operator is a general quadratic Hamiltonian,

$$H = iQ_{ab}c_a c_b + q \quad (3.30)$$

where Q is real and anti-symmetric as in Eq. (3.22). Isomorphic to the Clifford algebra, we define the Grassmann algebra \mathcal{G}_{2n} , a complex linear space of dimension $2n$ with basis vectors $\{\theta_i\}$ and some associative multiplication so that $\{\theta_i, \theta_j\} = 0$ and thus $\theta_i^2 = 0$. In other words \mathcal{G}_{2n} is an alternating tensor algebra over a $2n$ -dimensional complex space and repeating factors now immediately yield 0. The isomorphism from Clifford to Grassmann algebra is for a homogeneous product of operators defined by

$$\omega : \mathcal{C}_{2n} \rightarrow \mathcal{G}_{2n} : c_{i_1} c_{i_2} \dots c_{i_p} \mapsto \theta_{i_1} \theta_{i_2} \dots \theta_{i_p} \quad (3.31)$$

and extends to the full space via linearity. We will call $Z(\theta) = \omega(Z)$ the Grassmann form of an operator $Z \in \mathcal{C}_{2n}$. Performing canonical transformations in \mathcal{C}_{2n} then corresponds to identical transformations in \mathcal{G}_{2n} that due to their orthogonal nature retain the correct anti-commutation relations. Grassmann variables will prove to be very useful based on

their simple differentiation and integration rules. To introduce these we define the partial derivative as a linear operator on \mathcal{G}_{2n} with

$$\frac{\partial}{\partial \theta_a} 1 = 0 , \quad \frac{\partial}{\partial \theta_a} \theta_b = \delta_{ab} \quad (3.32)$$

and Leibniz's rule,

$$\frac{\partial}{\partial \theta_a} (\theta_b Z(\theta)) = \delta_{ab} Z(\theta) - \theta_b \frac{\partial}{\partial \theta_a} Z(\theta) . \quad (3.33)$$

As a result, partial derivatives anti-commute. Note that by taking a partial derivative, the corresponding Grassmann variable no longer appears in the resulting expression. Differentiation is thus rather a linear transformation $\mathcal{G}_{2n} \rightarrow \mathcal{G}_{2n-1}$, similar to standard integration. This is why integration and differentiation are identified for Grassmann variables,

$$\int d\theta_a \equiv \frac{\partial}{\partial \theta_a} : \mathcal{G}_{2n} \rightarrow \mathcal{G}_{2n-1} . \quad (3.34)$$

Integrating out all Grassmann variables is denoted by

$$\int D\theta = \int d\theta_{2n} d\theta_{2n-1} \dots d\theta_1 \quad (3.35)$$

where the order is chosen such that application on $\theta_1 \theta_2 \dots \theta_{2n}$ yields 1. Performing a canonical transformation $\theta_i \rightarrow \eta_i = M_{ij} \theta_j$ ($M \in O(2n)$) and thus a change of variables, the according change in derivatives is

$$\frac{\partial}{\partial \eta_a} = \sum_{b=1}^{2n} (M^{-1})_{ba} \frac{\partial}{\partial \theta_b} = \sum_{b=1}^{2n} M_{ab} \frac{\partial}{\partial \theta_b} \quad (3.36)$$

so that for a full integration

$$\int D\eta = (\det M)^{-1} \int D\theta = \int D\theta \quad (3.37)$$

In the context of Gaussian states we will often encounter quadratic forms, $\theta^T X \theta \in \mathcal{G}_{2n}$, with X complex and anti-symmetric as well as the bilinear form $\theta^T \eta \in \mathcal{G}_{4n}$. Two useful explicit expressions for Gaussian integrals then are

$$\begin{aligned} \int D\theta \exp\left(\frac{i}{2}\theta^T X \theta\right) &= i^n \text{Pf}(X) , \\ \int D\theta \exp\left(\theta^T \eta + \frac{i}{2}\theta^T X \theta\right) &= i^n \text{Pf}(X) \exp\left(-\frac{i}{2}\eta^T X^{-1} \eta\right) , \end{aligned} \quad (3.38)$$

where the infinite series in the definition of the exponentials reduce to finite sums and where $\text{Pf}(X)$ denotes the Pfaffian of an anti-symmetric matrix X , defined by

$$\text{Pf}(X) = \frac{1}{2^n n!} \sum_{\sigma \in S_{2n}} \text{sgn}(\sigma) X_{\sigma(1)\sigma(2)} \dots X_{\sigma(2n-1)\sigma(2n)} \quad (3.39)$$

so that $\text{Pf}(X)^2 = \det(X)$. Linking back to the Clifford algebra also the following property will be used extensively,

$$\text{tr}(XY) = (-2)^n \int D\theta \int D\mu e^{\theta^T \mu} X(\theta) Y(\mu) , \quad (3.40)$$

and can easily be proven by considering it term by term.

3.2.2 Gaussian states, operators and channels

With this primer on Grassmann analysis we are ready to formulate the definition of a Gaussian state. A state $\rho \in \mathcal{C}_{2n}$ is called Gaussian if it has a Gaussian Grassmann representation, *i.e.*

$$\rho(\theta) = \frac{1}{2^n} \exp\left(\frac{i}{2}\theta^T \Gamma \theta\right) \quad (3.41)$$

with Γ the real and anti-symmetric correlation matrix. This definition indeed allows for non-full-rank ρ . As an example consider the single-mode vacuum, $|0\rangle$, which we obviously would like to be Gaussian. Its density operator is $\rho = a^\dagger a = \frac{1}{2}(1 - ic_1 c_2)$ so that

$$\rho(\theta) = \frac{1}{2}(1 - i\theta_1 \theta_2) = \frac{1}{2} \exp\left(-\frac{i}{2}\theta^T \begin{pmatrix} 0 & 1 \\ -1 & 0 \end{pmatrix} \theta\right) \quad (3.42)$$

with correlation matrix $\Gamma = i\sigma^y$, a matrix that we will use a lot and call J (not to be confused with the complex structure from the previous Section). By applying Eq. (3.40) and Eq. (3.38) we can relate the correlation matrix to two-point correlation functions and thus to Ω ,

$$\Gamma_{ij} = \frac{i}{2} \text{tr}(\rho [c_i, c_j]) = -\frac{1}{2}\Omega_{ij}. \quad (3.43)$$

More generally, higher-order correlation functions yield zero for odd orders while for even orders

$$C_{i_1 i_2 \dots i_{2p}}^{2p} = \text{tr}(\rho c_{i_1} c_{i_2} \dots c_{i_{2p}}) = (-i)^p \text{Pf}(\Gamma|_{i_1, i_2, \dots, i_{2p}}). \quad (3.44)$$

where $\Gamma|_{i_1, i_2, \dots, i_{2p}}$ is the restriction of Γ to the indicated rows and columns. Eq. (3.44) hence is a re-expression of Wick's theorem for fermions in terms of a Pfaffian. As Γ is real and anti-symmetric, it can be brought in standard form by means of an orthogonal canonical transformation,

$$\Gamma = M \bigoplus_{i=1}^n \begin{pmatrix} \lambda_i & \\ -\lambda_i & \end{pmatrix} M^T. \quad (3.45)$$

Comparing with Eq. (3.27) we can choose M such that $0 \leq \lambda_i = \tanh 2\beta_i \leq 1$. More generally we have $\lambda_i \in [-1, 1]$ and thus $\Gamma^T \Gamma \leq 1$ (with the equality applying for a pure state). Accordingly transforming the Majoranas $\tilde{c}_i = M_{ij}^T c_j$, the density operator can be expressed as

$$\rho = \frac{1}{2^n} \prod_{i=1}^n (1 + i\lambda_i c_{2i-1} c_{2i}) \quad (3.46)$$

showing that the constraints on λ_i essentially encode positivity of ρ . As a generalization of Gaussian state we can define a Gaussian operator $X \in \mathcal{C}_{2n}$ with $\text{tr}(X) \neq 0$ as an operator with a Gaussian Grassmann representation

$$\rho(\theta) = C \exp\left(\frac{i}{2}\theta^T X \theta\right) \quad (3.47)$$

where C is some complex number while X is anti-symmetric but can be complex. One can show that the composition of Gaussian operators again yields a Gaussian operator.

In the previous Chapter, (CPTP) channels were introduced as maps between (density) operators and just like density operators we can require channels to be Gaussian: a linear map $\mathcal{E} : \mathcal{C}_{2n} \rightarrow \mathcal{C}_{2m}$ is Gaussian if and only if it admits an integral representation

$$\mathcal{E}(Z)(\theta) = C \int D\eta D\mu \exp \left(\frac{i}{2} \begin{pmatrix} \theta \\ \eta \end{pmatrix}^T \begin{pmatrix} A & B \\ -B^T & D \end{pmatrix} \begin{pmatrix} \theta \\ \eta \end{pmatrix} + i\eta^T \mu \right) Z(\mu) \quad (3.48)$$

where C is some complex number while

$$X = \begin{pmatrix} A & B \\ -B^T & D \end{pmatrix} \quad (3.49)$$

is an anti-symmetric complex matrix. As an example we consider a channel corresponding to a canonical rotation of Majoranas, *i.e.* $\mathcal{E}(c_i) = R_{ij} c_j$ which can be encoded by $A = D = 0$ and $B = R^T$ so that

$$\mathcal{E}(Z)(\theta) = C \int \exp(i\theta^T R^T \eta + i\eta^T \mu) Z(\mu) D\eta D\mu = Z(R\theta). \quad (3.50)$$

Gaussian channels are always parity preserving in the sense that they map even (odd) operators to even (odd) operators. Moreover, they map Gaussian operators to Gaussian operators. Consider for instance the application of \mathcal{E} to a Gaussian state with correlation matrix Γ_{in} ,

$$\begin{aligned} \mathcal{E}(\rho)(\theta) &= C \int D\eta D\mu e^{\frac{i}{2} \begin{pmatrix} \theta \\ \eta \end{pmatrix}^T \begin{pmatrix} A & B \\ -B^T & D \end{pmatrix} \begin{pmatrix} \theta \\ \eta \end{pmatrix}} e^{i\eta^T \mu} \frac{1}{2^n} e^{\frac{i}{2} \mu^T \Gamma_{\text{in}} \mu} \\ &= \frac{C}{2^n} i^n \text{Pf}(\Gamma_{\text{in}}) e^{\frac{i}{2} \theta^T A \theta} \int D\eta e^{\frac{i}{2} \eta^T (D + \Gamma_{\text{in}}^{-1}) \eta} e^{\eta^T (-iB^T \theta)} \\ &= \frac{C}{(-2)^n} \text{Pf}(\Gamma_{\text{in}}) \text{Pf}(D + \Gamma_{\text{in}}^{-1}) e^{\frac{i}{2} \theta^T \Gamma_{\text{out}} \theta} \end{aligned} \quad (3.51)$$

where the correlation matrix of the resulting Gaussian operator is given by

$$\Gamma_{\text{out}} = A + B(D + \Gamma_{\text{in}}^{-1})^{-1} B^T, \quad (3.52)$$

a Schur complement. The pre-exponential factor can be determined by utilizing Eq. (3.40),

$$\text{tr}(\mathcal{E}(\rho)) = C(-1)^n \text{Pf}(\Gamma_{\text{in}}) \text{Pf}(D + \Gamma_{\text{in}}^{-1}) \quad (3.53)$$

As a result, the map is only trace-preserving when $D = 0$. Requiring \mathcal{E} to preserve the identity operator as well, $A = 0$ and $\Gamma_{\text{out}} = B\Gamma_{\text{in}}B^T$. This set of so-called bistochastic maps is typically too restrictive for the applications in this work. Consequently, we will typically not require \mathcal{E} to be trace preserving but rather normalize the state after application of the channel. More important is complete positivity which can be imposed by requiring $C \geq 0$ and X to be real and $X^T X \leq 1$ where the equality yields a map that transforms pure states to pure states. The composition of completely positive Gaussian maps is again completely positive and Gaussian.

3.2.3 Application to the lattice

We will now apply the Grassmann formalism to define a Gaussian fermionic state on an extended d -dimensional lattice with a unit cell spanned by the vectors $\{\mathbf{a}_1, \mathbf{a}_2, \dots, \mathbf{a}_d\}$. Vertices are labeled by $\mathbf{x} = \sum_{i=1}^d n_i \mathbf{a}_i$ where $n_i \in \mathbb{Z}$ in the case of an infinite lattice while for finite lattices $n_i = 0, \dots, N_i$ and $N_s = \prod_{i=1}^d N_i$ is the total number of lattice sites. Fermionic operators, $a_{\mathbf{x},i}$, are placed on the vertices and build up the local Hilbert space with $i = 1, \dots, f$, the (Wannier) orbital index. Corresponding Majorana operators, $c_{\mathbf{x},i}$, can be defined as in Eq. (3.28) (and thus $i = 1, \dots, 2f$). A Gaussian state on the lattice then has a Grassmann form as in Eq. (3.41) where Grassmann variables are labeled by a positional and an orbital index. The correlation matrix can be expressed as

$$\Gamma_{\mathbf{xy}}^{ij} = \frac{i}{2} \text{tr} (\rho [c_{\mathbf{x},i}, c_{\mathbf{y},j}]) . \quad (3.54)$$

Following Wigner's theorem, lattice translations can be represented by unitary operators, $T_{\mathbf{x}}$, on the Hilbert space such that

$$T_{\mathbf{y}} c_{\mathbf{x},i} T_{\mathbf{y}}^\dagger = c_{\mathbf{x}+\mathbf{y},i} . \quad (3.55)$$

Requiring the Gaussian state, ρ , to be translation invariant under each of these $T_{\mathbf{x}}$ so that $\rho = T_{\mathbf{x}} \rho T_{\mathbf{x}}^\dagger$, we thus obtain

$$\Gamma_{\mathbf{xy}}^{ij} = \frac{i}{2} \text{tr} (\rho [c_{\mathbf{x},i}, c_{\mathbf{y},j}]) = \frac{i}{2} \text{tr} (\rho [c_{\mathbf{x}-\mathbf{y},i}, c_{\mathbf{0},j}]) = \Gamma_{\mathbf{x}-\mathbf{y}}^{ij} . \quad (3.56)$$

We can make use of this translation-invariant (TI) form by going to Fourier space,

$$\begin{aligned} a_{\mathbf{k},i} &= \frac{1}{\sqrt{N_s}} \sum_{\mathbf{n}} e^{-i\mathbf{k}\cdot\mathbf{x}} a_{\mathbf{x},i} & a_{\mathbf{k},i}^\dagger &= \frac{1}{\sqrt{N_s}} \sum_{\mathbf{x}} e^{i\mathbf{k}\cdot\mathbf{x}} a_{\mathbf{x},i}^\dagger \\ a_{\mathbf{x},i} &= \frac{1}{\sqrt{N_s}} \sum_{\mathbf{k}} e^{i\mathbf{k}\cdot\mathbf{x}} a_{\mathbf{k},i} & a_{\mathbf{x},i}^\dagger &= \frac{1}{\sqrt{N_s}} \sum_{\mathbf{k}} e^{-i\mathbf{k}\cdot\mathbf{x}} a_{\mathbf{k},i}^\dagger . \end{aligned} \quad (3.57)$$

Here, $\mathbf{k} = \frac{1}{N_i} (n_i (+\frac{1}{2})) \mathbf{b}_i$ for finite lattices with (anti-)periodic boundary conditions where \mathbf{b}_i are the reciprocal lattice vectors characterized by $\mathbf{a}_i \cdot \mathbf{b}_j = 2\pi\delta_{ij}$ and where the integers n_i are chosen such that the first Brillouin zone is covered. In the thermodynamic limit, \mathbf{k} -space becomes a continuum. Similarly transforming the Majorana operators one obtains $d_{\mathbf{k},i}$ operators but these are no longer Majoranas as they are not Hermitian, $d_{\mathbf{k},i}^\dagger = d_{-\mathbf{k},i}$. Indeed, Fourier transformation, though unitary, is not a canonical transformation for the Majorana operators leading to a mixing of \mathbf{k} and $-\mathbf{k}$ modes. Alternatively, one could define Hermitian Majorana operators in Fourier space, $c_{\mathbf{k},i}$, following the definition in Eq. (3.28). These different operator sets are linked via

$$\begin{aligned} \begin{pmatrix} d_{\mathbf{k},2i-1} \\ d_{\mathbf{k},2i} \end{pmatrix} &= \begin{pmatrix} 1 & 1 \\ i & -i \end{pmatrix} \begin{pmatrix} a_{\mathbf{k},i} \\ a_{-\mathbf{k},i}^\dagger \end{pmatrix} \\ \begin{pmatrix} c_{\mathbf{k},2i-1} \\ c_{\mathbf{k},2i} \end{pmatrix} &= \begin{pmatrix} 1 & 1 \\ i & -i \end{pmatrix} \begin{pmatrix} a_{\mathbf{k},i} \\ a_{\mathbf{k},i}^\dagger \end{pmatrix} . \end{aligned} \quad (3.58)$$

Defining the following $4f$ -dimensional vectors,

$$\begin{aligned}\bar{a}_{\mathbf{k}} &= \left(a_{\mathbf{k},1} \dots a_{\mathbf{k},f} \quad a_{-\mathbf{k},1}^\dagger \dots a_{-\mathbf{k},f}^\dagger \quad a_{-\mathbf{k},1} \dots a_{-\mathbf{k},f} \quad a_{\mathbf{k},1}^\dagger \dots a_{\mathbf{k},f}^\dagger \right)^T \\ \bar{c}_{\mathbf{k}} &= \left(c_{\mathbf{k},1} \dots c_{\mathbf{k},2f} \quad c_{-\mathbf{k},1} \dots c_{-\mathbf{k},2f} \right)^T \\ \bar{d}_{\mathbf{k}} &= \left(d_{\mathbf{k},1} \dots d_{\mathbf{k},2f} \quad d_{\mathbf{k},1}^\dagger \dots d_{\mathbf{k},2f}^\dagger \right)^T,\end{aligned}\tag{3.59}$$

the operator relations in \mathbf{k} -space can be rephrased as

$$\begin{aligned}\bar{d}_{\mathbf{k}} &= \begin{pmatrix} W & \bar{W} \\ & W & \bar{W} \end{pmatrix} \bar{a}_{\mathbf{k}} \\ \bar{c}_{\mathbf{k}} &= \begin{pmatrix} W & & \bar{W} \\ & \bar{W} & W \end{pmatrix} \bar{a}_{\mathbf{k}}\end{aligned}\tag{3.60}$$

and thus

$$\bar{c}_{\mathbf{k}} = \frac{1}{2} \begin{pmatrix} V & \bar{V} \\ \bar{V} & V \end{pmatrix} \bar{d}_{\mathbf{k}}\tag{3.61}$$

with

$$W = \begin{pmatrix} 1 \\ i \end{pmatrix}^{\oplus f} = \mathbb{1}_f \otimes \begin{pmatrix} 1 \\ i \end{pmatrix} \quad V = \begin{pmatrix} 1 & -i \\ i & 1 \end{pmatrix}^{\oplus f} = \mathbb{1}_f \otimes \begin{pmatrix} 1 & -i \\ i & 1 \end{pmatrix}.\tag{3.62}$$

Now let us return to the correlation matrix and write down its Fourier transformed version,

$$\begin{aligned}G_{\mathbf{kq}}^{ij} &= \mathcal{F}_{\mathbf{k},\mathbf{x}} \Gamma_{\mathbf{x}-\mathbf{y}}^{ij} \mathcal{F}_{\mathbf{y},\mathbf{q}}^\dagger = G^{ij}(\mathbf{k}) \delta_{\mathbf{kq}} \\ &= \frac{i}{2} \text{tr} \left(\rho \left[\mathcal{F}_{\mathbf{k},\mathbf{x}} c_{\mathbf{x},i}, c_{\mathbf{y},j} \mathcal{F}_{\mathbf{y},\mathbf{q}}^\dagger \right] \right) = \frac{i}{2} \text{tr} \left(\rho \left[d_{\mathbf{k},i}, d_{\mathbf{q},j}^\dagger \right] \right),\end{aligned}\tag{3.63}$$

with $\mathcal{F}_{\mathbf{k},\mathbf{x}} = \frac{1}{\sqrt{N_s}} e^{-i\mathbf{k}\cdot\mathbf{x}}$ encoding the unitary Fourier transformation. Translation invariance thus makes this matrix block diagonal in Fourier space so that all information about TI Gaussian fermionic states is contained in $G(\mathbf{k})$. E.g. calculating the two-point functions,

$$\tilde{G}^{ij}(\mathbf{k}) = \frac{i}{2} \text{tr} \left(\rho \left[(\bar{d}_{\mathbf{k}})_i, (\bar{d}_{\mathbf{k}}^\dagger)_j \right] \right)\tag{3.64}$$

we obtain

$$\tilde{G}(\mathbf{k}) = \begin{pmatrix} G(\mathbf{k}) & \\ & \overline{G(\mathbf{k})} \end{pmatrix}.\tag{3.65}$$

Similarly, one defines

$$\begin{aligned}C^{ij}(\mathbf{k}) &= \frac{1}{2} \langle \left[(\bar{a}_{\mathbf{k}})_i, (\bar{a}_{\mathbf{k}}^\dagger)_j \right] \rangle \\ \Gamma^{ij}(\mathbf{k}) &= \frac{i}{2} \langle \left[(\bar{c}_{\mathbf{k}})_i, (\bar{c}_{\mathbf{k}})_j \right] \rangle,\end{aligned}\tag{3.66}$$

displaying the following substructure,

$$\begin{aligned}C(\mathbf{k}) &= \begin{pmatrix} \frac{1}{2} - n^T(\mathbf{k}) & x(\mathbf{k}) \\ x^\dagger(\mathbf{k}) & n(-\mathbf{k}) - \frac{1}{2} \\ & & \frac{1}{2} - n^T(-\mathbf{k}) & x(-\mathbf{k}) \\ & & x(-\mathbf{k})^\dagger & n(\mathbf{k}) - \frac{1}{2} \end{pmatrix} \\ \Gamma(\mathbf{k}) &= \begin{pmatrix} \Gamma_{++}(\mathbf{k}) & \Gamma_{+-}(\mathbf{k}) \\ \Gamma_{-+}(\mathbf{k}) & \Gamma_{--}(\mathbf{k}) \end{pmatrix},\end{aligned}\tag{3.67}$$

with

$$\begin{aligned} n^{ij}(\mathbf{k}) &= \text{tr} \left(\rho a_{\mathbf{k},i}^\dagger a_{\mathbf{k},j} \right) = \overline{n^{ji}(\mathbf{k})} \\ x^{ij}(\mathbf{k}) &= \text{tr} \left(\rho a_{\mathbf{k},i} a_{-\mathbf{k},j} \right) = -x^{ji}(-\mathbf{k}) \\ \Gamma_{+\pm}^{ij}(\mathbf{k}) &= \frac{i}{2} \text{tr} \left(\rho [c_{\mathbf{k},i}, c_{\pm\mathbf{k},j}] \right) = \Gamma_{-\mp}^{ij}(-\mathbf{k}) \\ G^{ij}(\mathbf{k}) &= \frac{i}{2} \text{tr} \left(\rho [d_{\mathbf{k},i}, d_{\mathbf{k},j}^\dagger] \right) = \overline{G_{ij}(-\mathbf{k})}. \end{aligned} \quad (3.68)$$

These can all be linked back to $G(\mathbf{k})$. Indeed, using Eq. (3.60) and noting that $G(\mathbf{k}) = \overline{G(-\mathbf{k})}$, we find

$$\begin{aligned} \Gamma(\mathbf{k}) &= \frac{1}{2} \begin{pmatrix} V & \overline{V} \\ \overline{V} & V \end{pmatrix} \tilde{G}(\mathbf{k}) \frac{1}{2} \begin{pmatrix} V & \overline{V} \\ \overline{V} & V \end{pmatrix} \\ &= \frac{1}{2} \begin{pmatrix} \Re(VG(\mathbf{k})V) & \Re(VG(\mathbf{k})\overline{V}) \\ \Re(\overline{V}G(\mathbf{k})V) & \Re(\overline{V}G(\mathbf{k})\overline{V}) \end{pmatrix} \end{aligned} \quad (3.69)$$

and

$$\begin{aligned} C(\mathbf{k}) &= -i \begin{pmatrix} W^\dagger & & \\ W^T & & \\ & W^\dagger & \\ & & W^T \end{pmatrix} \tilde{G}(\mathbf{k}) \begin{pmatrix} W & \overline{W} & & \\ & W & \overline{W} & \\ & & W & \overline{W} \end{pmatrix} \\ &= -\frac{i}{4} \begin{pmatrix} W^\dagger G(\mathbf{k})W & W^\dagger G(\mathbf{k})\overline{W} & & \\ W^T G(\mathbf{k})W & W^T G(\mathbf{k})\overline{W} & & \\ & & W^\dagger \overline{G(\mathbf{k})}W & W^\dagger \overline{G(\mathbf{k})}\overline{W} \\ & & W^T \overline{G(\mathbf{k})}W & W^T \overline{G(\mathbf{k})}\overline{W} \end{pmatrix} \end{aligned} \quad (3.70)$$

so that

$$n(\mathbf{k}) = \frac{1}{2} + \frac{i}{4} W^T G^T(\mathbf{k}) \overline{W} \quad x(\mathbf{k}) = -\frac{i}{4} W^\dagger G(\mathbf{k}) \overline{W}. \quad (3.71)$$

Furthermore, we have that

$$\Gamma(\mathbf{k}) = \begin{pmatrix} J^{\oplus f} - 2 \Im(\overline{W}n(\mathbf{k})W^T) & -2 \Im(Wx(\mathbf{k})W^T) \\ -2 \Im(Wx(-\mathbf{k})W^T) & J^{\oplus f} - 2 \Im(\overline{W}n(-\mathbf{k})W^T) \end{pmatrix} \quad (3.72)$$

and

$$\begin{aligned} G(\mathbf{k}) &= J^{\oplus f} + i \left(-Wn^T(\mathbf{k})W^\dagger + \overline{W}n(-\mathbf{k})W^T \right. \\ &\quad \left. + Wx(\mathbf{k})W^T + \overline{W}x^\dagger(\mathbf{k})W^\dagger \right). \end{aligned} \quad (3.73)$$

As an illustration, $f = 1$ yields

$$\begin{aligned} \Gamma(\mathbf{k}) &= \begin{pmatrix} (1 - 2n(\mathbf{k}))J & -2(\Re(x(\mathbf{k}))\sigma^x + \Im(x(\mathbf{k}))\sigma^z) \\ 2(\Re(x(\mathbf{k}))\sigma^x + \Im(x(\mathbf{k}))\sigma^z) & (1 - 2n(-\mathbf{k}))J \end{pmatrix} \\ G(\mathbf{k}) &= \begin{pmatrix} i \left(-n(\mathbf{k}) + n(-\mathbf{k}) + x(\mathbf{k}) + \overline{x(\mathbf{k})} \right) & 1 - n(\mathbf{k}) - n(-\mathbf{k}) - x(\mathbf{k}) + \overline{x(\mathbf{k})} \\ -1 + n(\mathbf{k}) + n(-\mathbf{k}) - x(\mathbf{k}) + \overline{x(\mathbf{k})} & i \left(-n(\mathbf{k}) + n(-\mathbf{k}) - x(\mathbf{k}) - \overline{x(\mathbf{k})} \right) \end{pmatrix} \end{aligned} \quad (3.74)$$

where everything is expressed as a function of the expectation values of the \mathbf{k} -space number operator, $a_{\mathbf{k}}^\dagger a_{\mathbf{k}}$ and pairing term, $a_{\mathbf{k}} a_{-\mathbf{k}}$.

The formulas we just derived will be used extensively, e.g. to express expectation values of certain observables as a function of the correlation matrices. Consider for instance a general quadratic, translation-invariant and particle-number-conserving Hamiltonian,

$$H = \sum_{\mathbf{x}, \mathbf{y}} a_{\mathbf{x}, i}^\dagger H_{\mathbf{x}-\mathbf{y}}^{ij} a_{\mathbf{y}, j} + \tilde{E}, \quad (3.75)$$

where \tilde{E} is an energy offset. The energy expectation value for a TI, Gaussian state can simply be expressed by going to Fourier space where

$$H = \sum_{\mathbf{k}} a_{\mathbf{k}, i}^\dagger H^{ij}(\mathbf{k}) a_{\mathbf{k}, j} + \tilde{E}, \quad (3.76)$$

and $H^{ij}(\mathbf{k}) = \sum_{\mathbf{x}} e^{-i\mathbf{k}\cdot\mathbf{x}} H_{\mathbf{x}}^{ij}$ so that

$$E = \text{tr}(\rho H) = \sum_{\mathbf{k}} H^{ij}(\mathbf{k}) n^{ij}(\mathbf{k}). \quad (3.77)$$

More generally a quadratic Hamiltonian can be written as in Eq. (3.30). Expressed w.r.t. to the creation and annihilation operators gathered in the Nambu spinor,

$$\Upsilon_{\mathbf{x}} = \begin{pmatrix} a_{\mathbf{x}, 1} \dots a_{\mathbf{x}, f} & a_{\mathbf{x}, 1}^\dagger \dots a_{\mathbf{x}, f}^\dagger \end{pmatrix}^T \quad (3.78)$$

we thus obtain

$$H = \frac{1}{2} \sum_{AB} \Upsilon_A^\dagger H_{\text{BdG}}^{AB} \Upsilon_B + \tilde{E}, \quad (3.79)$$

with H_{BdG}^{AB} the Bogoliubov-de Gennes (BdG) single-particle Hamiltonian, \tilde{E} an energy offset and Υ collecting the Nambu spinors on all sites and the A, B labels discerning between the upper (annihilator) and lower (creator) half. As these are not independent, one always has $(\sigma^x \otimes \mathbb{1}_{N_s f}) H_{\text{BdG}}^T (\sigma^x \otimes \mathbb{1}_{N_s f}) = -H_{\text{BdG}}$ and thus that

$$H_{\text{BdG}} = \begin{pmatrix} \Xi & \Delta \\ -\bar{\Delta} & -\Xi^T \end{pmatrix}, \quad \Xi = \Xi^\dagger, \quad \Delta = -\Delta^T. \quad (3.80)$$

Further imposing translation invariance, $\Xi_{\mathbf{x}\mathbf{y}}^{ij} = \Xi_{\mathbf{x}-\mathbf{y}}^{ij}$ and $\Delta_{\mathbf{x}\mathbf{y}}^{ij} = \Delta_{\mathbf{x}-\mathbf{y}}^{ij}$, yields

$$H = \frac{1}{2} \sum_{\mathbf{k}} \Upsilon_{\mathbf{k}}^\dagger H_{\text{BdG}}(\mathbf{k}) \Upsilon_{\mathbf{k}} = \frac{1}{2} \sum_{\mathbf{k}} \Upsilon_{\mathbf{k}}^\dagger \begin{pmatrix} \Xi(\mathbf{k}) & \Delta(\mathbf{k}) \\ -\bar{\Delta}(-\mathbf{k}) & -\Xi^T(-\mathbf{k}) \end{pmatrix} \Upsilon_{\mathbf{k}} \quad (3.81)$$

where

$$\Upsilon_{\mathbf{k}} = \begin{pmatrix} a_{\mathbf{k}, 1} \dots a_{\mathbf{k}, f} & a_{-\mathbf{k}, 1}^\dagger \dots a_{-\mathbf{k}, f}^\dagger \end{pmatrix}^T, \quad (3.82)$$

$\Xi^{ij}(\mathbf{k}) = \sum_{\mathbf{x}} e^{-i\mathbf{k}\cdot\mathbf{x}} \Xi_{\mathbf{x}}^{ij}$ and $\Delta^{ij}(\mathbf{k}) = \sum_{\mathbf{x}} e^{-i\mathbf{k}\cdot\mathbf{x}} \Delta_{\mathbf{x}}^{ij}$. As a result, $\Xi^\dagger(\mathbf{k}) = \Xi(\mathbf{k})$ and $\Delta(\mathbf{k}) = -\Delta^T(-\mathbf{k})$ so that $(\sigma^x \otimes \mathbb{1}_f) H_{\text{BdG}}^T(-\mathbf{k}) (\sigma^x \otimes \mathbb{1}_f) = -H_{\text{BdG}}(\mathbf{k})$. Hence, the energy

expectation value for a Gaussian state can be expressed as

$$\begin{aligned} E &= \frac{1}{2} \sum_{\mathbf{k}} \text{tr} \left(\rho \Upsilon_{\mathbf{k}}^\dagger H_{\text{BdG}}(\mathbf{k}) \Upsilon_{\mathbf{k}} \right) + \tilde{E} \\ &= \frac{i}{2} \sum_{\mathbf{k}} \text{tr} \left(\tilde{H}_{\text{BdG}}(\mathbf{k}) G(\mathbf{k}) \right) + \frac{1}{4} \sum_{\mathbf{k}} \text{tr} \left(\tilde{H}_{\text{BdG}}(\mathbf{k}) \right) + \tilde{E} \end{aligned} \quad (3.83)$$

where $\tilde{H}_{\text{BdG}}(\mathbf{k}) = \frac{1}{4} (W - \overline{W}) H_{\text{BdG}}(\mathbf{k}) \begin{pmatrix} W^\dagger \\ W^T \end{pmatrix}$. Also the Von Neumann entropy can be expressed as a function of $G(\mathbf{k})$. To see this we express the Gaussian density matrix as in Eq. (3.46) and calculate

$$\begin{aligned} S &= -\text{tr} (\rho \ln \rho) \\ &= n \ln 2 - \frac{1}{2} \sum_{i=1}^n [(1 + \lambda_i) \ln(1 + \lambda_i) + (1 - \lambda_i) \ln(1 - \lambda_i)] . \end{aligned} \quad (3.84)$$

where to problem is reduced to finding $\{\lambda_i\}$, (the moduli of) the eigenvalues of Γ . However, Γ and $\bigoplus_{\mathbf{k}} G(\mathbf{k})$ are unitary equivalent and thus have the same eigenvalues. As a result, the λ_i can be obtained as (the moduli of) the eigenvalues of $G(\mathbf{k})$ and also be labeled with a momentum.

Slightly more tricky but relevant in the context of Sec. 5.4.2 is the calculation of the entanglement entropy between a finite patch of the lattice, R , and its complement. In terms of correlation matrices, tracing out this complement can easily be performed by removing the rows and columns corresponding to operators outside of R . Starting from a pure, TI and Gaussian state ρ with correlation matrix Γ (such that $\Gamma \Gamma^T = \mathbb{1}$), the reduced density matrix ρ_R with correlation matrix, Γ_R , will no longer be pure ($\Gamma_R \Gamma_R^T \leq \mathbb{1}$) and also translation invariance will be broken. For the calculation of the entanglement entropy (*i.e.* the Von Neumann entropy of ρ_R), one is thus obliged to diagonalize the full Γ_R which can become computationally intractable for large regions ($\sim 20\,000$ lattice sites).

To conclude we discuss the correlation matrix description of local, TI Gaussian channel, $\mathcal{E} : \mathcal{C}_{2N_s f_{\text{in}}} \rightarrow \mathcal{C}_{2N_s f_{\text{out}}}$, applied to a TI Gaussian state, ρ_{in} , with correlation matrix Γ_{in} and f_{in} orbitals per site. We already know that this will yield yet another Gaussian state, ρ_{out} , with f_{out} orbitals per site and a correlation matrix that can be expressed as a Schur complement (Eq. (3.52)). Locality of the channel implies $\mathcal{E} = \bigotimes_{\mathbf{x}} \mathcal{E}_{\mathbf{x}}^{\text{loc}}$ so that the X matrix in Eq. (3.48) is block-diagonal and only connects Grassmann variables at identical positions, *i.e.* $X = \bigoplus_{\mathbf{x}} X_{\mathbf{x}}^{\text{loc}}$. Translation invariance on the other hand requires these local blocks to be identical for each \mathbf{x} , *i.e.* $X = \mathbb{1}_{N_s} \otimes X^{\text{loc}}$. As result Fourier transforms commute with X so that

$$\begin{aligned} \bigoplus_{\mathbf{k}} G_{\text{out}}(\mathbf{k}) &= (\mathcal{F} \otimes \mathbb{1}_{2f_{\text{out}}}) \Gamma_{\text{out}} \left(\mathcal{F}^\dagger \otimes \mathbb{1}_{2f_{\text{out}}} \right) \\ &= (\mathcal{F} \otimes \mathbb{1}_{2f_{\text{out}}}) \left(\mathbb{1}_{N_s} \otimes A^{\text{loc}} + \left(\mathbb{1}_{N_s} \otimes B^{\text{loc}} \right) \right. \\ &\quad \left. \left(\left(\mathbb{1}_{N_s} \otimes D^{\text{loc}} \right) + \Gamma_{\text{in}}^{-1} \right)^{-1} \left(\mathbb{1}_{N_s} \otimes B^{\text{loc}T} \right) \right) \left(\mathcal{F}^\dagger \otimes \mathbb{1}_{2f_{\text{out}}} \right) \end{aligned} \quad (3.85)$$

$$\begin{aligned}
&= \mathbb{1}_{N_s} \otimes A^{\text{loc}} + \left(\mathbb{1}_{N_s} \otimes B^{\text{loc}} \right) \left(\left(\mathbb{1}_{N_s} \otimes D^{\text{loc}} \right) + \right. \\
&\quad \left. + \bigoplus_{\mathbf{k}} G_{\text{in}}^{-1}(\mathbf{k}) \right)^{-1} \left(\mathbb{1}_{N_s} \otimes B^{\text{loc}T} \right) \\
&= \bigoplus_{\mathbf{k}} \left(A^{\text{loc}} + B^{\text{loc}} \left(D^{\text{loc}} + G_{\text{in}}^{-1}(\mathbf{k}) \right)^{-1} B^{\text{loc}T} \right)
\end{aligned}$$

with the Fourier transform \mathcal{F} as introduced before and making use of the fact that the input state was TI so that

$$\Gamma_{\text{in}} = \left(\mathcal{F}^\dagger \otimes \mathbb{1}_{2f_{\text{in}}} \right) \bigoplus_{\mathbf{k}} G_{\text{in}}(\mathbf{k}) (\mathcal{F} \otimes \mathbb{1}_{2f_{\text{in}}}) . \quad (3.86)$$

The output state is translation-invariant as well and its Fourier transformed correlation matrix can be expressed as a local Schur complement in Fourier space. If ρ_{in} is pure and $X^{\text{loc}} X^{\text{loc}T} = \mathbb{1}$, ρ_{out} is pure as well. In that case \mathcal{E} has only a single Kraus operator and the channel comes down to a local and translation-invariant transformation applied to ρ_{in} .

3.3 Coherent states

The single-mode coherent state discussed in Sec. 3.1 represents a basic example of a broader class a bosonic coherent states. Also for fermions one can define coherent states and Perelomov showed that the notion can even be extended to any nilpotent Lie group generalizing the symplectic (orthogonal) group of canonical transformations for bosons (fermions) [185]. We do not go into the details of this generalized construction but rather focus on its application to fermionic coherent states. Consider therefore a set of n fermionic creation and annihilation operators. Canonical transformations on the level of Majoranas correspond to elements of $O(2n)$. This group decomposes in the Lie group $\text{SO}(2n)$ and the group of orthogonal transformations with determinant -1 . For now we will focus on the former and consider an $O \in \text{SO}(2n)$ such that $\tilde{c}_i = O_{ij} c_j$ is a canonical transformation. Again defining a Nambu spinor,

$$\Upsilon = \begin{pmatrix} a_1 \dots a_n & a_1^\dagger \dots a_n^\dagger \end{pmatrix}^T , \quad (3.87)$$

we have $c = (W \quad \overline{W}) \Upsilon$ so that the canonical transformation on the level of the creators and annihilators can be expressed as

$$\tilde{\Upsilon} = \frac{1}{2} \begin{pmatrix} W^\dagger \\ W^T \end{pmatrix} O (W \quad \overline{W}) = \begin{pmatrix} U & V \\ \overline{V} & \overline{U} \end{pmatrix} \Upsilon = Z \Upsilon , \quad (3.88)$$

where Z has to be unitary. We can represent this canonical transformation on the Hilbert space with a unitary operator, T , yielding

$$\tilde{\Upsilon}_i = T \Upsilon_i T^\dagger = Z_{ij} \Upsilon_j . \quad (3.89)$$

As $\text{SO}(2n)$ constitutes a Lie group, we can construct its Lie algebra by considering an infinitesimal transformation, *i.e.* $Z = \mathbb{1} + i\varepsilon \tilde{Z}$ with

$$\tilde{Z} = \begin{pmatrix} B & A \\ -\overline{A} & -\overline{B} \end{pmatrix} \quad (3.90)$$

Hermitian such that $A = -A^T$ and $B = B^\dagger$. Similarly, $T = 1 + i\varepsilon\tilde{T}$ so that $[\tilde{T}, \Upsilon_i] = \tilde{Z}_{ij}\Upsilon_j$. Hence, the Lie algebra is spanned by the quadratic combinations of creation and annihilation operators,

$$X_{ij} = a_i a_j \quad X^{ij} = a_j^\dagger a_i^\dagger \quad X_j^i = \frac{1}{2} (a_i^\dagger a_j - a_j a_i^\dagger), \quad (3.91)$$

The resulting algebra is indeed isomorphic to $\mathfrak{so}(2N)$. The commutation relations of its generating elements are

$$\begin{aligned} [X_{ij}, X_{kl}] &= [X^{ij}, X^{kl}] = 0 \\ [X_{ij}, X^{kl}] &= -X_i^k \delta_j^l + X_i^l \delta_j^k + X_j^k \delta_i^l - X_j^l \delta_i^k \\ [X_{ij}, X_l^k] &= -X_{il} \delta_j^k + X_{jl} \delta_i^k \\ [X^{ij}, X_l^k] &= +X^{ik} \delta_l^j - X^{ik} \delta_l^j \\ [X_i^j, X_l^k] &= -X_l^j \delta_i^k + X_i^k \delta_l^j. \end{aligned} \quad (3.92)$$

Coherent states are defined as generated from the vacuum by application of a general Lie algebra element, *i.e.*

$$|\xi, \alpha, \eta\rangle = \frac{1}{Z} \exp\left(-\frac{1}{2}\xi_{ij}X^{ij}\right) \exp\left(\alpha_k^l X_l^k\right) \exp\left(-\frac{1}{2}\eta^{ij}X_{ij}\right) |0\rangle. \quad (3.93)$$

Note the similarity between this form and the single-mode, bosonic coherent state in Sec. 3.1. Indeed, a similar reasoning for a single mode boson exactly yields the latter. For fermions, we can simplify the general form further,

$$|\xi\rangle = \frac{1}{Z} \exp\left(-\frac{1}{2}\xi_{ij}X^{ij}\right) |0\rangle, \quad (3.94)$$

as the second and third factor maximally yield an additional multiplicative prefactor. Furthermore ξ is anti-symmetric. Some interesting properties of these coherent states include:

- the normalization factor is given by $Z = \det(\mathbb{1} + \xi\xi^\dagger)^{\frac{1}{4}}$ so that the overlap between two coherent states is given by

$$\langle \xi | \eta \rangle = \det(\mathbb{1} + \xi\xi^\dagger)^{-\frac{1}{4}} \det(\mathbb{1} + \eta\eta^\dagger)^{-\frac{1}{4}} \det(\mathbb{1} + \xi^\dagger\eta)^{\frac{1}{2}}. \quad (3.95)$$

- the expectation values for the quadratic operators generating the Lie algebra are given by

$$\begin{aligned} \langle \xi | X_{ij} | \xi \rangle &= -\left(\xi(\mathbb{1} + \xi^\dagger\xi)^{-1}\right)_{ij} \\ &= \langle \xi | a_i a_j | \xi \rangle = x_{ij} \\ \langle \xi | X_j^i | \xi \rangle &= \left(\xi(\mathbb{1} + \xi^\dagger\xi)^{-1}\xi^\dagger - \frac{1}{2}\mathbb{1}\right)_{ji} \\ &= \langle \xi | a_i^\dagger a_j | \xi \rangle - \frac{1}{2}\delta_j^i = n_{ij} - \frac{1}{2}\delta_j^i, \end{aligned} \quad (3.96)$$

where we utilized the same notation as in Sec. 3.2.3.

An immediate consequence is that the n and x matrices satisfy

$$n^T x = xn \quad \text{and} \quad \left(n^T - \frac{1}{2} \right)^2 - x\bar{x} = \frac{1}{4}, \quad (3.97)$$

equivalent to the purity constraint, $\Gamma\Gamma^T = \mathbb{1}$, thereby establishing a Kähler structure. Conversely, if a state is pure and Gaussian, the corresponding n and x correlations matrices will satisfy Eq. (3.97). One can then attempt to solve the consistency relation $n^T = -x\xi$ by means of the (pseudo)inverse of x to write the state in a coherent form. This is possible as long as the state is not orthogonal to the vacuum. Indeed, the exponential in Eq. (3.94) always produces a non-zero vacuum contribution. Consequently, the determination of a coherent from will fail for odd-parity states. This does not come as a surprise. Odd parity states are obtained from the vacuum exactly by Hilbert space representations of the canonical transformations with determinant -1 (hence containing a particle-hole transformation) and we did not consider these in the derivation of Eq. (3.94). One could still build odd coherent states by replacing the vacuum in Eq. (3.94) by $a_i^\dagger |0\rangle$ for any i but we will not explore these further.

Similar to Sec. 3.2.3 we can apply the coherent state formalism to the lattice. For a coherent state we have

$$|\xi\rangle = \frac{1}{Z} \exp \left(\frac{1}{2} \xi_{\mathbf{xy}}^{ij} a_{\mathbf{x},i}^\dagger a_{\mathbf{y},j}^\dagger \right) |0\rangle. \quad (3.98)$$

Translation invariance then requires $\xi_{\mathbf{xy}}^{ij} = \xi_{\mathbf{x}-\mathbf{y}}^{ij}$ so that

$$|\xi\rangle = \frac{1}{Z} \exp \left(\frac{1}{2} g^{ij}(\mathbf{k}) a_{-\mathbf{k},i}^\dagger a_{\mathbf{k},j}^\dagger \right) |0\rangle, \quad (3.99)$$

so that $|\xi\rangle$ is a BCS pairing state with pairing function $g(\mathbf{k}) = \sum_{\mathbf{x}} e^{i\mathbf{k}\cdot\mathbf{x}} \xi_{\mathbf{x}}$. Fourier transforming n and x we get

$$\begin{aligned} n(\mathbf{k}) &= \overline{\mathcal{F}_{\mathbf{kx}}} n_{\mathbf{x}-\mathbf{y}} \mathcal{F}_{\mathbf{yq}}^T = \overline{g(\mathbf{k})} \left(\mathbb{1} + g(\mathbf{k})^T g(\mathbf{k}) \right)^{-1} g(\mathbf{k})^T \\ x(\mathbf{k}) &= \mathcal{F}_{\mathbf{kx}} x_{\mathbf{x}-\mathbf{y}} \mathcal{F}_{\mathbf{yq}}^\dagger = -g(\mathbf{k})^T \left(\mathbb{1} + \overline{g(\mathbf{k})} g(\mathbf{k})^T \right)^{-1}. \end{aligned} \quad (3.100)$$

Note the differences in the final result on the second line when compared to Eq. (3.96). This due to the fact that $\mathcal{F}_{\mathbf{kx}} \xi_{\mathbf{x}-\mathbf{y}} \mathcal{F}_{\mathbf{yq}}^\dagger = g(-\mathbf{k}) \delta_{\mathbf{kq}} = -g(\mathbf{k})^T \delta_{\mathbf{kq}}$ where the latter equality follows from ξ being odd. One then recovers $G(\mathbf{k})$ from $n(\mathbf{k})$ and $x(\mathbf{k})$ and the formulary in Sec. 3.2.3 can be used again to calculate energies, (entanglement) entropies, ...

3.4 Symmetries and phases

Symmetries and phases were already introduced in Chapter 2 but here we will delve deeper into the intricacies of symmetries for free-fermion Hamiltonians. More specifically we will reveal the substructure that certain global symmetries impose on both the Hamiltonian and symmetric, Gaussian states. We begin by examining U(1), SU(2), and their combination, all leading to a unitary action on the single-particle level. Subsequently, we explore time-reversal, particle-hole, and chiral symmetries. Here, the first two yield

an anti-unitary representation on the single-particle Hamiltonian. We will discover that these are the only symmetries with this particular property so that together with their composition (*i.e.* the chiral symmetry) they establish a comprehensive classification of all possible topological symmetries in free-fermion systems. This classification, known as the periodic table of topological insulators and superconductors, heavily relies on integer topological invariants, discussed in the penultimate Section. Finally, we will also examine the principle of dimensional reduction.

3.4.1 Global U(1) and SU(2) symmetry

Consider a translation-invariant, quadratic Hamiltonian on the lattice. Symmetries leaving this Hamiltonian invariant necessarily transform Nambu spinors, $\Upsilon_{\mathbf{x},i}$, in a linear manner. Therefore, the symmetry groups, G , considered in the following Sections will always have a(n) (anti-)unitary representation, \mathcal{U}_g ($g \in G$), on the Hilbert space such that

$$\mathcal{U}_g \Upsilon_{\mathbf{x},i} \mathcal{U}_g^\dagger = U_{\mathbf{x}\mathbf{y}}^{ij}(g) \Upsilon_{\mathbf{y},j}, \quad (3.101)$$

where the $U_{\mathbf{x}\mathbf{y}}^{ij}(g)$ factors are just numbers, not second-quantized operators. In addition to the invariance of the Hamiltonian, $[H, \mathcal{U}_g] = 0$, these symmetries should also preserve canonical anti-commutation relations. We will typically only consider global symmetries, $\mathcal{U}_g = \bigotimes_{\mathbf{x}} \mathcal{U}_g^{\text{loc}}$, and redefine \mathcal{U} as the latter, dropping the extra labels. Global U(1) (particle number) and SU(2) (spin rotation) symmetries are then defined by the following actions

$$\begin{aligned} \mathcal{U} a_{\mathbf{x},i} \mathcal{U}^\dagger &= u a_{\mathbf{x},i} \\ \mathcal{U} a_{\mathbf{x},i}^\sigma \mathcal{U}^\dagger &= U^{\sigma\sigma'} a_{\mathbf{x},i}^{\sigma'} \end{aligned} \quad (3.102)$$

where for the SU(2) symmetry the different fermionic operators per site are organized in multiplets with σ (spin) labels, split from the original i labels. The action of the SU(2) transformation figures exactly inside these multiplets and $U \in \text{SU}(2)$. For the Abelian U(1) group, on the other hand, one only has non-trivial 1D irreps and $u = \in \text{U}(1)$. The Baker–Campbell–Hausdorff formula then gives

$$\begin{aligned} \mathcal{U} &= \exp \left(-i\phi \sum_{i=1}^f a_{\mathbf{x},i}^\dagger a_{\mathbf{x},i} \right) = \exp(-i\phi n_{\mathbf{x}}) \\ \mathcal{U} &= \exp \left(-i \frac{\phi}{2} \sum_{i=1}^{\frac{f}{2}} a_{\mathbf{x},i}^\sigma {}^\dagger (\hat{\mathbf{n}} \cdot \boldsymbol{\sigma})_{\sigma\sigma'} a_{\mathbf{x},i}^{\sigma'} \right) = \exp(-i\phi \hat{\mathbf{n}} \cdot \mathbf{S}_{\mathbf{x}}) \end{aligned} \quad (3.103)$$

with $u = e^{i\phi}$ for U(1), respectively, $U = e^{i\frac{\phi}{2}\hat{\mathbf{n}} \cdot \boldsymbol{\sigma}}$ for SU(2). This shows that the total particle number per site, $n_{\mathbf{x}} = \sum_{i=1}^f a_{\mathbf{x},i}^\dagger a_{\mathbf{x},i}$, is the generator for U(1) while the total spin per site, $\mathbf{S}_{\mathbf{x}} = \sum_{i=1}^{\frac{f}{2}} a_{\mathbf{x},i}^\sigma {}^\dagger (\hat{\mathbf{n}} \cdot \boldsymbol{\sigma})_{\sigma\sigma'} a_{\mathbf{x},i}^{\sigma'}$, is the generator for SU(2). For free translation-invariant systems, invariance of the Hamiltonian under $U(1)$ and $SU(2)$ can be worked

out further on the single-particle level as

$$\begin{aligned} \begin{pmatrix} e^{-i\phi} \mathbb{1}_f & \\ & e^{i\phi} \mathbb{1}_f \end{pmatrix} H_{\text{BdG}}(\mathbf{k}) \begin{pmatrix} e^{i\phi} \mathbb{1}_f & \\ & e^{-i\phi} \mathbb{1}_f \end{pmatrix} &= H_{\text{BdG}}(\mathbf{k}) \\ \begin{pmatrix} \mathbb{1}_{\frac{f}{2}} \otimes U^\dagger & \\ & \mathbb{1}_{\frac{f}{2}} \otimes U \end{pmatrix} H_{\text{BdG}}(\mathbf{k}) \begin{pmatrix} \mathbb{1}_{\frac{f}{2}} \otimes U & \\ & \mathbb{1}_{\frac{f}{2}} \otimes U^\dagger \end{pmatrix} &= H_{\text{BdG}}(\mathbf{k}) \end{aligned} \quad (3.104)$$

and this $\forall e^{i\phi} \in \text{U}(1)$, respectively, $\forall U \in \text{SU}(2)$. Both symmetries thus have a unitary representation that preserves the single particle Hamiltonian. Using this representation we notice that a particle-number-conserving model cannot contain pairing terms while for $\text{SU}(2)$ -symmetric models, $\Xi(\mathbf{k}) = \Xi_1(\mathbf{k}) \otimes \mathbb{1}$ and $\Delta(\mathbf{k}) = \Delta_2(\mathbf{k}) \otimes J$. *I.e.* particle-number-conserving terms are symmetric while pairing terms have to be anti-symmetric.

A state $|\psi\rangle$ is symmetric under a certain \mathcal{U} when it is an eigenvector of the symmetry operation, *i.e.* when $\mathcal{U}|\psi\rangle = \lambda|\psi\rangle$. Expectation values of symmetric operators O ($\mathcal{U}O\mathcal{U}^\dagger = O$) then remain unchanged when performing a symmetry transformation. We can utilize this characterization of a symmetric state to work out what $\text{U}(1)$ and $\text{SU}(2)$ entail for the correlation matrix of a Gaussian, symmetric state. Indeed, for $\text{U}(1)$ symmetry, the $n(\mathbf{k})$ and $x(\mathbf{k})$ correlation matrices have to satisfy

$$\begin{aligned} n_{ij}(\mathbf{k}) &= \langle a_{\mathbf{k},i}^\dagger a_{\mathbf{k},j} \rangle = \langle \psi | \mathcal{U}^\dagger \mathcal{U} a_{\mathbf{k},i}^\dagger \mathcal{U}^\dagger \mathcal{U} a_{\mathbf{k},j} \mathcal{U}^\dagger \mathcal{U} | \psi \rangle \\ &= \langle \psi | \bar{\lambda} e^{-i\phi} a_{\mathbf{k},i}^\dagger e^{i\phi} a_{\mathbf{k},j} \lambda | \psi \rangle = \langle a_{\mathbf{k},i}^\dagger a_{\mathbf{k},j} \rangle \\ x_{ij}(\mathbf{k}) &= \langle a_{\mathbf{k},i} a_{-\mathbf{k},j} \rangle = \langle \psi | \mathcal{U}^\dagger \mathcal{U} a_{\mathbf{k},i} \mathcal{U}^\dagger \mathcal{U} a_{-\mathbf{k},j} \mathcal{U}^\dagger \mathcal{U} | \psi \rangle \\ &= \langle \psi | \bar{\lambda} e^{i\phi} a_{\mathbf{k},i} e^{i\phi} a_{-\mathbf{k},j} \lambda | \psi \rangle = e^{i2\phi} \langle a_{\mathbf{k},i} a_{-\mathbf{k},j} \rangle \end{aligned} \quad (3.105)$$

where we used that $|\lambda|^2 = 1$ since \mathcal{U} is unitary. As this has to be true $\forall e^{i\phi} \in \text{U}(1)$, $x(\mathbf{k}) = -\frac{i}{4} W^\dagger G(\mathbf{k}) \bar{W} = 0$ while there is no additional restriction for $n(\mathbf{k})$. We conclude that the Gaussian state is $\text{U}(1)$ -symmetric if and only if the correlation matrix decomposes as $G(\mathbf{k}) = G_1(\mathbf{k}) \otimes \mathbb{1} + G_2(\mathbf{k}) \otimes J$. Together, $\mathbb{1}$ and J compose the basis for a real representation of the complex numbers. Equivalent to the $\text{U}(1)$ -symmetric $G(\mathbf{k})$, we could thus consider its complexified form $G^C(\mathbf{k}) = G_1(\mathbf{k}) + iG_2(\mathbf{k})$ where now $G^{C\dagger}(\mathbf{k}) = -G^C(\mathbf{k})$ and $G^{C\dagger}(\mathbf{k})G^C(\mathbf{k}) = \mathbb{1}$. Similarly, imposing $\text{SU}(2)$ symmetry results in

$$\begin{aligned} n_{ij}^{\sigma\sigma'}(\mathbf{k}) &= \langle a_{\mathbf{k},i}^\sigma a_{\mathbf{k},j}^{\sigma'} \rangle = \langle \psi | \mathcal{U}^\dagger \mathcal{U} a_{\mathbf{k},i}^\sigma \mathcal{U}^\dagger \mathcal{U} a_{\mathbf{k},j}^{\sigma'} \mathcal{U}^\dagger \mathcal{U} | \psi \rangle \\ &= \langle \psi | \bar{\lambda} \bar{U}^{\sigma\tau} a_{\mathbf{k},i}^\tau U^{\sigma'\tau'} a_{\mathbf{k},j}^{\tau'} \lambda | \psi \rangle = \bar{U}^{\sigma\tau} n_{ij}^{\tau\tau'}(\mathbf{k}) U^{T\tau'\sigma'} \\ x_{ij}^{\sigma\sigma'}(\mathbf{k}) &= \langle a_{\mathbf{k},i}^\sigma a_{\mathbf{k},j}^{\sigma'} \rangle = \langle \psi | \mathcal{U}^\dagger \mathcal{U} a_{\mathbf{k},i}^\sigma \mathcal{U}^\dagger \mathcal{U} a_{\mathbf{k},j}^{\sigma'} \mathcal{U}^\dagger \mathcal{U} | \psi \rangle \\ &= \langle \psi | \bar{\lambda} U^{\sigma\tau} a_{\mathbf{k},i}^\tau U^{\sigma'\tau'} a_{\mathbf{k},j}^{\tau'} \lambda | \psi \rangle = U^{\sigma\tau} x_{ij}^{\tau\tau'}(\mathbf{k}) U^{T\tau'\sigma'} \end{aligned} \quad (3.106)$$

$\forall U \in \text{SU}(2)$. As a result, $n(\mathbf{k}) = \bar{U}n(\mathbf{k})U^T$ and $x(\mathbf{k}) = Ux(\mathbf{k})U^T$ implying that $n(\mathbf{k}) = n_1(\mathbf{k}) \otimes \mathbb{1}$ and $x(\mathbf{k}) = x_2(\mathbf{k}) \otimes J$, mimicking their corresponding Hamiltonian terms. The $G(\mathbf{k})$ correlation matrix can be expressed using Eq. (3.73) and the terms containing $n(\mathbf{k})$ will yield contributions of the form $\dots \otimes \mathbb{1} \otimes \mathbb{1}$ and $\dots \otimes \mathbb{1} \otimes J$ while those with $x(\mathbf{k})$ give $\dots \otimes J \otimes \sigma^x$ and $\dots \otimes J \otimes \sigma^z$. Therefore, a Gaussian, TI state is $\text{SU}(2)$ symmetric with spin $\frac{1}{2}$ when

$$G(\mathbf{k}) = G_0(\mathbf{k}) \otimes \mathbb{1} \otimes \mathbb{1} + G_1(\mathbf{k}) \otimes \mathbb{1} \otimes J + G_2(\mathbf{k}) \otimes J \otimes \sigma^x + G_3(\mathbf{k}) \otimes J \otimes \sigma^z. \quad (3.107)$$

Together, $\mathbb{1} \otimes \mathbb{1}$, $\mathbb{1} \otimes J$, $J \otimes \sigma^x$ and $J \otimes \sigma^z$ span a real representation of the quaternions so that the correlation matrix of a symmetric state can equivalently be formulated in quaternion form $G^{\mathbb{H}}(\mathbf{k}) = G_0(\mathbf{k}) + iG_1(\mathbf{k}) + jG_2(\mathbf{k}) + kG_3(\mathbf{k})$ where $G^{\mathbb{H}\dagger}(\mathbf{k}) = -G^{\mathbb{H}}(\mathbf{k})$ and $G^{\mathbb{H}\dagger}(\mathbf{k})G^{\mathbb{H}}(\mathbf{k}) \leq \mathbb{1}$.

The U(1) and SU(2) symmetry can also appear together. Then a TI free-fermion Hamiltonian will only have particle-number-conserving terms decomposing as $\Xi(\mathbf{k}) = \Xi_1(\mathbf{k}) \otimes \mathbb{1}$. A symmetric, Gaussian state will be characterized by a Fourier space correlation matrix,

$$G(\mathbf{k}) = G_0(\mathbf{k}) \otimes \mathbb{1} \otimes \mathbb{1} + G_1(\mathbf{k}) \otimes \mathbb{1} \otimes J. \quad (3.108)$$

As such it can again be complexified but the remaining freedom is even smaller than in the case of only U(1) symmetry.

3.4.2 CPT symmetries and the ten-fold way

In the previous Section we found global U(1) and SU(2) symmetry to be represented by a unitary transformation commuting with the single-particle Hamiltonian. Consequently, one could bring the latter in a block-diagonal form such that the unitaries are constant on each block. Now suppose we did this for all such global symmetries with unitary single-particle representations and consider one of the irreducible blocks. Within this block, only the three CPT¹ symmetries remain:

- Time-reversal symmetry (TRS), represented on the many-body level by \mathcal{T} , an anti-unitary operator such that

$$\mathcal{T}a_i\mathcal{T}^{-1} = (U_T)_{ij} a_j \quad (3.109)$$

where U_T is unitary. Invariance of a quadratic Hamiltonian, $H = a_i^\dagger H_{ij} a_j$, can hence be expressed on the level of the single-particle Hamiltonian, H_{ij} , by requiring

$$H = U_T^\dagger \bar{H} U_T, \quad (3.110)$$

where we used H as the matrix collecting H_{ij} . From context it should be clear if H signifies the many-body Hamiltonian or its single-particle equivalent.

- Particle-hole symmetry (PHS), represented on the many-body level by \mathcal{P} a unitary operator such that

$$\mathcal{P}a_i\mathcal{P}^\dagger = (\overline{U_P})_{ij} a_j^\dagger \quad (3.111)$$

where U_P is unitary. For the single-particle Hamiltonian, this requires

$$H = -U_P^\dagger \bar{H} U_P, \quad (3.112)$$

yielding $\text{tr}(H) = 0$.

- Chiral symmetry, *i.e.* the composition of TRS and PHS, represented on the many-body level by $\mathcal{C} = \mathcal{T} \cdot \mathcal{P}$, an anti-unitary operator such that

$$\mathcal{C}a_i\mathcal{C}^\dagger = (\overline{U_C})_{ij} a_j^\dagger \quad (3.113)$$

¹The nomenclature used here is quite provocative as the CPT acronym is not the same as in the well-known CPT theorem. Indeed, here P stands for particle-hole rather than for spatial parity symmetry.

where $U_C = \overline{U_P} \overline{U_T}$ is unitary. For the single-particle Hamiltonian this requires

$$H = -U_C^\dagger H U_C, \quad (3.114)$$

so that again $\text{tr}(H) = 0$.

These discrete symmetries can be rewritten as

$$\begin{aligned} T^{-1}HT &= H && \text{with } T = U_T \mathcal{K}, \\ P^{-1}HP &= -H && \text{with } P = U_P \mathcal{K}, \\ C^{-1}HC &= -H && \text{with } C = U_C, \end{aligned} \quad (3.115)$$

where \mathcal{K} is the anti-unitary complex conjugation operator. Hence, T and P are anti-unitary, respectively commuting and anti-commuting with the single-particle H . C , on the other hand is unitary but anti-commutes with H . Within an irreducible block of the single-particle Hamiltonian, this set of symmetries is exhaustive. Indeed, assume that the Hamiltonian was invariant under, say, two particle-hole operations P_1 and P_2 , then the composition $P_1 \cdot P_2$ would be a unitary symmetry of H with $U_{P_1} U_{P_2}$ commuting with H but we already excluded this kind of symmetries by working on the irreducible blocks of H . As a result P (and also T) is unique. For the product of both symmetries $T \cdot P$, we again obtain of unitary symmetry but this time it anti-commutes with the single-particle Hamiltonian. *I.e.* the result is not an ordinary unitary symmetry but rather a chiral symmetry. With these three peculiar types of symmetries, ten different symmetry classes can be discerned. To see this, we let H run over an ensemble of similar irreducible blocks with a certain symmetry rather than picking a specific example. Applying TRS twice to an arbitrary H in such an ensemble, we obtain $(\overline{U_T} U_T)^\dagger H (\overline{U_T} U_T) = H$ so that Schur's lemma requires $\overline{U_T} U_T = e^{i\alpha} \mathbb{1}$. As U_T is unitary, this implies $e^{2i\alpha} = 1$ or thus $\overline{U_T} U_T = \pm \mathbb{1}$. On the many-body level this implies $\mathcal{T}^2 a_i \mathcal{T}^{\dagger 2} = \pm a_i$ so that $\mathcal{T}^2 = (\pm 1)^n$ where $n = \sum_i a_i^\dagger a_i$. Consequently, there are three TRS classes: 0 (no TRS), 1 (TRS with $\overline{U_T} U_T = +\mathbb{1}$ and thus $\mathcal{T}^2 = 1$) and -1 (TRS with $\overline{U_T} U_T = -\mathbb{1}$ and thus $\mathcal{T}^2 = (-1)^n$ (*i.e.* the total fermion parity operator)). A similar argument applies for PHS, also resulting in three symmetry classes. For chiral symmetry, on the other hand, one obtains $U_C U_C = e^{i\alpha} \mathbb{1}$. This phase (or rather half of it) can thus be absorbed in U_C so that in the presence of the symmetry only a single possibility remains, $U_S^2 = \mathbb{1}$. Note that the combination of TRS and PHS immediately results in chiral symmetry with $\mathcal{C} = \mathcal{T} \cdot \mathcal{P}$ and thus $U_C = \overline{U_P} \overline{U_T}$. However, it can also exist when both are broken. Considering this, the CPT symmetries result in ten possible symmetry classes for non-interacting fermion systems, collected in Table 3.1.

Placing the fermionic model on a lattice, CPT symmetries will act locally and in a translation invariant manner so that the single-particle constraints they impose can be translated to Fourier space, respectively yielding

$$\begin{aligned} H(\mathbf{k}) &= U_T^\dagger \overline{H(-\mathbf{k})} U_T \\ H(\mathbf{k}) &= -U_P^\dagger H(-\mathbf{k})^T U_P, \\ H(\mathbf{k}) &= -U_C^\dagger H(\mathbf{k}) U_C \end{aligned} \quad (3.116)$$

for TRS, PHS and chiral symmetry. Note the minus signs due to the combination of complex conjugation and Fourier transformation. Up to now all of these concepts were introduced for a particle-number-conserving Hamiltonian as in Eq. (3.75). They can readily be

class\(<d></d>	s	T	P	C	0	1	2	3	4	5	6	7
A	0	0	0	0	\mathbb{Z}	0	\mathbb{Z}	0	\mathbb{Z}	0	\mathbb{Z}	0
AIII	1	0	0	1	0	\mathbb{Z}	0	\mathbb{Z}	0	\mathbb{Z}	0	\mathbb{Z}
AI	0	+1	0	0	\mathbb{Z}	0	0	0	$2\mathbb{Z}$	0	\mathbb{Z}_2	\mathbb{Z}_2
BDI	1	+1	+1	1	\mathbb{Z}_2	\mathbb{Z}	0	0	0	$2\mathbb{Z}$	0	\mathbb{Z}_2
D	2	0	+1	0	\mathbb{Z}_2	\mathbb{Z}_2	\mathbb{Z}	0	0	0	$2\mathbb{Z}$	0
DIII	3	-1	+1	1	0	\mathbb{Z}_2	\mathbb{Z}_2	\mathbb{Z}	0	0	0	$2\mathbb{Z}$
AII	4	-1	0	0	$2\mathbb{Z}$	0	\mathbb{Z}_2	\mathbb{Z}_2	\mathbb{Z}	0	0	0
CII	5	-1	-1	1	0	$2\mathbb{Z}$	0	\mathbb{Z}_2	\mathbb{Z}_2	\mathbb{Z}	0	0
C	6	0	-1	0	0	0	$2\mathbb{Z}$	0	\mathbb{Z}_2	\mathbb{Z}_2	\mathbb{Z}	0
CI	7	+1	-1	1	0	0	0	$2\mathbb{Z}$	0	\mathbb{Z}_2	\mathbb{Z}_2	\mathbb{Z}

Table 3.1: Periodic table of topological insulators and superconductors also called the ten-fold way of (and originally described by) Altland and Zirnbauer [187, 188]. For each class (with Bott clock label s [189]), the symmetries are displayed together with the type of topological invariant they can realize in d spatial dimensions. The table repeats itself periodically for higher d . Furthermore, the classes on the diagonal with \mathbb{Z} -type invariants are called the primary series while the two diagonals below are the first and second descendants.

extended to the more general case of a Bogoliubov-De Gennes Hamiltonian (Eq. (3.81)). For the latter we already noted that $(\sigma^x \otimes \mathbb{1}_f) H_{\text{BdG}}^T(-\mathbf{k}) (\sigma^x \otimes \mathbb{1}_f) = -H_{\text{BdG}}(\mathbf{k})$. This symmetry is not physical but rather follows from the description with codependent parts of the Nambu spinor. Nonetheless, H_{BdG} always have a PHS with $U_P = \sigma^x \otimes \mathbb{1}_f$ and thus $\mathcal{P}^2 = 1$. When no other symmetries are present and $d = 2$, the model thus resides in symmetry class D. Two examples of two-band class D models are:

- the p-wave superconductor as introduced in Sec. 2.4.2 with

$$H = \frac{1}{2} \sum_{\mathbf{k}} \begin{pmatrix} a_{\mathbf{k}}^\dagger & a_{-\mathbf{k}} \end{pmatrix} \mathbf{h}(\mathbf{k}) \cdot \boldsymbol{\sigma} \begin{pmatrix} a_{\mathbf{k}} \\ a_{-\mathbf{k}}^\dagger \end{pmatrix} \quad (3.117)$$

with $\mathbf{h}(\mathbf{k}) = (2\Delta \sin k_y \quad 2\Delta \sin k_x \quad -\mu - 2t(\cos k_x + \cos k_y))$ and typically $t > 0$.

- the Chern insulator (exhibiting the quantum anomalous Hall effect, *i.e.* a quantized Hall conductance without the presence of an external magnetic field)

$$H = \sum_{\mathbf{k}} \begin{pmatrix} a_{\mathbf{k},1}^\dagger & a_{\mathbf{k},2}^\dagger \end{pmatrix} \mathbf{h}(\mathbf{k}) \cdot \boldsymbol{\sigma} \begin{pmatrix} a_{\mathbf{k},1} \\ a_{\mathbf{k},2}^\dagger \end{pmatrix} \quad (3.118)$$

with $\mathbf{h}(\mathbf{k}) = (\sin k_x \quad \sin k_y \quad m + \cos k_x + \cos k_y)$.

Both are particle-hole symmetric with $U_P = \sigma^x$ and thus $\mathcal{P}^2 = 1$. However, for the former this is due to the Bogoliubov-De Gennes description while for the latter the symmetry is truly physical.

To conclude, we mention that PHS renders the single-particle spectrum symmetric. Indeed, if $|u^\alpha\rangle$ is an eigenvector of the single-particle Hamiltonian with energy e^α , its

particle-hole reversed partner $U_P^\dagger \mathcal{K}|u^\alpha\rangle$ also is an eigenvector but with energy $-e^\alpha$. In Fourier space, this implies that when $|u^\alpha(\mathbf{k})\rangle$ is an eigenvector of $H(\mathbf{k})$ with energy $e^\alpha(\mathbf{k})$, $U_P^\dagger \mathcal{K}|u^\alpha(\mathbf{k})\rangle$ is an eigenvector of $H(-\mathbf{k})$ with energy $-e^\alpha(\mathbf{k})$. Both eigenvectors can therefore only belong to the same band when this band crosses the Fermi level, yielding a critical model. Here, we typically only consider the gapped topological phases such that the latter eigenvector is a part of an inverted and well-separated band with the opposite sign.

3.4.3 Topological invariants: the Chern number

The interplay between dimensionality and possible CPT symmetries (as determined by the ten-fold way) allows for the definition of topological invariants for gapped, free-fermion Hamiltonians [82, 83]. These invariants are discrete and can thus only change when the excitation gap closes. During this process no symmetries are broken so that the corresponding phases are topological. The characteristic topological invariants differ in type: 0 (no non-trivial phases), \mathbb{Z} (topological phases characterized by an integer), \mathbb{Z}_2 (topological phases characterized by a parity) and $2\mathbb{Z}$ (topological phases characterized by an even integer) all exist. Table 3.1 shows when each of these is realized. Again we will focus on class D in 2D where the topological invariant under consideration is the Chern number,

$$C = \left(\frac{i}{2\pi} \right)^n \int_{\text{BZ}} \text{tr } \mathcal{F}^n, \quad (3.119)$$

with $n = \frac{d}{2} = 1$. Note that we integrate over the first Brillouin zone and thus work on an infinite lattice. Furthermore, \mathcal{F} is the Berry curvature, a differential form defined as

$$\mathcal{F} = d\mathcal{A} + \mathcal{A} \wedge \mathcal{A}. \quad (3.120)$$

Herein is $\mathcal{A}^{\alpha\beta} = A_i^{\alpha\beta}(\mathbf{k})dk_i$ the non-Abelian Berry connection with

$$A_i^{\alpha\beta}(\mathbf{k}) = \langle u_-^\alpha(\mathbf{k}) | \frac{\partial}{\partial k_i} | u_-^\beta(\mathbf{k}) \rangle. \quad (3.121)$$

where $\{|u_-^\alpha(\mathbf{k})\rangle\}$ are the f_- eigenvectors of $H(\mathbf{k})$ with a negative energy. The trace of the Berry curvature can be expressed as

$$\begin{aligned} \text{tr } \mathcal{F} &= \sum_{\alpha,\beta=1}^{f_-} d\mathcal{A}^{\alpha\alpha} + \mathcal{A}^{\alpha\beta} \wedge \mathcal{A}^{\beta\alpha} \\ &= \sum_{\alpha,\beta=1}^{f_-} \left(\frac{\partial}{\partial k_i} A_j^{\alpha\alpha}(\mathbf{k}) + A_i^{\alpha\beta}(\mathbf{k}) A_j^{\beta\alpha}(\mathbf{k}) \right) dk_i \wedge dk_j \\ &= \sum_{\alpha=1}^{f_-} \left(\frac{\partial}{\partial k_x} A_y^{\alpha\alpha}(\mathbf{k}) - \frac{\partial}{\partial k_y} A_x^{\alpha\alpha}(\mathbf{k}) \right) dk_x dk_y \\ &= \left(\frac{\partial}{\partial k_x} \text{tr}(A_y(\mathbf{k})) - \frac{\partial}{\partial k_y} \text{tr}(A_x(\mathbf{k})) \right) dk_x dk_y. \end{aligned} \quad (3.122)$$

However, note that there is some freedom in the $f_- + f_+$ eigenvectors $\{|u^\alpha(\mathbf{k})\rangle\}$ of $H(\mathbf{k})$ as they can always be altered by a phase, $|v^\alpha(\mathbf{k})\rangle = e^{i\theta^\alpha(\mathbf{k})} |u^\alpha(\mathbf{k})\rangle$, resulting in gauge

dependence for the Berry connection

$$A'_i^{\alpha\alpha}(\mathbf{k}) = \langle v^\alpha(\mathbf{k}) | \frac{\partial}{\partial k_i} | v^\alpha(\mathbf{k}) \rangle = A_i^{\alpha\alpha}(\mathbf{k}) + i \frac{\partial \theta^\alpha}{\partial k_i}(\mathbf{k}) \quad (3.123)$$

and thus also for its trace, derivatives *etc.* One could also collect the occupied eigenvectors in a $(f_- + f_+) \times f_-$ matrix

$$U_-(\mathbf{k}) = \left(\begin{array}{c|c|c} |u_-^1(\mathbf{k})\rangle & \dots & |u_-^{f_-}(\mathbf{k})\rangle \end{array} \right) \quad (3.124)$$

so that $\text{tr}(A_i) = \text{tr} \left(U_-^\dagger(\mathbf{k}) \frac{\partial}{\partial k_i} U_-(\mathbf{k}) \right)$, showing that gauge independent properties like the Chern number will not depend on the exact form of the $\{|u_-^\alpha(\mathbf{k})\rangle\}$ but rather on the occupied space spanned by these vectors and how this space behaves throughout the Brillouin zone. Therefore, a more general gauge transformation is given by $V_-(\mathbf{k}) = U_-(\mathbf{k})g(\mathbf{k})$ where $g(\mathbf{k})$ is an $f_- \times f_-$ unitary matrix with eigenvalues $\{e^{i\theta^\alpha(\mathbf{k})}\}$. For the corresponding change in the Berry connection and curvature, one obtains

$$\mathcal{A}' = g^{-1} \mathcal{A} g + g^{-1} d g \quad \mathcal{F}' = g^{-1} \mathcal{F} g, \quad (3.125)$$

manifestly showing that the Chern number is indeed gauge independent. Another way to capture the occupied space is via the spectral projector

$$P(\mathbf{k}) = \sum_{\alpha \text{ occ.}} |u^\alpha(\mathbf{k})\rangle \langle u^\alpha(\mathbf{k})| = U_-(\mathbf{k}) U_-^\dagger(\mathbf{k}) \quad (3.126)$$

or its counterpart $Q(\mathbf{k}) = \mathbb{1} - 2P(\mathbf{k})$ with eigenvalues ± 1 and the same eigenvectors as the Hamiltonian. Due to gauge independence these both belong to the Grassmannian manifold $\text{Gr}(f_-, f_+ + f_-) = U(f_- + f_+) \setminus (U(f_-) \times U(f_+))$. Topologically distinct maps from the Brillouin zone to this manifold are classified via their second (in general d^{th}) homotopy group, $\pi_2(\text{Gr}(f_-, f_+ + f_-)) = \mathbb{Z}$, *i.e.* an integer topological invariant,

$$\left(\frac{i}{2\pi} \right)^n \int_{\text{BZ}} \text{tr} (P \, (dP \wedge dP)^n). \quad (3.127)$$

This is exactly the Chern number. On a more practical note, we mention that the non-trivial twisting of the occupied space in case of a non-zero Chern number will result in an obstruction to define a smooth parameterization of the $\{|u_-^\alpha(\mathbf{k})\rangle\}$ throughout the complete Brillouin zone. Calculating the integrand of Eq. (3.119) in every \mathbf{k} -point will hence require patched parameterizations. While the corresponding Berry connections in overlapping regions will differ, the trace of the Berry curvature will be the same, yielding a single Chern number.

Until now we only considered an infinite lattice, resulting in a bulk topological invariant. One could also look at a finite system with an edge or systems with defects and ask if the topological invariants have some other physical interpretation there. This is typically done by introducing additional terms in the Hamiltonian yielding a defect Hamiltonian [190] that realizes gapless modes localized at the edge/defects. Proper indices can be defined that count these zero modes and turn out to be equal to the bulk topological invariants. This is the well-known bulk-boundary correspondence [191, 192].

Physically, the Chern number thus expresses the number of edge modes present in the system when placed on a finite lattice. However, there is a slight distinction between the Chern number for a class D theory without pairing terms (Eq. (3.75)) and a BdG Hamiltonian (Eq. (3.81)). For the former, C will correspond to the number of fermionic edge modes, while for the latter it counts the number of Majorana edge modes. This is consistent with the fact that any particle-number-conserving, translation invariant class D theory with Hamiltonian $H(\mathbf{k})$ can be expressed as a BdG Hamiltonian where

$$H_{\text{BdG}}(\mathbf{k}) = \begin{pmatrix} H(\mathbf{k}) & \\ & -H(-\mathbf{k})^T \end{pmatrix}. \quad (3.128)$$

Consequently, a basis for the occupied space is given by $(|u_-^\alpha(\mathbf{k})\rangle \ 0)^T$ and $(0 \ U_P^T|u_-^\alpha(\mathbf{k})\rangle)^T$ so that

$$\begin{aligned} \text{tr}(A_{\text{BdG}i}(\mathbf{k})) &= \sum_{\alpha=1}^{f_-} \langle u_-^\alpha(\mathbf{k}) | \frac{\partial}{\partial k_i} | u_-^\alpha(\mathbf{k}) \rangle \\ &\quad + \sum_{\alpha=1}^{f_-} \langle u_-^\alpha(\mathbf{k}) | \overline{U_P} \frac{\partial}{\partial k_i} U_P^T | u_-^\alpha(\mathbf{k}) \rangle = 2 \text{tr}(A_i(\mathbf{k})). \end{aligned} \quad (3.129)$$

As a result, the Chern number is twice as large as for the original Hamiltonian. Indeed, if the original Hamiltonian had C fermionic edge modes, this corresponds to a BdG Hamiltonian with $2C$ Majorana edge modes.

For the exemplary two-band models, we propose the following eigenvector parameterizations

$$\begin{aligned} |u_+(\mathbf{k})\rangle &= \frac{1}{\sqrt{2e(\mathbf{k})(e(\mathbf{k}) - h_3(\mathbf{k}))}} \begin{pmatrix} -h_1(\mathbf{k}) + ih_2(\mathbf{k}) \\ h_3(\mathbf{k}) - e(\mathbf{k}) \end{pmatrix} \\ |u_-(\mathbf{k})\rangle &= \frac{1}{\sqrt{2e(\mathbf{k})(e(\mathbf{k}) - h_3(\mathbf{k}))}} \begin{pmatrix} h_3(\mathbf{k}) - e(\mathbf{k}) \\ h_1(\mathbf{k}) + ih_2(\mathbf{k}) \end{pmatrix} \end{aligned} \quad (3.130)$$

with eigenenergies $e(\mathbf{k}) = |\mathbf{h}(\mathbf{k})|$ and $-e(-\mathbf{k})$. Note that the eigenvectors are not well defined when $e(\mathbf{k}) = h_3(\mathbf{k})$, i.e. when $\hat{\mathbf{h}}(\mathbf{k})$ reaches the north pole. In this case, we can define an alternative parameterization

$$\begin{aligned} |v_+(\mathbf{k})\rangle &= \frac{1}{\sqrt{2e(\mathbf{k})(e(\mathbf{k}) + h_3(\mathbf{k}))}} \begin{pmatrix} h_3(\mathbf{k}) + e(\mathbf{k}) \\ h_1(\mathbf{k}) + ih_2(\mathbf{k}) \end{pmatrix} \\ |v_-(\mathbf{k})\rangle &= \frac{1}{\sqrt{2e(\mathbf{k})(e(\mathbf{k}) + h_3(\mathbf{k}))}} \begin{pmatrix} -h_1(\mathbf{k}) + ih_2(\mathbf{k}) \\ h_3(\mathbf{k}) + e(\mathbf{k}) \end{pmatrix} \end{aligned} \quad (3.131)$$

that does not pose any problem in the north pole but becomes divergent in the south pole. When both poles are reached (e.g. when $0 < |\mu| < 4t$ and $|\Delta| > 0$ in the p-wave superconductor), neither basis will yield a smooth parameterization of the occupied space throughout the complete Brillouin zone, thus signaling non-trivial topological behavior. This will be reflected by a non-zero Chern number. To calculate C explicitly, we determine $Q(\mathbf{k})$ using a combination of both parameterizations,

$$Q(\mathbf{k}) = \begin{cases} \mathbb{1} - 2|u_-(\mathbf{k})\rangle\langle u_-(\mathbf{k})| = \hat{\mathbf{h}}(\mathbf{k}) \cdot \boldsymbol{\sigma} & \forall \mathbf{k} : e(\mathbf{k}) \neq h_3(\mathbf{k}) \\ \mathbb{1} - 2|v_-(\mathbf{k})\rangle\langle v_-(\mathbf{k})| = \hat{\mathbf{h}}(\mathbf{k}) \cdot \boldsymbol{\sigma} & \forall \mathbf{k} : e(\mathbf{k}) \neq -h_3(\mathbf{k}) \end{cases} \quad (3.132)$$

so that $Q(\mathbf{k}) = \hat{\mathbf{h}}(\mathbf{k}) \cdot \boldsymbol{\sigma} \forall \mathbf{k}$. Indeed, even though the parameterizations and the corresponding Berry connections differ, $Q(\mathbf{k})$ is gauge invariant and well-defined throughout the complete Brillouin zone. The Chern number can hence be calculated as

$$\begin{aligned} C &= \frac{i}{2\pi} \int_{\text{BZ}} \text{tr}(P (\text{d}P \wedge \text{d}P)) \\ &= \frac{-1}{8} \frac{i}{2\pi} \int_{\text{BZ}} \text{tr}(Q (\text{d}Q \wedge \text{d}Q)) \\ &= \frac{-1}{8} \frac{i}{2\pi} \int_{\text{BZ}} \text{tr} \left(\hat{h}_a \sigma^a \frac{\partial \hat{h}_b}{\partial k_i} \sigma^b \frac{\partial \hat{h}_c}{\partial k_j} \sigma^c \right) \text{d}k_i \wedge \text{d}k_j \\ &= \frac{-1}{8} \frac{i}{2\pi} \int_{\text{BZ}} \hat{h}_a \frac{\partial \hat{h}_b}{\partial k_i} \frac{\partial \hat{h}_c}{\partial k_j} 2i \epsilon_{abc} \text{d}k_i \wedge \text{d}k_j \\ &= \frac{1}{8\pi} \int_{\text{BZ}} \hat{\mathbf{h}} \cdot \frac{\partial \hat{\mathbf{h}}}{\partial k_i} \times \frac{\partial \hat{\mathbf{h}}}{\partial k_j} \text{d}k_i \wedge \text{d}k_j = \frac{1}{4\pi} \int_{\text{BZ}} \hat{\mathbf{h}} \cdot \frac{\partial \hat{\mathbf{h}}}{\partial k_x} \times \frac{\partial \hat{\mathbf{h}}}{\partial k_y} \text{d}k_x \text{d}k_y. \end{aligned} \quad (3.133)$$

Note that this correspond to the number of times $\hat{\mathbf{h}}(\mathbf{k})$ wraps around the unit sphere and thus indeed yields an integer topological invariant. The resulting Chern numbers:

- for the p-wave superconductor,

$$C = \frac{1}{4\pi} \int_{\text{BZ}} \frac{4\Delta^2 (2t(\cos k_x + \cos k_y) + \mu \cos k_x \cos k_y)}{e^3(\mathbf{k})} \text{d}k_x \text{d}k_y, \quad (3.134)$$

yielding a trivial phase when $|\mu| > 4t$, a topological phase with $C = 1$ when $-4t < \mu < 0$ and $|\Delta| > 0$ and a second topological phase but now with $C = -1$ when $0 < \mu < 4t$ and $|\Delta| > 0$.

- for the Chern insulator,

$$C = \frac{1}{4\pi} \int_{\text{BZ}} \frac{\cos k_x + \cos k_y + m \cos k_x \cos k_y}{e^3(\mathbf{k})} \text{d}k_x \text{d}k_y, \quad (3.135)$$

yielding a trivial phase when $|m| > 2$, a topological phase with $C = 1$ when $-2 < m < 0$ and a second topological phase but now with $C = -1$ when $0 < m < 2$. One could also consider the BdG version of the Chern insulator model. The occupied space is spanned by $(|u_-(\mathbf{k})\rangle \ 0)^T$ and $(0 \ \sigma^x |u_-(\mathbf{k})\rangle)^T$ with $|u_-(\mathbf{k})\rangle$ the occupied eigenvector of the original Hamiltonian. Consequently,

$$\begin{aligned} Q_{\text{BdG}}(\mathbf{k}) &= \mathbb{1} - 2 \begin{pmatrix} |u_-(\mathbf{k})\rangle \langle u_-(\mathbf{k})| & 0 \\ 0 & 0 \end{pmatrix} - 2 \begin{pmatrix} 0 & 0 \\ 0 & \sigma^x |u_-(\mathbf{k})\rangle \langle u_-(\mathbf{k})| \sigma^x \end{pmatrix} \\ &= \begin{pmatrix} \mathbb{1} & \\ \sigma^x & \end{pmatrix} \begin{pmatrix} \hat{\mathbf{h}}(\mathbf{k}) \cdot \boldsymbol{\sigma} & \\ & \hat{\mathbf{h}}(\mathbf{k}) \cdot \boldsymbol{\sigma} \end{pmatrix} \begin{pmatrix} \mathbb{1} & \\ & \sigma^x \end{pmatrix} \end{aligned} \quad (3.136)$$

so that indeed $C_{\text{BdG}} = 2C$. We can also extend this model to contain pairing terms, e.g. by setting

$$H_{\text{BdG}}(\mathbf{k}) = \begin{pmatrix} \mathbf{h}(\mathbf{k}) \cdot \boldsymbol{\sigma} & i\Delta\sigma^y \\ -i\bar{\Delta}\sigma^y & -(\mathbf{h}(-\mathbf{k}) \cdot \boldsymbol{\sigma})^T \end{pmatrix} \quad (3.137)$$

with still $\mathbf{h}(\mathbf{k}) = (\sin k_x \quad \sin k_y \quad m + \cos k_x + \cos k_y)$. Note that with

$$U = \frac{1}{\sqrt{2}} \begin{pmatrix} 1 & 0 & 0 & 1 \\ 0 & 1 & 1 & 0 \\ 0 & 1 & -1 & 0 \\ 1 & 0 & 0 & -1 \end{pmatrix} \quad (3.138)$$

the Hamiltonian can be brought in block diagonal form

$$H_{\text{BdG}}(\mathbf{k}) = \begin{pmatrix} H^+(\mathbf{k}) & \\ & -H^{-T}(\mathbf{k}) \end{pmatrix} \quad (3.139)$$

where $H^\pm(\mathbf{k}) = \mathbf{h}(\mathbf{k}) \cdot \boldsymbol{\sigma} \pm \Delta \sigma^z$ so that the occupied space is spanned by

$$U \begin{pmatrix} |u_+^+(\mathbf{k})\rangle \\ 0 \end{pmatrix} \quad \text{and} \quad U \begin{pmatrix} 0 \\ |u_-^-(\mathbf{k})\rangle \end{pmatrix} \quad (3.140)$$

so that

$$Q_{\text{BdG}}(\mathbf{k}) = U \begin{pmatrix} \hat{\mathbf{h}}^+(\mathbf{k}) \cdot \boldsymbol{\sigma} & \\ & \hat{\mathbf{h}}^- \cdot \boldsymbol{\sigma} \end{pmatrix} U. \quad (3.141)$$

As a result, the Chern number can be determined as the sum of the Chern numbers calculated via Eq. (3.133) for $\hat{\mathbf{h}}^+(\mathbf{k})$ and $\hat{\mathbf{h}}^-(\mathbf{k})$. This allows for a phase with odd $C_{\text{BdG}} = \pm 1$ to form for m between $\mp(2 + \Delta)$ and $\mp(2 - \Delta)$ for a small Δ . Indeed, since $\Delta \neq 0$, the BdG Hamiltonian is no longer “twice the original” so that its Chern numbers also do not have to be the originals doubles anymore.

3.4.4 Dimensional reduction

Dimensional reduction is a trick to relate topological invariants in a higher dimension to those of a restricted version of the model in a lower dimension. Rather than discussing this idea in full generality, we will focus on 2D class D models again and express the Chern number in terms of 1D invariants. Therefore, consider the Fourier space single-particle Hamiltonian, $H(\mathbf{k})$. Within each phase, this Hamiltonian is gapped and periodic so that we can interpret $H(\mathbf{k})$ as a gapped, adiabatic cycle along k_x (or, equivalently, k_y) between $H(0, k_y)$ and $H(\pi, k_y)$. The 1D models at these specific k_x inherit PHS from the 2D system (as opposed to the other k_x) and can therefore be classified in either class D or BDI (TRS can emerge upon restricting $k_x = 0, \pi$). One concludes that the reduced 1D models can at least realize a \mathbb{Z}_2 -type topological invariant. This is

$$W_{2n+1} = e^{2\pi i \text{CS}_{2n+1}[\mathcal{A}]} \quad (3.142)$$

with $2n + 1 = d$ and

$$\text{CS}_{2n+1}[\mathcal{A}] = \int_{\text{BZ}} \mathcal{Q}_{2n+1}(\mathcal{A}) \quad (3.143)$$

the Chern-Simons (CS) invariant where $\mathcal{Q}_{2n+1}(\mathcal{A})$, the Chern-Simons form, is a function of the Berry connection \mathcal{A} , defined as before. For a general n ,

$$\mathcal{Q}_{2n+1}(\mathcal{A}) = \frac{1}{n!} \left(\frac{i}{2\pi} \right)^{n+1} \int_0^1 dt \text{tr}(\mathcal{A} \mathcal{F}_t^n) \quad \text{with} \quad \mathcal{F}_t = t d\mathcal{A} + t^2 \mathcal{A} \wedge \mathcal{A} \quad (3.144)$$

reducing to

$$\mathcal{Q}_1(\mathcal{A}) = \frac{i}{2\pi} \text{tr}(\mathcal{A}) \quad (3.145)$$

when $n = 0$. The nomenclature in the above is somewhat flawed as a gauge transformation does change the CS ‘‘invariant’’. Indeed, under a gauge transformation g , the CS form changes as

$$\mathcal{Q}_{2n+1}(\mathcal{A}') - \mathcal{Q}_{2n+1}(\mathcal{A}) = \omega_{2n+1}[g] + d\alpha_{2n+1}(\mathcal{A}, g) \quad (3.146)$$

with

$$\omega_{2n+1}[g] = \frac{(-1)^n n!}{(2n+1)!} \left(\frac{i}{2\pi} \right)^{n+1} \text{tr}((g^{-1}dg)^{2n+1}) \quad (3.147)$$

the winding number density and $d\alpha_{2n+1}(\mathcal{A}, g)$ a total derivative term disappearing upon integration over the Brillouin zone so that

$$\text{CS}_{2n+1}[\mathcal{A}'] - \text{CS}_{2n+1}[\mathcal{A}] = \text{integer}. \quad (3.148)$$

I.e. while the CS invariant is only invariant up to an integer, W_{2n+1} is truly gauge independent. We remark that the CS invariant is also not quantized in general. This only happens when the symmetries required to be in a first (second) descendant class for s odd (even) are present, making $\text{W}_{2n+1} = \pm 1$ a true \mathbb{Z}_2 topological invariant. For 1D class D models, this invariant can also be interpreted as a $U(1)$ Wilson loop defined on the BZ ($\simeq S^1$) with the corresponding CS invariant equal to the electric polarization. In this context, the non-invariance of $\text{CS}_1[\mathcal{A}]$ is related to the fact that the displacement of electron coordinates in periodic systems has a meaning only within a unit cell, *i.e.* two coordinates that differ by an integer multiple of the lattice constant should be identified. Specifically for the reduced Hamiltonians under consideration, one obtains a polarization

$$P(k_x) = \text{CS}_1[\mathcal{A}] = \int_{\text{BZ}} \frac{i}{2\pi} \text{tr}(A_y(\mathbf{k})) dk_y \quad (3.149)$$

that is only quantized to integers and half-integers when $k_x = 0, \pi$ but can be defined for other k_x nonetheless. Moreover, this quantity is only gauge invariant when considered modulo 1.

If the 2D model becomes BDI upon reduction to 1D, phase diagrams can become even richer as a \mathbb{Z} -type topological invariant can now be realized in the form of the winding number

$$\nu_{2n+1}[q] = \int_{\text{BZ}} \omega_{2n+1}[q] \quad (3.150)$$

with $\omega_{2n+1}[q]$ again the winding number density. When $n = 0$, this reduces to

$$\nu_1[q] = \frac{i}{2\pi} \int_{\text{BZ}} \text{tr} \left(q^{-1}(k) \frac{\partial q}{\partial k}(k) \right) dk. \quad (3.151)$$

Herein, the matrix $q(k)$ is defined so that

$$Q(k) = \begin{pmatrix} & q(k) \\ q^\dagger(k) & \end{pmatrix}. \quad (3.152)$$

This decomposition is always possible due to chiral symmetry and thus also carries the complete information about the gauge invariant occupied space. Indeed, since $U_C^2 = \mathbb{1}$, the spectrum of U_C consists of ± 1 and only when both are equal in number (and thus $\text{tr}(U_C) = 0$), the model is gapped. One can thus always find a constant unitary diagonalizing U_C so that

$$\tilde{U}_C = V^\dagger U_C V = \begin{pmatrix} \mathbb{1} & \\ & -\mathbb{1} \end{pmatrix} \quad (3.153)$$

and thus

$$\tilde{H}(k) = V^\dagger H(k) V = \begin{pmatrix} & D(k) \\ D^\dagger(k) & \end{pmatrix}. \quad (3.154)$$

Because they have the same eigenvectors, the spectral operator $Q(k)$ will take the same form as the Hamiltonian, thus allowing to calculate the winding number in the aforementioned way. Note, however, that the same symmetries as in class D are still present and therefore a quantized CS invariant can also be derived. Both topological invariants can be related most easily in the basis described above. There, the occupied space can be parametrized by

$$|u_-^\alpha(\mathbf{k})\rangle = \frac{1}{\sqrt{2}} \begin{pmatrix} |n^\alpha\rangle \\ -q^\dagger(\mathbf{k})|n^\alpha\rangle \end{pmatrix} \quad (\alpha = 1, \dots, f_-) \quad (3.155)$$

where the $f_- \{|n^\alpha\rangle\}$ form an orthonormal basis. Choosing the standard basis, the Berry connection is given by

$$\text{tr}(A_y(\mathbf{k})) = \frac{1}{2} \text{tr} \left(U_-^\dagger(\mathbf{k}) \frac{\partial}{\partial k_y} U_-(\mathbf{k}) \right) = \frac{1}{2} \text{tr} \left(q(\mathbf{k}) \frac{\partial}{\partial k_y} q^\dagger(\mathbf{k}) \right) \quad (3.156)$$

so that $\nu_1[q^\dagger] = 2 \text{CS}_1[\mathcal{A}]$ and hence

$$W_1 = (-1)^{\nu_1}. \quad (3.157)$$

The \mathbb{Z}_2 Chern-Simons invariant W_1 is thus equal to the parity of the winding number. Specifically for the reduced models under consideration with emergent TRS, we find that

$$W_1(k_x) = (-1)^{\nu_1(k_x)} = (-1)^{2P(k_x)} \quad (3.158)$$

and the equivalent for cycling along k_y .

In the previous paragraph we saw that the reduced 1D models will always realize a topological \mathbb{Z}_2 CS invariant. Interestingly, this invariant can also be determined by only considering the time-reversal invariant momenta (TRIMs), *i.e.* those momentum modes where $\mathbf{k} = -\mathbf{k}$. In these TRIMs, the ground state $G(\mathbf{k})$ becomes real so that it can be regarded as a standard correlation matrix with a definite parity, determined by its Pfaffian. Expressing this parity in terms of the operators at the TRIM, one obtains

$$P(\mathbf{k}) = \text{Pf}(G(\mathbf{k} = -\mathbf{k})) = \langle (-1)^{\sum_{i=1}^f a_{\mathbf{k},i}^\dagger a_{\mathbf{k},i}} \rangle. \quad (3.159)$$

We can link these to the CS invariants. Indeed, due to the inherited PHS, the occupied space at $-k_y$ is related to the unoccupied space at k_y when $k_x = 0, \pi$ such that we can choose

$$|u_-^\alpha(-\mathbf{k})\rangle = U_P^\dagger \mathcal{K} |u_+^\alpha(\mathbf{k})\rangle. \quad (3.160)$$

Consequently, the polarization at $k_x = 0, \pi$ can be expressed as

$$\begin{aligned} P(k_x) &= \frac{i}{2\pi} \int_0^\pi \text{tr}(A_y(\mathbf{k})) dk_y + \frac{i}{2\pi} \int_0^\pi \text{tr}(A_y(-\mathbf{k})) dk_y \\ &= \frac{i}{2\pi} \int_0^\pi \text{tr}\left(U_-^\dagger(\mathbf{k}) \frac{\partial}{\partial k_y} U_-(\mathbf{k})\right) dk_y \\ &\quad - \frac{i}{2\pi} \int_0^\pi \text{tr}\left(U_+^T(\mathbf{k}) \frac{\partial}{\partial k_y} \overline{U_+(\mathbf{k})}\right) dk_y \\ &= \frac{i}{2\pi} \int_0^\pi \text{tr}\left(U^\dagger(\mathbf{k}) \frac{\partial}{\partial k_y} U(\mathbf{k})\right) dk_y \end{aligned} \quad (3.161)$$

where $U(\mathbf{k}) = (U_+(\mathbf{k}) \ U_-(\mathbf{k}))$ now contains all the eigenvectors with $U_-(\mathbf{k}) = U_P^\dagger \overline{U_+}(-\mathbf{k})$ and therefore constitutes a Bogoliubov transformation diagonalizing $H(\mathbf{k})$,

$$H(\mathbf{k}) = U^\dagger(\mathbf{k}) \begin{pmatrix} \bigoplus_\alpha e^\alpha(\mathbf{k}) & \\ & -\bigoplus_\alpha e^\alpha(-\mathbf{k}) \end{pmatrix} U(\mathbf{k}) \quad (3.162)$$

with $e^\alpha(\mathbf{k}) > 0$. Applying Jacobi's formula, one obtains

$$P(k_x) = \frac{i}{2\pi} \int_0^\pi \frac{1}{\det U(\mathbf{k})} \frac{\partial}{\partial k_y} (\det U(\mathbf{k})) dk_y = \frac{i}{2\pi} \ln \left(\frac{\det U(k_x, \pi)}{\det U(k_x, 0)} \right) \quad (3.163)$$

or thus

$$W_1(k_x) = \frac{\det U(k_x, 0)}{\det U(k_x, \pi)}. \quad (3.164)$$

Utilizing $U(\mathbf{k})$ as a Bogoliubov transformation $\Upsilon_{\mathbf{k}} \rightarrow \tilde{\Upsilon}_{\mathbf{k}} = U(\mathbf{k})^\dagger \Upsilon_{\mathbf{k}}$, the single-particle Hamiltonian diagonalizes and has a particularly simple ground state correlation matrix, $\tilde{G}(\mathbf{k}) = J^{\oplus f}$. Consequently, the correlation matrix in the original operators is given by $G(\mathbf{k}) = Z(\mathbf{k}) \tilde{G}(\mathbf{k}) Z^\dagger(\mathbf{k})$ with $Z(\mathbf{k}) = VU(\mathbf{k})V^{-1}$ (based on Eq. (3.60)). Since $U(\mathbf{k})$ is real and orthogonal in the TRIMs, the ground state parity can be expressed as $P(\mathbf{k}) = \text{Pf}(G(\mathbf{k} = -\mathbf{k})) = \det(U(\mathbf{k})) \text{Pf}(\tilde{G}(\mathbf{k})) = \det(U(\mathbf{k}))$. Put differently, we found that

$$W_1(k_x) = (-1)^{\nu_1(k_x)} = P(k_x, 0)P(k_x, \pi) \quad k_x = 0, \pi \quad (3.165)$$

with $P(\mathbf{k})$ the ground state parity and $\nu_1(k_x)$ the winding number in class BDI and $\nu_1(k_x) = 2P(k_x)$ (which is gauge dependent) for class D models. We remind the reader that the same reasoning can be followed for adiabatic cycling along k_y .

The premise of dimensional reduction and thus the goal of this Section was to link the Chern number to the guaranteed \mathbb{Z}_2 invariants of the reduced 1D models (and thus the parities in the TRIMs). Writing this Chern number as

$$C = \frac{i}{2\pi} \int_{\text{BZ}} \left(\frac{\partial}{\partial k_x} \text{tr}(A_y(\mathbf{k})) - \frac{\partial}{\partial k_y} \text{tr}(A_x(\mathbf{k})) \right) dk_x dk_y \quad (3.166)$$

and choosing a gauge where

$$\frac{\partial}{\partial k_y} \text{tr}(A_x(\mathbf{k})) = 0, \quad (3.167)$$

it can be seen as the winding number of the polarization along k_x

$$C = \frac{i}{2\pi} \int_{-\pi}^{\pi} dk_x \frac{\partial}{\partial k_x} \left(\int_{-\pi}^{\pi} \text{tr}(A_y(\mathbf{k})) dk_y \right) dk_y = \int_{-\pi}^{\pi} dk_x \frac{\partial P}{\partial k_x}(k_x). \quad (3.168)$$

Again invoking PHS symmetry but now for a general k_x , one obtains that

$$\begin{aligned} P(k_x) + P(-k_x) &= \frac{i}{2\pi} \int_{-\pi}^{\pi} \text{tr}(A_y(\mathbf{k})) dk_y + \frac{i}{2\pi} \int_{-\pi}^{\pi} \text{tr}(A_y(-\mathbf{k})) dk_y \\ &= \frac{i}{2\pi} \int_{-\pi}^{\pi} \text{tr} \left(U_-^\dagger(\mathbf{k}) \frac{\partial}{\partial k_y} U_-(\mathbf{k}) \right) dk_y \\ &\quad - \frac{i}{2\pi} \int_{-\pi}^{\pi} \text{tr} \left(U_+^T(\mathbf{k}) \frac{\partial}{\partial k_y} \overline{U_+(\mathbf{k})} \right) dk_y \\ &= \frac{i}{2\pi} \int_{-\pi}^{\pi} \text{tr} \left(U^\dagger(\mathbf{k}) \frac{\partial}{\partial k_y} U(\mathbf{k}) \right) dk_y = 0 \end{aligned} \quad (3.169)$$

so that

$$C = 2 \int_0^\pi dk_x \frac{\partial P}{\partial k_x}(k_x) = 2(P(k_x = \pi) - P(k_x = 0)). \quad (3.170)$$

Even though this is only true in the specific gauge of Eq. (3.167) as polarizations are gauge dependent, the parity of $2(P(k_x = \pi) - P(k_x = 0))$ is gauge invariant and hence fixes the parity of the Chern number in every gauge. Again using ν_1 , this can be expressed as

$$C = \nu_1(k_x = \pi) + \nu_1(k_x = 0) = \nu_1(k_y = \pi) + \nu_1(k_y = 0) \mod 2 \quad (3.171)$$

which is gauge invariant due to the modulo operation. Utilizing that the Berry connections under consideration are those for the BdG Hamiltonian, we can apply Eq. (3.165) to link the parity of the Majorana Chern number to the parities in the TRIMs,

$$e^{i\pi C} = P(0, 0)P(\pi, 0)P(0, \pi)P(\pi, \pi) \quad (3.172)$$

This immediately shows that an odd C , implies a different $\nu_1(k_{x(y)} = 0)$ and $\nu_1(k_{x(y)} = \pi)$ and thus three equal TRIM parities while the fourth is different. In Chapter 5 we will see that parity configurations like this are obstructed for Gaussian fermionic TNS in 2D with exponentially decaying correlations, typically complicating variational optimization in these phases. We end this paragraph with some technical remarks. The reasoning above to link C and the \mathbb{Z}_2 descendants was followed in a specific gauge but can also be made more general and fully gauge independent [193]. Furthermore, the calculation of the polarization in the reduced 1D models requires a globally continuous set of eigenvectors parameterizing the occupied space. This may be obstructed but the Hamiltonian can then be extended to resolve the technical issues at hand [194]. The gauge invariant results for the relation with the TRIM parities remain valid nonetheless.

As an illustration we will consider the two exemplary models introduced in the first section.

- The 1D reduced models for the p-wave superconductor at $k_x = 0, \pi$ are determined by

$$\begin{aligned} \mathbf{h}(0, k_y) &= (2\Delta \sin k_y \quad 0 \quad -\mu - 2t - 2t \cos k_y) \\ \mathbf{h}(\pi, k_y) &= (2\Delta \sin k_y \quad 0 \quad -\mu + 2t - 2t \cos k_y) \end{aligned}, \quad (3.173)$$

hence describing Kitaev chains of class BDI with $U_T = \sigma^z$ and $U_C = \sigma^y$. Via a unitary transformation,

$$V = \frac{1}{\sqrt{2}} \begin{pmatrix} 1 & 1 \\ i & -i \end{pmatrix}, \quad (3.174)$$

U_C can be diagonalized bringing the Hamiltonian in the block-off-diagonal form of Eq. (3.154). Indeed, the reduced Hamiltonians become

$$H(k_y) = \begin{pmatrix} 0 & h_3(k_y) - ih_1(k_y) \\ h_3(k_y) + ih_1(k_y) & 0 \end{pmatrix} \quad (3.175)$$

with the components of the \mathbf{h} vector as in Eq. (3.173) and $U_C = \sigma^z$ as chiral symmetry. Proposing an occupied space of the form in Eq. (3.155), one obtains

$$|u_-(k_y)\rangle = \frac{1}{\sqrt{2}} \begin{pmatrix} 1 \\ -e^{-i\theta(k_y)} \end{pmatrix} \quad (3.176)$$

as $q(k_y) = e^{i\theta(k_y)}$ is a scalar. We now require this to be an occupied eigenvector of the new $H(k_y)$ with energy $-|\mathbf{h}(k_y)|$. This happens when $\theta(k_y)$ is the phase of $h_3(k_y) - ih_1(k_y)$ or equivalently

$$q(k_y) = \frac{h_3(k_y) - ih_1(k_y)}{|\mathbf{h}(k_y)|}. \quad (3.177)$$

Note that as the original Hamiltonian is gapped (we always choose $|\Delta| > 0$), this is defined for all k_y . Consequently the winding numbers of the 1D reductions can be calculated as

$$\nu_1(k_x) = \begin{cases} 0 & |\mu + 2t| > 2t \\ -\text{sgn}(\Delta) & |\mu + 2t| < 2t \\ 0 & |\mu - 2t| > 2t \\ -\text{sgn}(\Delta) & |\mu - 2t| < 2t \end{cases} \quad . \quad (3.178)$$

The winding numbers are different in both reductions for any $|\mu| < 4t$ while for $|\mu| > 4t$ both are trivial. An immediate consequence is that the gauge independent Chern-Simons invariants $W_1 = (-1)^{\nu_1}$ also differ in the two reductions when $|\mu| < 4t$ and can be linked to the TRIM parities as prescribed in Eq. (3.165). Indeed, when $0 < \mu < 4t$, the Bogoliubov transformation to bring the Hamiltonian in the form of Eq. (3.162) is $U = \mathbb{1}$ in the TRIMs $(0, 0)$, $(0, \pi)$ and $(\pi, 0)$, yielding a parity $P = +1$ while for (π, π) , $U = \sigma^x$ resulting in an odd parity. For $-4t < \mu < 0$ the parities are reversed. We conclude that in the topological phases (with an odd number of Majorana edge modes), the reduced models are topologically distinct and hence require a parity configuration that is inadmissible for regular GfTNS. This is consistent with the observed obstructions when simulating the p-wave superconductor in its topological phases (see Sec. 5.2).

- The 1D reductions for the Chern insulator at $k_x = 0, \pi$ are determined by

$$\begin{aligned} \mathbf{h}(0, k_y) &= (0 \quad \sin k_y \quad m + 1 + \cos k_y) \\ \mathbf{h}(\pi, k_y) &= (0 \quad \sin k_y \quad m - 1 + \cos k_y) \end{aligned} \quad , \quad (3.179)$$

hence residing in class BDI with $U_T = \mathbb{1}$ and $U_C = \sigma^x$. Via a unitary transformation,

$$V = \frac{1}{\sqrt{2}} \begin{pmatrix} 1 & 1 \\ 1 & -1 \end{pmatrix}, \quad (3.180)$$

U_C can be diagonalized yielding

$$H(k_y) = \begin{pmatrix} 0 & h_3(k_y) + ih_2(k_y) \\ h_3(k_y) - ih_2(k_y) & 0 \end{pmatrix} \quad (3.181)$$

for the reduced models with the components of the \mathbf{h} vector as in Eq. (3.179) and $U_C = \sigma^z$ as chiral symmetry. Proposing an occupied space of the form in Eq. (3.155), one obtains

$$q(k_y) = \frac{h_3(k_y) + ih_2(k_y)}{|\mathbf{h}(k_y)|}. \quad (3.182)$$

The winding numbers of the 1D reductions can hence be calculated as

$$\nu_1(k_x) = \begin{cases} 0 & |m+1| > 1 \\ -1 & |m+1| < 1 \\ 0 & |m-1| > 1 \\ -1 & |m-1| < 1 \end{cases} \quad k_x = 0 \quad . \quad (3.183)$$

The winding numbers are different in both reductions for any $|m| < 2$ (*i.e.* for both topological phases) while for $|m| > 2$ both are trivial. An immediate consequence is that the gauge independent Chern-Simons invariants $W_1 = (-1)^{\nu_1}$ also differ in the two reductions when $|m| < 2$ in correspondence to the observed odd fermion Chern number. However, no parity obstructions arise because the TRIM parities are not linked to the winding numbers since we considered the non-BdG Hamiltonian. To establish this link anyway, we determine the reduced models for the BdG Hamiltonian,

$$H(k_x = 0, \pi; k_y) = \begin{pmatrix} \mathbf{h}(k_x, k_y) \cdot \boldsymbol{\sigma} & \\ & -\mathbf{h}(k_x, k_y) \cdot \boldsymbol{\sigma} \end{pmatrix} \quad (3.184)$$

with the $\mathbf{h}(\mathbf{k})$ vectors as in Eq. (3.179). This model is again class BDI with $U_T = \mathbb{1}$ and $U_P = U_C = \sigma^x \otimes \mathbb{1}$. We now use the constant unitary

$$V = \frac{1}{\sqrt{2}} \begin{pmatrix} 1 & 1 & 1 \\ 1 & 1 & -1 \\ 1 & -1 & -1 \end{pmatrix} \quad (3.185)$$

to diagonalize U_C and bring $H(k_y)$ in a block-off-diagonal form

$$H(k_y) = \begin{pmatrix} & \sigma^y h_2(k_y) + \sigma^z h_3(k_y) \\ \sigma^y h_2(k_y) + \sigma^z h_3(k_y) & \end{pmatrix}. \quad (3.186)$$

The occupied space can hence be parametrized as in Eq. (3.155),

$$|u_-^1(\mathbf{k})\rangle = \begin{pmatrix} 1 \\ 0 \\ -q^\dagger(k_y) \begin{pmatrix} 1 \\ 0 \end{pmatrix} \end{pmatrix} \quad |u_-^2(\mathbf{k})\rangle = \begin{pmatrix} 0 \\ 1 \\ -q^\dagger(k_y) \begin{pmatrix} 0 \\ 1 \end{pmatrix} \end{pmatrix} \quad (3.187)$$

and to determine $q(k_y)$ we use that the two negative eigenvalues of $H(k_y)$ are equal to $-|\mathbf{h}(k_y)|$ so that the Hermitian matrix

$$q(k_y) = \frac{\sigma^y h_2(k_y) + \sigma^z h_3(k_y)}{|\mathbf{h}(k_y)|} \quad (3.188)$$

indeed results in occupied eigenvectors. These are again well-defined for all k_y . For the winding number, one obtains

$$\begin{aligned} \nu_1(k_x = 0, \pi) &= \frac{i}{2\pi} \int_{-\pi}^{\pi} \text{tr} \left(q \frac{\partial q}{\partial k_y} \right) dk_y \\ &= \frac{i}{2\pi} \int_{-\pi}^{\pi} \text{tr} \left(\sigma^a \frac{h_a}{|\mathbf{h}|} \sigma^b \left(\frac{1}{|\mathbf{h}|} \frac{\partial h_b}{\partial k_y} - \frac{h_b h_c}{|\mathbf{h}|^3} \frac{\partial h_c}{\partial k_y} \right) \right) dk_y \quad (3.189) \\ &= \frac{i}{\pi} \int_{-\pi}^{\pi} \frac{1}{|\mathbf{h}|^2} \left(h_a \frac{\partial h_a}{\partial k_y} - h_b \frac{\partial h_b}{\partial k_y} \right) dk_y = 0. \end{aligned}$$

We conclude that by combining the single-particle Hamiltonian at \mathbf{k} and $-\mathbf{k}$ in the BdG Hamiltonian, the resulting model is always trivial. This is consistent with the observed TRIM parities. Indeed these are all equal to -1 as there is always one state filled and one state empty for each \mathbf{k} . This also implies that the Majorana Chern number will always be even, therefore not causing any parity obstructions. Finally, we could add the superconducting terms to the model again. The reduced models retain the same symmetries as before and after diagonalizing U_C , we find

$$H(k_y) = \begin{pmatrix} & D(k_y) \\ D^\dagger(k_y) & \end{pmatrix}. \quad (3.190)$$

with $D(k_y) = \sigma^y (h_2(k_y) - i\Delta) + \sigma^z h_3(k_y)$. Note that the negative eigenvalues of $H(k_y)$ are now different. Indeed, we saw in Eq. (3.139) that these are given by $-|\mathbf{h}^\pm(k_x = 0, \pi; k_y)| = -e^\pm(k_y)$. Hence, a valid $q(k_y)$ is

$$q(k_y) = \begin{pmatrix} e^-(k_y) & \\ & e^+(k_y) \end{pmatrix}^{-1} D(k_y) \quad (3.191)$$

with winding numbers as depicted in Fig. 3.1. These are consistent with both the TRIM parities and the Chern numbers.

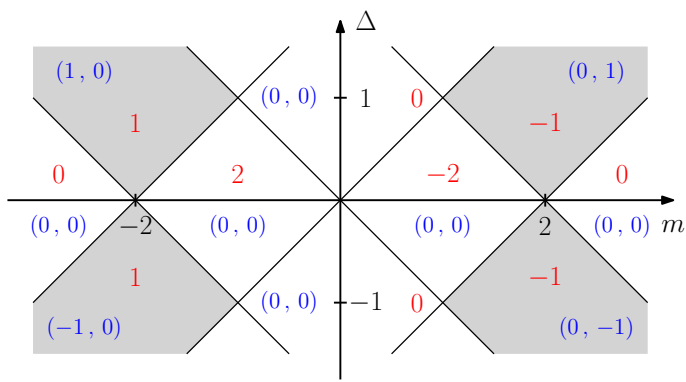


Figure 3.1: Phase diagram for the quantum anomalous Hall superconductor with Majorana Chern numbers (red) and winding numbers in $k_x = 0$ and $k_x = \pi$ (blue). Parity obstructions for regular GfTNS will arise in the gray-colored phases.

Chapter 4

Fermionic tensor network methods

In recent years, tensor network *Ansätze*, such as matrix product states (MPS) [165] and Projected Entangled-Pair States (PEPS) [174], have proven increasingly successful in describing ground states of quantum many-body systems. Both types of TNS owe their versatile applicability to an inherent area law of entanglement as present in low-energy states of local and gapped Hamiltonians [36, 172]. Moreover, their use can be extended to critical models with violations of this area law by using the technique of finite-entanglement scaling [53, 54, 195, 196] (see also Sec. 5.4.2). In addition to their numerical applications, tensor networks have also proven to be conceptually important, particularly in the classification of topological phases [88, 89].

Crucial in the numerical progress was the development of a toolbox filled with tensor network methods for variational optimization (e.g. DMRG [104] and the Variational optimization of Uniform MPS (VUMPS) [197, 198, 199] in 1D and the Corner Transfer Matrix Renormalization Group (CTMRG) [200, 201, 202] as well as channel PEPS in 2D [203], possibly aided by automatic differentiation (AD) [204, 205, 206]), (imaginary) time-evolution (e.g. Time Evolving Block Decimation (TEBD) [207, 208] (with simple [209] and full updates [210]) and the Time-Dependent Variational Principle (TDVP) [211, 199]), incorporation of excitations [212, 213], *etc.* However, many (if not all) of these methods were originally formulated in the setting of spin systems. Here, we intend their application to fermions and therefore need either a reformulation of those fermions in terms of spins or an adaption of the methods to the anti-commuting nature of the degrees of freedom. In 1D, the former approach can always be followed by invoking a Jordan-Wigner transformation [214]. Although some tentative results exist, a full-fledged and equally attractive generalization of such a transformation does not exist in higher dimensions. Hence, we are forced to explicitly integrate the fermions into our formalism. Possible routes to do so have already been proposed, e.g. in [215] where the fermionic degrees of freedom are replaced by Grassmann numbers. For the resulting Grassmann tensor networks, interesting results have been obtained both numerically [216] and conceptually [217, 218]. An alternative to the Grassmann formalism, originally introduced for the MERA, writes the local tensors as a (normally-ordered) product of physical and virtual operators acting on the vacuum [219, 220, 221]. To maintain the celebrated diagrammatic language of tensor networks, all these tensors are required to have even parity. The composite spaces on the other hand can have odd sectors such that crossings of the corresponding legs in a tensor diagram will yield additional minus signs. To keep track of

these minus signs, one “resolves” crossings by replacing them with so-called swap gates. With this technique many of the standard tensor network methods can be rephrased for fermions. However, to keep track of the minus signs one has to be careful in the manipulation of tensor diagrams. Indeed, every additional crossing has to be resolved with a new swap gate. Therefore, this method, though highly successful and conceptually sound can become quite unwieldy.

In this Chapter we present an alternative based on the seminal work of Bultinck *et al.* [89, 222] Here, fermions are integrated in the tensor network formalism by constructing the latter from \mathbb{Z}_2 -graded linear spaces, also called super vector spaces. However, as the intention of the authors was to classify fermionic topological phases in 1D and 2D, this discussion was primarily conceptual. In this Chapter, we extend the formalism toward numerical implementation. We thus build fermionic MPS and PEPS (in the thermodynamic limit) and consider tangent space methods like the VUMPS algorithm and the quasi-particle excitation *Ansatz*. Benchmark simulations have been performed in both 1D (with a focus on excitations) and 2D (aimed at the reproduction of Gaussian correlation functions).

This project has been a joint endeavor together with Lukas Devos and Lander Burgelman based on the foundations laid out by Nick Bultinck, Bram Vanhecke, Laurens Vanderstraeten and in broader sense by Jutho Haegeman and Frank Verstraete. Simulations have been performed with the `TensorTrack` package [223], a `MatLab` library incorporating many (symmetric) tensor network algorithms to which the fermionic features were added by the author. Benchmark simulations in 1D have been performed by Lukas Devos. Simulations in 2D were performed by the author. The work has not been published yet but will be made available soon as a preprint.

4.1 Fermionic tensors

Before delving into specific fermionic tensor network states (fTNS) and their corresponding algorithms, we first discuss the concept of a \mathbb{Z}_2 -graded tensor. To ensure the desired properties of these tensors, we work from a list of desiderata and demonstrate how the \mathbb{Z}_2 -graded formalism neatly implements them. We also provide a justification for the diagrammatic notation and conclude by discussing tensor properties such as Hermiticity and unitarity. These properties serve as the foundation for various tensor manipulations and decompositions that we introduce in the subsequent Section.

4.1.1 Preliminaries

The wavefunction of an arbitrary fermionic many-body state is given by

$$|\Psi\rangle = \sum_{\sigma_1, \dots, \sigma_N} \psi_{\sigma_1 \dots \sigma_N} \left(a_1^\dagger \right)^{\sigma_1} \dots \left(a_N^\dagger \right)^{\sigma_N} |\Omega\rangle \quad (4.1)$$

where $|\Omega\rangle$ is the Fock vacuum and $\{a_i^\dagger\}_{i=1,\dots,N}$ collects N fermionic creation operators satisfying canonical anti-commutation relations. Note that the order of the indices in this expression is important; swapping a_1^\dagger and a_2^\dagger , for instance, would introduce an extra

factor $(-1)^{\sigma_1\sigma_2}$, thus altering the coefficients. The idea behind a tensor network state is to provide an efficient parametrization of the $\psi_{\sigma_1\dots\sigma_N}$ coefficients as their number grows exponentially with N . Conceptually, a clear way to arrive at this point starts from virtual modes. Consider therefore an exemplary system with four physical, fermionic modes, that we can represent schematically as

$$\psi_{\sigma_1\sigma_2\sigma_3\sigma_4} = \begin{array}{c} \sigma_1 \\ \diagup \quad \diagdown \\ \textcircled{\psi} \\ \diagdown \quad \diagup \\ \sigma_4 \quad \sigma_3 \end{array} . \quad (4.2)$$

To every physical degree of freedom we associate two virtual, fermionic modes and arrange these in maximally entangled pairs to create

$$|\Psi_{\text{virt}}\rangle = \prod_e \frac{1}{\sqrt{2}} \left(1 + a_{e,l}^\dagger a_{e,r}^\dagger \right) |\Omega_{\text{virt}}\rangle = \begin{array}{c} \textcircled{\dots} \\ \diagup \quad \diagdown \\ \textcircled{\dots} \end{array} \quad (4.3)$$

where e labels the edges along which the entangled pairs are oriented and l (left) and r (right) discerns between both sides of these edges. Next, we introduce a linear operator that maps the virtual state onto a physical many-body state. In a tensor network, this map is a product of local maps

$$\mathcal{A}[j] = \sum_{\alpha_1\dots\alpha_n, \sigma_j} A[j]_{\alpha_1\dots\alpha_n}^{\sigma_j} (a_j^\dagger)^\sigma (a_1)^{\alpha_1} \dots (a_n)^{\alpha_n} \quad (4.4)$$

where the creator acts on the physical mode while the annihilators act on the n (in this case two) virtual degrees of freedom per site. The tensor network state is obtained by projecting back on the virtual vacuum state,

$$|\Psi\rangle = \langle \Omega_{\text{virt}} | \left(\prod_j \mathcal{A}[j] \right) |\Psi_{\text{virt}}\rangle |\Omega_{\text{phys}}\rangle . \quad (4.5)$$

Schematically, $|\Psi\rangle$ can be represented as

$$|\Psi\rangle = \begin{array}{c} \sigma_1 \\ \diagup \quad \diagdown \\ \textcircled{\mathcal{A}[1]} \quad \textcircled{\mathcal{A}[2]} \\ \diagdown \quad \diagup \\ \textcircled{\mathcal{A}[4]} \quad \textcircled{\mathcal{A}[3]} \\ \diagup \quad \diagdown \\ \sigma_4 \quad \sigma_3 \end{array} . \quad (4.6)$$

In the case where both the physical and virtual degrees of freedom are bosonic, this procedure gives rise to a tensor network representation for $|\Psi\rangle$ where the coefficients $\psi_{\sigma_1\dots\sigma_N}$ can be computed by contracting local tensors. Indeed, promoting the arrays $A[j]$ to tensors living in the tensor product of the local virtual and physical spaces, contraction of these tensors yields $|\Psi\rangle$. In the fermionic case, however, the anti-commutation relations generate a number of minus signs such that the state can no longer be obtained as a simple contraction of local tensors.

In order to overcome the aforementioned difficulties, we need to incorporate the minus signs into the local tensor operations. To keep everything as close as possible to the bosonic formalism, we require the following properties:

- In the definition of the linear map, $\mathcal{A}[j]$, the ordering of the virtual modes should be important and a permutation of these modes has to lead to minus signs in $A[j]$.
- We want the well-known diagrammatic notation of tensor networks to survive. One should thus be able to represent all relevant tensor network operations as diagrams where the composite blocks can be moved around in a continuous manner. Note that this immediately requires the tensors to be parity even, equivalent to parity preserving $\mathcal{A}[j]$ such that they commute.
- We require the existence of an `ncon`-like [224] procedure for the numerical computation of tensor contractions, *i.e.* a single-line command, independent of the order of its arguments.

A priori it is not clear whether a formalism satisfying these three constraints even exists. Indeed, for the more general anyonic degrees of freedom with non-trivial braiding rules [77] there is simply no alternative to the “swap-gate approach” where every line crossing in the network diagram has to be resolved by hand. However, the rules for fermions are just simple enough so that we can satisfy the desiderata, though not in a trivial way. To see this consider the following type of diagrams that we will also encounter in Sec. 4.2,

$$(4.7)$$

Here the numbers denote the order of the indices in the definition of the tensors (which is the same for ρ and ρ'). If a consistent method exists, we can calculate ρ' by the following `ncon`-like command, for instance in `TensorTrack`,

$$\rho' = \text{contract}(B, [-1, 3, 1], \rho, [1, 2], A, [2, 3, -2]),$$

corresponding to

$$(4.8)$$

where we place the arguments as in the `contract` command, first draw all tensor legs downward and in the order of the tensor’s definition to then connect contracted legs horizontally with their vertical position corresponding to the contraction order. In this way, the `contract` command and its corresponding diagram are uniquely linked. By continuous deformation of the latter we recover the tensor network diagram we intended. However, the order of the tensors in the contraction command should not matter. Therefore, also

$$\rho' = \text{contract}(B, [-1, 3, 1], A, [2, 3, -2], \rho, [1, 2]),$$

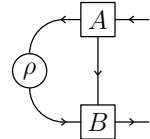
should give the correct result. Drawing its corresponding tensor diagram like before, we obtain

$$(4.9)$$

Subsequently deforming this by dragging the full (and even) A tensor through the ρ legs, we get

$$\Gamma^{(\rho)} = \Gamma[B] \xrightarrow{\rho} \Gamma[A]. \quad (4.10)$$

Note that the self-crossing, corresponding to the introduction of a fermionic minus sign on this leg and setting Eq. (4.10) apart from Eq. (4.8), cannot be removed in a continuous manner. This means we are left with two conflicting results. Does this mean that all hope is lost? No. In fact there are two possible ways out of this impasse. The first is to demand all diagrams to be crossing-free, thus avoiding all fermionic minus signs upon contraction. This may seem drastic but for typical MPS methods the connection graphs are planar so that there always exists one, and only one, contraction command so that the resulting tensor diagram is crossing-free. For our example, this would force us to use the first contraction while the second diagram would be precluded. Hence, we are immediately granted a self-consistency check when calling the contraction command. While elegant for MPS, matters turn bleak for PEPS since planar connection graphs typically no longer exist. One should thus write down the tensor diagram with the inevitable crossings, introduce tensors that take these away (*i.e.* swap gates) and then use the planar contraction code for the result. Of course this invalidates what we set out to do. Luckily there is a second option. Rather than forbidding (self-)crossings, we will keep track of them but in a way that does not require any spectacular changes to standard contraction routines, namely by using arrows. This idea is not new and is typically used in globally symmetric tensor network codes with symmetries [225]. For fermions, arrows can tell us exactly where self-crossings (and the corresponding fermionic minus signs) appear. Indeed, consider again Eq. (4.7) but now choose an orientation on all legs, so that the arrows on the horizontal (contracted) legs all point in the same direction (here to the left) for the first contraction command. *I.e.* choose



$$(4.11)$$

corresponding to

$$\Gamma[B] \xrightarrow{\rho} \Gamma[A]. \quad (4.12)$$

With the same arrows, the second contraction command yields

$$\Gamma[B] \xleftarrow{\rho} \Gamma[A]. \quad (4.13)$$

Hence, self-crossings correspond to arrows pointing in the opposite direction (here to the right). As many codes already have tensor objects with oriented legs, the fermionic contraction routine just has to compare these arrows to the order of the tensors in the function call. By adding fermionic minus signs for all “opposite” arrows, it can then correct for the self crossings, making the result for both contractions identical and thus allowing to remove all self crossings.

We conclude that the combination of the three desiderata we put forward is possible for fermions but requires either a prohibition on line crossing or oriented legs to compensate for them. In this work we will opt for the latter. However, this choice has far-reaching consequences. Consider for instance the diagrammatic representation of a matrix,

$$\begin{array}{c} \text{---} \\ \boxed{A} \\ \text{---} \end{array}, \quad (4.14)$$

and suppose you want to contract both legs. Precluding crossings, the only way to do so is

$$\begin{array}{c} \text{---} \\ \boxed{A} \\ \text{---} \end{array}, \quad (4.15)$$

yielding $A_{ii} = \text{tr}(A)$, the standard trace without any fermionic minus signs. However, with oriented legs, two possibilities exist. Either

$$\begin{array}{c} \rightarrow \\ \boxed{A} \\ \leftarrow \end{array}, \quad (4.16)$$

yielding the standard trace again as the contracted arrow points to the left or

$$\begin{array}{c} \leftarrow \\ \boxed{A} \\ \rightarrow \end{array}, \quad (4.17)$$

where the contracted arrow points to the right yielding a so-called *supertrace*, $A_{ii}(-1)^{|i|}$ with $|i|$ indicating the parity of the i -th basis vector w.r.t. which A is represented (see below).

4.1.2 Graded tensor networks

In this Section we introduce \mathbb{Z}_2 -graded Hilbert spaces and their tensor products. We show that these form a natural mathematical framework incorporating the three requirements from the previous Section by giving the legs/spaces an orientation, leading to a supertrace.

\mathbb{Z}_2 -graded Hilbert spaces are (in our case finite) Hilbert spaces with the defining property that they decompose in two orthogonal sectors

$$V = V^0 \oplus^\perp V^1, \quad (4.18)$$

referred to as even and odd, respectively. If a given basis state $|i\rangle$ only has support in one of the two sectors, it has a definite grading or parity which we denote by $|i|$. These vectors are called homogeneous, and inhomogeneous vectors can always be decomposed into a sum of homogeneous ones. Consequently, one can always introduce an orthonormal, homogeneous basis $\{|i\rangle\}$, solely consisting of homogeneous basis vectors where $\langle i|j\rangle = \delta_{ij}$.

Now, consider homomorphisms between two \mathbb{Z}_2 -graded Hilbert spaces V and W . A homomorphism is defined to be even (odd) when it is parity-preserving (-changing) meaning that it maps V^0 into W^0 (W^1) and V^1 into W^1 (W^0). Noting that $\text{Hom}(V, W)$ is a Hilbert space itself and that any homomorphism can be decomposed in a parity-preserving and a parity-changing part, we thus find that the homomorphisms constitute a graded Hilbert space as well. In particular, one can consider the dual space $V^* = \text{Hom}(V, \mathbb{C})$ containing

the linear forms on V and use the inner product structure of V to construct the canonical, anti-linear isomorphism $V \rightarrow V^* : |v\rangle \mapsto \langle v|$ where $\langle v|(|w\rangle) = \langle v|w\rangle \forall |v\rangle, |w\rangle \in V$. As the complex field is only trivially graded in the sense that $\mathbb{C} = \mathbb{C} \oplus \{0\}$ and as the inner product between vectors with a different grading yields zero, one immediately obtains that $\langle i|$ has the same grading as $|i\rangle$ when this vector is homogeneous. V^* thus inherits its (identical) grading from V .

In order to describe many-body states, we need to consider tensor products of graded Hilbert spaces, e.g. $V_1 \otimes V_2$. Note that this space is graded as well when the parity of the natural basis states $|i\rangle_1 \otimes |j\rangle_2$ is defined by $|i| + |j| \bmod 2$ (hence a \mathbb{Z}_2 grading) with $\{|i\rangle_1\}$ and $\{|j\rangle_2\}$ homogeneous basis sets in V_1 and V_2 , respectively.¹ Furthermore, this space is still a Hilbert space in the sense that it has an inner product inherited from V_1 and V_2 , $\langle |v_1\rangle \otimes |v_2\rangle, |w_1\rangle \otimes |w_2\rangle \rangle = \langle v_1|w_1\rangle \langle v_2|w_2\rangle$, extended via sesquilinearity to the whole space. The same applies for $V_2 \otimes V_1$ and both spaces can be connected by the isomorphism

$$\mathcal{F} : V_1 \otimes V_2 \rightarrow V_2 \otimes V_1 : |i\rangle_1 \otimes |j\rangle_2 \mapsto (-1)^{|i||j|} |j\rangle_2 \otimes |i\rangle_1 , \quad (4.19)$$

also called fermionic reordering. Indeed, this swapping prescription will encode the fermionic anti-commutation relations. We will use the notation \mathcal{F} very loosely and refer to objects related by this isomorphism as being the same. This is possible since the precise order of subsequent applications of \mathcal{F} is irrelevant. Consider for instance, a four-leg fermionic tensor $A \in V \otimes V \otimes V^* \otimes V^*$, defined as

$$A = A_{\alpha\beta\gamma\delta} |\alpha\rangle |\beta\rangle \langle\gamma| \langle\delta| \quad (4.20)$$

where, from this point on, we adopt the Einstein summation convention and we omit the \otimes symbol for taking tensor products. Because of the swapping prescription, the ordering of the indices in the above tensor is important. *I.e.* while changing the ordering leads to minus signs in the tensor elements, e.g.

$$A = \left((-1)^{|\alpha||\beta|} A_{\alpha\beta\gamma\delta} \right) |\beta\rangle |\alpha\rangle \langle\gamma| \langle\delta| , \quad (4.21)$$

the tensor itself, related to the original A by a single \mathcal{F} application, is regarded as being the same. On each tensor we impose that the global parity is even, *i.e.* if the total parity of the indices is odd, the corresponding element should be zero:

$$A_{\alpha\beta\gamma\delta} = 0 \quad \text{when} \quad |\alpha| + |\beta| + |\gamma| + |\delta| = 1 \bmod 2 . \quad (4.22)$$

This implies that we can commute tensors, a feature that will be crucial when introducing the diagrammatic notation later on for which the order of the tensors remains unspecified.

We also introduce a canonical contraction map

$$\mathcal{C} : V^* \otimes V \rightarrow \mathbb{C} : \langle i| |j\rangle \mapsto \mathcal{C}(\langle i| |j\rangle) = \langle i|j\rangle = \delta_{ij} . \quad (4.23)$$

Together with the reordering isomorphism, this can be extended consistently to $\tilde{\mathcal{C}} = \mathcal{C} \circ \mathcal{F} : V \otimes V^* \rightarrow \mathbb{C}$ with

$$\tilde{\mathcal{C}}(|i\rangle \langle j|) = (-1)^{|i||j|} \mathcal{C}(\langle j| |i\rangle) = (-1)^{|i||j|} \delta_{ij} \quad (4.24)$$

¹In this way, the grading of $V \otimes W^*$ is also compatible with that of $\text{Hom}(V, W)$.

incorporating the famous supertrace. Again, we will typically not write the reordering isomorphism explicitly so that with a slight misuse of notation one can say that $\tilde{\mathcal{C}} = \mathcal{C}$ just denotes contracting. As an example, suppose we are given two tensors

$$\begin{aligned} B &= B_{\alpha\beta\gamma} |\alpha\rangle \langle\beta| \langle\gamma| \\ C &= C_{\delta\varepsilon} |\delta\rangle \langle\varepsilon| , \end{aligned} \quad (4.25)$$

then we can compute the contraction of the second index of B with the first index of C as

$$\begin{aligned} \mathcal{C}_{21}(B \otimes C) &= \mathcal{C}_{\beta\delta} \left(B_{\alpha\beta\gamma} C_{\delta\varepsilon} |\alpha\rangle \langle\beta| \langle\gamma| |\delta\rangle \langle\varepsilon| \right) \\ &= \mathcal{C}_{\beta\delta} \left(B_{\alpha\beta\gamma} C_{\delta\varepsilon} (-1)^{|\beta||\gamma|} |\alpha\rangle \langle\gamma| \langle\beta| |\delta\rangle \langle\varepsilon| \right) \\ &= \left(\sum_{\beta} B_{\alpha\beta\gamma} C_{\beta\varepsilon} (-1)^{|\beta||\gamma|} \right) |\alpha\rangle \langle\gamma| \langle\varepsilon| . \end{aligned} \quad (4.26)$$

Note that we tacitly assumed that the internal ordering of the resulting tensor is given by concatenating the ordering of the uncontracted indices of the original tensors.

Together with taking tensor products, reordering and contraction allow the calculation of any overlap or the application of any operator to a fermionic state since all these operations can be reformulated in terms of \otimes, \mathcal{F} and \mathcal{C} . The fundamental difference with bosonic tensor networks is that do so, supertraces, appearing in a fermionic tensor network, have to be compensated. Let us illustrate this for the overlap between two tensors with the same structure, e.g.

$$A = A_{\alpha\beta\gamma} |\alpha\rangle \langle\beta| \langle\gamma| \quad \text{and} \quad B = B_{\delta\varepsilon\zeta} |\delta\rangle \langle\varepsilon| \langle\zeta| . \quad (4.27)$$

The inner product was defined as

$$\langle A, B \rangle = \overline{A_{\alpha\beta\gamma}} B_{\delta\varepsilon\zeta} \langle\alpha|\delta\rangle \langle\beta|\varepsilon\rangle \langle\gamma|\zeta\rangle = \overline{A_{\alpha\beta\gamma}} B_{\alpha\beta\gamma} . \quad (4.28)$$

This is exactly equal to the contraction of B with the conjugate of A , when this conjugate is defined as

$$A^* = \overline{A_{\alpha\beta\gamma}} \langle\gamma| \langle\beta| \langle\alpha| , \quad (4.29)$$

i.e. we change the kets into bras and vice versa, reverse their ordering and we take the conjugate of the tensor elements. However, when the tensors also contain bras, e.g.

$$A = A_{\alpha\beta\gamma} |\alpha\rangle \langle\beta| \langle\gamma| \quad \text{and} \quad B = B_{\delta\varepsilon\zeta} |\delta\rangle \langle\varepsilon| \langle\zeta| , \quad (4.30)$$

supertraces appear and

$$\begin{aligned} \langle A, B \rangle &= \overline{A_{\alpha\beta\gamma}} B_{\delta\varepsilon\zeta} \langle\alpha|\delta\rangle \langle\varepsilon|\beta\rangle \langle\zeta|\gamma\rangle \\ &= \overline{A_{\alpha\beta\gamma}} |\gamma\rangle \langle\beta| \langle\alpha| (-1)^{|\varepsilon|} (-1)^{|\zeta|} B_{\delta\varepsilon\zeta} |\delta\rangle \langle\varepsilon| \langle\zeta| \\ &= \mathcal{C}(A^* \mathcal{P}(B)) \end{aligned} \quad (4.31)$$

where \mathcal{P} adds extra parity factors to the dual vectors of B . For the norm of a fermionic tensor one thus obtains $\|A\| = \sqrt{\langle A, A \rangle} = \sqrt{\mathcal{C}(A^* \mathcal{P}(A))}$, yielding the Frobenius norm of the tensor entries. In this regard, one might question why we did not include these parities in the definition of the conjugate as well. The rationale behind this is that while it would eliminate the additional minus signs in this particular case, it would not hold true in an extended tensor network where A^* is not solely contracted with A . In fact, adopting the alternative definition could introduce even more parities than the ones we eliminated here. Therefore, the precise definition of A^* in terms of minus signs is ultimately a matter of convention.

As a second example we consider the application of an operator $T : V \otimes V^* \rightarrow V \otimes V^* : |\beta_1\rangle \langle \beta_2| \mapsto T_{\beta_1 \beta_2}^{\alpha_1 \alpha_2} |\alpha_1\rangle \langle \alpha_2|$. This is equivalent to the contraction of the tensor $T_{\beta_1 \beta_2}^{\alpha_1 \alpha_2} |\alpha_1\rangle \langle \alpha_2| |\beta_2\rangle \langle \beta_1|$, isomorphic to T , with the argument $v = v^{\beta_1 \beta_2} |\beta_1\rangle \langle \beta_2| \in V \otimes V^*$, supplemented with parity factors for the dual vectors in v . Indeed,

$$\begin{aligned} T(v) &= T_{\beta_1 \beta_2}^{\alpha_1 \alpha_2} v^{\beta_1 \beta_2} |\alpha_1\rangle \langle \alpha_2| \\ &= \mathcal{C}_{\beta \gamma} \left(T_{\beta_1 \beta_2}^{\alpha_1 \alpha_2} |\alpha_1\rangle \langle \alpha_2| |\beta_2\rangle \langle \beta_1| (-1)^{|\gamma_2|} v^{\gamma_1 \gamma_2} |\gamma_1\rangle \langle \gamma_2| \right) \\ &= \mathcal{C}(T\mathcal{P}(v)). \end{aligned} \quad (4.32)$$

Note that with these definitions and conventions, the fermionic tensor network machinery satisfies the criteria we put forward in the previous Section. Indeed,

- the ordering of (co)vectors in the definition of fermionic tensors is important and extra minus signs will appear when permuting them due to the swapping prescription \mathcal{F} .
- we required all tensors to be even so that they can be shuffled around, making the idea of contracting larger networks consistent and manageable.
- each index has a directionality, captured by its correspondence to a vector or a dual vector. This can be incorporated in a consistent contraction routine.

4.1.3 Diagrammatic notation

The fermionic tensors and their contractions can be represented using tensor network diagrams. We can, for instance, depict the tensor A from Eq. (4.20) with a diagram

$$A = A_{\alpha \beta \gamma \delta} |\alpha\rangle \langle \beta| \langle \gamma| \langle \delta| = \begin{array}{c} \alpha \quad \beta \\ \delta \quad \gamma \\ \textcircled{A} \end{array}, \quad (4.33)$$

where each leg corresponds to a (dual) vector space labeled with the same Greek index as in Eq. (4.20) and where the arrows indicate whether we have vectors (outgoing) or dual vectors (incoming). Contractions between different tensors are represented by connecting the corresponding legs. For example, we can represent the contraction in Eq. (4.26) as

$$\begin{array}{c} \alpha \\ \nearrow \\ \textcircled{B} \\ \swarrow \\ \gamma \end{array} \leftarrow \begin{array}{c} \textcircled{C} \\ \leftarrow \varepsilon \end{array}. \quad (4.34)$$

Taking the conjugate of a fermionic tensor, all vectors are turned into dual vectors and vice-versa. Diagrammatically, this implies that all arrows have to be flipped. *I.e.*, if we have a tensor

$$A = A_{\alpha\beta\gamma} |\alpha\rangle \langle\beta| \langle\gamma| = \begin{array}{c} \alpha \\ \nearrow \\ \textcircled{A} \\ \searrow \\ \gamma \end{array} \leftarrow \beta , \quad (4.35)$$

its conjugate can be depicted as

$$A^* = \overline{A_{\alpha\beta\gamma}} |\gamma\rangle |\beta\rangle \langle\alpha| = \begin{array}{c} \alpha \\ \nearrow \\ \textcircled{A^*} \\ \searrow \\ \gamma \end{array} \rightarrow \beta . \quad (4.36)$$

For the (quadratic) norm of A , one thus obtains that

$$|\langle A, A \rangle|^2 = \mathcal{C}(A^* \mathcal{P}(A)) = \begin{array}{c} \textcircled{A} \\ \nearrow \\ \textcircled{A^*} \\ \searrow \\ \textcircled{P} \end{array} . \quad (4.37)$$

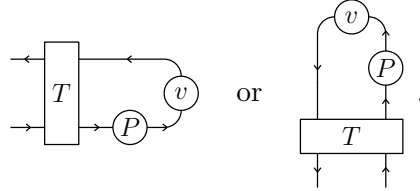
where we show that the action of \mathcal{P} is equivalent to placing P tensors on the outgoing legs of A^* with

$$\alpha \leftarrow \textcircled{P} \leftarrow \beta = (-1)^{|\alpha|} \delta_{\alpha\beta} |\alpha\rangle \langle\beta| . \quad (4.38)$$

Note that the parity tensor differs only slightly from the unit tensor, defined by

$$\alpha \leftarrow \textcircled{I} \leftarrow \beta = \delta_{\alpha\beta} |\alpha\rangle \langle\beta| . \quad (4.39)$$

Finally, for the application of an operator T , we will typically follow the convention that the legs corresponding to the (co)domain are placed to the right (left) or top (bottom) of the tensor. The arguments will thus be appended from the right or from the top. Diagrammatically, the exemplary application of T in Eq. (4.32) thus translates to



4.1.4 Tensor properties

Having introduced the diagrammatic notation, we will now elaborate on tensor operations necessary for typical tensor network algorithms. To get there, we first deduce the diagrammatic notation for applying the adjoint of an arbitrary fermionic homomorphism T . We will demonstrate this for $T : V \otimes V^* \otimes V \rightarrow V \otimes V^*$, isomorphic to the tensor

$$T = T_{\beta_1\beta_2\beta_3}^{\alpha_1\alpha_2} |\alpha_1\rangle \langle\alpha_2| \langle\beta_3| |\beta_2\rangle \langle\beta_1| = \begin{array}{c} \alpha_1 \leftarrow \\ \textcircled{T} \\ \alpha_2 \rightarrow \\ \beta_1 \leftarrow \\ \beta_2 \rightarrow \\ \beta_3 \leftarrow \end{array} \quad (4.40)$$

but the results can readily be extended to any arbitrary homomorphism. The adjoint $T^\dagger : V \otimes V^* \rightarrow V \otimes V^* \otimes V$ is defined by the property that $\langle v, T^\dagger w \rangle = \langle T v, w \rangle$ should hold $\forall v \in V \otimes V^* \otimes V$ and $\forall w \in V \otimes V^*$. As discussed in the previous Section, we can express this as a contraction of the corresponding \mathbb{Z}_2 -graded tensors with P tensors to incorporate supertraces. Indeed,

$$T(v) = \mathcal{C}(T \mathcal{P}(v)) = \begin{array}{c} \text{Diagram showing } T \text{ tensor with } P \text{ and } v \text{ tensors} \end{array} \quad (4.41)$$

and

$$T^\dagger(w) = \mathcal{C}(T^\dagger \mathcal{P}(w)) = \begin{array}{c} \text{Diagram showing } T^\dagger \text{ tensor with } P \text{ and } w \text{ tensors} \end{array} \quad (4.42)$$

The defining property for T^\dagger can thus be rephrased as

$$\mathcal{C}(v^* \mathcal{P}(T^\dagger(w))) = \mathcal{C}(T(v)^* \mathcal{P}(w)) \quad (4.43)$$

or equivalently

$$\begin{array}{c} \text{Diagram showing } T^\dagger \text{ tensor with } P \text{ and } w \text{ tensors} \\ = \\ \text{Diagram showing } T^* \text{ tensor with } P \text{ and } w \text{ tensors} \end{array} \quad (4.44)$$

since

$$T(v)^* = \begin{array}{c} \text{Diagram showing } T^* \text{ tensor with } P \text{ and } v^* \text{ tensors} \end{array} = \begin{array}{c} \text{Diagram showing } T^* \text{ tensor with } P \text{ and } v^* \text{ tensors} \end{array} \quad (4.45)$$

We conclude that applying T^\dagger corresponds to contraction with

$$\begin{array}{c} \text{Diagram showing } T^\dagger \text{ tensor} \\ = \\ \text{Diagram showing } T^* \text{ tensor} \end{array} \quad (4.46)$$

I.e. the adjoint tensor, T^\dagger , is obtained by taking the conjugate of T , followed by mirroring it w.r.t. the codomain-domain (left-right) axis. In this way, the (co)domain arrows on the right (left) of the original tensor are now on the other side. Note that the reflection of T^* has no influence on the tensor. It is rather a diagrammatic operation, redrawing the legs, to retain the meaning of the right (left) side as (co)domain of the homomorphism. In symbols, the reflection corresponds to a relabeling $\alpha \leftrightarrow \beta$ of T^* , thus leaving the tensor object unchanged.

Building on this, an arbitrary endomorphism,

$$T : V \otimes V^* \otimes \dots \otimes V \rightarrow V \otimes V^* \otimes \dots \otimes V, \quad (4.47)$$

with tensor

$$T = T_{\beta_1 \beta_2 \dots \beta_n}^{\alpha_1 \alpha_2 \dots \alpha_n} |\alpha_1\rangle \langle \alpha_2| \dots |\alpha_n\rangle \langle \beta_n| \dots |\beta_2\rangle \langle \beta_1|$$

$$= \begin{array}{c} \alpha_1 \leftarrow \\ \alpha_2 \rightarrow \\ \vdots \\ \alpha_n \leftarrow \end{array} \boxed{T} \begin{array}{c} \beta_1 \leftarrow \\ \beta_2 \rightarrow \\ \vdots \\ \beta_n \leftarrow \end{array} \quad (4.48)$$

is Hermitian when $T = T^\dagger$ or diagrammatically,

$$\begin{array}{c} \alpha_1 \leftarrow \\ \alpha_2 \rightarrow \\ \vdots \\ \alpha_n \leftarrow \end{array} \boxed{T} \begin{array}{c} \beta_1 \leftarrow \\ \beta_2 \rightarrow \\ \vdots \\ \beta_n \leftarrow \end{array} = \begin{array}{c} \alpha_1 \leftarrow \\ \alpha_2 \rightarrow \\ \vdots \\ \alpha_n \leftarrow \end{array} \boxed{T^\dagger} \begin{array}{c} \beta_1 \leftarrow \\ \beta_2 \rightarrow \\ \vdots \\ \beta_n \leftarrow \end{array} = \begin{array}{c} \alpha_1 \leftarrow \\ \alpha_2 \rightarrow \\ \vdots \\ \alpha_n \leftarrow \end{array} \boxed{T^*} \begin{array}{c} \beta_1 \leftarrow \\ \beta_2 \rightarrow \\ \vdots \\ \beta_n \leftarrow \end{array} . \quad (4.49)$$

In components this translates to $T_{\beta_1 \beta_2 \dots \beta_n}^{\alpha_1 \alpha_2 \dots \alpha_n} = T_{\beta_1 \beta_2 \dots \beta_n}^{\dagger \alpha_1 \alpha_2 \dots \alpha_n} = \overline{T_{\alpha_1 \alpha_2 \dots \alpha_n}^{\beta_1 \beta_2 \dots \beta_n}}$, which, grouping the α and β indices, comes down to $T_\beta^\alpha = T_{\dagger \beta}^\alpha = \overline{T_\alpha^\beta}$, thus yielding the standard Hermitian condition. Analogously, an arbitrary operator T , e.g. with tensor

$$T = T_{\beta_1 \beta_2 \dots \beta_n}^{\alpha_1 \alpha_2 \dots \alpha_m} |\alpha_1\rangle \langle \alpha_2| \dots |\alpha_m\rangle |\beta_n\rangle \dots \langle \beta_2| \langle \beta_1|$$

$$= \begin{array}{c} \alpha_1 \leftarrow \\ \alpha_2 \rightarrow \\ \vdots \\ \alpha_m \leftarrow \end{array} \boxed{T} \begin{array}{c} \beta_1 \leftarrow \\ \beta_2 \rightarrow \\ \vdots \\ \beta_n \leftarrow \end{array} \quad (4.50)$$

is defined to be left-isometric when application of T followed by T^\dagger onto an arbitrary $v \in V \otimes V \otimes \dots \otimes V^*$ returns the argument. We can again reformulate this as a contraction. T is left-isometric when $T^\dagger(T(v)) = \mathcal{C}(T^\dagger \mathcal{P}(T \mathcal{P}(v))) = v$, or diagrammatically

$$\begin{array}{c} \leftarrow \\ \leftarrow \\ \vdots \\ \rightarrow \end{array} \boxed{T^\dagger} \begin{array}{c} \rightarrow \\ \rightarrow \\ \vdots \\ \leftarrow \end{array} \boxed{P} \begin{array}{c} \leftarrow \\ \leftarrow \\ \vdots \\ \rightarrow \end{array} \boxed{T} \begin{array}{c} \rightarrow \\ \rightarrow \\ \vdots \\ \leftarrow \end{array} \boxed{P} \begin{array}{c} \leftarrow \\ \leftarrow \\ \vdots \\ \rightarrow \end{array} v = \begin{array}{c} \leftarrow \\ \leftarrow \\ \vdots \\ \rightarrow \end{array} v , \quad (4.51)$$

such that a left-isometry is characterized by

$$\begin{array}{c} \leftarrow \\ \leftarrow \\ \vdots \\ \rightarrow \end{array} \boxed{T^\dagger} \begin{array}{c} \rightarrow \\ \rightarrow \\ \vdots \\ \leftarrow \end{array} \boxed{P} \begin{array}{c} \leftarrow \\ \leftarrow \\ \vdots \\ \rightarrow \end{array} \boxed{T} \begin{array}{c} \rightarrow \\ \rightarrow \\ \vdots \\ \leftarrow \end{array} \boxed{P} \begin{array}{c} \leftarrow \\ \leftarrow \\ \vdots \\ \rightarrow \end{array} = \begin{array}{c} \leftarrow \\ \leftarrow \\ \vdots \\ \rightarrow \end{array} \boxed{I} \begin{array}{c} \leftarrow \\ \leftarrow \\ \vdots \\ \rightarrow \end{array} . \quad (4.52)$$

Similarly, T is right-isometric when application of T^\dagger followed by T onto an arbitrary $v \in V \otimes V^* \otimes \dots \otimes V$ yields v again, i.e. $T(T^\dagger(v)) = \mathcal{C}(T \mathcal{P}(T^\dagger \mathcal{P}(v))) = v$, or diagrammatically

$$\begin{array}{c} \leftarrow \\ \leftarrow \\ \vdots \\ \rightarrow \end{array} \boxed{T} \begin{array}{c} \rightarrow \\ \rightarrow \\ \vdots \\ \leftarrow \end{array} \boxed{P} \begin{array}{c} \leftarrow \\ \leftarrow \\ \vdots \\ \rightarrow \end{array} \boxed{T^\dagger} \begin{array}{c} \rightarrow \\ \rightarrow \\ \vdots \\ \leftarrow \end{array} \boxed{P} \begin{array}{c} \leftarrow \\ \leftarrow \\ \vdots \\ \rightarrow \end{array} v = \begin{array}{c} \leftarrow \\ \leftarrow \\ \vdots \\ \rightarrow \end{array} v . \quad (4.53)$$

We conclude that T is a right-isometry if

$$\begin{array}{c} \text{---} \\ | \\ \text{---} \\ T \\ | \\ \vdots \\ | \\ \text{---} \\ P \\ | \\ \end{array} \quad \begin{array}{c} \text{---} \\ | \\ \text{---} \\ T^\dagger \\ | \\ \vdots \\ | \\ \text{---} \\ P \\ | \\ \end{array} = \begin{array}{c} \text{---} \\ | \\ \text{---} \\ I \\ | \\ \text{---} \\ P \\ | \\ \vdots \\ | \\ \text{---} \\ I \\ | \\ \end{array}. \quad (4.54)$$

In case of a unitary operator, both apply. These conditions can again be expressed in components yielding standard results: T is left- (right-)isometric when $T^\dagger_\alpha^\beta T_\beta^\gamma = \delta_\alpha^\gamma$ ($T_\beta^\alpha T^\dagger_\gamma = \delta_\gamma^\alpha$).

4.1.5 Tensor manipulations

In order to express some more convoluted tensor properties (e.g. Hermiticity of fermionic Matrix Product Operators (MPOs) (see Sec. 4.3.2 and Appendix A.2)) or in order to derive tensor decompositions (see Sec. 4.1.6), unitary tensor manipulations like the fusing of legs or the flipping of arrows will be indispensable. Again, we will perform these operations as a contraction with a dedicated tensor. Therefore, we start by introducing the so-called fusers, representing a unitary map between two legs (corresponding to the spaces V_1 and V_2) and a single leg (corresponding to $V_1 \otimes V_2$) with a higher dimension. Associating a tensor

$$\begin{aligned} F &= F_{\beta_1}^{\alpha_1 \alpha_2} |\alpha_1\rangle |\alpha_2\rangle \langle \beta_1| \\ &= \begin{array}{c} \alpha_1 \leftarrow \\ \alpha_2 \leftarrow \\ \text{---} \\ F \\ \text{---} \\ \beta_1 \end{array}. \end{aligned} \quad (4.55)$$

with this unitary (or its hermitian conjugate), we thus have that

$$\begin{array}{c} \text{---} \\ | \\ \text{---} \\ F \\ | \\ \text{---} \\ F^\dagger \\ | \\ \text{---} \\ \text{---} \\ | \\ \text{---} \\ I \\ | \\ \text{---} \\ I \\ | \\ \text{---} \end{array} = \begin{array}{c} \text{---} \\ | \\ \text{---} \\ I \\ | \\ \text{---} \\ I \\ | \\ \text{---} \end{array} \quad (4.56)$$

and

$$\begin{array}{c} \text{---} \\ | \\ \text{---} \\ F^\dagger \\ | \\ \text{---} \\ F \\ | \\ \text{---} \\ \text{---} \\ | \\ \text{---} \\ \text{---} \\ | \\ \text{---} \\ I \\ | \\ \text{---} \end{array} = \begin{array}{c} \text{---} \\ | \\ \text{---} \\ I \\ | \\ \text{---} \end{array}. \quad (4.57)$$

Dual vectors can also be incorporated, e.g.

$$\begin{aligned} F &= F_{\beta_1}^{\alpha_1 \alpha_2} |\alpha_1\rangle \langle \alpha_2| |\beta_1\rangle \langle \beta_1| \\ &= \begin{array}{c} \alpha_1 \leftarrow \\ \alpha_2 \rightarrow \\ \text{---} \\ F \\ \text{---} \\ \beta_1 \end{array}. \end{aligned} \quad (4.58)$$

with F unitary so that

$$\begin{array}{c} \text{---} \\ | \\ \text{---} \\ F \\ | \\ \text{---} \\ P \\ | \\ \text{---} \\ F^\dagger \\ | \\ \text{---} \\ \text{---} \\ | \\ \text{---} \\ I \\ | \\ \text{---} \\ P \\ | \\ \text{---} \end{array} = \begin{array}{c} \text{---} \\ | \\ \text{---} \\ I \\ | \\ \text{---} \\ P \\ | \\ \text{---} \end{array} \quad (4.59)$$

and

$$\begin{array}{c} \text{---} \\ | \\ \text{---} \\ F^\dagger \\ | \\ \text{---} \\ P \\ | \\ \text{---} \\ F \\ | \\ \text{---} \\ \text{---} \\ | \\ \text{---} \\ \text{---} \\ | \\ \text{---} \\ P \\ | \\ \text{---} \end{array} = \begin{array}{c} \text{---} \\ | \\ \text{---} \\ P \\ | \\ \text{---} \end{array}. \quad (4.60)$$

I.e. P tensors appear in the defining contractions for the fusers. However, attention should be paid to the correct interpretation of these diagrams. Note that they both contain P tensors with arrows pointing to the right rather than to the left as we originally drew them in Eq. (4.38). While still the same tensor, one should contract with the correct leg of the fusers. E.g. in Eq. (4.59) the second leg of the P tensor should be contracted with the third leg of F while the P 's first leg should be contracted with F^\dagger 's first leg. In symbols the left side of Eq. (4.59) hence becomes

$$\begin{aligned} & \mathcal{C}_{\gamma'\beta_1} \left(\mathcal{C}_{\gamma\alpha'_1} \left(F_{\beta_1}^{\alpha_1\alpha_2} |\alpha_1\rangle\langle\alpha_2| |\beta_1\rangle (-1)^{|\gamma|} \delta_{\gamma\gamma'} |\gamma\rangle\langle\gamma'| \right. \right. \\ & \quad \left. \left. \overline{F_{\alpha'_1}^{\beta'_1\beta'_2}} \langle\alpha'_1| |\beta'_2\rangle\langle\beta'_1| \right) \right) = \\ &= F_\gamma^{\alpha_1\alpha_2} \overline{F_\gamma^{\beta'_1\beta'_2}} |\alpha_1\rangle\langle\alpha_2| |\beta'_2\rangle\langle\beta'_1| \\ &= \delta_{\alpha_1\beta'_1} \delta_{\alpha_2\beta'_2} |\alpha_1\rangle\langle\alpha_2| |\beta'_2\rangle\langle\beta'_1| \\ &= \delta_{\alpha_1\beta'_1} |\alpha_1\rangle\langle\beta'_1| \quad \delta_{\alpha_2\beta'_2} \langle\alpha_2| |\beta'_2| \end{aligned} \tag{4.61}$$

where from the second to the third line we used that $F_\gamma^\alpha F^{\dagger\gamma}_\beta = \delta_\beta^\alpha$. Note that this final result corresponds to the right side of Eq. (4.59) as the former part is the identity tensor while the latter is an internally permuted version of the P tensor. Indeed, if we want a left-pointing P with the incoming α index on the left as in Eq. (4.59), its incoming leg should be placed before the outgoing thus requiring the internal permutation, hence removing the typical $(-1)^{|\alpha|}$ in P . Note that doing the same for an identity tensor would exactly lead to a parity factor.

Another useful type of unitaries (that can also be regarded as a fuser but with a trivial leg) are flippers. Consider for instance the linear map $f : V \rightarrow V^* : |\alpha\rangle \mapsto f_\beta^\alpha \langle\beta|$ with tensor

$$f = f_\beta^\alpha \langle\alpha| \langle\beta| = \alpha \rightarrow \boxed{f} \leftarrow \beta \tag{4.62}$$

where we choose the orientation of the triangular shape according to the arrow direction of the domain. Now, let f be unitary, satisfying

$$\rightarrow \boxed{f} \leftarrow \boxed{f^\dagger} \rightarrow = \rightarrow \boxed{P} \rightarrow \tag{4.63}$$

and

$$\leftarrow \boxed{f^\dagger} \rightarrow \boxed{P} \rightarrow \leftarrow \boxed{f} \leftarrow = \leftarrow \boxed{I} \leftarrow , \tag{4.64}$$

e.g. by choosing $f_\beta^\alpha = \delta_\beta^\alpha$. Applying f to a leg of a tensor then corresponds to flipping the arrow of this leg, *i.e.* to going from a vector to a dual vector. Similarly, one could use f^\dagger to unitarily flip incoming legs. To illustrate this, consider again the A tensor from Eq. (4.20). We could flip its first arrow by applying f which corresponds to contracting with the second leg of the f tensor. Additionally, we could flip its fourth leg by applying f^\dagger . Application of this operator corresponds to contraction with the second leg of the f^\dagger tensor but now also including a P tensor in between. Consequently, the flipped object is given by

$$\tag{4.65}$$

However, note that the contraction of f^\dagger and P is unitary as well. Therefore, one could equally well use contraction with f^\dagger (without a P in between) to unitarily flip the fourth leg of A . More generally any invertible transformation could be utilized, also yielding non-unitary flippers.

4.1.6 Tensor decompositions

Typical tensor network algorithms heavily rely on tensor versions of matrix decompositions like QR, SVD and the polar decomposition. To get these for fermionic tensors, consider again an arbitrary tensor

$$A = A_{\beta_1 \beta_2 \dots \beta_n}^{\alpha_1 \alpha_2 \dots \alpha_m} |\alpha_1\rangle \langle \alpha_2| \dots |\alpha_m\rangle |\beta_n\rangle \dots \langle \beta_2| \langle \beta_1| = \begin{array}{c} \alpha_1 \leftarrow \\ \alpha_2 \rightarrow \\ \vdots \\ \alpha_m \leftarrow \end{array} \boxed{A} \begin{array}{l} \beta_1 \leftarrow \\ \beta_2 \rightarrow \\ \vdots \\ \beta_n \leftarrow \end{array}, \quad (4.66)$$

corresponding to a homomorphism. One could interpret its matrix representation A_β^α as a fused version of A where all the domain legs (on the right) and all the codomain legs (on the left) are fused together (using a specific choice for the fusers), *i.e.*

$$\begin{aligned} A_\beta^\alpha |\alpha\rangle \langle \beta| &= \alpha \leftarrow \boxed{A} \leftarrow \beta \\ &= \alpha \leftarrow \dots \leftarrow \boxed{A} \leftarrow \dots \leftarrow \beta \end{aligned} \quad (4.67)$$

thus yielding a two-leg tensor (a.k.a. a matrix). As this two-leg object is even, it only consists of a non-zero even-even and odd-odd sector. In both these sectors, A_β^α is just a $m \times n$ matrix on which one can, for instance, perform a QR (LQ) decomposition, $A_\beta^\alpha = Q_\gamma^\alpha R_\beta^\gamma$ ($A_\beta^\alpha = L_\gamma^\alpha Q_\beta^\gamma$). Here, Q is a left- (right-)isometric matrix while R (L) is an upper- (lower-)triangular, square matrix as long as $m \geq n$ ($m \leq n$). When $m < n$ ($m > n$), Q is square and unitary while R (L) consists of a upper- (lower-)triangular part supplemented with additional dense rows (columns). We can again promote these matrices to two-leg tensors so that the fused A tensor decomposes as

$$\boxed{A} = \boxed{Q} \leftarrow \boxed{R} \leftarrow \text{ and } \boxed{A} = \boxed{L} \leftarrow \boxed{Q} \leftarrow \quad (4.68)$$

with

$$\boxed{Q^\dagger} \leftarrow \boxed{Q} \leftarrow = \leftarrow \boxed{I} \leftarrow \text{ and } \boxed{Q} \leftarrow \boxed{Q^\dagger} \leftarrow = \leftarrow \boxed{I} \leftarrow \quad (4.69)$$

for QR and LQ decomposition respectively. Now, we can split the outer legs in the decomposition in a way consistent with how we fused them before to obtain a tensorial version of the QR (LQ) decomposition for A . We illustrate this for the QR decomposition of a tensor

$$A = A_{\beta_1 \beta_2}^{\alpha_1 \alpha_2} |\alpha_1\rangle \langle \alpha_2| \langle \beta_2| |\beta_1\rangle = \begin{array}{c} \alpha_1 \leftarrow \\ \alpha_2 \rightarrow \\ \beta_1 \leftarrow \\ \beta_2 \rightarrow \end{array} \boxed{A} \begin{array}{l} \end{array}. \quad (4.70)$$

Transforming A to a two-leg object is possible with

$$\begin{array}{c} \text{---} \\ | \\ A \\ | \\ \text{---} \end{array} = \begin{array}{c} \text{---} \\ | \\ F^\dagger \\ | \\ A \\ | \\ \tilde{F} \\ \text{---} \end{array} \quad (4.71)$$

where we choose

$$\begin{aligned} F &= (-1)^{|\alpha_2|} |\alpha_1\rangle\langle\alpha_2| \langle\alpha| = \begin{array}{c} \alpha_1 \leftarrow \\ \alpha_2 \rightarrow \\ \text{---} \\ | \\ F \\ | \\ \text{---} \end{array} \leftarrow \alpha \\ \tilde{F} &= (-1)^{|\beta_1|} \langle\beta_1| |\beta_2\rangle \langle\beta| = \begin{array}{c} \beta_1 \leftarrow \\ \beta_2 \rightarrow \\ \text{---} \\ | \\ \tilde{F} \\ | \\ \text{---} \end{array} \leftarrow \beta \end{aligned} \quad (4.72)$$

for the fusers. An immediate consequence is that

$$\begin{array}{c} \text{---} \\ | \\ A \\ | \\ \text{---} \end{array} = \begin{array}{c} \text{---} \\ | \\ (P) \\ | \\ \text{---} \end{array} \rightarrow \begin{array}{c} \text{---} \\ | \\ F \\ | \\ \text{---} \end{array} \rightarrow \begin{array}{c} \text{---} \\ | \\ A \\ | \\ \text{---} \end{array} \leftarrow \begin{array}{c} \text{---} \\ | \\ \tilde{F}^\dagger \\ | \\ (P) \\ | \\ \text{---} \end{array} \rightarrow \begin{array}{c} \text{---} \\ | \\ I \\ | \\ \text{---} \end{array}. \quad (4.73)$$

Note that other unitary fusers would yield an identical result. However, this choice was made so that the entries of the two-leg tensor are exactly A_β^α . Performing the QR decomposition on the two-leg A , we obtain

$$\begin{array}{c} \text{---} \\ | \\ A \\ | \\ \text{---} \end{array} = \begin{array}{c} \text{---} \\ | \\ Q \\ | \\ R \\ | \\ \text{---} \end{array} \leftarrow \quad (4.74)$$

where Q is left-isometric and thus

$$\begin{array}{c} \text{---} \\ | \\ Q^\dagger \\ | \\ Q \\ | \\ \text{---} \end{array} = \begin{array}{c} \text{---} \\ | \\ I \\ | \\ \text{---} \end{array}. \quad (4.75)$$

Splitting the outer legs in the decomposition is possible in the same way as in Eq. (4.73), yielding

$$\begin{array}{c} \text{---} \\ | \\ A \\ | \\ \text{---} \end{array} = \underbrace{\begin{array}{c} \text{---} \\ | \\ (P) \\ | \\ \text{---} \end{array} \rightarrow \begin{array}{c} \text{---} \\ | \\ F \\ | \\ \text{---} \end{array} \rightarrow \begin{array}{c} \text{---} \\ | \\ Q \\ | \\ R \\ | \\ \text{---} \end{array} \leftarrow \begin{array}{c} \text{---} \\ | \\ \tilde{F}^\dagger \\ | \\ (P) \\ | \\ \text{---} \end{array} \rightarrow \begin{array}{c} \text{---} \\ | \\ I \\ | \\ \text{---} \end{array}}_{\begin{array}{c} \text{---} \\ | \\ Q \\ | \\ \text{---} \end{array} \quad \begin{array}{c} \text{---} \\ | \\ R \\ | \\ \text{---} \end{array}}, \quad (4.76)$$

i.e. a full tensorial version of the decomposition. While possible to split, the inner leg remains fused as splitting has no interpretation here. Note that the multi-leg Q is still left-isometric since

$$\begin{aligned} &\begin{array}{c} \text{---} \\ | \\ Q^\dagger \\ | \\ (P) \\ | \\ Q \\ | \\ \text{---} \end{array} = \\ &= \begin{array}{c} \text{---} \\ | \\ Q^\dagger \\ | \\ F^\dagger \\ | \\ (P) \\ | \\ (P) \\ | \\ (P) \\ | \\ \text{---} \end{array} \rightarrow \begin{array}{c} \text{---} \\ | \\ F \\ | \\ \text{---} \end{array} \rightarrow \begin{array}{c} \text{---} \\ | \\ Q \\ | \\ \text{---} \end{array} \\ &= \begin{array}{c} \text{---} \\ | \\ Q^\dagger \\ | \\ Q \\ | \\ \text{---} \end{array} = \begin{array}{c} \text{---} \\ | \\ I \\ | \\ \text{---} \end{array}. \end{aligned} \quad (4.77)$$

We conclude that QR (LQ) decomposition of an arbitrary fermionic tensor is always possible, yielding a left- (right-)isometric Q with the same leg structure on the left (right) and a R with the same leg structure on the right (left) as the original tensor. The polar decomposition can be introduced along the same lines. Here, $A_\beta^\alpha = Q_\gamma^\alpha R_\beta^\gamma$ ($A_\beta^\alpha = R_\gamma^\alpha Q_\beta^\gamma$)

when $m \geq n$ ($m \leq n$) with R a positive semi-definite and Hermitian matrix while Q is left-(right)-isometric. In this case, it does make sense to split the inner leg in the same way as the outer R leg as this allows the resulting R tensor to be Hermitian in the fermionic tensor sense. Finally, we consider the singular-value decomposition $A_{\beta}^{\alpha} = U_{\gamma}^{\alpha} \Lambda_{\gamma'}^{\gamma} V_{\beta}^{\gamma'}$ where U is left-isometric, V is right-isometric and Λ is diagonal and collects the non-zero singular values of A_{β}^{α} . Again, we promote the U, V and Λ matrices to two-leg fermionic tensors and split the outer legs in the same way as the original tensor while leaving the inner legs fused, yielding

$$\begin{array}{c} \text{---} \\ | \end{array} \begin{array}{c} \text{---} \\ A \\ \vdots \\ \text{---} \end{array} \begin{array}{c} \text{---} \\ | \end{array} = \begin{array}{c} \text{---} \\ | \end{array} \begin{array}{c} \text{---} \\ U \\ \vdots \\ \text{---} \end{array} \begin{array}{c} \text{---} \\ | \end{array} \begin{array}{c} \text{---} \\ \Lambda \\ \text{---} \end{array} \begin{array}{c} \text{---} \\ | \end{array} \begin{array}{c} \text{---} \\ V \\ \vdots \\ \text{---} \end{array} \begin{array}{c} \text{---} \\ | \end{array}$$

where U and V are left- and right-isometries, respectively, in the fermionic tensor sense.

4.2 Uniform fermionic MPS

In this section we explain how to use the formalism of \mathbb{Z}_2 -graded vector spaces for parametrizing and manipulating fermionic matrix product states (fMPS). We discuss the canonical form, how to apply it for the calculation of expectation values and also consider the tangent space for the fMPS manifold. Subsequently, we combine these ingredients to discuss the VUMPS and TDVP algorithms for uniform fMPS as well as the quasi-particle excitation *Ansatz*. We do not intend to re-derive these concepts in full detail but rather want to highlight where the fermionic nature of the composite tensors induces differences when compared to the bosonic analogues.

4.2.1 General form

Conceptually, an MPS is introduced by associating two virtual, fermionic degrees of freedom to every site in a 1D chain. In a first step, these virtual modes are arranged in neighboring, maximally entangled states as

$$\begin{aligned} |\Psi_{\text{virt}}\rangle &= \prod_e \left(1 + a_{e,l}^{\dagger} a_{e,r}^{\dagger} \right) |\Omega_{\text{virt}}\rangle \\ &= \sim\circ\circ\sim\circ\circ\sim\circ\sim\sim . \end{aligned} \tag{4.78}$$

Next, we introduce a linear map, projecting the two virtual modes on each site onto a single physical mode,

$$\mathcal{A}[j] = A[j]_{\alpha_1 \alpha_2}^{\sigma} (a_{j,l})^{\alpha_1} (a_{j,r})^{\alpha_2} . \tag{4.79}$$

(Note the slight alterations in the ordering and normalization compared to Eq. (4.3) and Eq. (4.4). The reason being the nice form of the final result.) The map $\mathcal{A}[j]$ is such that it is fermion-parity preserving, *i.e.* $A[j]_{\alpha_1 \alpha_2}^{\sigma} = 0$ if $\sigma + \alpha_1 + \alpha_2 \bmod 2 \neq 0$. When projected back onto the virtual vacuum, this yields a fermionic MPS,

$$|\Psi(\mathbf{A})\rangle = \langle \Omega_{\text{virt}} | \prod_j \mathcal{A}[j] | \Psi_{\text{virt}} \rangle | \Omega_{\text{phys}} \rangle . \tag{4.80}$$

In this expression all factors have an even fermion parity. Hence, when they do not contain the same operators, they can be commuted. Therefore, a factor

$$\langle 0 | (a_r)^{\alpha_r} (a_l)^{\alpha_l} \left(1 + a_l^\dagger a_r^\dagger \right) | 0 \rangle = \delta_{\alpha_l \alpha_r} \quad (4.81)$$

is obtained for each virtual link in the chain, yielding

$$|\Psi(\mathbf{A})\rangle = (\dots A[1]^{\sigma_1} A[2]^{\sigma_2} \dots) \dots |\sigma_1\rangle |\sigma_2\rangle \dots \quad (4.82)$$

We can reinterpret this result as a virtual contraction,

$$|\Psi(\mathbf{A})\rangle = \mathcal{C}_{\text{virt}} \left(\prod_j \left(A[j]_{\alpha_j \gamma_j}^{\beta_j} |\alpha_j\rangle |\beta_j\rangle \langle \gamma_j| \right) \right), \quad (4.83)$$

where the contracted, \mathbb{Z}_2 -graded MPS tensors are defined and labeled as

$$\begin{array}{c} \alpha \leftarrow \boxed{A[j]} \leftarrow \gamma \\ \downarrow \\ \beta \end{array} = A[j]_{\alpha \gamma}^{\beta} |\alpha\rangle |\beta\rangle \langle \gamma|. \quad (4.84)$$

For the following, the $A[j]$ are typically chosen equal on each site, yielding a uniform fMPS for which the diagrammatic notation is given by

$$|\Psi(A)\rangle = \leftarrow \boxed{A} \leftarrow \boxed{A} \leftarrow \boxed{A} \leftarrow \boxed{A} \leftarrow \boxed{A} \leftarrow \dots \quad (4.85)$$

As each leg in this diagram corresponds to a single fermionic mode, both the virtual and physical (dual) vector spaces have dimension 2. Evidently, one could introduce more virtual modes per site, say χ , yielding a virtual space with bond dimension $D = 2^\chi$. In the same way the local, physical space can be enlarged, containing f fermionic modes and thus having a dimension $d = 2^f$. Finally, one could generalize the MPS construction even further by allowing any natural number for the bond dimension and subdividing the D basis vectors in an even (odd) subset of $D_e(D_o)$ homogeneous basis vectors with $D = D_e + D_o$. [89]

4.2.2 Gauge fixing

As is the case for their bosonic counterparts, fermionic MPS contain gauge freedom, meaning that a transformation

$$\leftarrow \boxed{A} \leftarrow \rightarrow \leftarrow \circlearrowleft \leftarrow \boxed{A} \leftarrow \circlearrowright \leftarrow \quad (4.86)$$

leaves $|\Psi(A)\rangle$ invariant for any $X = X_\beta^\alpha |\alpha\rangle \langle \beta|$ with X_β^α invertible. Using these gauge transformations, one can always bring $|\Psi(A)\rangle$ in the center-site gauge

$$|\Psi(A)\rangle = \leftarrow \boxed{A_l} \leftarrow \boxed{A_l} \leftarrow \boxed{A_c} \leftarrow \boxed{A_r} \leftarrow \boxed{A_r} \leftarrow, \quad (4.87)$$

(e.g. by subsequent QR (LQ) or polar decompositions of A) where we define the tensors $\{A_l, A_r, C, A_c\}$ by the relations

$$\begin{array}{c} \leftarrow \square A_c \leftarrow \\ \downarrow \end{array} = \begin{array}{c} \leftarrow \square A_l \leftarrow \square C \leftarrow \\ \downarrow \end{array} = \begin{array}{c} \leftarrow \square C \leftarrow \square A_r \leftarrow \\ \downarrow \end{array} \quad (4.88)$$

and the left- and right-orthonormality conditions

$$\begin{array}{c} \leftarrow \square A_l \leftarrow \\ \downarrow \end{array} = \begin{array}{c} \circlearrowleft I \circlearrowright \\ \end{array}, \quad \begin{array}{c} \leftarrow \square A_r \leftarrow \\ \downarrow \end{array} = \begin{array}{c} \circlearrowleft P \circlearrowright \\ \end{array}, \quad (4.89)$$

expressing that A_l is left-isometric from its outgoing to its incoming legs while A_r is right-isometric from its left to its physical and right leg. Indeed, Eq. (4.89) is equivalent to

$$\begin{array}{c} \leftarrow \square A_l^\dagger \leftarrow \square A_l \leftarrow \\ \downarrow \end{array} = \begin{array}{c} \circlearrowleft I \circlearrowright \\ \end{array}, \quad \begin{array}{c} \leftarrow \square A_r \leftarrow \square A_r^\dagger \leftarrow \\ \downarrow \end{array} = \begin{array}{c} \circlearrowleft I \circlearrowright \\ \end{array}, \quad (4.90)$$

showing that placing the P on the physical leg of A_r , the right fixed-point is an identity as well. However, we did not adhere to the left-right conventions of the previous Section in Eq. (4.89) (also using conjugates rather than adjoints in the bottom layer) as we intend to similarize the diagrams for fermionic and the standard bosonic tensor network methods as much as possible.

Utilizing the center-site gauge, the expectation value of a local operator, isomorphic to a two-leg tensor O , can easily be evaluated as

$$\langle \Psi(A) | O | \Psi(A) \rangle = \begin{array}{c} \leftarrow \square A_l \leftarrow \square A_l \leftarrow \square A_c \leftarrow \square A_r \leftarrow \square A_r \leftarrow \\ \downarrow \quad \downarrow \quad \downarrow \quad \downarrow \quad \downarrow \\ \rightarrow \square A_l^* \rightarrow \square A_l^* \rightarrow \square A_c^* \rightarrow \square A_r^* \rightarrow \square A_r^* \rightarrow \\ \end{array} = \begin{array}{c} \leftarrow \square A_c \leftarrow \\ \downarrow \end{array} \circlearrowleft O \circlearrowright \begin{array}{c} \circlearrowleft P \circlearrowright \\ \end{array}. \quad (4.91)$$

For the norm of a fermionic MPS, we obtain

$$\langle \Psi(A) | \Psi(A) \rangle = \begin{array}{c} \leftarrow \square A_c \leftarrow \\ \downarrow \end{array} \circlearrowleft P \circlearrowright = \begin{array}{c} \leftarrow \square C \leftarrow \\ \downarrow \end{array} \circlearrowleft P \circlearrowright,$$

such that for a normalized MPS, A_C and C are normalized to unity.

4.2.3 Tangent space

Deriving $|\Psi(A)\rangle$ w.r.t. the entries in A and taking superpositions of the result, one obtains a general tangent vector for the MPS manifold in $|\Psi(A)\rangle$,

$$|\Phi(B; A)\rangle = \sum_j \begin{array}{c} \leftarrow \square A \leftarrow \square A \leftarrow \square B \leftarrow \square A \leftarrow \square A \leftarrow \\ \downarrow \quad \downarrow \quad \downarrow \quad \downarrow \quad \downarrow \\ j \end{array}, \quad (4.92)$$

parametrized by the tensor B . Gauge transformations can be performed and absorbed in B so that a general tangent vector can equally well be expressed as

$$|\Phi(B; A)\rangle = \sum_j \leftarrow \boxed{A_l} \leftarrow \boxed{A_l} \leftarrow \boxed{B} \leftarrow \boxed{A_r} \leftarrow \boxed{A_r} \leftarrow . \quad (4.93)$$

Moreover, the multiplicative gauge invariance for A translates to an additive gauge invariance for B ,

$$\leftarrow \boxed{B} \leftarrow \rightarrow \leftarrow \boxed{B} \leftarrow \downarrow + \leftarrow \boxed{A_l} \leftarrow \circled{X} \leftarrow - \leftarrow \circled{X} \leftarrow \boxed{A_r} \leftarrow \downarrow . \quad (4.94)$$

We can remove this gauge invariance by defining canonical forms for $|\Phi(B; A)\rangle$, e.g. by imposing

$$0 = \begin{array}{c} \leftarrow \boxed{B} \leftarrow \\ \downarrow \\ \circlearrowright \end{array} \quad (4.95)$$

However, one can only impose this condition when the tangent vector is orthogonal to the MPS as it implies that

$$\langle \Psi(A) | \Phi(B; A) \rangle = |\mathbb{Z}| \begin{array}{c} \leftarrow \boxed{B} \leftarrow \\ \downarrow \\ \circlearrowright \end{array} \quad (4.96)$$

In the following we will see that, conveniently, these are the most relevant tangent vectors so that we can safely work with this gauge condition, implying that B is an element of the right null-space of A_l^* and can thus be written as

$$\leftarrow \boxed{B} \leftarrow \downarrow = \leftarrow \boxed{V_l} \leftarrow \circled{X} \leftarrow . \quad (4.97)$$

Here, V_l describes a basis for the null-space and therefore has dimension $(d-1)D$ on its incoming leg. X (*i.e.* a different X from the one we used before), on the other hand, essentially encodes a linear combination of these basis elements and thus contains the only free parameters in B . Furthermore, we orthonormalize V_l in the same way as A_l (Eq. (4.89)) so that

$$\begin{array}{c} \rightarrow \boxed{V_l^*} \rightarrow \\ \downarrow \\ \circlearrowright \end{array} + \begin{array}{c} \rightarrow \boxed{A_l^*} \rightarrow \\ \downarrow \\ \circlearrowright \end{array} = \begin{array}{c} \rightarrow \\ \downarrow \end{array} \quad (4.98)$$

due to completeness. Analogously, a right-canonical form can be derived,

$$\leftarrow \boxed{B} \leftarrow \downarrow = \leftarrow \circled{X} \leftarrow \boxed{V_r} \leftarrow \downarrow \quad (4.99)$$

where V_r encodes a basis for the left null-space of A_r^* and is normalized in the same way as A_r . When brought in this right-canonical form,

$$\begin{array}{c} \leftarrow \boxed{B} \leftarrow \\ \downarrow \\ \rightarrow \boxed{A_r^*} \rightarrow \end{array} \circled{P} = 0. \quad (4.100)$$

An important feature of the canonical form for tangent vectors is that the overlap of two such vectors can easily be computed as

$$\langle \Phi(B_2; A) | \Phi(B_1; A) \rangle = |\mathbb{Z}| \begin{array}{c} \leftarrow \boxed{B_1} \leftarrow \\ \downarrow \\ \rightarrow \boxed{B_2^*} \rightarrow \end{array} \circled{P} = |\mathbb{Z}| \begin{array}{c} \leftarrow X_1 \leftarrow \\ \downarrow \\ \rightarrow X_2^* \rightarrow \end{array} \circled{P}. \quad (4.101)$$

4.2.4 Fermionic VUMPS and TDVP algorithms

Tangent vectors can be utilized to derive the tangent space projector $P_{|\Psi(A)\rangle}$ in (and orthogonal to) a point, $|\Psi(A)\rangle$, on the MPS manifold, as explained in Appendix A.1. This operator plays a key role in establishing both the VUMPS and TDVP algorithm. For the former, application of the variational principle to the MPS manifold to find the $|\Psi(A)\rangle$ with the lowest energy for a Hamiltonian H , requires the differentiation of the energy expectation value,

$$E = \frac{\langle \Psi(A) | H | \Psi(A) \rangle}{\langle \Psi(A) | \Psi(A) \rangle}, \quad (4.102)$$

w.r.t. the variational parameters in $|\Psi(A)\rangle$ or rather w.r.t. their complex conjugates. Doing so, one obtains a Galerkin condition for the variational minimum

$$P_{|\Psi(A)\rangle} (H - E) |\Psi(A)\rangle = 0 \quad (4.103)$$

where the second term drops out as $P_{|\Psi(A)\rangle}$ projects orthogonally to $|\Psi(A)\rangle$. (Note that this is not problematic as the equation is automatically satisfied in this direction.) However, it is typically retained in order to fix divergences due to the extensive nature of H (see Appendix A.2 for more details). For TDVP, assuming that an MPS state remains on the MPS manifold through time-evolution and can therefore be described with a time-dependent tensor $A(t)$, substitution in the time-dependent Schrödinger equation yields

$$|\Phi(\dot{A}; A)\rangle = -iH |\Psi(A)\rangle. \quad (4.104)$$

Herein, the left-hand side is a tangent vector of the MPS manifold in $|\Psi(A)\rangle$ while the right-hand side is not. Nonetheless, one can approximate the latter by projecting it down on the tangent space, yielding the TDVP equation,

$$|\Phi(\dot{A}; A)\rangle = -iP_{|\Psi(A)\rangle} H |\Psi(A)\rangle. \quad (4.105)$$

Again the lack of support for $P_{|\Psi(A)\rangle}$ in the direction of $|\Psi(A)\rangle$ forms no problem as we do not want to change its norm or phase.

Both in the VUMPS and TDVP algorithm, $P_{|\Psi(A)\rangle} H |\Psi(A)\rangle$ plays an essential role. Appendix A.1 learns that this tangent vector can be written in the form of Eq. (4.93) with either

$$\begin{array}{c} \leftarrow \boxed{B} \leftarrow \\ \downarrow \\ \leftarrow \boxed{A'_c} \leftarrow \\ \downarrow \\ \leftarrow \boxed{A_l} \leftarrow \circled{C} \leftarrow \end{array} \quad (4.106)$$

i.e. the left gauge or

$$\leftarrow \boxed{B} \leftarrow = \leftarrow \boxed{A'_c} \leftarrow - \leftarrow \circlearrowleft \boxed{C} \leftarrow \boxed{A_r} \leftarrow , \quad (4.107)$$

the right gauge, where

$$\begin{aligned} \leftarrow \boxed{A'_c} \leftarrow &= \begin{array}{c} \text{---} \\ \leftarrow \boxed{A_l} \leftarrow \text{---} \boxed{A_c} \text{---} \boxed{A_r} \leftarrow \\ \text{---} \\ H \\ \text{---} \\ \leftarrow \boxed{A_l^*} \rightarrow \text{---} \text{---} \rightarrow \boxed{A_r^*} \\ \text{---} \\ P \\ \text{---} \end{array} \end{aligned} \quad (4.108)$$

and

$$\begin{aligned} \leftarrow \circlearrowleft \boxed{C'} \leftarrow &= \begin{array}{c} \text{---} \\ \leftarrow \boxed{A_l} \leftarrow \text{---} \circlearrowleft \boxed{C} \leftarrow \boxed{A_r} \leftarrow \\ \text{---} \\ H \\ \text{---} \\ \leftarrow \boxed{A_l^*} \rightarrow \text{---} \text{---} \rightarrow \boxed{A_r^*} \\ \text{---} \\ P \\ \text{---} \end{array} \end{aligned} \quad (4.109)$$

and where both choices for B are related by an additive gauge transform with $X = C'$. Note that the application of the Hamiltonian to the MPS can indeed be formulated as a simple contraction of $|\Psi(A)\rangle$ with the H tensor, isomorphic to the Hamiltonian operator, since the state only has outgoing legs. In Appendix A.2 we explain the details of how to work out these expressions if H is given by an MPO.

Once computed, A'_c and C' and hence also the expression for $P_{|\Psi(A)\rangle} H |\Psi(A)\rangle$ in terms of a B tensor can be used to express the TDVP equation as $\dot{A} = -iB$. Combining this with the Euler method, one obtains $A(t+dt) = A(t) - i dt \dot{A}$. After gauge fixing and normalization by rescaling the new $A(t+dt)$, this can be repeated for further time steps. In the VUMPS algorithm, on the other hand, we want that $|\Phi(B; A)\rangle = P_{|\Psi(A)\rangle} H |\Psi(A)\rangle = 0$ or thus $B = 0$ so that

$$\leftarrow \boxed{A'_c} \leftarrow = \leftarrow \circlearrowleft \boxed{C'} \leftarrow \boxed{A_r} \leftarrow = \leftarrow \boxed{A_l} \leftarrow \circlearrowleft \boxed{C} \leftarrow \quad (4.110)$$

while Eq. (4.88) also still applies. As the gauge transformation that relates A_l and A_r is unique up to a factor (for injective MPS), this implies that C and C' have to be proportional, resulting in the VUMPS fixed-point equations, $A'_c \propto A_c$ and $C' \propto C$, that together with the gauge-fixing conditions describe the variational minimum. After solving these, one still has to perform an SVD or polar decomposition to derive new A_l and A_r in line with the obtained A_c and C [198]. Afterwards, the same steps can be repeated until a variational minimum is obtained. More variations and extensions of this algorithm exist, e.g. the integration of unit cells [226], but will not be considered here.

4.2.5 Quasi-particle excitations

The tangent space described by Eq. (4.93) was found by taking derivatives of the translation-invariant MPS *Ansatz* w.r.t. its parameters. However, a more general tangent space can be obtained by starting from a fermionic MPS with site-dependent tensors,

$$|\Psi(\mathbf{A})\rangle = \leftarrow \boxed{A[j-1]} \leftarrow \boxed{A[j]} \leftarrow \boxed{A[j+1]} \leftarrow , \quad (4.111)$$

and differentiating it w.r.t. its parameters. In this way, one obtains the general tangent vector

$$|\Phi(\mathbf{B}; \mathbf{A})\rangle = \sum_j \leftarrow \boxed{A[j-1]} \leftarrow \boxed{B[j]} \leftarrow \boxed{A[j+1]} \leftarrow \quad (4.112)$$

with a site-dependent $B[j]$ tensor which can be used to describe non-translation-invariant excitations on top of an MPS. However, when both the Hamiltonian and its ground state are translation invariant, we can label the excited states by their momentum p and again take the A tensors to be identical. The momentum p sector of the tangent space can then be targeted by setting $B[j] = e^{ipj}B$ so that

$$|\Phi_p(B; A)\rangle = \sum_j e^{ipj} \leftarrow \boxed{A} \leftarrow \boxed{B} \leftarrow \boxed{A} \leftarrow . \quad (4.113)$$

These states can be regarded as elementary excitations on top of uniform fermionic MPS that are, in the spirit of the single-mode approximation, local perturbations in a momentum superposition. As was the case for the $p = 0$ tangent vectors in Eq. (4.93), we can absorb gauge transformations for the A tensors in B so that

$$|\Phi_p(B; A)\rangle = \sum_j e^{ipj} \leftarrow \boxed{A_l} \leftarrow \boxed{B} \leftarrow \boxed{A_r} \leftarrow . \quad (4.114)$$

This leads to an additive gauge transformation,

$$\leftarrow \boxed{B} \leftarrow \rightarrow \leftarrow \boxed{B} \leftarrow + \leftarrow \boxed{A_l} \leftarrow \circled{X} \leftarrow - e^{ip} \leftarrow \circled{X} \leftarrow \boxed{A_r} \leftarrow , \quad (4.115)$$

that can again be removed by imposing either Eq. (4.95) or Eq. (4.100), *i.e.* the left, respectively right, gauge condition for $|\Phi_p(B; A)\rangle$, resulting in identical canonical forms for the B tensor as in the $p = 0$ case (Eq. (4.97) and Eq. (4.99)). For the overlap, between two $|\Phi_p(B; A)\rangle$ states, one obtains

$$\begin{aligned} \langle \Phi_q(B_2; A) | \Phi_p(B_1; A) \rangle &= \sum_j e^{i(p-q)j} \leftarrow \boxed{A_l} \leftarrow \boxed{B_1} \leftarrow \boxed{A_r} \leftarrow \\ &\quad \rightarrow \boxed{A_l^*} \rightarrow \boxed{B_2} \rightarrow \boxed{A_r^*} \rightarrow \\ &= 2\pi\delta(p-q) \circlearrowleft \boxed{B_1} \circlearrowright \circled{P} = 2\pi\delta(p-q) \circlearrowleft \circled{X_1} \circlearrowright \circled{P} \\ &\quad \circlearrowleft \boxed{B_2^*} \circlearrowright \end{aligned} \quad (4.116)$$

where we used that only terms with B tensors on the same sites are non-zero due to the gauge condition.

In order to calculate B tensors corresponding to the elementary excitations of a certain Hamiltonian, we apply the variational principle to $|\Phi_p(B; A)\rangle$. Therefore, we differentiate the (momentum-dependent) excitation energy,

$$\omega = \frac{\langle \Phi_p(B; A) | H - E | \Phi_p(B; A) \rangle}{\langle \Phi_p(B; A) | \Phi_p(B; A) \rangle}, \quad (4.117)$$

w.r.t. the complex conjugate of the parameters in B , *i.e.* X from Eq. (4.97) or Eq. (4.99). As $|\Phi_p(B; A)\rangle$ is linear in X (and B), the numerator and denominator are quadratic in these tensors, resulting in a generalized eigenvalue problem after differentiation,

$$\frac{\partial}{\partial X} (\langle \Phi_p(B; A) |) (H - E) |\Phi_p(B; A) \rangle = \omega \frac{\partial}{\partial X} (\langle \Phi_p(B; A) |) |\Phi_p(B; A) \rangle, \quad (4.118)$$

with the same holding for differentiation w.r.t. (the conjugate) of B . Enforcing the left or right gauge, this reduces to an ordinary eigenvalue problem as the right-hand side of the equation becomes particularly easy to evaluate. To further illustrate this, we work out the eigenvalue equation for B ,

$$\sum_{jj'} e^{ip(j-j')} \frac{H - E}{\omega |Z|} = \text{circled } P \quad (4.119)$$

for a Hamiltonian with an MPO representation. Invoking translation invariance, we obtain a single sum over the separation $n = j' - j - 1$ between the j and j' index, multiplied by $|Z|$ so that this factor drops out on both sides. Finally, we make use of the fact that H is an MPO,

$$\omega \rightarrow B \leftarrow = \sum_{n=1}^{+\infty} \frac{e^{ip}}{\lambda^{n+2}} G_l \leftarrow O \leftarrow (e^{ip} E_l^r)^n \leftarrow O \leftarrow G_r + \text{circled } P \quad (4.120)$$

$$+ \sum_{n=1}^{+\infty} \frac{e^{-ip}}{\lambda^{n+2}} \begin{array}{c} \text{Diagram showing a central block } (e^{-ip} E_r^l)^n \text{ connected to } G_l \text{ and } G_r \text{ via } O \text{ and } A_l, \\ \text{with a loop } P \text{ around the central block.} \end{array} + \frac{1}{\lambda} \begin{array}{c} \text{Diagram showing a central block } B \text{ connected to } G_l \text{ and } G_r \text{ via } O, \\ \text{with a loop } P \text{ around the central block.} \end{array} .$$

Here G_l and G_r are the left and right environments as defined in Appendix A.2 (i.e. the dominant eigenvectors of E_l^l , respectively E_r^r with $\lambda = 1$ their common eigenvalue). Furthermore, E_l^l and E_r^r are the mixed transfer matrices,

$$\begin{array}{ccc} \text{Diagram: } E_r^l & = & \begin{array}{c} A_l \\ O \\ A_r^* \end{array} \\ \text{Diagram: } E_l^r & = & \begin{array}{c} A_r \\ O \\ A_l^* \end{array} \end{array} \quad \text{and} \quad \begin{array}{ccc} \text{Diagram: } E_r^r & = & \begin{array}{c} A_r \\ O \\ A_r^* \end{array} \\ \text{Diagram: } E_l^l & = & \begin{array}{c} A_l \\ O \\ A_l^* \end{array} \end{array} . \quad (4.121)$$

The geometric sums hereof in Eq. (4.120) can be expressed as a function of their respective dominant eigenvectors so that the eigenvalue equation can be solved for the excitation spectrum. Though this yields $D^2(d-1)$ solutions, only the lowest have a physical meaning. Indeed, for a given value of the momentum, one typically finds a limited number of excitations living on an isolated branch in the spectrum. All the other solutions are organized in continuous bands corresponding to scattering states. It is not expected that (all of) these states are approximated well with the quasi-particle *Ansatz*. We also note that we did not take into account additional symmetries here. However, doing so it can become necessary for B to have a non-trivial charge in order to target the lowest excitations. This is typically done by giving B an auxiliary leg with a non-trivial charge (e.g. see Sec. 4.4.2).

4.3 Uniform fermionic PEPS

Fermionic PEPS (fPEPS) represent the 2D analogue of the fermionic MPS discussed in the previous sections. Here, we explain how one constructs fermionic PEPS within the framework of \mathbb{Z}_2 -graded Hilbert spaces. Next, contraction of these tensor network is considered with the aim to calculate expectation values. We restrict the discussion to the boundary MPS (also MPS-MPO) approach used in Sec. 4.4.3 and Sec. 5.4.3. As such, the fermionic version of CTMRG will not be considered.

4.3.1 General form

The conceptual construction of a 2D fermionic PEPS strongly resembles that of the 1D fermionic MPS. To each lattice site we associate virtual, fermionic degrees of freedom but now in both spatial directions. For a simple square lattice, we thus have a pair of virtual degrees of freedom per lattice site in both the horizontal and the vertical direction. Next,

neighboring virtual fermions are brought in a maximally entangled state,

$$\begin{aligned} |\Psi_{\text{virt}}\rangle &= \prod_{e_h} \left(1 + a_{e_h,l}^\dagger a_{e_h,r}^\dagger \right) \prod_{e_v} \left(1 + a_{e_v,d}^\dagger a_{e_v,u}^\dagger \right) |\Omega_{\text{virt}}\rangle \\ &= \begin{array}{c} \text{Diagram showing two sets of four wavy lines (two horizontal, two vertical) with curly braces above and below them, connected by a central node.} \end{array}, \end{aligned} \quad (4.122)$$

after which we introduce a linear, parity-preserving map, locally projecting the four virtual modes per site onto a single physical mode,

$$\mathcal{A}[j] = A[j]_{\alpha_1 \alpha_2 \alpha_3 \alpha_4}^{\sigma} (a_{j,l})^{\alpha_1} (a_{j,d})^{\alpha_2} (a_{j,u}^\dagger)^{\sigma} (a_{j,r})^{\alpha_3} (a_{j,r})^{\alpha_4}. \quad (4.123)$$

(Note the slight alterations in ordering and normalization compared to Eq. (4.3) and Eq. (4.4).) As was the case in 1D, each virtual link amounts to a Kronecker delta connecting neighboring virtual indices so that the final result can again be reinterpreted as a contraction of local \mathbb{Z}_2 -graded tensors,

$$|\Psi(A)\rangle = \mathcal{C}_{\text{virt}} \left(\prod_j \left(A[j]_{\alpha_j \beta_j \delta_j \varepsilon_j}^{\gamma_j} |\alpha_j\rangle |\beta_j\rangle |\gamma_j\rangle \langle \delta_j| \langle \varepsilon_j| \right) \right), \quad (4.124)$$

where the fPEPS tensors are defined and labeled as

$$\begin{array}{c} \text{Diagram of a tensor } A[j] \text{ with indices } \alpha, \beta, \gamma, \delta. \text{ It has two horizontal legs } \alpha \text{ and } \beta \text{ pointing left, and two diagonal legs } \gamma \text{ and } \delta \text{ pointing up-right.} \end{array} = A[j]_{\alpha \beta \delta \varepsilon}^{\gamma} |\alpha\rangle |\beta\rangle |\gamma\rangle \langle \delta| \langle \varepsilon|. \quad (4.125)$$

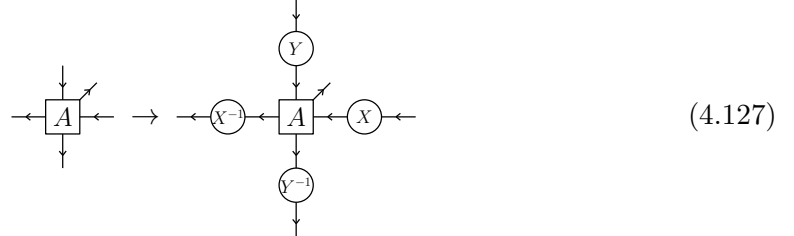
Assuming translation invariance, the fPEPS construction can thus be summarized as

$$\begin{array}{c} \text{Diagram showing a 3x3 grid of tensors } A \text{ arranged in a triangular lattice. Horizontal and vertical indices are labeled with arrows.} \end{array} |\Psi(A)\rangle = \begin{array}{c} \text{Diagram showing a 3x3 grid of tensors } A \text{ arranged in a triangular lattice. Horizontal and vertical indices are labeled with arrows.} \end{array}. \quad (4.126)$$

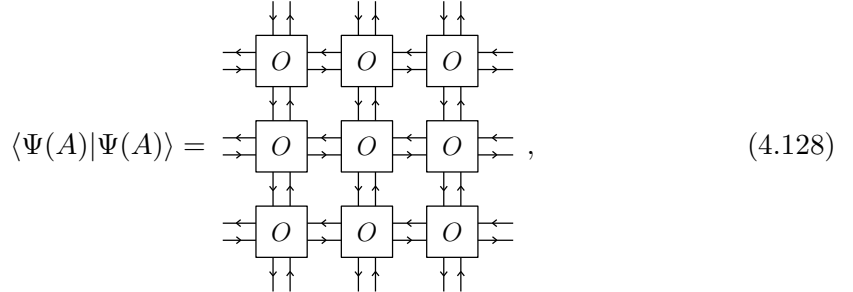
As was the case for fMPS, both the physical and virtual Hilbert spaces can be enlarged. Taking f fermions on the physical level for instance, amounts to a local Hilbert space of dimension $d = 2^f$ whereas for the virtual spaces arbitrary, natural bond dimensions D are possible, resulting in a fPEPS object living in a dD^4 -dimensional, graded Hilbert space. Also note that in the contraction of this object, fermionic minus signs due to supertraces are inevitable in contrast to what we observed in 1D for fMPS.

4.3.2 Contracting fermionic PEPS

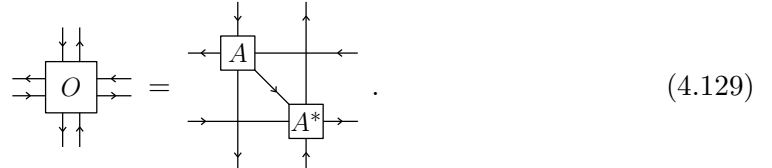
Analogous to the 1D case, fermionic PEPS have gauge freedom due to their specific virtual structure, *i.e.* an operation



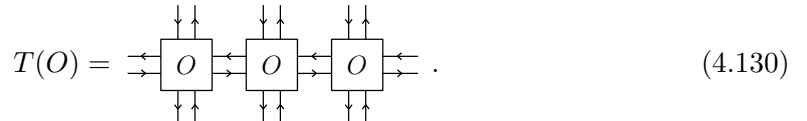
leaves the fermionic PEPS unchanged where different gauge transforms can be applied in both directions. A simple canonical form, as found in 1D, cannot be derived in two dimensions (as simple entanglement cuts cannot be performed due to the loops in the diagrams). Just like their bosonic counterparts, fermionic PEPS thus require approximate methods for their contraction. One possible approach to do so hinges on the determination of boundary MPS. We will first illustrate this for the calculation of the norm of a fermionic PEPS,



where the double-layer tensor O is defined by



Indeed, all the physical legs in $|\Psi(A)\rangle$ point outward so that no P tensors appear when taking the norm by contracting with its conjugate. In order to contract this tensor network, we calculate the leading top and bottom eigenvector (also called fixed points) of the linear transfer matrix,



Once computed, both can be contracted, yielding the norm of $|\Psi(A)\rangle$. To obtain the fixed points, we approximate them by a uniform MPS with a certain boundary bond dimension χ and with two “physical” legs instead of one. E.g. we propose

$$|\zeta(M)\rangle = \leftarrow \boxed{M} \leftarrow \boxed{M} \leftarrow \boxed{M} \leftarrow \quad (4.131)$$

for the top boundary state. The relevant eigenvalue equation then becomes

$$\begin{array}{c} \text{---} \rightarrow M \leftarrow M \leftarrow M \text{---} \\ \downarrow \uparrow \quad \downarrow \uparrow \quad \downarrow \uparrow \\ \text{---} \rightarrow O \leftarrow O \leftarrow O \text{---} \\ \downarrow \uparrow \quad \downarrow \uparrow \quad \downarrow \uparrow \\ \text{---} \end{array} = \Lambda_t \begin{array}{c} \text{---} \rightarrow M \leftarrow M \leftarrow M \text{---} \\ \downarrow \uparrow \quad \downarrow \uparrow \quad \downarrow \uparrow \\ \text{---} \end{array}. \quad (4.132)$$

Note that this is not equivalent to the equation obtained by applying the corresponding operator, $T|\zeta(M)\rangle = \Lambda_t |\Psi(M)\rangle$. Indeed, in the latter P tensors are placed on all the upward pointing legs of $|\zeta(M)\rangle$. Therefore, we redefine our transfer operator by

$$\tilde{T}(\tilde{O}) = \begin{array}{c} \text{---} \downarrow \uparrow \text{---} \downarrow \uparrow \text{---} \downarrow \uparrow \text{---} \\ \text{---} \rightarrow \tilde{O} \leftarrow \tilde{O} \leftarrow \tilde{O} \text{---} \\ \downarrow \uparrow \quad \downarrow \uparrow \quad \downarrow \uparrow \\ \text{---} \end{array} = \begin{array}{c} \text{---} \downarrow \uparrow \text{---} \downarrow \uparrow \text{---} \downarrow \uparrow \text{---} \\ \text{---} \rightarrow O \leftarrow O \leftarrow O \text{---} \\ \downarrow \uparrow \quad \downarrow \uparrow \quad \downarrow \uparrow \\ \text{---} \end{array} \quad (4.133)$$

where the circular tensors correspond to P . Application of this slightly altered operator to $|\zeta(M)\rangle$ then amounts to the desired eigenvalue equation. Similarly, the solution of the bottom fixed-point equation could be approximated by an MPS having the structure of the adjoint of $|\zeta(M)\rangle$, *i.e.*

$$\langle \zeta(N) | = \begin{array}{c} \downarrow \uparrow \text{---} \downarrow \uparrow \text{---} \downarrow \uparrow \text{---} \\ \rightarrow N^* \rightarrow N^* \rightarrow N^* \rightarrow \end{array}. \quad (4.134)$$

The appropriate eigenvalue equation then becomes $\langle \zeta(N) | \tilde{T} = \Lambda_b \langle \zeta(N) |$, corresponding to

$$\begin{array}{c} \text{---} \uparrow \text{---} \uparrow \text{---} \uparrow \text{---} \\ \text{---} \rightarrow O \leftarrow O \leftarrow O \text{---} \\ \downarrow \uparrow \quad \downarrow \uparrow \quad \downarrow \uparrow \\ \text{---} \rightarrow N^* \rightarrow N^* \rightarrow N^* \rightarrow \end{array} = \Lambda_b \begin{array}{c} \downarrow \uparrow \text{---} \downarrow \uparrow \text{---} \downarrow \uparrow \text{---} \\ \rightarrow N^* \rightarrow N^* \rightarrow N^* \rightarrow \end{array}. \quad (4.135)$$

A useful feature of these fixed-point definitions, is that the bottom eigenvalue equation can be rewritten in the form of the top equivalent. Taking the adjoint of the bottom equation, we obtain $\tilde{T}^\dagger |\zeta(N)\rangle = \overline{\Lambda_b} |\zeta(N)\rangle$, *i.e.* the top equation but now for \tilde{T}^\dagger . Indeed, $|\zeta(M)\rangle$ is the right eigenvector of \tilde{T} (as an operator) while $\langle \zeta(N) |$ is the left eigenvector. While this seems to have done the trick, writing out the resulting equation in a diagram,

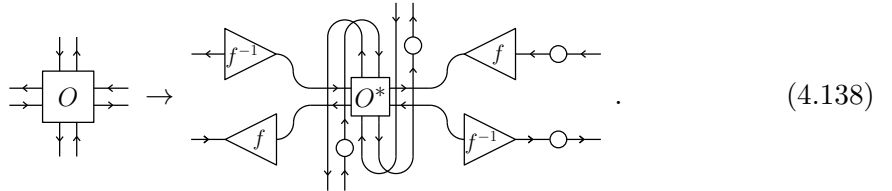
$$\begin{array}{c} \text{---} \leftarrow N \leftarrow N \leftarrow N \text{---} \leftarrow \\ \text{---} \rightarrow O^* \leftarrow O^* \leftarrow O^* \text{---} \\ \text{---} \uparrow \uparrow \quad \uparrow \uparrow \quad \uparrow \uparrow \\ \text{---} \end{array} = \overline{\Lambda_b} \begin{array}{c} \text{---} \leftarrow N \leftarrow N \leftarrow N \text{---} \leftarrow \\ \uparrow \uparrow \quad \uparrow \uparrow \quad \uparrow \uparrow \\ \text{---} \end{array}, \quad (4.136)$$

shows that this is still not formally identical to Eq. (4.132). Indeed, even though the P tensors and the twisted legs can be absorbed in the MPO tensor, the virtual arrows of this operator are still pointing in the wrong way. Therefore, we flip them by using an

arbitrary flipper, where

$$\begin{array}{c} \rightarrow f \leftarrow P \leftarrow f^{-1} \rightarrow \\ \leftarrow f^{-1} \rightarrow P \rightarrow f \leftarrow \end{array} = \begin{array}{c} \rightarrow I \rightarrow \\ \leftarrow I \leftarrow \end{array} . \quad (4.137)$$

We then conclude that the bottom fixed-point equation can be transformed to a top fixed-point equation as in Eq. (4.132) but with $M \rightarrow N$, $\Lambda_t \rightarrow \overline{\Lambda}_b$ and



With Λ_t being the dominant eigenvalue of \tilde{T} and $\overline{\Lambda_b}$ of \tilde{T}^\dagger , we also immediately have that $\Lambda_t = \Lambda_b = \Lambda$. To solve the (top) fixed-point equations for M and N , the VUMPS algorithm can be applied again but now for MPS tensors with two physical legs. This introduces some slight alterations to the method that we worked out in Appendix A.3.

After computing the fixed-points (in their center-site gauge) with the VUMPS algorithm, the norm and local expectation values of fermionic PEPS can easily be computed. For instance, sequential application of the eigenvalue equation to the overlap between the boundary states yields

$$\begin{aligned} \langle \Psi(A) | \Psi(A) \rangle &= \Lambda^{|\mathbb{Z}|} \langle \zeta(N) | \zeta(M) \rangle \\ &= \Lambda^{|\mathbb{Z}|} \quad \begin{array}{c} \xrightarrow{\hspace{-1cm}} \boxed{M_l} \xleftarrow{\hspace{-1cm}} \boxed{M_c} \xleftarrow{\hspace{-1cm}} \boxed{M_r} \xleftarrow{\hspace{-1cm}} \\ \downarrow \circlearrowleft \quad \downarrow \circlearrowleft \quad \downarrow \circlearrowleft \\ \xrightarrow{\hspace{-1cm}} \boxed{N_l^*} \xrightarrow{\hspace{-1cm}} \boxed{N_c^*} \xrightarrow{\hspace{-1cm}} \boxed{N_r^*} \xrightarrow{\hspace{-1cm}} \end{array} . \end{aligned} \quad (4.139)$$

Indeed, with every application of Eq. (4.132) or Eq. (4.135), an additional $T(O)$ layer appears, finally yielding the expression for the norm up to a (possibly infinite) factor. Essentially, this factor is equal to Λ^{N_v} with N_v the infinite number of vertical layers. Furthermore, Appendix A.3 learns that $\Lambda = \lambda^{N_h}$ with N_h the (infinite) number of sites in the horizontal direction and λ the dominant eigenvalue obtained in the determination of the environments (Eq. (A.39)). We thus obtain that $\langle \Psi(A) | \Psi(A) \rangle = \lambda^{N_h N_v} \langle \zeta(N) | \zeta(M) \rangle$. For the remaining MPS overlap, we determine left and right environments,

$$E_l \xrightarrow{\quad M_l \quad} = \mu E_l \quad \text{and} \quad E_r \xrightarrow{\quad M_r \quad} = \mu E_r \quad (4.140)$$

that we normalize as

$$E_l \xleftarrow[C_M]{\quad} E_r = 1 \quad (4.141)$$

with C_M (C_N) the canonical C tensor for the top (bottom) boundary MPS so that $\langle \Psi(A) | \Psi(A) \rangle = \lambda^{N_h N_v} \mu^{N_h}$. This shows that normalizing an arbitrary PEPS is not

straightforward. However, the calculation of local expectation values is. Indeed, consider a strictly local operator W , then

$$\langle \Psi(A) | W | \Psi(A) \rangle = \begin{array}{c} \text{Diagram showing a tensor network for } \langle \Psi(A) | W | \Psi(A) \rangle. \\ \text{The network consists of four layers of tensors labeled } O. \\ \text{Vertical indices (up and down arrows) connect the } O \text{ tensors in adjacent layers.} \\ \text{A central vertical index connects the } O \text{ tensor in the second layer to the } O_W \text{ tensor in the third layer.} \\ \text{The } O_W \text{ tensor is connected to two } O \text{ tensors in the fourth layer.} \end{array} \quad (4.142)$$

with

$$\begin{array}{c} \text{Diagram showing the definition of } O_W. \\ \text{It shows } O_W \text{ as a tensor with two horizontal indices (left and right) and one vertical index (up and down).} \\ \text{It is equated to a circuit diagram where } A \text{ (input) and } A^* \text{ (output) are connected through a } W \text{ operator.} \end{array} \quad (4.143)$$

Using the fixed points, this reduces to

$$\langle \Psi(A) | W | \Psi(A) \rangle = \lambda^{N_h(N_v-1)} \begin{array}{c} \text{Diagram showing the reduced tensor network for } \langle \Psi(A) | W | \Psi(A) \rangle. \\ \text{It shows three layers of tensors labeled } M_l, M_c, M_r \text{ (left, center, right environments).} \\ \text{Vertical indices connect } M_l \text{ to } O, O \text{ to } O_W, O_W \text{ to } O, O \text{ to } M_c, M_c \text{ to } M_r. \\ \text{Horizontal indices connect } M_l \text{ to } N_l^*, N_l^* \text{ to } N_c^*, N_c^* \text{ to } N_r^*, N_r^* \text{ to } M_r. \\ \text{Small circles indicate bond contractions between } O \text{ and } O_W, O_W \text{ and } O, \text{ and } O \text{ and } M_c. \end{array} \quad (4.144)$$

where environments can be defined as

$$\begin{array}{c} \text{Diagram showing the definition of environments } E_l \text{ and } E_r. \\ \text{It shows } E_l \text{ as a tensor with left and right indices and a central } O \text{ tensor.} \\ \text{It is equated to } \mu \text{ times a tensor with only left and right indices.} \\ \text{Similarly, } E_r \text{ is shown as a tensor with left and right indices and a central } O \text{ tensor,} \\ \text{equated to } \mu \text{ times a tensor with only left and right indices.} \end{array} \quad (4.145)$$

with

$$\begin{array}{c} \text{Diagram showing the product of environments } E_l \text{ and } E_r. \\ \text{It shows } E_l \text{ and } E_r \text{ tensors side-by-side.} \\ \text{A circle labeled } C_M \text{ is placed between them.} \\ \text{A circle labeled } C_N^* \text{ is placed below them.} \\ \text{The result is equal to 1.} \end{array} \quad (4.146)$$

so that

$$\begin{array}{c} \text{Diagram showing the final expression for } \langle \Psi(A) | W | \Psi(A) \rangle. \\ \text{It shows the same structure as equation (4.144), but with environments } E_l \text{ and } E_r \text{ instead of } M_l, M_c, M_r. \\ \text{The central } O \text{ tensor is replaced by } O_W, \text{ which is then connected to } O \text{ tensors in } E_l \text{ and } E_r. \\ \text{Small circles indicate bond contractions between } O \text{ and } O_W, O_W \text{ and } O, \text{ and } O \text{ and } N_c^*. \end{array} \quad (4.147)$$

However, as we did not explicitly normalize the PEPS, we are rather interested in

$$\frac{\langle \Psi(A) | W | \Psi(A) \rangle}{\langle \Psi(A) | \Psi(A) \rangle} \quad (4.148)$$

where the norm can also be expressed as

$$\begin{aligned} \langle \Psi(A) | \Psi(A) \rangle &= \lambda^{N_h(N_v-1)} \\ &\quad \text{Diagram: } \begin{array}{c} \text{---} \boxed{M_l} \text{---} \boxed{M_c} \text{---} \boxed{M_r} \text{---} \text{---} \\ \downarrow \quad \downarrow \quad \downarrow \quad \downarrow \\ \text{---} \boxed{O} \text{---} \boxed{O} \text{---} \boxed{O} \text{---} \text{---} \\ \downarrow \quad \downarrow \quad \downarrow \quad \downarrow \\ \text{---} \boxed{N_l^*} \text{---} \boxed{N_c^*} \text{---} \boxed{N_r^*} \text{---} \text{---} \\ \uparrow \quad \uparrow \quad \uparrow \quad \uparrow \\ \text{---} \end{array} \\ &= \lambda^{N_h(N_v-1)} \mu^{N_h} \end{aligned} \quad (4.149)$$

so that

$$\frac{\langle \Psi(A) | W | \Psi(A) \rangle}{\langle \Psi(A) | \Psi(A) \rangle} = \frac{1}{\mu} \quad \text{Diagram: } \begin{array}{c} \text{---} \boxed{M_c} \text{---} \text{---} \\ \downarrow \quad \downarrow \\ \text{---} \boxed{O_W} \text{---} \text{---} \\ \downarrow \quad \downarrow \\ \text{---} \boxed{N_c^*} \text{---} \text{---} \\ \uparrow \quad \uparrow \\ \text{---} \end{array} . \quad (4.150)$$

In this way, all the (possibly infinite) prefactors have been eliminated. We conclude that calculating local expectation values poses no problem for fermionic PEPS. Similarly, two-point correlation functions (in the horizontal and vertical direction) can be calculated efficiently in this way (see Sec. 4.4.3).

The contraction of (fermionic) PEPS becomes particularly manageable when the linear transfer operator is Hermitian. Indeed, when $\tilde{T} = \tilde{T}^\dagger$, the bottom fixed point is just the adjoint of the top fixed point and both have the same real eigenvalue. As a result only a single VUMPS run has to be performed to obtain both. Furthermore, the norm can be expressed as

$$\begin{aligned} \langle \Psi(A) | \Psi(A) \rangle &= \lambda^{N_h N_v} \langle \Psi(M) | \Psi(M) \rangle \\ &= \lambda^{N_h N_v} \quad \text{Diagram: } \begin{array}{c} \text{---} \boxed{M_l} \text{---} \boxed{M_c} \text{---} \boxed{M_r} \text{---} \text{---} \\ \downarrow \quad \downarrow \quad \downarrow \\ \text{---} \boxed{M_l^*} \text{---} \boxed{M_c^*} \text{---} \boxed{M_r^*} \text{---} \text{---} \\ \uparrow \quad \uparrow \quad \uparrow \\ \text{---} \end{array} = \lambda^{N_h N_v} . \end{aligned} \quad (4.151)$$

with $\lambda \in \mathbb{R}$ and positive so that it can be regarded as a norm per site. Hence, dividing each A tensor with $\sqrt{\lambda}$ immediately yields a normalized PEPS. This raises the question of how one can impose Hermiticity on PEPS. Using Eq. (4.138), we know that when

$$\text{Diagram: } \begin{array}{c} \text{---} \boxed{O} \text{---} \text{---} \\ \downarrow \quad \uparrow \\ \text{---} \end{array} = \begin{array}{c} \text{---} \boxed{f^{-1}} \text{---} \text{---} \\ \text{---} \boxed{O^*} \text{---} \text{---} \\ \text{---} \boxed{f} \text{---} \text{---} \\ \downarrow \quad \uparrow \\ \text{---} \end{array} . \quad (4.152)$$

\tilde{T} will be Hermitian. By splitting this equality in its top and bottom layer while also using Eq. (4.137) on the physical leg we thus get that

(4.153)

in combination with

(4.154)

represents a sufficient condition for Hermiticity. Taking the conjugate of the top equation we do retrieve the bottom, thus showing that both are compatible and that imposing Eq. (4.153), we are guaranteed to have a Hermitian \tilde{T} . Note that we restricted to unitary flippers. Indeed, for more arbitrary flippers, the top and bottom equation are not necessarily each others conjugate. To conclude, we note that using the techniques above, one could for instance calculate the energy density of a fermionic PEPS. Combining this with automatic differentiation, the gradient of the energy density can be computed, thus allowing a variational optimization of the states.

4.4 Applications

In this final Section, we discuss three applications of the fermionic TNS methods to interesting models. The first two are 1D examples and we will aim to reproduce exact results on the ground state energy as well as on the lowest excited states. While the first example for the Kitaev chain is particularly simple, the 1D Hubbard model considered thereafter is more involved and shows that fMPS can capture relevant qualitative features like spin-charge separation. Finally, the third example is a benchmark in 2D where peculiar correlation functions of Gaussian fermionic TNS (GfTNS) will be reproduced by utilizing the boundary MPS approach. These GfTNS, introduced in the next Chapter, are optimized to approximate chiral superconductors and therefore display characteristic polynomially decaying tails in their correlation functions.

4.4.1 Excitations in the 1D Kitaev chain

Consider the 1D Kitaev chain as introduced in Eq. (2.82),

$$H = - \sum_i \left(t a_i^\dagger a_{i+1} + h.c. \right) - \mu \sum_i a_i^\dagger a_i - \sum_i \left(\Delta a_i^\dagger a_{i+1}^\dagger + h.c. \right). \quad (4.155)$$

Applying a Fourier transform, we rewrite this as

$$H = \frac{1}{2} \sum_k \Upsilon_k^\dagger \begin{pmatrix} \Xi(k) & \Delta(k) \\ -\Delta(-k) & -\Xi(-k) \end{pmatrix} \Upsilon_k + \frac{1}{2} \sum_k \Xi(k) \quad (4.156)$$

with $\Xi(k) = -2t \cos k - \mu$, $\Delta(k) = -2i\Delta \sin k$ and $\Upsilon_k = \begin{pmatrix} a_k^\dagger & a_k \end{pmatrix}$ the Fourier space Nambu spinor. We will use fMPS (optimized with VUMPS) and the quasi-particle excitation *Ansatz* to find the ground state and the lowest excitations for $\Delta = t$ and $\mu = \pm t, \pm 2t, \pm 3t$, thus covering the three phases as well as the critical points in between while keeping the same superconducting term. Because this model is quadratic, it can be solved analytically by a Bogoliubov transformation $\Upsilon_k \rightarrow \tilde{\Upsilon}_k = U(k)\Upsilon_k$, yielding

$$H = \sum_k e(k) \tilde{a}_k^\dagger \tilde{a}_k + \frac{1}{2} \sum_k (\Xi(k) - e(k)) \quad (4.157)$$

with

$$e(k) = \sqrt{(2t \cos(k) + \mu)^2 + (2\Delta \sin(k))^2} \quad (4.158)$$

the positive single-particle energies. The ground state energy hence is

$$E_0 = \frac{1}{2} \sum_k (\Xi(k) - e(k)). \quad (4.159)$$

Optimizing fMPS for the selected points in the phase diagram, we already reproduce the exact ground state energy up to machine precision for $D = 10$ when the model is gapped. Evidently, one needs a higher bond dimension at the critical points but even there $D = 100$ already results in an energy density error $\sim 10^{-10}$. These minute energy errors hence show that the method is functioning correctly. At least it does for all $\mu \leq 2$. For $\mu > 2$, VUMPS becomes unstable. We can understand this by considering the limit $\mu \gg t$ where the chemical potential dominates the Hamiltonian and requires all sites to be occupied. As all tensors have to be parity-even, this forces MPS approximations to realize a substructure, *i.e.*

$$|\psi\rangle = \begin{array}{ccccccccc} & 0 & \xleftarrow{A_1} & 1 & \xleftarrow{A_2} & 0 & \xleftarrow{A_1} & 1 & \xleftarrow{A_2} & 0 \\ & \downarrow 1 & & \downarrow 1 & & \downarrow 1 & & \downarrow 1 & & \downarrow 1 \end{array} \quad (4.160)$$

or, energetically equivalent,

$$|\psi\rangle = \begin{array}{ccccccccc} & 1 & \xleftarrow{A_2} & 0 & \xleftarrow{A_1} & 1 & \xleftarrow{A_2} & 0 & \xleftarrow{A_1} & 1 \\ & \downarrow 1 & & \downarrow 1 & & \downarrow 1 & & \downarrow 1 & & \downarrow 1 \end{array} \quad (4.161)$$

In a fully translation-invariant MPS, VUMPS will gravitate towards a superposition of both, making the MPS non-injective and thus destabilizing VUMPS. To avoid this, one could work with a two-site unit cell, giving the MPS the possibility to choose between the substructures. The same phenomenon occurs (to a lesser extent) all through the trivial phase where $\mu > 2t$.

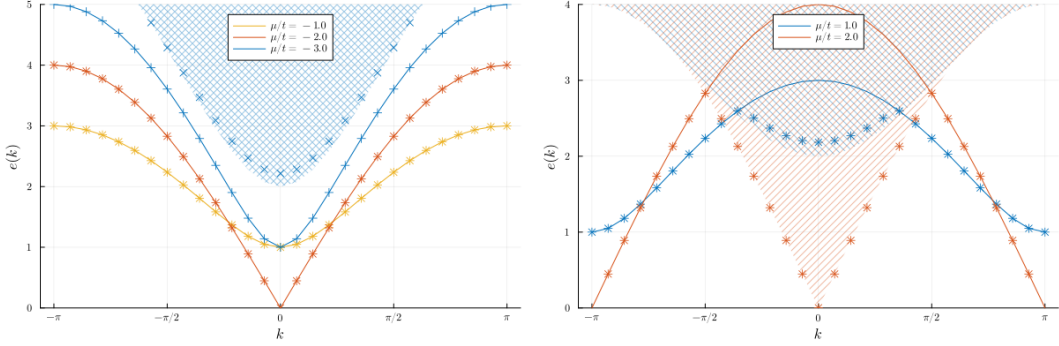


Figure 4.1: Dispersion relations for the Kitaev chain. Solid lines correspond to the exact single-particle dispersion relation (Eq. (4.157)) while $+(x)$ -sign markers display results obtained with the excitation *Ansatz* where the B tensor has a non-trivial odd (a trivial even) charge. Shaded regions depict scattering states as obtained from the exact dispersion relation. In the gapped points $D = 6$ while for the critical points $D \approx 50$.

Based on Eq. (4.157), the elementary excitations are obtained by filling one of the \tilde{a}_k fermion modes. The corresponding dispersion relations are displayed by the solid lines in Fig. 4.1 for the parameter choices requiring a single-site unit cell (*i.e.* we do not consider $\mu = 3t$ any further). These are compared to excitation energies obtained via the excitation *Ansatz*. For $\mu < t$ the reproduction is almost exact, even at the critical point, and this with modest bond dimensions. Note that in and on the boundary of the topological phase excitations with either even or odd parity yield identical results. We can understand this from [89] where the exact fMPS tensors for the Majorana chain ($\Delta = t, \mu = 0$) were shown to commute with a parity-odd matrix. By absorbing this matrix in B , we could change its parity while maintaining the energy. The same happens all through the topological phases, in line with making a choice between filling or vacating the fermion mode built up by the isolated Majorana modes at the end of an infinitely long chain. In the trivial phase, this argument does not hold anymore and therefore only the parity-odd excitations reproduce the exact dispersion relation. Parity-even excitations approximate the bottom of the two-particle scattering states continuum, displayed by the blue-shaded area. For $\mu > t$, the picture is very similar with both parities giving identical results. However, now scattering states already cut out regions of the single-particle dispersion relation. Furthermore, at the critical point $\mu/t = 2$, the MPS excitation energies at $k = \pi$ become negative, signalling the instability with respect to breaking the translation invariance down to a two-site unit cell, as explained above.

4.4.2 Spin-charge separation in the Hubbard model

As a second example we turn to the Hubbard model (Eq. (2.78)) in 1D at half-filling for $U/t = 1, 3, 10$. This interacting model can be solved exactly using the Bethe *Ansatz*, making it an ideal benchmark. Even more so because also MPS has already been applied, albeit by first using a Jordan-Wigner transformation to translate the fermions to spins [227]. Here, we apply MPS directly to the fermionic model. Note that the Hamiltonian has both global U(1) and SU(2) symmetry. Together with the fermionic superselection

sectors, the local physical space hence contains three irreps: $(0, 0, 0)$, $(0, 0, 2)$ and $(1, \frac{1}{2}, 1)$ where the elements respectively signify the fermion parity (even (0) or odd (1)), the $SU(2)$ spin charge ($S = 0$ or $S = \frac{1}{2}$) and the $U(1)$ charge (empty (0), singly occupied (1) and fully occupied (2)). However, as $U(1)$ is an Abelian symmetry, we can apply an arbitrary shift of the irreps on the physical leg. At half-filling, the most convenient choice is labeling the single occupancy with the label zero, as the ground state then has total (shifted) $U(1)$ charge zero. Consequently, the physical labels become $(0, 0, \pm 1)$ and $(1, \frac{1}{2}, 0)$. Imposing the global $\mathbb{Z}_2 \otimes SU(2) \otimes U(1)$ symmetry on the full fMPS is possible by enforcing it on all of the separate tensors. The virtual charges for each leg can then be split into two groups that do not mix due to the \mathbb{Z}_2 -grading of the physical charges, dividing $SU(2)$ into integer and half-integer irreps and $U(1)$ into even and odd irreps. As no symmetries can be broken due to the MWHC theorem, MPS again has to realize a two-site pattern. On even sites, the possible sectors are

$$\begin{array}{ccccccc} (0, 0, \pm 1) & (0, 0, \pm 3) & \dots & & (1, \frac{1}{2}, 0) & (1, \frac{1}{2}, \pm 2) & \dots \\ (0, 1, \pm 1) & (0, 1, \pm 3) & \dots & \text{and} & (1, \frac{3}{2}, 0) & (1, \frac{3}{2}, \pm 2) & \dots \\ \vdots & \vdots & \ddots & & \vdots & \vdots & \ddots \end{array} \quad (4.162)$$

while on odd sites we have

$$\begin{array}{ccccccc} (0, 0, 0) & (0, 0, \pm 2) & \dots & & (1, \frac{1}{2}, \pm 1) & (1, \frac{1}{2}, \pm 3) & \dots \\ (0, 1, 0) & (0, 1, \pm 2) & \dots & \text{and} & (1, \frac{3}{2}, \pm 1) & (1, \frac{3}{2}, \pm 3) & \dots \\ \vdots & \vdots & \ddots & & \vdots & \vdots & \ddots \end{array} \quad (4.163)$$

The energy densities obtained in this way were compared to the exact Bethe *Ansatz* results [129] and again a high precision was reached with relatively low D for all three parameter choices.

For the quasi-particle excitations, we have two options. Either the B tensor follows the two-site pattern,

$$\begin{aligned} |\Phi_p^k(B_1, B_2)\rangle = \sum_{m \text{ even}} e^{ipm} & \left(\begin{array}{ccccccccc} & & & & k & & & & \\ & m-2 & m-1 & m & m+1 & m+2 & m+3 & & \\ \leftarrow & \boxed{A_1} & \leftarrow \boxed{A_2} & \leftarrow \boxed{B_1} & \leftarrow \boxed{A_2} & \leftarrow \boxed{A_1} & \leftarrow \boxed{A_2} & \leftarrow & \\ \downarrow & & \\ & & & & & & & & \end{array} \right. \\ & + \left. \begin{array}{ccccccccc} & & & & k & & & & \\ & m-2 & m-1 & m & m+1 & m+2 & m+3 & & \\ \leftarrow & \boxed{A_1} & \leftarrow \boxed{A_2} & \leftarrow \boxed{A_1} & \leftarrow \boxed{B_2} & \leftarrow \boxed{A_1} & \leftarrow \boxed{A_2} & \leftarrow & \\ \downarrow & & \end{array} \right) \end{aligned} \quad (4.164)$$

so that the possible irreps for its auxiliary leg are given by $(0, 0, 0)$, $(1, \frac{1}{2}, \pm 1)$, ..., i.e. a trivial excitation, an electronic excitation, etc. These are all “physical” excitations in the sense that they have non-zero overlaps with physical operators (i.e. operators that are made by combinations of fermionic creation and annihilation operators) acting on the ground state. More interesting are the excitations corresponding to a B tensor that disrupts the two-site pattern,

$$|\Xi_p^k(B)\rangle = \sum_{m \text{ even}} e^{ipm} \begin{array}{ccccccccc} & & & & k & & & & \\ & m-2 & m-1 & m & m+1 & m+2 & & & \\ \leftarrow & \boxed{A_1} & \leftarrow \boxed{A_2} & \leftarrow \boxed{B} & \leftarrow \boxed{A_1} & \leftarrow \boxed{A_2} & \leftarrow & & \\ \downarrow & \downarrow & \downarrow & \downarrow & \downarrow & \downarrow & & & \end{array} , \quad (4.165)$$

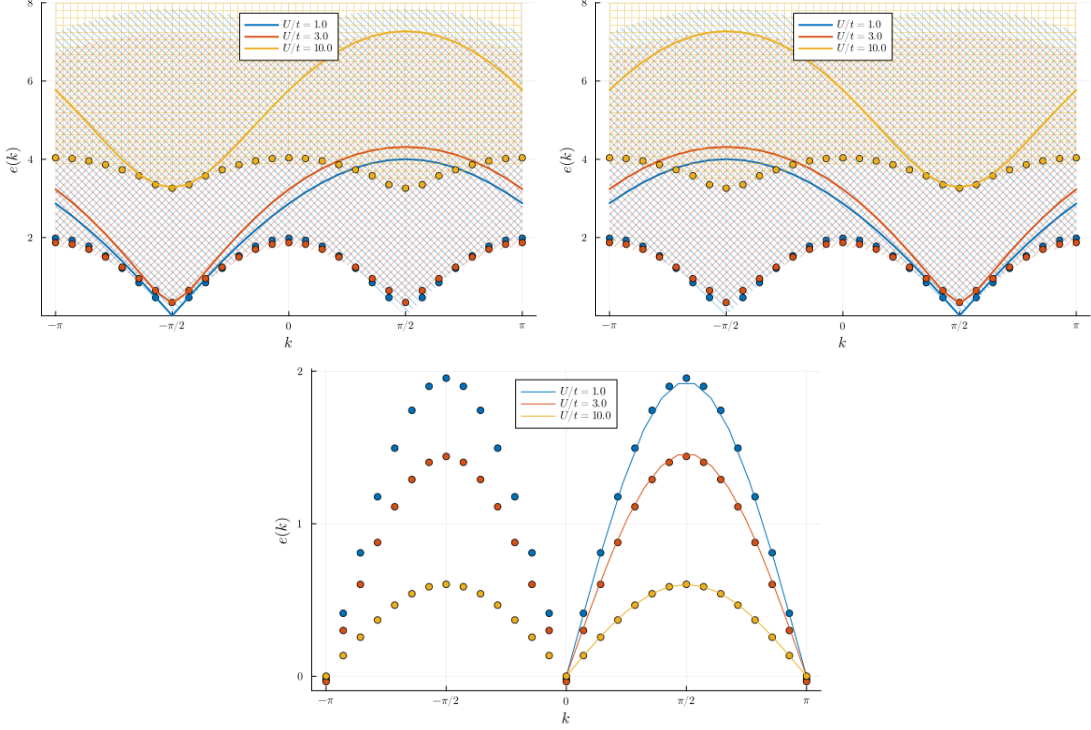


Figure 4.2: Dispersion relations for the 1D Hubbard model at half-filling. Solid lines correspond to the exact Bethe *Ansatz* dispersion relations [129] while circular markers display results obtained with the excitation *Ansatz* for holons (top left panel), anti-holons (top right panel) and spinons (bottom panel). The bond dimensions utilized for these calculations are $D = 32$ for $U/t = 10$, $D = 55$ for $U/t = 3$ and $D = 116$ for $U/t = 1$.

as the possible auxiliary irreps now are $(1, 0, \pm 1), (0, \frac{1}{2}, 0), \dots$. The former correspond to a charged particle without spin that is either a U(1) charge higher or lower than single occupancy, *i.e.* a spinless hole-like or electron-like excitation. These are the so-called holons and anti-holons (also chargons). The second possibility corresponds to a neutral particle with a spin, *i.e.* a spinon. These represent the elementary excitations, demonstrating the principle of spin-charge separation. On a quantitative level, the numerically obtained dispersion relations in Fig. 4.2 clearly reproduce the exact Bethe *Ansatz* results up to finite D effects.

4.4.3 Long-range correlations in chiral superconductors

To demonstrate the fermionic TNS methods in 2D, we reproduce the correlation functions of Gaussian fermionic TNS. More specifically, we optimize the latter for a certain model via the techniques outlined in the next Chapter, translate the resulting states back to generic fermionic PEPS (see Sec. 5.3) and then use the boundary MPS method to calculate real-space correlations. These can then be compared to analogous results calculated directly from the Gaussian state, thus serving as a benchmark. For the Hamiltonian, we consider the p-wave superconductor (Eq. (2.84)) at $\Delta/t = 1$ and $\mu/t = 2$. This is a

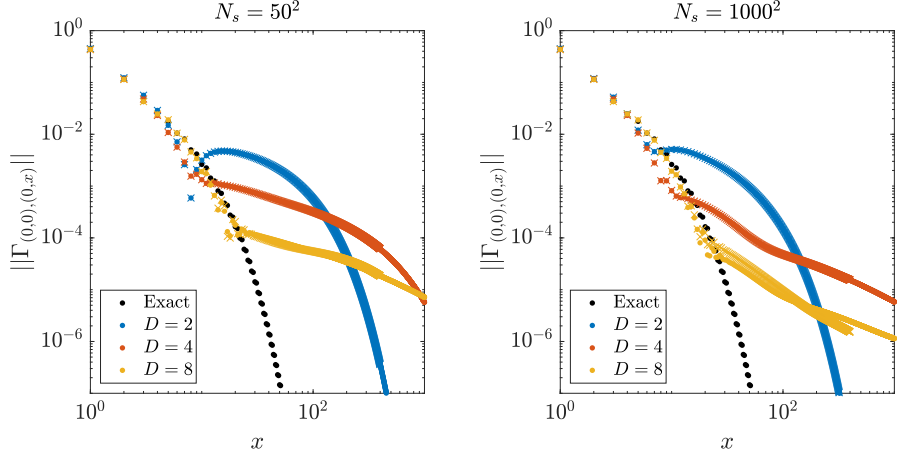


Figure 4.3: Real-space correlations (more specifically $\|\Gamma_{(0,0),(0,x)}\|$, the Frobenius norm of the real-space correlation matrix between sites $(0,0)$ and $(x,0)$) for the chiral p-wave superconductor at $\Delta/t = 1$ and $\mu/t = 2$. Exact results are compared to those for GfTNS (circular markers) optimized on small ($N_s = 50^2$, left panel) and large lattices ($N_s = 1000^2$, right panel) and with bond dimensions $D = 2, 4, 8$. The \times -sign markers correspond to analogous results obtain by applying the boundary MPS method (with $\chi = 200$) to contract the generic fTNS obtained from the optimized GfTNS.

gapped but chiral model with Majorana Chern number $C = 1$. Other studies have found that in chiral phases, variationally optimized PEPS tend to reproduce the exponentially decaying correlation functions up to a certain correlation length (regulated by the PEPS bond dimension D), after which a (possibly polynomial) long-range tail takes over [228]. Here, we observe similar features for the optimized GfTNS with polynomial tails that can be explained from the no-go theorem of Dubail and Read [217]. Indeed, Fig. 4.3 shows that if the bond dimension, D , and the finite system size, used during the GfTNS optimization, N_s , are high enough, the exact, exponentially decaying region is followed by a polynomial regime. However, Fig. 4.3 also shows that this polynomial regime is followed again by a second exponential decay. If D and N_s are too low, the polynomial region shrinks or completely disappears. If $D = 2$, for instance, the two exponential regimes immediately follow each other (independent of N_s). For $D = 4$ on the other hand, $N_s = 50^2$ results in a small polynomial regime quickly followed by the second exponential decay while $N_s = 1000^2$ results in a significantly longer polynomial tail. If $D = 8$, the second exponential region is never even probed for x ranging up to 1000. The reason behind this peculiar behavior will be explained in Sec. 5.2 by means of the no-go theorem and the specifics of the GfTNS *Ansatz*. Here, we focus on the ability of generic fTNS to reproduce the long-range correlations and find that the Gaussian results are reproduced to a good degree. Indeed, for $D = 2$ and $D = 4$ a boundary MPS with bond dimension $\chi = 200$ reproduces $\|\Gamma_{(0,0),(0,x)}\|$ (*i.e.* the Frobenius norm of the real-space correlation matrix between sites $(0,0)$ and $(x,0)$) almost perfectly. Only for the largest PEPS bond dimension, $D = 8$, $\chi = 200$ is too small to fully capture the correlations. Although boundary MPS with higher χ should be (and currently are being) computed, Fig. 4.3 already demonstrates that the fermionic PEPS methods function as desired.

Chapter 5

Gaussian fermionic tensor network methods

In this Chapter we combine the notions of a Gaussian state and a tensor network state to construct Gaussian fermionic TNS (GfTNS). We present two possible definitions and show that these are equivalent under straightforward conditions. Furthermore, we discuss the integration of global symmetries as well as variational optimization using Riemannian gradient descent. Throughout this process, we encountered some challenges, which we address by examining the underlying conceptual issues. We conclude the methodological part of this Chapter with different strategies to rephrase (symmetric) GfTNS as generic fTNS. Finally, all of these concepts are applied to critical systems, in particular those with a Fermi surface. First, we show that these Fermi surfaces do not pose intrinsic difficulties for TNS despite their violation of the area law of entanglement scaling. Next, we solidify this claim by demonstrating a finite-entanglement scaling procedure. Finally, we discuss an ongoing application where we aim to demonstrate that projected entangled pair states (PEPS) can represent Fermi surface spin liquids.

5.1 Definition

To define Gaussian fermionic tensor network states, we explore two approaches: the Kraus-Schuch (KS) method, which maximally exploits the Gaussian property and constructs the GfTNS by applying a local Gaussian map to a Gaussian state of maximally entangled pairs, and the Gu-Verstraete-Wen (GVW) construction, which primarily relies on the tensor network structure and utilizes Grassmann variables to contract local Gaussian tensors. Under mild constraint we demonstrate these to be equivalent. For concreteness, the analysis is focused on a 2D square lattice but it can be extended to more complex lattice structures.

5.1.1 Kraus-Schuch formalism

Consider the 2D square lattice built up by a periodic repetition of $N_1 \times N_2 = N_s$ unit cells, spanned by $\mathbf{a}_1 = \mathbf{e}_x$ and $\mathbf{a}_2 = \mathbf{e}_y$. To each vertex we attribute f physical fermionic orbitals with creation (annihilation) operators $a_{\mathbf{x},j}^\dagger$ ($a_{\mathbf{x},j}$) where $j = 1, \dots, f$ is the orbital index. Corresponding Majorana operators are denoted by $c_{\mathbf{x},2j-1} = a_{\mathbf{x},j}^\dagger + a_{\mathbf{x},j}$ and

$c_{\mathbf{x},2j} = -i(a_{\mathbf{x},j}^\dagger - a_{\mathbf{x},j})$. Within this framework, a PEPS *Ansatz* can be obtained by first introducing four sets of virtual fermions per site, $\{a_{\mathbf{x},i}^l\}$, $\{a_{\mathbf{x},i}^r\}$, $\{a_{\mathbf{x},i}^d\}$ and $\{a_{\mathbf{x},i}^u\}$, respectively in the left, right, down- and upward direction where for the horizontal (vertical) operators $i = 1, \dots, \frac{\chi_1}{2} (\frac{\chi_2}{2})$ (thus assuming χ_1 and χ_2 to be even). The corresponding Majoranas are $\{c_{\mathbf{x},i}^l\}$, $\{c_{\mathbf{x},i}^r\}$, $\{c_{\mathbf{x},i}^d\}$ and $\{c_{\mathbf{x},i}^u\}$ with $i = 1, \dots, \chi_1(\chi_2)$. Next, an entangled-pair state, ρ_{in} , is constructed on the virtual level by maximally entangling neighboring fermions in both directions (see Sec. 4.3.1). *I.e.* we apply the quadratic operators

$$H_{\mathbf{x},i} = \frac{1}{\sqrt{2}} \left(1 + a_{\mathbf{x},i}^{r\dagger} a_{\mathbf{x}\rightarrow,i}^l \right) \quad \text{and} \quad V_{\mathbf{x},i} = \frac{1}{\sqrt{2}} \left(1 + a_{\mathbf{x},i}^{u\dagger} a_{\mathbf{x}\uparrow,i}^d \right) \quad (5.1)$$

to the vacuum where $\mathbf{x}_\rightarrow = \mathbf{x} + \mathbf{e}_x$ and $\mathbf{x}_\uparrow = \mathbf{x} + \mathbf{e}_y$ yielding a pure and Gaussian state with

$$G_{\text{in}}(\mathbf{k}) = \begin{pmatrix} e^{ik_x} & & \\ & e^{ik_x} & \\ -e^{-ik_x} & & \\ & -e^{-ik_x} & \end{pmatrix}^{\oplus \frac{\chi_1}{2}} \oplus \begin{pmatrix} & e^{ik_y} & & \\ & & e^{ik_y} & \\ -e^{-ik_y} & & & \\ & -e^{-ik_y} & & \end{pmatrix}^{\oplus \frac{\chi_2}{2}} \quad (5.2)$$

where operators are ordered as $\{d_{\mathbf{k},1}^l, d_{\mathbf{k},1}^r, \dots, d_{\mathbf{k},\chi_1}^l, d_{\mathbf{k},\chi_1}^r, d_{\mathbf{k},1}^d, d_{\mathbf{k},1}^u, \dots, d_{\mathbf{k},\chi_2}^d, d_{\mathbf{k},\chi_2}^u\}$. The elementary building blocks herein already contain some repetition such that a more fundamental block would be

$$G(k) = \begin{pmatrix} & \pm e^{\pm ik} \\ \mp e^{\mp ik} & \end{pmatrix}. \quad (5.3)$$

Again this corresponds to a pure and Gaussian state but now consisting of maximally correlated Majorana pairs. Indeed, Eq. (5.3) corresponds to the ground state correlation matrix of the Majorana chain, *i.e.* the Kitaev chain with $t = \mp\Delta > 0$ (Eq. (2.82)). Combining two such states and performing a local Majorana rotation, we recover the blocks in Eq. (5.2). We conclude that the virtual entangled-pair state can be constructed from χ_i virtual Majorana chains in the direction of \mathbf{a}_i . When χ_i is even, a pairwise combination of these chains is equivalent to chains of entangled fermions.

In a fermionic PEPS, the maximally correlated state ρ_{in} is locally projected onto the physical level by a channel $\mathcal{E} = \bigotimes_{\mathbf{x}} \mathcal{E}_{\mathbf{x}}^{\text{loc}}$ encoding the fermionic PEPS tensor and yielding the (possibly mixed) $\rho_{\text{out}} = \mathcal{E}(\rho_{\text{in}})$. By increasing the number of virtual Majoranas, the variational freedom in \mathcal{E} can be enlarged with $D_i = \sqrt{2}^{\chi_i}$ as the effective bond dimension in the direction of \mathbf{a}_i . Since ρ_{in} is a free-fermion state, Gaussianity of the PEPS can be enforced by restricting the channel \mathcal{E} to be Gaussian as well (see Sec. 3.1). Not only can then both the input and the output state be fully described in terms of their real and antisymmetric correlation matrices, but there is also a link between both, prescribed by \mathcal{E} , in the form of a Schur complement,

$$\Gamma_{\text{out}} = A + B \left(D + \Gamma_{\text{in}}^{-1} \right)^{-1} B^T \quad (5.4)$$

If we want the GfTNS to be translation-invariant, then $\mathcal{E}_{\mathbf{x}}^{\text{loc}}$ has to be identical for all \mathbf{x} . Sec. 3.2.3 then learns that the Schur complement applies locally in Fourier space,

$$G_{\text{out}}(\mathbf{k}) = A^{\text{loc}} + B^{\text{loc}} \left(D^{\text{loc}} - G_{\text{in}}(\mathbf{k}) \right)^{-1} B^{\text{loc}T}, \quad (5.5)$$

where the purity of the input state was used to replace $G_{\text{in}}^{-1}(\mathbf{k})$ by $-G_{\text{in}}(\mathbf{k})$ and where

$$X^{\text{loc}} = \begin{pmatrix} A^{\text{loc}} & B^{\text{loc}} \\ -B^{\text{loc}T} & D^{\text{loc}} \end{pmatrix} \quad (5.6)$$

describes the local channel as in Eq. (3.48). Expressing the remaining inverse in Eq. (5.5) as the quotient of the adjugate and the determinant, one obtains that every entry of $G_{\text{out}}(\mathbf{k})$ is the quotient of trigonometric polynomials of degree $\leq 2\chi_i$ in the direction of reciprocal vector \mathbf{b}_i .

From Sec. 3.4.1 we know how symmetries and in particular U(1) and SU(2) symmetry are realized in translation-invariant Gaussian states. A natural way to enforce these on GfTNS is by starting with symmetric input states and projecting these in a symmetric way to the physical level. Therefore, we verify if the input correlation matrices have the correct substructure. For U(1) symmetry, this is certainly not the case as the elementary $G(k)$ block contains both a J and a σ_x contribution while U(1) symmetry requires only $\mathbb{1}$ and J blocks. There also does not exist a \mathbf{k} -independent, orthogonal transformation that brings the basic block in the desired form and therefore our only hope to obtain a U(1)-symmetric input state consists of enlarging the elementary block to

$$G(k) = \begin{pmatrix} & \pm e^{\pm ik} & & \\ \mp e^{\mp ik} & & & \\ & & & \pm e^{\pm ik} \\ & \mp e^{\mp ik} & & \end{pmatrix}. \quad (5.7)$$

This still does not contain the correct blocks but, as we already mentioned, now an orthogonal transformation exists,

$$R = \begin{pmatrix} 1 & & & \\ & 1 & & \\ & & 1 & \\ & & & 1 \end{pmatrix}, \quad (5.8)$$

bringing it in the desired form since $R G(k) R^T = \begin{pmatrix} & \pm e^{\pm ik} & & \\ \mp e^{\mp ik} & & & \\ & & & \pm e^{\pm ik} \\ & \mp e^{\mp ik} & & \end{pmatrix} \otimes \mathbb{1}$. I.e. working with this elementary block and thus with entangled virtual fermions rather than with maximally correlated Majorana modes, we obtain a U(1)-symmetric input state. An immediate consequence is that U(1) symmetry requires χ to be even. Similar ideas can be utilized for SU(2) symmetry where $G_{\text{in}}(\mathbf{k})$ should have a quaternionic decomposition (Eq. (3.107)). Clearly this is not possible with a single $G(k)$ block because the dimension is too small. A pair of Majorana bonds (equivalent to full virtual fermions) as in Eq. (5.7) is not sufficient either as this matrix does not have the symmetric form and cannot be orthogonally transformed in it either. The next enlargement consists of three $G(k)$ blocks. However, this would result in a spin-1 irrep and is therefore forbidden. Indeed, we want our fPEPS to be Gaussian such that operators on the physical and virtual level are only coupled quadratically, implying that modes with different irreps cannot couple. As the SU(2)-symmetric models under consideration only have physical spin- $\frac{1}{2}$ fermions, a spin-1 irrep on the virtual level is precluded. Consequently, we have to resort to a combination

of four $G(k)$ blocks, corresponding to entangled pairs of virtual spin- $\frac{1}{2}$ fermions. Note that is indeed enough as this correlation matrix can be orthogonally transformed, e.g. by

$$R = \begin{pmatrix} & & & -1 \\ 1 & & & -1 \\ & 1 & & \\ & & 1 & \\ & & & 1 \\ & 1 & & \\ & & 1 & \\ & & & 1 \end{pmatrix}, \quad (5.9)$$

to the manifestly symmetric form, yielding

$$G_{\text{in}}(\mathbf{k}) = \left(\begin{pmatrix} e^{-ik_x} \\ e^{ik_x} \end{pmatrix} \otimes J \otimes \sigma_x \right)^{\oplus \frac{\chi_1}{4}} \oplus \left(\begin{pmatrix} e^{-ik_y} \\ e^{ik_y} \end{pmatrix} \otimes J \otimes \sigma_x \right)^{\oplus \frac{\chi_2}{4}}. \quad (5.10)$$

where the χ_i now have to be quadruples.

Once we have the manifestly symmetric $G_{\text{in}}(\mathbf{k})$, we can enforce the same symmetry on the GfTNS by requiring the channel correlation matrix, X^{loc} , to be manifestly symmetric as well. *I.e.* for U(1), X^{loc} should have complex structure and thus $X^{\text{loc}} \cong X^{\mathbb{C}} = X^0 + iX^1$ with $X^{\mathbb{C}} = -X^{\mathbb{C}\dagger}$ and $X^{\mathbb{C}}X^{\mathbb{C}\dagger} \leq \mathbb{1}$. For SU(2) symmetry on the other hand, we require X^{loc} to have a quaternionic structure with $X^{\text{loc}} \cong X^{\mathbb{H}} = X^0 + iX^1 + jX^2 + kX^3$ with $X^{\mathbb{H}} = -X^{\mathbb{H}\dagger}$ and $X^{\mathbb{H}}X^{\mathbb{H}\dagger} \leq \mathbb{1}$. Now that the structure of the parametric manifold is clear, we can utilize the formulas obtained in Chapter 3 to express a cost function, e.g. the (free) energy, in terms of these parameters. Also the gradient can be calculated analytically. We combined these in an efficient variational Riemannian optimization algorithm that is discussed in more detail in the Supplemental Material of Sec. 5.4.1 and Sec. 5.4.2 (Appendix C).

5.1.2 Gu-Verstraete-Wen formalism

The Gu-Verstraete-Wen (GVW) construction [215] represents an alternative to the Kraus-Schuch formalism and contracts local Gaussian tensors to construct the GfTNS. To define the local building blocks, one replaces the virtual modes by independent Grassmann variables $\theta_{\mathbf{x},i}^h, \bar{\theta}_{\mathbf{x},i}^h, \theta_{\mathbf{x},i}^v$ and $\bar{\theta}_{\mathbf{x},i}^v$, respectively in the left, right, down- and upward direction and with $i = 1, \dots, \frac{\chi}{2}$ (hence assuming $\chi_1 = \chi_2 = \chi$, all even). As we explained in Chapter 3, the Grassmann variables are mutually anti-commuting and square to zero. Moreover, we make them anti-commute with the physical creation operators $a_{\mathbf{x},j}^\dagger$. The Gaussian fermionic tensor at site \mathbf{x} is then defined by

$$T_{\mathbf{x}} = \exp \left(\frac{1}{2} \zeta_{\mathbf{x}}^T A \zeta_{\mathbf{x}} \right), \quad (5.11)$$

where A is a $(f + 2\chi) \times (f + 2\chi)$ anti-symmetric matrix containing the variational parameters, and $\zeta_{\mathbf{x}} \equiv (a_{\mathbf{x}}^{\dagger T}, \theta_{\mathbf{x}}^{h T}, \bar{\theta}_{\mathbf{x}}^{h T}, \theta_{\mathbf{x}}^{v T}, \bar{\theta}_{\mathbf{x}}^{v T})^T$ is a $(f + 2\chi)$ -dimensional vector of the creation operators and virtual Grassmann variables assigned to site \mathbf{x} . Note that in Eq. (5.11) we have taken A to be independent of \mathbf{x} , which means that we are restricting ourselves to

translation-invariant states. With the definition of the tensors in place, we can now define the (unnormalized) contracted fermionic tensor network state via the following Berezin integral,

$$|\psi\rangle = \int [D\theta] \int [D\bar{\theta}] \prod_{\mathbf{x}} e^{\bar{\theta}_{\mathbf{x}}^h T \theta_{\mathbf{x}+e_x}^h} e^{\bar{\theta}_{\mathbf{x}}^v T \theta_{\mathbf{x}+e_y}^v} T_{\mathbf{x}} |0\rangle. \quad (5.12)$$

While this may all seem cryptic, it is easy to show that $\mathcal{G}(M)$, the Grassmann algebra of M Grassmann variables, is isomorphic to a super vector space of dimension 2^M and thus to the Clifford algebra of M fermionic creation and annihilation operators. To illustrate how this isomorphism works, consider the case of a single Grassmann number θ . To every monomial we associate a basis state of the super vector space as follows,

$$\theta^n \cong |n\rangle, \quad n \in \{0, 1\}. \quad (5.13)$$

The dual space is isomorphic to polynomials of another Grassmann number $\bar{\theta}$,

$$\bar{\theta}^n \cong \langle n|, \quad n \in \{0, 1\}. \quad (5.14)$$

The evaluation/contraction map is then given by the following Berezin integral,

$$\mathcal{C} : \langle n| \otimes |m\rangle \cong \bar{\theta}^n \theta^m \rightarrow \int d\theta \int d\bar{\theta} e^{\bar{\theta}\theta} \bar{\theta}^n \theta^m = \langle n|m\rangle = \delta_{nm}. \quad (5.15)$$

This mapping of monomials of Grassmann numbers to basis states of a super vector space generalizes straightforwardly to the case with more than one Grassmann number. Keeping this in mind, we can interpret the definition of the local tensor in Eq. (5.11) as a coherent state (see Eq. (3.3)) that couples the f physical fermions to 2χ virtual fermions. The Berezin integral on the other hand, performs the contraction of these local coherent states by means of the $e^{\bar{\theta}_{\mathbf{x}} \theta_{\mathbf{x}+e_x/y}}$ factors. In essence, the GVW construction thus comes down to a contraction of local, coherent states, hence making $|\psi\rangle$ Gaussian. Note that the bond dimension of the GfTNS is $D = 2^{\frac{\chi}{2}}$, where, as stated earlier, χ is even in the GVW construction. Hence, the virtual Grassmann numbers correspond to full fermions (as apposed to the possibility of entangled Majorana modes in the KS formalism).

Because we are considering TI states, the Gaussian Grassmann integral in Eq. (5.12) can be simplified further by going to momentum space. Defining $\zeta_{\mathbf{k}} = \frac{1}{\sqrt{N_s}} \sum_{\mathbf{x}} e^{i\mathbf{k}\cdot\mathbf{x}} \zeta_{\mathbf{x}}$, we can write

$$|\psi\rangle = \int [D\theta] \int [D\bar{\theta}] \exp \left(\frac{1}{2} \sum_{\mathbf{k}} \zeta_{-\mathbf{k}}^T [A + M(\mathbf{k})] \zeta_{\mathbf{k}} \right) |0\rangle.$$

Here, $M(\mathbf{k})$ is defined as $M(\mathbf{k}) = 0_f \oplus \tilde{M}(\mathbf{k})$, with 0_f a $f \times f$ zero matrix, and

$$\tilde{M}(\mathbf{k}) = \begin{pmatrix} 0_{\frac{\chi}{2}} & -e^{ik_x} \mathbb{1}_{\frac{\chi}{2}} \\ e^{-ik_x} \mathbb{1}_{\frac{\chi}{2}} & 0_{\frac{\chi}{2}} \end{pmatrix} \oplus \begin{pmatrix} 0_{\frac{\chi}{2}} & -e^{ik_y} \mathbb{1}_{\frac{\chi}{2}} \\ e^{-ik_y} \mathbb{1}_{\frac{\chi}{2}} & 0_{\frac{\chi}{2}} \end{pmatrix}. \quad (5.16)$$

From Eq. (5.1.2) we understand why working with Grassmann variables is beneficial. Indeed, writing $A = \begin{pmatrix} B & -C^T \\ C & D \end{pmatrix}$, with $f \times f$ submatrix B , $2\chi \times f$ submatrix C , and $2\chi \times 2\chi$ submatrix D , we can use the integrals in Eq. (3.38) to obtain

$$|\psi\rangle \propto e^{\frac{1}{2} \sum_{\mathbf{k}} a_{-\mathbf{k}}^\dagger (B + C^T [D + \tilde{M}(\mathbf{k})]^{-1} C) a_{\mathbf{k}}^\dagger} |0\rangle. \quad (5.17)$$

Here, we have assumed that $D + \tilde{M}(\mathbf{k})$ is non-degenerate at every \mathbf{k} and refer to the next Section for the degenerate case. Note that $|\psi\rangle$ takes the form of a general BCS pairing state with pairing function

$$g(\mathbf{k}) = (B + C^T [D + \tilde{M}(\mathbf{k})]^{-1} C). \quad (5.18)$$

As a result, symmetries can be implemented quite easily. Indeed, by imposing the same restrictions on $g(\mathbf{k})$ as on the pairing term expectation values we immediately implement a global symmetry on $|\psi\rangle$. SU(2) symmetry, for instance, is enforced by demanding the pairing function to decompose as $\dots \otimes J$ such that also A has to decompose in this way. On the other hand, imposing U(1) requires $g(\mathbf{k})$ to be zero yielding $|\psi\rangle = |0\rangle$. Indeed, due to its pairing form, particle number fluctuations in $|\psi\rangle$ only fully disappear in the GVW formalism when the state becomes trivial.

The relatively simple expression for the GfTNS in Eq. (5.17) allows to express cost functions and their analytical gradient in terms of the variational parameters in the complex, anti-symmetric A (see Sec. 3.3). With these expressions, a gradient descent can again be performed to optimize the GVW states for a certain Hamiltonian. For more details we refer the reader to the Supplemental Material in Sec. 5.4.2 (Appendix B). There, we also discuss a procedure to fix a gauge on the virtual legs in the GfTNS Ansatz. This becomes important when the optimization process is pushed to very high bond dimensions. We did this in Sec. 5.4.2 (Appendix E) to verify the results in [229] for our more general Gaussian *Ansatz*. Like Franco-Rubio *et al.* we noticed that a power-law improvement of the energy precision cannot be sustained in GfMPS approximations of critical states. This is due to their suboptimal use of the bond dimension. This feature has some repercussions on results in Sec. 5.4.1. Hence we refer the reader to this Section for more details.

Having introduced both the KS and the GVW formalism for GfTNS, we ask ourselves the question how they are related. It should be noted that in general the KS formalism is broader as it can deal with mixed states, as it can attribute non-trivial charges to local tensors and as it incorporates effective bond dimensions that are half-integer powers of 2. However, if one requires the KS states to exhibit any of these exotic features it is equivalent to the GVW formalism. We explain this in more detail in Sec. 5.4.2 (Appendix H).

5.2 No-go theorem and parity obstructions

The integration of Gaussian features into TNS simplifies both their numerical and conceptual analysis. However, this simplification also comes at a cost as the combination of constraints eliminates possible realizations of topological behavior. This is the subject of the no-go theorem of Dubail and Read for Gaussian fermionic TNS. In [217] they show that a GfTNS cannot realize topologically non-trivial behavior (for instance in the form of a non-zero Chern number) unless the state becomes singular. Reverting to Eq. (5.5) and Eq. (5.18), these singularities manifest themselves as zeros in the determinants of $D - G_{\text{in}}(\mathbf{k})$ (where we dropped the superscript), respectively, $D + \tilde{M}(\mathbf{k})$. Hence, if we require the GfTNS to be regular (as typically happens during numerical optimization), they will be unable to realize a non-zero Chern number. We can rephrase (a part of)

this no-go theorem in the form of a more tangible parity obstruction. Consider therefore an arbitrary pure Gaussian state. As its real-space correlation matrix is real valued, its Fourier transformed correlation matrix necessarily has the property that $G(-\mathbf{k}) = \overline{G(\mathbf{k})}$. This implies that $G(\mathbf{k})$ is real and anti-symmetric in points where $\mathbf{k} = -\mathbf{k}$ (the TRIMs). These $G(\mathbf{k})$ can thus be interpreted as ordinary, pure correlation matrices with a definite parity,

$$\langle P_{\mathbf{k}} \rangle = \text{Pf}(G(\mathbf{k})) = \langle (-1)^{\sum_j a_{\mathbf{k},j}^\dagger a_{\mathbf{k},j}} \rangle. \quad (5.19)$$

Any pure Gaussian state hence has a specific TRIM parity configuration. E.g. $|\psi_{\text{in}}\rangle$ with $G_{\text{in}}(\mathbf{k})$ built up from repetitions of the basic block in Eq. (5.3) (where we choose the + sign) amounts to $\langle P_{\mathbf{k}} \rangle_{\text{in}} = \text{Pf}(G_{\text{in}}(\mathbf{k})) = (e^{i\mathbf{k}\cdot\mathbf{a}_1})^{\chi_1} (e^{i\mathbf{k}\cdot\mathbf{a}_2})^{\chi_2}$ so that the center of the Brillouin zone always has an even parity, $\langle P_0 \rangle_{\text{in}} = 1$, while for the other TRIMs $\langle P_{\frac{\mathbf{b}_i}{2}} \rangle_{\text{in}} = (-1)^{\chi_i}$ and $\langle P_{\frac{\mathbf{b}_1+\mathbf{b}_2}{2}} \rangle_{\text{in}} = (-1)^{\chi_1+\chi_2}$. A $\frac{\mathbf{b}_i}{2}$ jump in Fourier space thus corresponds to an extra factor $(-1)^{\chi_i}$. Remarkably, this virtual parity configuration is lifted to the physical level by the Gaussian channel \mathcal{E} . Indeed, in order for the full pure GfTNS *Ansatz* to have a fixed global parity, the projectors from the virtual to the physical level (*i.e.* the Kraus operators of $\mathcal{E}_{\mathbf{x}}^{\text{loc}}$) are designed to be parity conserving (changing). Combining this with their local and translation-invariant nature, GfTNS have the same (opposite) parity configuration as the input state, unless they are singular (for a rigorous proof, see Appendix B). We conclude that pure, regular GfTNS can only realize $2^d \times 2$ (even/odd χ_i in each direction and parity conserving or changing \mathcal{E}) parity configurations while for an arbitrary, pure Gaussian state, there are 2^{2^d} possible configurations. Certain parity configurations thus cannot be reached by GfTNS in spatial dimensions, d , larger than 1. Combining this with the relation between TRIM parities and the Majorana Chern number in Eq. (3.172), we observe that exactly those TRIM parity configurations that yield odd (and thus non-zero) Majorana Chern numbers are obstructed for regular GfTNS. *I.e.* at least for odd C , the no-go theorem can be rephrased as a parity obstruction.

An interesting aspect of the no-go theorem is that it does not exclude topological phases altogether but rather restricts them to singular GfTNS. Now, one could ask if a singular GfTNS is even possible with a finite bond dimension and if so, if it gives a non-zero C . In this regard, the work of Wahl *et al.*[176] is relevant as they demonstrate that already for $D = 2$ a whole one-parameter family of GfPEPS exists that do exactly this. Furthermore, they show that the non-analyticity in Fourier spaces induces polynomially decaying correlations in real space, already explaining Fig. 4.3 to some extent. When C is odd and the no-go theorem induces a parity obstruction, the singularity should also relieve this obstruction. This happens by realizing the non-analyticity exactly in the problematic TRIM(s). The determinant of $D - G_{\text{in}}(\mathbf{k})$ (or equivalently $D + \tilde{M}(\mathbf{k})$) then becomes zero but the same happens for the numerator, so that the state can realize an unconventional parity at the TRIM. As we describe in Sec. 5.4.2 (Appendix A) this can cause a purely virtual symmetry, also observed in [177]. For even Majorana Chern numbers, there is no parity obstruction. Therefore, the singular point(s) required by the no-go theorem can be situated anywhere in the Brillouin zone in $\pm\mathbf{k}$ pairs.

Now that we understand the no-go theorem as well as the corresponding parity obstructions, we can explain how these influence numerical optimization of GfTNS within topological phases as well as on the critical lines separating them. In general, these op-

timizations are performed starting from a random initial guess and without imposing singular behavior via additional constraints. As a result, GfTNS will never become truly singular (as this requires fine-tuning of the aforementioned determinants) and can neither realize true chirality. However, they can realize chirality in an approximate way. Indeed, as we describe in Sec. 5.4.2 (Appendix F), the GfTNS will decrease the determinants upon optimization resulting in a near-singular state. Considering the chirality we show that the trivial $C = 0$ is realized by compensating the Berry curvature generated all through the Brillouin zone in a very small region around the problematic TRIM(s). In this way the state is never truly chiral but only due to a very small region in \mathbf{k} space. In real space, this results in polynomial decay of correlations up to certain (large) length scale. Moreover, the compensating region in \mathbf{k} space is found to shrink by increasing the bond dimension as well as the finite system size N_s used during the GfTNS optimization¹. Indeed, a higher N_s samples more points close to the problematic TRIM(s) so that the cost function tries to shrink this region further. In real space we thus expect polynomial tails up to some finite length scale after which a standard exponential decay takes over. By increasing N_s and D this length scale should increase. All of these features can be confirmed for the chiral p-wave superconductor in Fig. 4.3.

5.3 Reformulation as generic fTNS

Although they are Gaussian and parametrized in terms of the parametric X (KS) or A (GVW) matrices, GfTNS remain TNS and should therefore have a \mathbb{Z}_2 -graded representation. To obtain this reformulation of GfTNS as generic TNS, there exist multiple strategies. First, we will touch upon a top-down approach where a closed expression relates the generic tensor entries to the parametric matrices. Afterwards we consider a more general bottom-up method where the Gaussian correlation matrix is brought in a canonical form leading to small blocks with corresponding tensors that in the end contract to the full generic tensor. The former have the advantage of being computationally superior while the latter give more conceptual insight and can deal with some special cases.

5.3.1 Pfaffian formulas (the top-down approach)

Consider a general fermionic, coherent state in the Grassmann formalism,

$$T = \exp\left(\frac{1}{2}\zeta^T A \zeta\right), \quad (5.20)$$

i.e. a Gaussian tensor as in Eq. (5.11) with Grassmann variables θ_i collected in ζ . Expanding the exponential, we can write the tensor as

$$T = \sum_{\{n_i\}=0}^1 T_{n_1, n_2, \dots, n_N} \theta_1^{n_1} \theta_2^{n_2} \dots \theta_N^{n_N}. \quad (5.21)$$

where T_{n_1, n_2, \dots, n_N} are the tensor entries due to the isomorphism in Eq. (5.13) and its straightforward extensions. Given a bit string of n_i 's, the corresponding tensor element

¹One has to use finite lattices with (anti-)periodic boundary conditions as continuous integrals over the Brillouin zone (e.g. to compute the energy density of a GfTNS) cannot be performed analytically for $d > 1$

can be obtained as follows: take the expansion in Eq. (5.21), take all Grassmann variables for which $n_i = 0$ and put them equal to zero by hand, and integrate over those Grassmann variables for which $n_i = 1$. We now apply the same procedure to the exponential expression in Eq. (5.20). This gives

$$T_{\{n_i\}} = \prod_{i:n_i=1} \int d\theta_i \exp \left(\frac{1}{2} \zeta_{\{n_i\}}^T A[n_i] \zeta_{\{n_i\}} \right), \quad (5.22)$$

where the product over integrals is descending order, and $\zeta_{\{n_i\}}$ is the vector of Grassmann variables for which $n_i = 1$, and $A[n_i]$ is the corresponding submatrix of A where only the rows and columns are kept corresponding to the Grassmann variables with $n_i = 1$. The remaining integral can be calculated using Eq. (3.38) so that

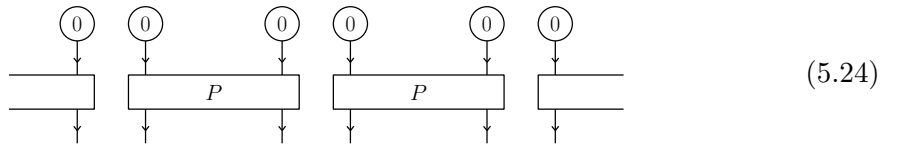
$$T_{\{n_i\}} = \text{Pf}(A[n_i]). \quad (5.23)$$

With this formula, the local tensors in the GVW formalism can thus be rephrased by \mathbb{Z}_2 -graded equivalents. Note that this immediately restricts the method to pure GFTNS with even-parity tensors, where the bond dimension is an integer power of two. A slight generalization exists [230] making use of the Bloch-Messiah decomposition for fermionic Bogoliubov transformations [231], allowing for local tensors with non-trivial parities. Furthermore, the interplay with other symmetry groups also complicates the method. Indeed, when the GFTNS is required to have an additional global symmetry (e.g. as in Sec. 5.4.3), tensor entries are typically not stored as a full tensor according to some basis, but rather in smaller non-zero blocks, corresponding to certain combinations of irreps on each of the tensor legs [225, 223]. Together with non-trivial prefactors hailing from the corresponding Clebsch-Gordan coefficients (or 6j-symbols), this necessitates combining and/or rescaling the Pfaffians from Eq. (5.23) before storing them. Moreover, the presence of a non-trivial charge for the local tensor complicates this even further. However, a symmetry-consistent extension of Eq. (5.23) should be possible and we are currently working on its development.

5.3.2 Channel decomposition (the bottom-up approach)

A more conceptually transparent alternative for the top-down method, is obtained by representing both the input state and the local channel in the KS formalism by means of elementary \mathbb{Z}_2 -graded tensors. Constructing the complete local tensor then comes down to contracting these ingredients. Moreover, global symmetries can easily be integrated by already making the elementary tensors symmetric.

A \mathbb{Z}_2 -graded representation of the input state is not hard to come by. Indeed, consider for instance a chain of entangled pairs of virtual fermions as in Eq. (4.78). Equivalently, this state can be obtained by contracting



where 0 corresponds the vacuum of the corresponding virtual mode while

$$\begin{array}{c} \downarrow \\ \boxed{P} \\ \downarrow \end{array} = \begin{array}{c} \downarrow \\ | \\ \downarrow \end{array} + \begin{array}{c} \downarrow \\ \boxed{a^\dagger} \xleftarrow{\quad} \boxed{a^\dagger} \\ \downarrow \end{array} . \quad (5.25)$$

The tensors corresponding to creation and annihilation operators are parity-odd and therefore require an odd auxiliary leg so that we can define

$$\begin{array}{c} \downarrow \\ \boxed{a^\dagger} \\ \downarrow \\ 1 \end{array} \leftarrow_3 = |1\rangle_1 \langle 0|_2 \langle 1|_3 \quad \begin{array}{c} \downarrow \\ \boxed{a^\dagger} \\ \downarrow \\ 1 \end{array} \leftarrow_1 = |1\rangle_1 |1\rangle_2 \langle 0|_3 . \quad (5.26)$$

We can then apply an SVD decomposition to the P operators so that by contracting the square-root of S with U (V) to yield L (R), we arrive at

(5.27)

As a result the entangled-pair state can be rephrased as a fMPS with local tensor

$$\xrightarrow{A_{in}} = \xrightarrow{R} \xrightarrow{L} . \quad (5.28)$$

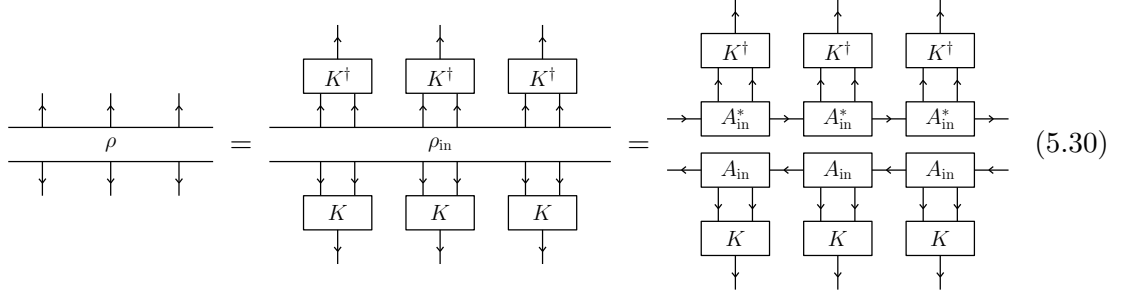
A general input state with an even number of virtual Majoranas can hence be constructed by a tensor product of these fMPS. For an odd χ_i , on the other hand, the input state is a Majorana chain. Also for these states, one can derive an exact fMPS description, again with $D = 2$ [89]. Combining two such Majorana chains one can reduce the $D = 4$ bond dimension back to $D = 2$ recovering the A_{in} from Eq. (5.28). One can also incorporate symmetries. E.g. attributing (shifted) U(1) labels to the even and odd basis states in Eq. (5.28), one can equally well regard this as a manifestly U(1)-symmetric fMPS. Following a similar procedures for entangled virtual singlets in the case of spinful fermions, the elementary blocks for SU(2)-symmetric input states (see Eq. (5.10)) can also be translated to a manifestly SU(2)-symmetric fMPS with $D = 4$.

Next up is the translation-invariant Gaussian channel \mathcal{E} from ρ_{in} to ρ . The local version of this channel, \mathcal{E}^{loc} , converts operators from $\mathcal{C}(2\chi)$, where $\chi = \sum_i \chi_i$, to $\mathcal{C}(2f)$. Indeed, the physical Clifford algebra contains f fermionic modes and thus $2f$ Majoranas. On the other hand, the virtual Clifford algebra has $2\chi_i$ Majoranas (χ_i on each side) in the direction of \mathbf{a}_i , resulting in an even, total amount of 2χ . If we assume the GfTNS to be pure, \mathcal{E} , as well as its local version, have only one Kraus operator such that $\mathcal{E}^{\text{loc}}(Z) = KZK^\dagger$ for all $Z \in \mathcal{C}(2\chi)$ and with K the linear Kraus operator from the local virtual to the local physical Hilbert space. With Eq. (3.48) we can calculate the left-hand side of this operator equality for the 2χ local Majoranas and their homogeneous combinations. Equating the result with KZK^\dagger , one obtains a system of equations that relates the local

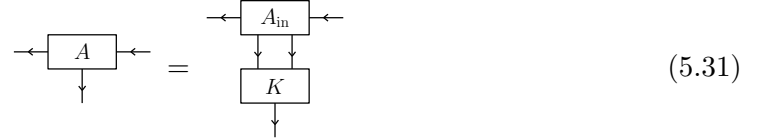
projector K to the channel correlation matrix X and thus to the variational parameters. Solving this system we can reinterpret the Kraus operator as a generic \mathbb{Z}_2 -graded tensor, e.g.



for $f = 1$ physical fermion and $\chi = 2$ virtual Majorana modes (here in 1D). We then obtain



such that the local \mathbb{Z}_2 -graded tensor can be obtained by contracting the K tensor with the input state fMPS,



This process can readily be extended to arbitrary f and χ and to higher spatial dimensions.

Directly solving the equations relating K to X is typically not the smartest way to continue. More elegantly, one can perform an SVD-like decomposition of \mathcal{E}^{loc} into a purely virtual rotation, $\mathcal{E}^{\text{rot,v}}$, a canonical projection \mathcal{E}^{can} and a physical rotation $\mathcal{E}^{\text{rot,p}}$. For each of these channels, the corresponding Kraus operators (as well as their \mathbb{Z}_2 -graded tensors) can be determined relatively easily. Let us, in order to understand this, first consider the channel correlation matrices for the virtual and physical rotations as determined in Sec. 3.2.2,

$$M^{\text{rot,v}} = \begin{pmatrix} R^{\text{v}T} \\ -R^{\text{v}} \end{pmatrix} \quad M^{\text{rot,p}} = \begin{pmatrix} R^{\text{p}T} \\ -R^{\text{p}} \end{pmatrix} \quad (5.32)$$

with $R^{\text{v}} \in SO(2\chi)$ and $R^{\text{p}} \in SO(2f)$. The effect of these rotation on the correlation matrix, Γ , of a Gaussian state defined for their respective modes is $\Gamma \rightarrow R^T \Gamma R$. Based on this, we can decompose \mathcal{E}^{loc} as $\mathcal{E}^{\text{rot,p}} \cdot \mathcal{E}^{\text{can}} \cdot \mathcal{E}^{\text{rot,v}}$ where \mathcal{E}^{can} is a Gaussian channel but now with correlation matrix

$$X^{\text{can}} = \begin{pmatrix} A^{\text{can}} & B^{\text{can}} \\ -B^{\text{can}T} & D^{\text{can}} \end{pmatrix} = \begin{pmatrix} \bigoplus_{i=1}^f \lambda_i J & \bigoplus_{i=1}^f \sqrt{1-\lambda_i^2} \mathbb{1} \\ -\bigoplus_{i=1}^f \sqrt{1-\lambda_i^2} \mathbb{1} & -\bigoplus_{i=1}^f \lambda_i J \\ & \pm J \\ & -J^{\oplus(\chi-f-1)} \end{pmatrix} \quad (5.33)$$

where $\lambda_i \in [-1, 1]$ and the last two blocks only occur when $\chi > f$. To see that this decomposition is possible, we apply the composite channel to an arbitrary, pure Gaussian

state on the virtual level and study its effect on the correlation matrix, Γ^v , via consecutive application of the Schur complement formula

$$\begin{aligned}\Gamma^p &= R^{pT} \left(A^{\text{can}} + B^{\text{can}} \left(D^{\text{can}} - R^{vT} \Gamma^v R^v \right)^{-1} B^{\text{can}T} \right) R^p \\ &= R^{pT} A^{\text{can}} R^p + R^{pT} B^{\text{can}} R^{vT} \left(R^v D^{\text{can}} R^{vT} - \Gamma^v \right)^{-1} R^v B^{\text{can}T} R^p.\end{aligned}\quad (5.34)$$

This corresponds to the effect of \mathcal{E} when

$$X = \begin{pmatrix} R^{pT} & \\ & R^v \end{pmatrix} X^{\text{can}} \begin{pmatrix} R^p & \\ & R^{vT} \end{pmatrix}. \quad (5.35)$$

Decomposing X in this way is always possible by first using the anti-symmetry in the physical block to determine a $R^p \in SO(2f)$ (e.g. via Schur decomposition of the A sub-matrix in X) so that

$$X = \begin{pmatrix} R^{pT} & \\ & \mathbb{1} \end{pmatrix} \begin{pmatrix} A' = \bigoplus_{i=1}^f \lambda_i J & B' \\ B'^T & D' \end{pmatrix} \begin{pmatrix} R^p & \\ & \mathbb{1} \end{pmatrix}. \quad (5.36)$$

As the GfTNS is pure, $XX^T = \mathbb{1}$. This is also true for its orthogonally transformed version in the above equation, yielding

$$\begin{cases} A'A'^T + B'B'^T = \mathbb{1}_{2f} \\ D'D'^T + B'^TB' = \mathbb{1}_{2\chi} \\ A'B' = -B'D' \end{cases}. \quad (5.37)$$

Substituting the block diagonal form of A' in the first equation, gives

$$B'B'^T = \bigoplus_{i=1}^f (1 - \lambda_i^2) \mathbb{1}. \quad (5.38)$$

The SVD of B' thus reads $U \left(\bigoplus_{i=1}^f \sqrt{1 - \lambda_i^2} \mathbb{1}_{2f} \quad 0_{2(\chi-f)} \right) V^T$ with $U \in O(2f)$ and $V \in O(2\chi)$. Inserting this again in the first line of Eq. (5.37) shows that U must commute with the first block of the middle matrix so that

$$B' = \left(\bigoplus_{i=1}^f \sqrt{1 - \lambda_i^2} \mathbb{1}_{2f} \quad 0_{2(\chi-f)} \right) \left(\begin{matrix} U & \\ & \mathbb{1}_{2(\chi-f)} \end{matrix} \right) V^T. \quad (5.39)$$

The product of the latter two matrices will be called O and $O \in O(2\chi)$. Substituting the decomposition for B' in the third line of Eq. (5.37) results in

$$\begin{aligned}- \left(\bigoplus_{i=1}^f \sqrt{1 - \lambda_i^2} \mathbb{1}_{2f} \quad 0_{2(\chi-f)} \right) OD' &= \\ \left(\bigoplus_{i=1}^f \lambda_i J \right) \left(\bigoplus_{i=1}^f \sqrt{1 - \lambda_i^2} \mathbb{1}_{2f} \quad 0_{2(\chi-f)} \right) O.\end{aligned}\quad (5.40)$$

Multiplication with O^T from the right then yields

$$OD'OT = \begin{pmatrix} -\bigoplus_{i=1}^f \lambda_i J & \\ & D'' \end{pmatrix}, \quad (5.41)$$

where D'' is real, anti-symmetric and $D''D''^T = \mathbb{1}$. Indeed, the latter follows from substitution of the decomposition of B' in the second line of Eq. (5.37),

$$D'D'^T = O^T \begin{pmatrix} \bigoplus_{i=1}^f (\lambda_i^2 \mathbb{1}) & \\ & \mathbb{1} \end{pmatrix} O. \quad (5.42)$$

Putting the pieces together, we obtain

$$X = \begin{pmatrix} R^{pT} & \\ & O^T \end{pmatrix} \begin{pmatrix} \bigoplus_{i=1}^f \lambda_i J & \bigoplus_{i=1}^f \sqrt{1-\lambda_i^2} \mathbb{1} \\ -\bigoplus_{i=1}^f \sqrt{1-\lambda_i^2} \mathbb{1} & -\bigoplus_{i=1}^f \lambda_i J \end{pmatrix} \begin{pmatrix} R^p & \\ & O \end{pmatrix}. \quad (5.43)$$

Finally performing a Schur decomposition of D'' , this matrix can be brought in the canonical form via a purely virtual orthogonal matrix \tilde{O} but it is possible that one of the J blocks requires a minus sign to make sure that the composition of O and $\mathbb{1}_{2(\chi-f)} \oplus \tilde{O}$, *i.e.* R^{vT} , is special orthogonal. We conclude that using two Schur decompositions and an SVD, one can indeed bring X in the canonical form via a composition of two rotations, one on the physical level and one on the virtual.

The only missing piece now remains the determination of the Kraus operators for the physical and virtual rotations as well as for the canonical projection channel. The Hilbert space representation K^{rot} of a rotation $\mathcal{E}^{\text{rot}} : \mathcal{C}_{2n} \rightarrow \mathcal{C}_{2n} : c_i \mapsto \mathcal{E}^{\text{rot}}(c_i) = c'_i = R_{ij}c_j = K^{\text{rot}}c_iK^{\text{rot}\dagger}$ is well-established and given by

$$K^{\text{rot}} = \exp \left(-\frac{1}{4} u_{kl} c_k c_l \right) \quad (5.44)$$

where $u = \log R$ is a real and anti-symmetric matrix. This formula can be applied for the Kraus operators of both the virtual and physical rotations. The Kraus operator for the canonical projection, on the other hand, should be calculated using the Grassmann integral from Eq. (3.48). However, as X^{can} is block-diagonal, we can reduce the problem to the composite blocks, *i.e.* we need the Kraus operators for channels with correlation matrices

$$X^{\text{can},1} = \begin{pmatrix} \lambda J & \sqrt{1-\lambda^2} \mathbb{1} \\ -\sqrt{1-\lambda^2} \mathbb{1} & -\lambda J \end{pmatrix} \quad \text{and} \quad X^{\text{can},2} = \pm J. \quad (5.45)$$

For the former, one obtains

$$\begin{aligned} \mathcal{E}^{\text{can},1}(1) &= 1 + i\lambda c_1 c_2 & \mathcal{E}^{\text{can},1}(c_1 c_2) &= -i\lambda + c_1 c_2 \\ \mathcal{E}^{\text{can},1}(c_1) &= \sqrt{1-\lambda^2} c_1 & \mathcal{E}^{\text{can},1}(c_2) &= \sqrt{1-\lambda^2} c_2, \end{aligned} \quad (5.46)$$

such that

$$K^{\text{can},1} = \sqrt{1+\lambda} |0\rangle\langle 0| + \sqrt{1-\lambda} |1\rangle\langle 1|. \quad (5.47)$$

Similarly, the second prototypical channel yields

$$K^{\text{can},2} = \begin{cases} \langle 1 |, & X^{\text{can},2} = +J \\ \langle 0 |, & X^{\text{can},2} = -J \end{cases}. \quad (5.48)$$

Note that only the $+J$ block in X^{can} corresponds to an odd Kraus operator. As a result, the ordering of the different Kraus operators for the blocks of X^{can} does not matter.

We conclude that a \mathbb{Z}_2 -graded tensor for the Gaussian projector can be obtained from the local channel correlation matrix, X , by

1. orthogonally transforming this matrix to its canonical form (Eq. (5.33)) via two Schur decompositions and an SVD;
2. determining the Kraus operators for the physical and virtual Majorana rotations corresponding to these special orthogonal transformations (Eq. (5.44));
3. determining the Kraus operator for the canonical channel by building it up from the basic blocks in Eq. (5.47) and Eq. (5.48);
4. reinterpreting these parts as \mathbb{Z}_2 -graded tensors yielding the final result after contraction.

Graphically, this yields tensor diagrams like

$$K = K^{\text{rot},v} + \lambda + 0 \quad (5.49)$$

for our simple exemplary channel. As was the case for the input states, symmetries can be built in rather easily. For instance, SU(2) symmetry requires X to be quaternionic. The decomposition of X in terms of two Schur decompositions and an SVD can then be performed while manifestly maintaining the quaternionic form so that R^p , R^v and X^{can} have quaternionic form. This in turn leads to manifestly SU(2)-symmetric tensors constituting K . Together with the symmetric fMPS for the input state, the resulting \mathbb{Z}_2 -graded tensor therefore inherits the symmetry as well. Nearly identical considerations apply for U(1) symmetry. We also note that (one of) the elementary canonical blocks could have an odd charge. More generally, the channel decomposition method can incorporate non-trivial charges in the same way, thus extending the top-down method from the previous Section. Finally, also bond dimensions equal to (odd powers of) $\sqrt{2}$ are incorporated as these are already encoded in the fMPS for the Majorana chain input state. Indeed, while the Majorana chain is represented with bond dimension 2, every pair of Majorana chains can be compressed to a $D = 2$ MPS. Hence, the final PEPS bond dimension for a given value of χ_i is given by $2^{\lceil \frac{\chi}{2} \rceil}$.

5.4 Applications

5.4.1 Tensor networks can resolve Fermi surfaces

This first application of the GfTNS *Ansatz* to systems with Fermi surfaces resulted in a paper published in Physical Review Letters. The author performed all simulations and wrote the manuscript. Co-authors are Norbert Schuch, Frank Verstraete and Jutho Haegeman.

Tensor Networks Can Resolve Fermi Surfaces

Quinten Mortier^{1,*}, Norbert Schuch^{2,3}, Frank Verstraete¹, and Jutho Haegeman¹

¹*Department of Physics and Astronomy, Ghent University, Krijgslaan 281, S9, 9000 Gent, Belgium*

²*Max-Planck-Institute of Quantum Optics, Hans-Kopfermann-Straße 1, 85748 Garching, Germany*

and Munich Center for Quantum Science and Technology, Schellingstraße 4, 80799 München, Germany

³*University of Vienna, Faculty of Physics, Boltzmanngasse 5, 1090 Wien, Austria*

and University of Vienna, Faculty of Mathematics, Oskar-Morgenstern-Platz 1, 1090 Wien, Austria



(Received 18 January 2022; accepted 12 October 2022; published 8 November 2022)

We demonstrate that projected entangled-pair states are able to represent ground states of critical, fermionic systems exhibiting both 1d and 0d Fermi surfaces on a 2D lattice with an efficient scaling of the bond dimension. Extrapolating finite size results for the Gaussian restriction of fermionic projected entangled-pair states to the thermodynamic limit, the energy precision as a function of the bond dimension is found to improve as a power law, illustrating that an arbitrary precision can be obtained by increasing the bond dimension in a controlled manner. In this process, boundary conditions and system sizes have to be chosen carefully so that nonanalyticities of the *Ansatz*, rooted in its nontrivial topology, are avoided.

DOI: 10.1103/PhysRevLett.129.206401

In one spatial dimension, physically relevant states of quantum many-body systems with a local and gapped Hamiltonian can be represented efficiently by matrix product states (MPS) [1,2]. A natural extension of this construction to higher dimensions was formulated in the form of projected entangled-pair states (PEPS) [3,4]. Both *Ansätze* owe their versatile applicability to an inherent area law of entanglement [5,6]. However, critical systems, with correlations following a power-law decay, can violate this area law in a logarithmic manner. Do tensor networks like MPS and PEPS then still represent efficient *Ansätze* for the relevant states of such critical models? In one dimension, this question was already answered in an affirmative way. For gapped and critical models alike, finite-size ground states can be represented faithfully as MPS with a cost that scales polynomially in the system size [7]. In the thermodynamic limit, local quantities can still be obtained efficiently from MPS ground state approximations, even for critical systems. The theory of finite-entanglement scaling dictates corrections to local observables that vanish algebraically in the bond dimension [8–12]. Finite-entanglement scaling with PEPS has recently also been explored for two-dimensional critical systems which are described by bosonic conformal field theory [13–16]. Here, we aim to investigate how efficiently we can approximate fermionic critical states, in particular those exhibiting Fermi surfaces.

In fermionic systems, logarithmic violations of the area law of entanglement go hand in hand with the presence of codimension one Fermi surfaces [17,18]. These discontinuities in the system's momentum distribution manifest themselves already in translation-invariant, quadratic models as continuous sets of zero energy modes in Fourier space. However, the relation between the presence of Fermi surfaces and the entanglement scaling is not qualitatively

altered by the presence or absence of interactions. Therefore, we will focus on free-fermion systems with a Fermi surface, which allows for the application of the Gaussian and fermionic version of the PEPS *Ansatz* (GfPEPS) [19], thereby reducing the computational cost of the required simulations. We first show that in one dimension these states can reproduce the aforementioned power-law improvement of the precision as a function of the bond dimension by considering the critical points of the Kitaev chain. Subsequently, both 1D and 0D Fermi surfaces in 2D lattice systems are treated by considering the *p*-wave superconductor. In both cases, we again obtain a power-law relation between bond dimension and precision in the thermodynamic limit (albeit with different exponents), indicating that PEPS can describe gapless models and in particular Fermi surfaces of arbitrary dimensions.

Gaussian fermionic PEPS.—Consider a 2D lattice built up by a periodic repetition of $N_1 \times N_2 = N$ unit cells, spanned by \mathbf{a}_1 and \mathbf{a}_2 . To each vertex we attribute f physical fermionic orbitals with creation (annihilation) operators $a_{\mathbf{n}}^{j\dagger}(a_{\mathbf{n}}^j)$, where $\mathbf{n} = n_i \mathbf{a}_i$ with $n_i = 0, \dots, N_i - 1$ is the site and $j = 1, \dots, f$ the orbital index. Corresponding Majorana operators are denoted by $c_{\mathbf{n}}^{2j-1} = a_{\mathbf{n}}^{j\dagger} + a_{\mathbf{n}}^j$ and $c_{\mathbf{n}}^{2j} = -i(a_{\mathbf{n}}^{j\dagger} - a_{\mathbf{n}}^j)$. Within this framework, a PEPS *Ansatz* is obtained by first introducing four sets of virtual Majoranas per site: $\{c_{\mathbf{n}}^{l,i_1}\}$, $\{c_{\mathbf{n}}^{r,i_1}\}$, $\{c_{\mathbf{n}}^{d,i_2}\}$, and $\{c_{\mathbf{n}}^{u,i_2}\}$ with $i_1 = 1, \dots, \chi_1$ and $i_2 = 1, \dots, \chi_2$. Next, a maximally correlated state ρ_{in} is constructed on the virtual level by entangling neighboring Majoranas in both directions (see Fig. 1). This is realized by placing the Majoranas in their joint vacuum, essentially creating χ_i virtual Majorana chains in the direction of \mathbf{a}_i . Finally, the maximally

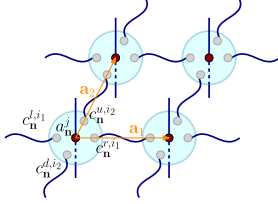


FIG. 1. Schematic of a GfPEPS on a 2D lattice with unit vectors \mathbf{a}_1 and \mathbf{a}_2 . Majorana modes (gray balls) are entangled (blue lines) to form a maximally correlated state which is locally projected by a Gaussian map (big blue circles) to the physical fermions (red balls).

correlated state is locally projected onto the physical level by a channel $\mathcal{E} = \bigotimes_{\mathbf{n}} \mathcal{E}_{\mathbf{n}}^{\text{loc}}$ encoding the fermionic PEPS tensor and yielding the (possibly mixed) $\rho_{\text{out}} = \mathcal{E}(\rho_{\text{in}})$ (see Supplemental Material [20] for more details on ρ_{in} and \mathcal{E}). By increasing the number of virtual Majoranas, the variational set can be enlarged. Note that, as the number of Majoranas can be different in each direction, the resulting effective bond dimensions, $D_i = \sqrt{2^{\chi_i}}$, can differ as well.

Since ρ_{in} is a free-fermion state, Gaussianity of the PEPS can be enforced by restricting the channel \mathcal{E} to be Gaussian as well [21,22]. Not only can then both the input and the output state be fully described in terms of their real and antisymmetric correlation matrices, $\Gamma_{\mathbf{nm}}^{ij} = (i/2)\text{Tr}(\rho[c_{\mathbf{n}}^i, c_{\mathbf{m}}^j])$, but there is also a link between both, prescribed by \mathcal{E} , in the form of a Schur complement, $\Gamma_{\text{out}} = A + B(D + \Gamma_{\text{in}}^{-1})^{-1}B^T$. Here, \mathcal{E} is in fact parametrized by $A = \bigoplus_{\mathbf{n}} A_{\mathbf{n}}^{\text{loc}}$ and analogous decompositions apply for B and D with $A_{\mathbf{n}}^{\text{loc}} \in \mathbb{R}^{2f \times 2f}$, $B_{\mathbf{n}}^{\text{loc}} \in \mathbb{R}^{2f \times 2(\chi_1 + \chi_2)}$, and $D_{\mathbf{n}}^{\text{loc}} \in \mathbb{R}^{2(\chi_1 + \chi_2) \times 2(\chi_1 + \chi_2)}$. Furthermore, $X = \begin{pmatrix} A & B \\ -B^T & D \end{pmatrix}$ is anti-symmetric and $XX^T \leq \mathbb{1}$ with the equality holding for a pure state.

For translation-invariant Gaussian states, it is more convenient to work in Fourier space where these states can be described completely in terms of the Fourier transformed correlation matrix, $G_{\mathbf{kq}}^{ij} = (i/2)\text{Tr}(\rho[d_{\mathbf{k}}^i, d_{\mathbf{q}}^j])$. Herein, $d_{\mathbf{k}}^i = (1/\sqrt{N}) \sum_{\mathbf{n}} e^{-i\mathbf{k}\cdot\mathbf{n}} c_{\mathbf{n}}^i$ with momentum modes \mathbf{k} . In the case of periodic boundary conditions these are given by $\mathbf{k} = \sum_i (k_i/N_i) \mathbf{b}_i$, where \mathbf{b}_i are the reciprocal lattice vectors and $k_i = 0, \dots, N_i - 1$, whereas for antiperiodic boundary conditions $\mathbf{k} = \sum_i (1/N_i)(k_i + \frac{1}{2}) \mathbf{b}_i$. The Fourier transformed correlation matrix is anti-Hermitian, $GG^\dagger \leq \mathbb{1}$ (with the equality again holding for a pure state) and for translation-invariant states G decomposes in diagonal blocks $G = \bigoplus_{\mathbf{k}} G(\mathbf{k})$ with, for instance,

$$G_{\text{in}}(\mathbf{k}) = \begin{pmatrix} 0 & e^{i\mathbf{k}\cdot\mathbf{a}_1} \\ -e^{-i\mathbf{k}\cdot\mathbf{a}_1} & 0 \end{pmatrix}^{\oplus \chi_1} \oplus \begin{pmatrix} 0 & e^{i\mathbf{k}\cdot\mathbf{a}_2} \\ -e^{-i\mathbf{k}\cdot\mathbf{a}_2} & 0 \end{pmatrix}^{\oplus \chi_2} \quad (1)$$

for the input state [20]. Assuming translation invariance of the PEPS, so that $\mathcal{E}_{\mathbf{n}}^{\text{loc}}$ is independent of \mathbf{n} , the transition matrix X decomposes into identical blocks and yields $G_{\text{out}}(\mathbf{k}) = A^{\text{loc}} + B^{\text{loc}}[D^{\text{loc}} - G_{\text{in}}(\mathbf{k})]^{-1}B^{\text{loc}}$ where the purity of the input state was used to replace $G_{\text{in}}^{-1}(\mathbf{k})$ by $-G_{\text{in}}(\mathbf{k})$.

As real-space correlation matrices are real valued, their Fourier transformed analogues have the property that $G(-\mathbf{k}) = G^*(\mathbf{k})$. This implies that $G(\mathbf{k})$ is real and antisymmetric in points where $\mathbf{k} = -\mathbf{k}$, the time-reversal invariant modes (TRIMs). For pure Gaussian states, these $G(\mathbf{k})$ can thus be interpreted as ordinary, pure correlation matrices with a definite parity $\langle P_{\mathbf{k}} \rangle = \langle (-1)^{\sum_j a_{\mathbf{k}}^j a_{\mathbf{k}}^{\dagger}} \rangle = \langle \prod_j i d_{\mathbf{k}}^{(1)} d_{\mathbf{k}}^{(2)} \rangle = \text{Pf}[G(\mathbf{k})]$. Any pure fermionic Gaussian state hence has a specific TRIM parity configuration. E.g., the $G_{\text{in}}(\mathbf{k})$ of the input state [Eq. (1)] amounts to $\langle P_{\mathbf{k}} \rangle_{\text{in}} = \text{Pf}[G_{\text{in}}(\mathbf{k})] = (e^{i\mathbf{k}\cdot\mathbf{a}_1})^{\chi_1} (e^{i\mathbf{k}\cdot\mathbf{a}_2})^{\chi_2}$ so that the center of the Brillouin zone always has an even parity, $\langle P_{\mathbf{0}} \rangle_{\text{in}} = 1$, while for the other TRIMs $\langle P_{(\mathbf{b}_i/2)} \rangle_{\text{in}} = (-1)^{\chi_i}$ and $\langle P_{[(\mathbf{b}_1+\mathbf{b}_2)/2]} \rangle_{\text{in}} = (-1)^{\chi_1 + \chi_2}$. A $(\mathbf{b}_i/2)$ jump in Fourier space thus corresponds to an extra factor $(-1)^{\chi_i}$. Remarkably, this virtual parity configuration is lifted to the physical level by the Gaussian channel \mathcal{E} . Indeed, in order for the full pure PEPS *Ansatz* to have a fixed global parity, the projectors from the virtual to the physical level (i.e., the Kraus operators of $\mathcal{E}_{\mathbf{n}}^{\text{loc}}$) are designed to be parity conserving (changing) [19]. Combining this with their local and translation-invariant nature, GfPEPS have the same (opposite) parity configuration as the valence bond state. We conclude that pure, regular GfPEPS can only realize $2^d \times 2$ (even/odd χ_i in each direction and parity conserving or changing \mathcal{E}) parity configurations while for an arbitrary, pure Gaussian state, there are 2^{2d} possible configurations. Certain parity configurations thus cannot be reached by GfPEPS in spatial dimensions larger than 1, unless singular behavior is present [23–26].

Kitaev chain.—Consider the 1D Kitaev chain of length N with Hamiltonian $H = -t \sum_{n=0}^{N-1} (a_n^\dagger a_{n+1} + \text{H.c.}) - \Delta \sum_{n=0}^{N-1} (a_n^\dagger a_{n+1}^\dagger + \text{H.c.}) - \mu \sum_{n=0}^{N-1} a_n^\dagger$. Further assume that t is positive and that (anti-)periodic boundary conditions, $a_{n+N} = (-1)a_n$, apply. In Fourier space this can be expressed as $H = \sum_k \Upsilon_k^\dagger [\mathbf{h}(k) \cdot \boldsymbol{\sigma}] \Upsilon_k - (\mu/2)N$, where $\mathbf{h}(k) = (-2t \cos k, -2i\Delta \sin k, -\mu)$, $\Upsilon_k = (a_k \ a_{-k}^\dagger)^T$ and the k values are as prescribed in the previous section. For $|\mu| > 2t$, the system is in a trivial phase with the ground state reducing to a product state when $\Delta = 0$ and all momentum modes filled (empty) when $\mu > 2t$ ($\mu < -2t$). For $\Delta \neq 0$ and $|\mu| < 2t$, on the other hand, the system is in a topological phase with winding number $|\nu| = 1$ and an isolated gapless Majorana mode on both ends of the wire when the chain is cut. Critical lines lie at $\mu = \pm 2t$ and at $\Delta = 0$ when $|\mu| < 2t$ (Fig. 2). We optimized GfMPS by

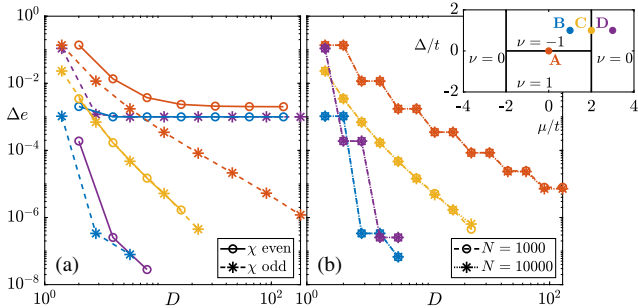


FIG. 2. (a) Energy density error of optimized GfMPS for a Kitaev chain with $N = 1000$ and periodic boundary conditions at 4 different points in the phase diagram (shown in the inset) as a function of the bond dimension $D = \sqrt{2}^\chi$. GfMPS with a χ that reproduces the exact parity configuration can approximate the exact solution with an arbitrary precision whereas the precision of parity obstructed GfMPS saturates to values of order $1/N$. (b) Energy density error of optimized GfMPS for a Kitaev chain with anti-periodic boundary conditions. As the TRIM in $k = 0$ is avoided, fixed energy errors due to incorrect parity configurations do not occur. Results for two system sizes were compared, showing that the thermodynamic limit is well probed at $N = 1000$.

minimizing their energy density for both gapless and gapped parameter choices and for a number of virtual Majorana modes, χ , ranging from 1 to 15. The resulting energy density errors, defined as the difference between the GfMPS energy density and that of the exact ground state at the system size under consideration, are displayed in Fig. 2.

In the left panel, periodic boundary conditions apply and for the critical hopping model at $(t, \mu, \Delta) = (1, 0, 0)$ (point A in the phase diagram), a power-law improvement of the precision is obtained in the case of an odd number of virtual Majoranas. An even χ , on the other hand, yields a saturating profile for Δe . Similar observations apply in the chiral phase (point B) but with an even faster convergence as the area law of entanglement is not violated. In particular, GfMPS constitute an exact ground state with $\chi = 1$ when $\Delta = \pm t$, $\mu = 0$. For gapless Hamiltonians on the critical lines between the chiral and trivial regions [e.g., point C at $(t, \mu, \Delta) = (1, 2, 1)$], we obtain a power-law improvement of the precision but with a higher exponent than for the critical line between the two topological phases. These findings exemplify well-known results about the approximation of one-dimensional critical points with MPS where the rate of convergence depends on the conformal field theory (and, in particular, the central charge) underlying the critical point. Note that point C is indeed an Ising-like transition (with conformal charge $c = 1/2$), whereas point A corresponds to a massless Dirac fermion (with $c = 1$). Finally, optimization in the trivial phase (point D) results in profiles similar to those in the chiral phase but with the odd and even χ curves interchanged.

In the previous section we explained how the number of virtual Majorana modes determines the parity configuration of the regular GfMPS *Ansatz*: an even (odd) χ should be used when the parity in the two TRIMs is equal (opposite). When using a χ with the wrong parity, one TRIM (and thus 1 out of N modes in momentum space) cannot have the correct correlation matrix, leading to an energy density error of order $1/N$, which is confirmed in Fig. 2(a). Only singular behavior with nonanalyticities in the problematic TRIMs can circumvent the fixed parity structure but this fine-tuned case is not supported by our variational method [20]. There is also a link between the parity configuration and the \mathbb{Z}_2 invariant characterizing the topological features of the model [27]. Here, this is reflected by the fact that an even χ should be used in the trivial phase while an odd χ should be utilized in the topological regions, in accordance with the relevant underlying physics with isolated Majorana edge modes. When using antiperiodic boundary conditions, the TRIM in the zone center is never sampled. As a result, fixed energy errors due to an incorrect parity configuration will never occur and the resulting energy convergence curves will not saturate. This is confirmed in Fig. 2(b) and thus proves to be the most pragmatic solution to study the convergence of the energy precision. Again, we report a seemingly exponential improvement in the gapped models whereas a power-law scaling (with different exponents in A and C) is obtained at criticality. Finally, note that adding one extra virtual Majorana to a GfMPS with a correct parity configuration does not improve the energy precision (in points A, B, and D). Indeed, this extra virtual Majorana chain decouples completely from the physical system, yielding a singular norm-zero state when closed with periodic boundary conditions. Closing with antiperiodic boundary conditions on the other hand yields a nonzero norm but with the same energy as with one Majorana less. Only in point C, which is on the critical line between the phases with opposing parity configurations, does the addition of one virtual Majorana improve the results. Indeed, as the TRIM at $k = \pi$ coincides with the Fermi surface at this critical line, its ground state parity is not uniquely defined.

p-wave superconductor.—Switching to 2D, the analog of the Kitaev chain is the *p*-wave superconductor on a square lattice. The Hamiltonian has an identical Fourier space description but now with $\mathbf{h}(\mathbf{k}) = -2[t(\cos k_x + \cos k_y), i\Delta(\sin k_x + i \sin k_y), (\mu/2)]$, where the phase difference between the two spatial components of the pairing term is necessary to open a gap. Again taking $t > 0$, topologically, trivial regions are found when $|\mu| > 4t$. For $0 < \mu < 4t$, one obtains a chiral phase with Chern number $C = -1$, whereas $-4t < \mu < 0$ yields $C = +1$. Critical lines lie in between and at analogous places as for the 1D Kitaev chain (Fig. 3). For $\Delta = 0$ and $-4t < \mu < 4t$ the model exhibits a 1D Fermi surface. In order to circumvent fixed energy errors related to

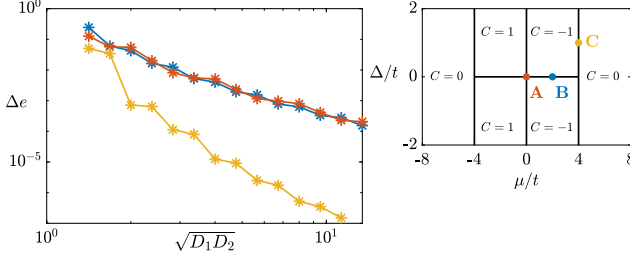


FIG. 3. Energy density error of optimized GfPEPS for the p -wave superconductor (left) (with its phase diagram on the right panel) and linear size $L = 1000$ (thus probing the thermodynamic limit) as a function of the geometric mean of the bond dimensions $\sqrt{D_1 D_2}$. In all the considered cases the energy precision improves polynomially with $\sqrt{D_1 D_2}$, albeit with different exponents for A and B with 1D Fermi surfaces and C with a Dirac cone.

problematic parity configurations, we will only work with antiperiodic boundary conditions in both directions so that for any system size the TRIM in the Brillouin zone center is not sampled. Furthermore, the utilized linear system sizes are always even so that also the other TRIMS are avoided.

GfPEPS were first optimized for point A where $\mu = 0$ and the model reduces to spinless fermions hopping on a square lattice, exhibiting a one-dimensional Fermi surface that divides the Brillouin zone in a filled and a vacated half. The energy density errors as a function of both the geometric mean of the bond dimensions, $\sqrt{D_1 D_2}$, and the linear system size, $L = \sqrt{N} = N_1 = N_2$, are displayed in Fig. 4. The right panel shows that by increasing the system size and keeping $\sqrt{D_1 D_2}$ fixed, the energy error saturates, indicating that the thermodynamic limit is probed. For the largest system size, this is the case for all the considered bond dimensions and the curve for $L = 1000$ in Fig. 4(a) can hence be taken as the energy density error as a function of $\sqrt{D_1 D_2}$ in the thermodynamic limit. Herein, a power-law improvement of the precision can clearly be discerned. This curve was also copied in Fig. 3, where we compare it to results obtained in a similar way for the B and C points in the phase diagram. The B point was studied because the exact parity configuration of the target state cannot be reproduced by GfPEPS in this case due to the incommensurate filling. The GfPEPS will thus approximate singular behavior. However, as we used antiperiodic boundary conditions, this does not spoil the energy convergence study and Fig. 3 confirms that the energy precision increases according to the same power law as for the square lattice hopping model. We conclude that 2D models with 1D (and thus codimension one) Fermi surfaces can (even in the thermodynamic limit) be approximated by PEPS with an arbitrary precision by increasing the bond dimension in a controlled way. To solidify this claim even more, Fig. 5 displays the occupation number $\langle n(\mathbf{k}) \rangle = \langle a_{\mathbf{k}}^\dagger a_{\mathbf{k}} \rangle$ of the GfPEPS with the highest bond dimension, $(\chi_1, \chi_2) = (8, 7)$, for point A and B, clearly showing that

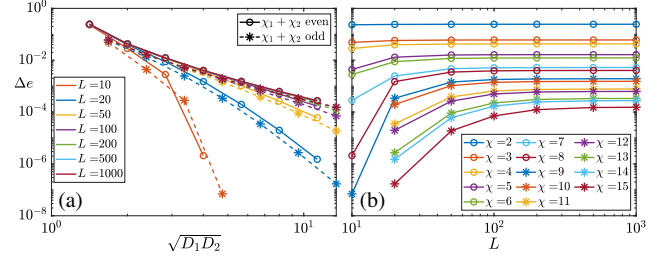


FIG. 4. Energy density error of optimized GfPEPS for the square lattice hopping model (point A in Fig. 3) as a function of (a) the geometric mean of the bond dimensions $\sqrt{D_1 D_2}$ and (b) the linear system size L . In the latter, $\chi = \chi_1 + \chi_2$ with $\chi_1 = \chi_2(+1)$ when χ is even (odd). The thermodynamic limit is probed for all bond dimensions when $L = 1000$ and the onset of a power law can be discerned in the left panel. Results for even and odd χ are displayed separately to obtain smooth curves.

the Fermi surfaces are resolved successfully. In the bottom panels the filling profile along the diagonal of the Brillouin zone is compared for multiple bond dimensions, again demonstrating that by increasing the bond dimension, the sharp edges of the Fermi surface are reproduced to a good degree (see also Supplemental Material [20] for additional results). Point C, on the other hand, is interesting because in this case the criticality exists only in one \mathbf{k} mode, essentially realizing a 0D Fermi surface with a linear dispersion around it, i.e., a Dirac cone. Optimizing GfPEPS at point C shows that energy precision again increases according to a power law. Just as in the 1D case the exponent of this power law is higher than in the A and B

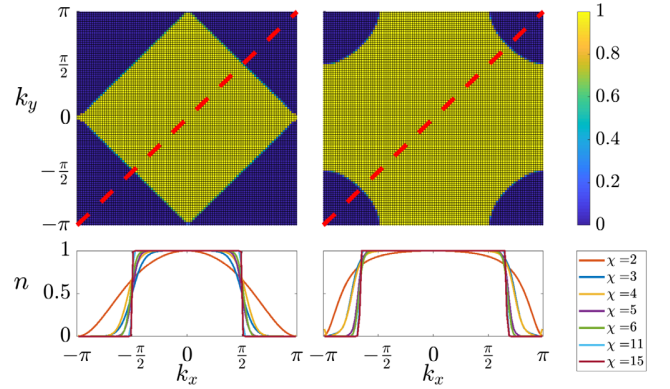


FIG. 5. The top panels display the occupation number $n(\mathbf{k}) = \frac{1}{2}[1 + (i/2)(G^{11}(\mathbf{k}) - G^{22}(\mathbf{k})) + \frac{1}{2}(G^{12}(\mathbf{k}) + G^{21}(\mathbf{k}))]$ of the optimized GfPEPS with the highest bond dimension, $(\chi_1, \chi_2) = (8, 7)$, for the spinless, square lattice hopping model with commensurate (left) and incommensurate (right) filling (i.e., points A and B in Fig. 3, respectively). In the bottom panels, occupations are compared for different combinations of Majorana numbers along the diagonal of the Brillouin zone (red line where $k_x = k_y$), showing that the sharp edges of the Fermi surface are reproduced increasingly well.

points. Indeed, the area law of entanglement is not violated in C.

Conclusions.—We studied whether projected entangled-pair states can be used to describe critical systems exhibiting Fermi surfaces. This question was answered in an affirmative way. Indeed, the Gaussian and fermionic version of the PEPS *Ansatz* was successfully applied to 2D free-fermion systems with both 1D and 0D Fermi surfaces. More specifically, we considered two critical points of the *p*-wave superconductor with a 1D Fermi surface and observed that in the thermodynamic limit the precision of the GfPEPS approximations increased according to similar power laws as a function of the bond dimension. This is the 2D extension of earlier results hereabout in 1D, that were also reproduced for the gapless Kitaev chain. Furthermore, 0D Fermi surfaces exhibiting Dirac cones were also shown to pose no difficulties for PEPS as the energy precision for yet another critical point of the *p*-wave superconductor also increased according to a power law but with an even higher exponent.

Though we did not address the ability of fermionic PEPS to approximate interacting systems with a Fermi surface directly, the qualitative features of the convergence that we obtain should be robust against adding interactions. Indeed, it has been amply demonstrated that the success of PEPS (and tensor networks more generally) is not affected by the strength of interactions, but by the scaling of entanglement. As interactions are not expected to affect the entanglement scaling of critical points and Fermi surfaces [28,29], neither should be the ability for PEPS to approximate them. Moreover, energy densities obtained in this Letter present an upper bound to those a generic (non-Gaussian) PEPS would be able to attain for the same (quadratic) Hamiltonian. Indeed, it can be expected that discarding the free-fermion structure would further improve the accuracy as already demonstrated for the 1D case [30]. Furthermore, the variationally optimized Gaussian PEPS obtained in this Letter can play a significant role also in the case of interacting systems. Indeed, the ground state of an interacting system can first be approximated in a mean-field-like manner by a Gaussian PEPS, which is then converted to a generic (fermionic) PEPS tensor [19] (using e.g. the formalism of super vector spaces [31]), in order to serve as the initial state for a full-fledged variational optimization over the set of all PEPS. Note that the effective bond dimensions of the Gaussian PEPS in our simulations should be within reach of current state-of-the-art PEPS algorithms and make this a feasible approach, that will be investigated further in forthcoming work.

We would like to thank Erez Zohar, Karel Van Acoleyen, and Ignacio Cirac for inspiring discussions. This work has received support from the European Research Council (ERC) under the European Union’s Horizon 2020 program [Grant Agreements No. 715861 (ERQUAF),

647905 (QUTE), 636201 (WASCOSYS), and 863476 (SEQUAM)], and from the DFG (German Research Foundation) under Germany’s Excellence Strategy (EXC2111–390814868).

* quinten.mortier@ugent.be

- [1] M. Fannes, B. Nachtergaele, and R. F. Werner, Finitely correlated states on quantum spin chains, *Commun. Math. Phys.* **144**, 443 (1992).
- [2] I. Cirac, D. Perez-Garcia, N. Schuch, and F. Verstraete, Matrix product states and projected entangled pair states: Concepts, symmetries, and theorems, *Rev. Mod. Phys.* **93**, 045003 (2021).
- [3] F. Verstraete and J. I. Cirac, Valence-bond states for quantum computation, *Phys. Rev. A* **70**, 060302(R) (2004).
- [4] F. Verstraete and J. I. Cirac, Renormalization algorithms for quantum-many body systems in two and higher dimensions, [arXiv:cond-mat/0407066](https://arxiv.org/abs/cond-mat/0407066).
- [5] M. B. Hastings, Solving gapped Hamiltonians locally, *Phys. Rev. B* **73**, 085115 (2006).
- [6] M. M. Wolf, F. Verstraete, M. B. Hastings, and J. I. Cirac, Area Laws in Quantum Systems: Mutual Information and Correlations, *Phys. Rev. Lett.* **100**, 070502 (2008).
- [7] F. Verstraete and J. I. Cirac, Matrix product states represent ground states faithfully, *Phys. Rev. B* **73**, 094423 (2006).
- [8] T. Nishino, K. Okunishi, and M. Kikuchi, Numerical renormalization group at criticality, *Phys. Lett. A* **213**, 69 (1996).
- [9] L. Tagliacozzo, T. R. de Oliveira, S. Iblisdir, and J. I. Latorre, Scaling of entanglement support for matrix product states, *Phys. Rev. B* **78**, 024410 (2008).
- [10] F. Pollmann, S. Mukerjee, A. M. Turner, and J. E. Moore, Theory of Finite-Entanglement Scaling at One-Dimensional Quantum Critical Points, *Phys. Rev. Lett.* **102**, 255701 (2009).
- [11] B. Pirvu, G. Vidal, F. Verstraete, and L. Tagliacozzo, Matrix product states for critical spin chains: Finite-size versus finite-entanglement scaling, *Phys. Rev. B* **86**, 075117 (2012).
- [12] B. Vanhecke, J. Haegeman, K. Van Acoleyen, L. Vanderstraeten, and F. Verstraete, Scaling Hypothesis for Matrix Product States, *Phys. Rev. Lett.* **123**, 250604 (2019).
- [13] M. Rader and A. M. Läuchli, Finite Correlation Length Scaling in Lorentz-Invariant Gapless iPEPS Wave Functions, *Phys. Rev. X* **8**, 031030 (2018).
- [14] P. Corboz, P. Czarnik, G. Kapteijns, and L. Tagliacozzo, Finite Correlation Length Scaling with Infinite Projected Entangled-Pair States, *Phys. Rev. X* **8**, 031031 (2018).
- [15] P. Czarnik and P. Corboz, Finite correlation length scaling with infinite projected entangled pair states at finite temperature, *Phys. Rev. B* **99**, 245107 (2019).
- [16] B. Vanhecke, J. Hasik, F. Verstraete, and L. Vanderstraeten, A scaling hypothesis for projected entangled-pair states, [arXiv:2102.03143](https://arxiv.org/abs/2102.03143).
- [17] M. M. Wolf, Violation of the Entropic Area Law for Fermions, *Phys. Rev. Lett.* **96**, 010404 (2006).

- [18] D. Gioev and I. Klich, Entanglement Entropy of Fermions in Any Dimension and the Widom Conjecture, *Phys. Rev. Lett.* **96**, 100503 (2006).
- [19] C. V. Kraus, N. Schuch, F. Verstraete, and J. I. Cirac, Fermionic projected entangled pair states, *Phys. Rev. A* **81**, 052338 (2010).
- [20] See Supplemental Material at <http://link.aps.org/supplemental/10.1103/PhysRevLett.129.206401> for more details on the *Ansatz*, the applied optimization algorithm and additional results.
- [21] S. Bravyi, Lagrangian representation for fermionic linear optics, *Quantum Inf. Comput.* **5**, 216 (2005).
- [22] N. Schuch, M. M. Wolf, and J. I. Cirac, Gaussian matrix product states, in *Proceedings of the Conference on Quantum Information and Many Body Quantum Systems* (Edizioni della Normale, Pisa, 2008), p. 129.
- [23] J. Dubail and N. Read, Tensor network trial states for chiral topological phases in two dimensions and a no-go theorem in any dimension, *Phys. Rev. B* **92**, 205307 (2015).
- [24] T. B. Wahl, H.-H. Tu, N. Schuch, and J. I. Cirac, Projected Entangled-Pair States Can Describe Chiral Topological States, *Phys. Rev. Lett.* **111**, 236805 (2013).
- [25] T. B. Wahl, S. T. Haßler, H.-H. Tu, J. I. Cirac, and N. Schuch, Symmetries and boundary theories for chiral projected entangled pair states, *Phys. Rev. B* **90**, 115133 (2014).
- [26] S. Yang, T. B. Wahl, H.-H. Tu, N. Schuch, and J. I. Cirac, Chiral Projected Entangled-Pair State with Topological Order, *Phys. Rev. Lett.* **114**, 106803 (2015).
- [27] A. Y. Kitaev, Unpaired Majorana fermions in quantum wires, *Phys. Usp.* **44**, 131 (2001).
- [28] B. Swingle, Entanglement Entropy and the Fermi Surface, *Phys. Rev. Lett.* **105**, 050502 (2010).
- [29] W. Ding, A. Seidel, and K. Yang, Entanglement Entropy of Fermi Liquids via Multidimensional Bosonization, *Phys. Rev. X* **2**, 011012 (2012).
- [30] A. Franco-Rubio and J. I. Cirac, Gaussian matrix product states cannot efficiently describe critical systems, [arXiv: 2204.02478](https://arxiv.org/abs/2204.02478).
- [31] N. Bultinck, D. J. Williamson, J. Haegeman, and F. Verstraete, Fermionic matrix product states and one-dimensional topological phases, *Phys. Rev. B* **95**, 075108 (2017).

Supplemental Material for: “Tensor networks can resolve Fermi surfaces”

Quinten Mortier,^{1,*} Norbert Schuch,^{2,3} Frank Verstraete,¹ and Jutho Haegeman¹

¹*Department of Physics and Astronomy, Ghent University, Krijgslaan 281, S9, 9000 Gent, Belgium*

²*Max-Planck-Institute of Quantum Optics, Hans-Kopfermann-Straße 1, 85748 Garching, Germany, and Munich Center for Quantum Science and Technology, Schellingstraße 4, 80799 München, Germany*

³*University of Vienna, Faculty of Physics, Boltzmanngasse 5, 1090 Wien, Austria, and University of Vienna, Faculty of Mathematics, Oskar-Morgenstern-Platz 1, 1090 Wien, Austria*

GAUSSIAN FERMIONIC PEPS

The Gaussian fermionic Projected Entangled-Pair State (GfPEPS) ansatz, introduced in the main text, is constructed from an input state, ρ_{in} , obtained by entangling neighboring virtual Majorana operators. Onto this input state, one applies a local, translation-invariant and Gaussian projection, $\mathcal{E} = \bigotimes_{\mathbf{n}} \mathcal{E}_{\mathbf{n}}^{\text{loc}}$, yielding the GfPEPS output state ρ_{out} . Below we discuss the ingredients in this recipe in some more detail.

Input state

Entangling neighboring Majorana operators to obtain ρ_{in} is done by placing them in their joint vacuum (or occupied) state, essentially creating virtual Majorana chains. To see this, consider the Hamiltonian for the maximally correlated Majorana chain of length N

$$H = -t \sum_{n=0}^{N-1} (a_n^\dagger a_{n+1} + h.c.) - \Delta \sum_{n=0}^{N-1} (a_n^\dagger a_{n+1}^\dagger + h.c.), \quad (1)$$

where $\Delta = \pm t$ and periodic boundary conditions are in place. Introducing Majorana operators, this reduces to

$$H = it \sum_{n=0}^{N-1} \begin{cases} c_{n+1}^1 c_n^2 & \Delta = t \\ c_n^1 c_{n+1}^2 & \Delta = -t \end{cases}. \quad (2)$$

When we construct the “bond fermions”,

$$b_n = \frac{1}{2} \begin{cases} c_{n+1}^1 - ic_n^2 & \Delta = t \\ c_n^1 - ic_{n+1}^2 & \Delta = -t \end{cases}, \quad (3)$$

this can be rewritten as $H = t \sum_{n=0}^{N-1} (1 - 2b_n^\dagger b_n)$, showing that in the ground state all bond fermions are filled (empty) when $t > 0$ ($t < 0$) so that the ground state energy is given by $E_{\text{gs}} = -N|t|$. Being the ground state of a quadratic, translation-invariant Hamiltonian, these states are also Gaussian and translation-invariant. Consequently, they can be described in terms of their Fourier transformed correlation matrix which can be obtained by Fourier transforming the Majorana operators such that for the Hamiltonian, one obtains

$$H = it \sum_k e^{\mp ik} d_k^1 d_k^2 = \frac{i}{2} \sum_k \begin{pmatrix} d_k^1 & d_k^2 \end{pmatrix} \begin{pmatrix} & te^{\mp ik} \\ -te^{\pm ik} & \end{pmatrix} \begin{pmatrix} d_k^1 \\ d_k^2 \end{pmatrix} \quad \text{with } \Delta = \pm t. \quad (4)$$

The ground state correlation matrix hence is

$$G(k) = -\text{sgn}(t) \begin{pmatrix} e^{\mp ik} \\ -e^{\pm ik} \end{pmatrix}. \quad (5)$$

As discussed in the main text, tensor products of these states (in both directions) are used as the input onto which a Gaussian projection is applied to construct GfPEPS. Always choosing $-\Delta = t < 0$, yields the input correlation matrix in Eq. (2). Note, however, that this choice requires an odd Gaussian projection, flipping all time-reversal invariant mode (TRIM) parities, to reproduce an odd Brillouin zone center parity as, for instance, happens in the fermionic

hopping model. Typically, we restrict ourselves to Gaussian projections with even Kraus operators and build the desired Brillouin zone center parity in the input state. For example, in the case of the hopping model we can choose one virtual Majorana chain with $\Delta = t > 0$ while for all the others $-\Delta = t < 0$. Indeed, in this way the input correlation matrix becomes

$$G_{\text{in}}(\mathbf{k}) = \begin{pmatrix} e^{ik_x} & -e^{-ik_x} \\ -e^{-ik_x} & e^{ik_x} \end{pmatrix}^{\oplus (\chi_x - 1)} \oplus \begin{pmatrix} e^{ik_y} \\ -e^{-ik_y} \end{pmatrix}^{\oplus \chi_y}, \quad (6)$$

for a square lattice, thus reproducing the desired parity in the Brillouin zone center. Combining this with odd lattice lengths in both directions, one can avoid the erroneous TRIM parity in (π, π) . Another possibility lies in the use of anti-periodic boundary conditions, *i.e.* we consider again the Hamiltonian of Eq. (1) but now with $a_N = -a_0$. One can repeat all the steps and the ground state will again be a product state of filled/empty bond fermions (with the difference that the bond fermion closing the loop is defined with an extra minus sign). Furthermore, the Fourier transformation of the Majoranas differs as $c_{n+N}^i = -c_n^i$ implies that the inverse Fourier transform only gives the correct behavior when the momenta are given by $k = \frac{2\pi}{N}(n + \frac{1}{2})$ ($n = 0, \dots, N - 1$). In this case, the ground state remains translation-invariant and Gaussian so that it is still described by Eq.(5) but now with the new momenta, allowing to avoid erroneous TRIMs.

Gaussian channel

After constructing the input state, the channel $\mathcal{E}_{\text{n}}^{\text{loc}}$ has to be applied at each lattice site, projecting from the virtual level with $2(\chi_1 + \chi_2)$ Majorana operators to the physical level with f physical fermions (and thus $2f$ physical Majorana operators). As ρ_{in} is Gaussian by construction, the $\mathcal{E}_{\text{n}}^{\text{loc}}$ channel should preserve this property for ρ_{out} to be Gaussian as well. This is possible when $\mathcal{E}_{\text{n}}^{\text{loc}}$ is a so-called Gaussian channel [?]. To properly define this, we have to introduce the Grassmann form of Gaussian fermionic states. Consider therefore a general state, ρ , defined within the framework of n fermionic creation (annihilation) operators a_i^\dagger (a_i) ($i = 1, \dots, n$), satisfying canonical anti-commutation relations. Corresponding Majorana operators are denoted by $c_{2i-1} = a_i^\dagger + a_i$ and $c_{2i} = -i(a_i^\dagger - a_i)$ where $\{c_i, c_j\} = 2\delta_{ij}$. As a result, any fermionic operator Z can be represented as a linear combination of Majorana operator products,

$$Z = \alpha + \sum_{p=1}^{2n} \sum_{1 \leq a_1 < \dots < a_p \leq 2n} \alpha_{a_1, \dots, a_p} c_{a_1} \dots c_{a_p} \quad (7)$$

making the operator space a Clifford algebra. We denote this algebra, generated by the $2n$ Majorana operators, as \mathcal{C}_{2n} . Isomorphic to it, one defines the Grassmann algebra \mathcal{G}_{2n} . The latter is a complex linear space of dimension $2n$ with basis vectors $\{\theta_i\}_{i=1, \dots, 2n}$ and a multiplication so that $\{\theta_i, \theta_j\} = 0$. The isomorphism from Clifford to Grassmann algebra is for a homogeneous product of operators defined by

$$\omega : \mathcal{C}_{2n} \rightarrow \mathcal{G}_{2n} : c_a c_b \dots c_z \mapsto \theta_a \theta_b \dots \theta_z \quad (8)$$

and extends to the full space via linearity. Building on this isomorphism, we will call $Z(\theta) = \omega(Z)$ the Grassmann form of Z . A state with density operator ρ is then defined to be Gaussian if its Grassmann form is given by

$$\rho(\theta) = \frac{1}{2^n} \exp\left(\frac{i}{2}\theta^T \Gamma \theta\right) \quad (9)$$

with Γ the real and anti-symmetric correlation matrix for which $\Gamma \Gamma^T \leq \mathbb{1}$ (with the equality applying in case of pure state) and $\Gamma_{ij} = \frac{i}{2}(\rho[c_i, c_j])$. An immediate consequence is that Gaussian states satisfy Wick's theorem so that any expectation value can be determined by using only the two-point functions in the correlation matrix. Furthermore, a general operator $Z \in \mathcal{C}_{2n}$ is said to be a Gaussian operator (but not necessarily a Gaussian state) when it has the same quadratic exponential Grassmann form but now also non-normalized operators and operators with a complex, anti-hermitian correlation matrix are allowed. One can check that the input state ρ_{in} discussed in the previous section satisfies the definition of a pure, Gaussian state. A GfPEPS can hence be obtained by retaining this characteristic upon locally projecting from the virtual to the physical level. This requirement is imposed on the channel \mathcal{E} , mapping ρ_{in} onto ρ_{out} . Indeed, $\mathcal{E} : \mathcal{C}_{2n} \rightarrow \mathcal{C}_{2m}$ transforms a Gaussian state into another Gaussian state when its Jamolkowski dual is a Gaussian operator itself. This can be expressed with Grassmann operators by requiring that

$$\mathcal{E}(Z)(\theta) = C \int \exp\left(\frac{i}{2}\begin{pmatrix} \theta \\ \eta \end{pmatrix}^T \begin{pmatrix} A & B \\ C & D \end{pmatrix} \begin{pmatrix} \theta \\ \eta \end{pmatrix} + i\eta^T \mu\right) Z(\mu) D\eta D\mu \quad (10)$$

where $C \geq 0$ makes sure that the trace is preserved while the channel correlation matrix $X = \begin{pmatrix} A & B \\ C & D \end{pmatrix}$ is real, anti-symmetric and so that $XX^T \leq \mathbb{1}$ (with the equality holding for projection onto a pure state) (see also [?]). Furthermore, θ contains the Grassmann numbers in \mathcal{G}_{2m} while η and μ are copies of those in \mathcal{G}_{2n} . The integral operation $\int d\theta_i$ on Grassmann numbers is defined to be equivalent to the derivative (*i.e.* it removes θ_i from all homogeneous combinations containing it, and maps the other combinations to zero), so that only the terms with all η and μ variables in the expansion of the exponential will survive integration. For these combinations $D\eta = d\eta_{2n}...d\eta_1$ so that $\int \eta_1...\eta_{2n} D\eta = 1$ and analogous for $D\mu$. Using these properties, one can immediately derive the correlation matrix Γ of $\rho_{\text{out}} = \mathcal{E}(\rho_{\text{in}})$ when those of the input state and the channel are known. It turns out that the output correlation matrix is given by a Schur complement,

$$\Gamma = A - B(D + \Gamma_{\text{in}}^{-1})^{-1}C. \quad (11)$$

We also require the projection to be local and identical at each site so that $\mathcal{E} = \bigotimes_{\mathbf{n}} \mathcal{E}_{\mathbf{n}}^{\text{loc}}$ with $\mathcal{E}_{\mathbf{n}}^{\text{loc}} : \mathcal{C}_{2\chi_1+\chi_2} \rightarrow \mathcal{C}_{2f}$, independent of the position \mathbf{n} (this label will thus be dropped). This only happens when X decomposes in N local and identical blocks, $X = X^{\text{loc}} \oplus \mathbb{1}^N$, with the real and anti-symmetric $X^{\text{loc}} \in \mathbb{R}^{2(f+|\chi|) \times 2(f+|\chi|)}$ for which $X^{\text{loc}}X^{\text{loc}}^T \leq \mathbb{1}$ (with the equality again holding for a pure state), containing all the variational freedom in the ansatz. Not only this projection, but also the input state is translation-invariant. We can exploit this property maximally by going to Fourier space, where ρ_{in} is fully described in terms of its Fourier transformed correlation matrix, which is unitarily equivalent with Γ_{in} and therefore also anti-hermitian with $G_{\text{in}}G_{\text{in}}^\dagger = \mathbb{1}$ due to its purity. As both ρ_{in} and \mathcal{E} are translation-invariant, this is also the case for the GfPEPS so that this state too can be fully described by its (block diagonal) Fourier transformed correlation matrix. Furthermore, the fact that $X = X^{\text{loc}} \oplus \mathbb{1}^N$ makes Fourier transformation commute with the Schur complement of Eq. (11) so that

$$G(\mathbf{k}) = A^{\text{loc}} - B^{\text{loc}}(D^{\text{loc}} - G_{\text{in}}(\mathbf{k}))^{-1}C^{\text{loc}} \quad (12)$$

where the purity of ρ_{in} was used to replace the inner inverse. Finally, note that the GfPEPS we considered up to now could also be mixed when $X^{\text{loc}}X^{\text{loc}}^T < \mathbb{1}$, thus rather yielding a GfPEPO than a GfPEPS. For the simulations described in the main text, however, we restricted ourselves to pure states, thus choosing $X^{\text{loc}}X^{\text{loc}}^T = \mathbb{1}$.

OPTIMIZATION ALGORITHM

In this Letter we optimized GfPEPS for free-fermion models with a Hamiltonian that can always be cast in the Bogoliubov-de Gennes (BdG) form

$$H = \frac{1}{2} \sum_{\mathbf{n}, \mathbf{m}} \Upsilon_{\mathbf{n}}^\dagger H_{\mathbf{n}\mathbf{m}}^{\text{BdG}} \Upsilon_{\mathbf{m}} + \tilde{E} \quad (13)$$

where \tilde{E} is an energy offset (typically proportional to number of lattice sites N) and $\Upsilon_{\mathbf{n}} = (\{a_{\mathbf{n}}^i\}, \{a_{\mathbf{n}}^{i\dagger}\})^T$ is the Nambu spinor. Assuming translation invariance, it is again more convenient to work in Fourier space where

$$H = \frac{1}{2} \sum_{\mathbf{k}} \Upsilon_{\mathbf{k}}^\dagger H_{\text{BdG}}(\mathbf{k}) \Upsilon_{\mathbf{k}} + \tilde{E} \quad (14)$$

with $\Upsilon_{\mathbf{k}} = (\{a_{\mathbf{k}}^i\}, \{a_{-\mathbf{k}}^{i\dagger}\})^T$. For the variational optimization, the energy density was utilized as cost function and can be expressed as

$$\begin{aligned} e &= \frac{1}{N} \langle H \rangle = \frac{1}{2N} \sum_{\mathbf{k}} \langle \Upsilon_{\mathbf{k}}^\dagger H_{\text{BdG}}(\mathbf{k}) \Upsilon_{\mathbf{k}} \rangle + \frac{\tilde{E}}{N} \\ &= \frac{i}{2N} \sum_{\mathbf{k}} \text{Tr}(\tilde{H}_{\text{BdG}}(\mathbf{k}) G_{\text{out}}(\mathbf{k})) + \frac{1}{4N} \sum_{\mathbf{k}} \text{Tr}(\tilde{H}_{\text{BdG}}(\mathbf{k})) + \frac{\tilde{E}}{N} \end{aligned} \quad (15)$$

where $\tilde{H}_{\text{BdG}}(\mathbf{k}) = V^{-1\dagger} H_{\text{BdG}}(\mathbf{k}) V^{-1}$ with V the constant matrix transforming the Fourier space Nambu spinor in the $\{d_{\mathbf{k}}^i\}$ operators. Note that the energy density is linear in the GfPEPS correlation matrix so that its gradient can

easily be expressed as

$$\frac{\partial e}{\partial X^{\text{loc}}} = \frac{i}{2N} \sum_{\mathbf{k}} \text{Tr} \left(\tilde{H}_{\text{BdG}}(\mathbf{k}) \frac{\partial G_{\text{out}}}{\partial X^{\text{loc}}}(\mathbf{k}) \right). \quad (16)$$

The variational parameters are collected in the anti-symmetric matrix $X^{\text{loc}} \in \mathbb{R}^{2(f+\chi_1+\chi_2) \times 2(f+\chi_1+\chi_2)}$, describing the transformation between $G_{\text{in}}(\mathbf{k})$ and $G_{\text{out}}(\mathbf{k})$. In case of a pure state, this matrix satisfies $X^{\text{loc}} X^{\text{loc}^\dagger} = \mathbb{1}$ so that it can be parameterized as $X^{\text{loc}} = Q^T J^{\oplus(f+\chi_1+\chi_2)} Q$ with $Q \in O(2(f + \chi_1 + \chi_2))$ and $J = \begin{pmatrix} 0 & 1 \\ -1 & 0 \end{pmatrix}$. Replacing a single J block by its transpose, it is possible to construct all admissible X^{loc} by using only a $Q \in SO(2(f + \chi_1 + \chi_2))$, yielding a $(2(f + \chi_1 + \chi_2) - 1)(f + \chi_1 + \chi_2)$ -dimensional variational manifold. On this manifold, a Riemannian limited memory quasi-Newton (L-BFGS) procedure was applied to find the minimum of $e(X^{\text{loc}})$. The optimization was started from a random initial guess for the smallest system sizes while for larger systems the optimized results for smaller system sizes with the same bond dimension were used as initial guesses. In this way the computation time was reduced significantly as the initial guesses for larger systems were already close to the optima, again signaling that these results can be extrapolated to the thermodynamic limit. Singular behavior, when necessary (e.g. to compensate for incorrect parity configurations), is only realized approximately in our method. Indeed, one always starts from a random and thus regular GfPEPS and will therefore never truly reach the fine-tuned case where $\det(D - G_{\text{in}}(\mathbf{k}))$ exactly equals zero for some \mathbf{k} . Consequently, the parity and filling will remain erroneous in this \mathbf{k} mode, resulting in fixed energy errors. Therefore, the most pragmatic solution to study the energy density precision consists in avoiding singular \mathbf{k} modes by applying appropriate boundary conditions and/or choosing adjusted system sizes.

Finally, we also comment on some other variations of the optimization method. Simulations can, for instance, be performed at elevated temperatures, utilizing a mixed GfPEPS ansatz where $X^{\text{loc}} X^{\text{loc}^\dagger} < \mathbb{1}$. This can be enforced by taking $X^{\text{loc}} = \tan Q$ with Q anti-symmetric (again resulting in a $(2(f + \chi_1 + \chi_2) - 1)(f + \chi_1 + \chi_2)$ -dimensional variational manifold). Not only does this approach complicate the expressions for the analytic gradient of the energy density, the energy density cost function should also be replaced by the free energy density, thus adding an entropic contribution. Especially the latter becomes significantly more complicated to compute. Therefore, one might resort to cost functions directly expressing the distance between the exact and the GfPEPS correlation matrices. However, the determination of analytic gradients should also be possible for these cost functions, for instance precluding trace norm distances in most cases. Moreover, this approach requires the exact solution for the correlation matrix.

ADDITIONAL RESULTS

p-Wave superconductor

In the main text, the energy density precision was used as a measure for the ability of the ansatz to reproduce the exact ground state of the considered models. The claim that Fermi surfaces were successfully resolved was further substantiated by comparing the exact Fourier space occupation with the GfPEPS results in Fig. 5. To solidify these results even further, we compare (the norms of) the $\langle a_{\mathbf{k}} a_{-\mathbf{k}} \rangle$ expectation values below for different bond dimensions as these, together with the modal occupation completely fix the Fourier transformed correlation matrix $G(\mathbf{k})$ and thus the Gaussian state.

Fig. 1 illustrates that increasing the number of virtual Majorana's (and thus the bond dimension D), these expectation values approach zero, *i.e.* the exact value. Note that in the fine-tuned case of point A in the phase diagram, one exactly samples \mathbf{k} modes on the Fermi surface. For these, the GfPEPS will approximate the exact Fermi surface with a smooth transition from one to zero in the modal occupation. On the diagonal this yields a $n(\mathbf{k}) \approx \frac{1}{2}$. Combining this with the requirement that $G(\mathbf{k})G^\dagger(\mathbf{k}) = \mathbb{1}$ implies that also $|\langle a_{\mathbf{k}} a_{-\mathbf{k}} \rangle| \approx \frac{1}{2}$. As result, there will always be a 0.5 expectation value for the GfPEPS in the bottom, left panel of Fig. 1, no matter the bond dimension. This also demonstrates that imposing $U(1)$ symmetry on the GfPEPS ansatz to target the Fermi surface would never work. Indeed, doing so, the $\langle a_{\mathbf{k}} a_{-\mathbf{k}} \rangle$ expectation values would be set to zero, enforcing a constant $n(\mathbf{k})$ across the Brillouin zone. Put differently, one cannot do without $U(1)$ -breaking in order for the ansatz to realize a transition between the occupied and vacated parts of the Brillouin zone. In the B point of the phase diagram where $(t, \mu, \Delta) = (1, 2, 0)$, the Fermi surface is not sampled exactly. One can again observe that $\langle a_{\mathbf{k}} a_{-\mathbf{k}} \rangle$ approaches zero as the bond dimension increases, but now without fixed errors. We conclude that the GfPEPS do approximate the exact ground states, as

the combination of Fig. 1 with Fig. 5 in the main text illustrates that the exact correlation matrix is approximated increasingly well.

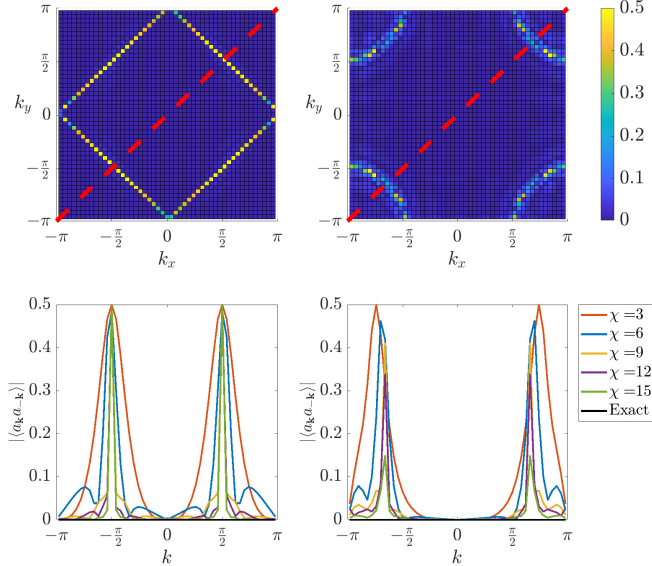


FIG. 1. The top panels display $|\langle a_{\mathbf{k}} a_{-\mathbf{k}} \rangle| = -\frac{i}{4} [(G^{11}(\mathbf{k}) - G^{22}(\mathbf{k})) - i(G^{12}(\mathbf{k}) + G^{21}(\mathbf{k}))]$ of the optimized GfPEPS with the highest bond dimension, $(\chi_1, \chi_2) = (8, 7)$, for the spinless, square lattice hopping model with commensurate (left) and incommensurate (right) filling (*i.e.* points A and B in Fig. 3 of the main text, respectively). In the bottom panel, these expectation values are compared for different combinations of Majorana numbers along the diagonal of the Brillouin zone (red line where $k_x = k_y = k$), showing that as the bond dimension increases, the exact result is reproduced to a good degree.

We also add a comparison between the real-space correlation functions $\langle a_{\mathbf{n}}^\dagger a_{\mathbf{0}} \rangle$ of the optimized GfPEPS and their exact counterparts in the x - and y -direction. Fig. 2 confirms that increasing the bond dimension, the exact result is approximated increasingly well. Indeed, the exact $\langle a_{\mathbf{n}}^\dagger a_{\mathbf{0}} \rangle$ correlation function oscillates between zero (for sites separated by an odd number of lattice lengths (these points were not included in Fig. 2)) and a positive value decreasing to zero as $\frac{1}{|\mathbf{n}|}$ (when $n_x + n_y$ is even). The GfPEPS results typically yield a small value when $n_x + n_y$ is odd but, more importantly, when $n_x + n_y$ is even, they follow the polynomial scaling up to a certain distance (the correlation length) after which they decrease faster, reach zero and/or even become negative. Increasing the bond dimension, the correlation length grows with the result for $(\chi_1, \chi_2) = (8, 7)$ realizing a correlation length up to almost 100 sites in x -direction. Again this confirms that the exact correlations and thus the exact ground states are approximated increasingly well with higher D .

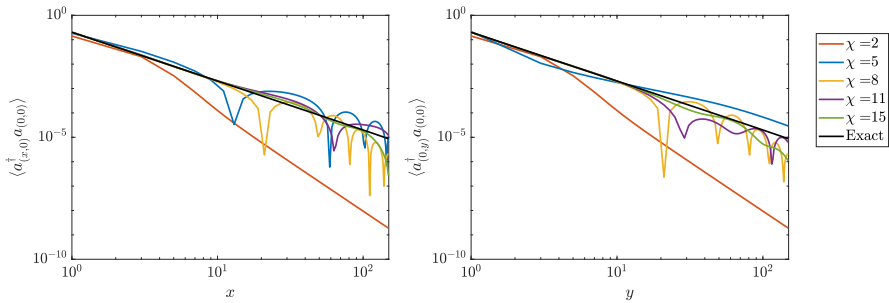


FIG. 2. Real-space $\langle a_{\mathbf{n}}^\dagger a_{\mathbf{0}} \rangle$ correlation functions in both the x - (left) and the y - (right) direction for GfPEPS with different combinations of Majorana numbers as well as for the exact ground state. Expectation values were only displayed for sites separated by an even number of lattice lengths as for odd separations these values are very small, complicating the readability of the graph. As the total number of Majorana modes, χ , (and thus the bond dimension) increases, the correlation length increases, improving the correspondence between the GfPEPS and the exact result in both directions.

Chern insulator

The main text restricted itself to the numerical study of the Kitaev chain and its 2d equivalent, the p-wave superconductor, as these models contain the necessary critical features, *i.e.* both 0d and 1d Fermi surfaces. The results, however, do extend to other models. To motivate this, we include Fig. 3, displaying the energy density precision for the Chern insulator with the following Fourier space Hamiltonian

$$H = \sum_{\mathbf{k}} \begin{pmatrix} a_{\mathbf{k}}^{1\dagger} & a_{\mathbf{k}}^{2\dagger} \end{pmatrix} \mathbf{h}(\mathbf{k}) \cdot \boldsymbol{\sigma} \begin{pmatrix} a_{\mathbf{k}}^1 \\ a_{\mathbf{k}}^2 \end{pmatrix}. \quad (17)$$

Here, $\mathbf{h}(\mathbf{k}) = (\sin k_1 \quad \sin k_2 \quad \Delta + \cos k_1 + \cos k_2)$ and $\boldsymbol{\sigma}$ contains the Pauli matrices. For $|\Delta| > 2$, this model is topologically trivial, while a chiral phase with Chern number $C = 1$ ($C = -1$) is found when $0 < \Delta < 2$ ($-2 < \Delta < 0$). Critical points are located at $\Delta = -2, 0, 2$. At the boundaries between trivial and chiral phases, the dispersion relation displays only one 0d Fermi surface, located at the Brillouin zone center when $\Delta = -2$ and at (π, π) when $\Delta = 2$. The dispersion around this critical mode is linear, *i.e.* it exhibits a Dirac cone. The critical point between the two chiral phases, on the other hand, has two Dirac cones at $(0, \pi)$ and $(\pi, 0)$ and is therefore expected to contain more entanglement than the other critical points, in analogy to what we observed for the 1d Kitaev chain. GfPEPS were optimized for both types of critical models (namely for $\Delta = 0$ and $\Delta = 2$) and an even number of virtual Majorana modes was used in both directions to reproduce the exact parity configuration. Again, the bottom panels show that the thermodynamic limit is probed for all bond dimensions when $L = 1000$ and even though there is no violation of the area law of entanglement, (the onset of) a power-law improvement of the precision can be discerned from the top panels. However, the exponents are different, indicating that fewer Dirac cones require a lower bond dimension to obtain the same precision. Furthermore, the precision improvement is in both cases faster than that of the square lattice hopping model which does violate the area law of entanglement. The fact that our findings hold up in an essentially different model, indicates their more general validity.

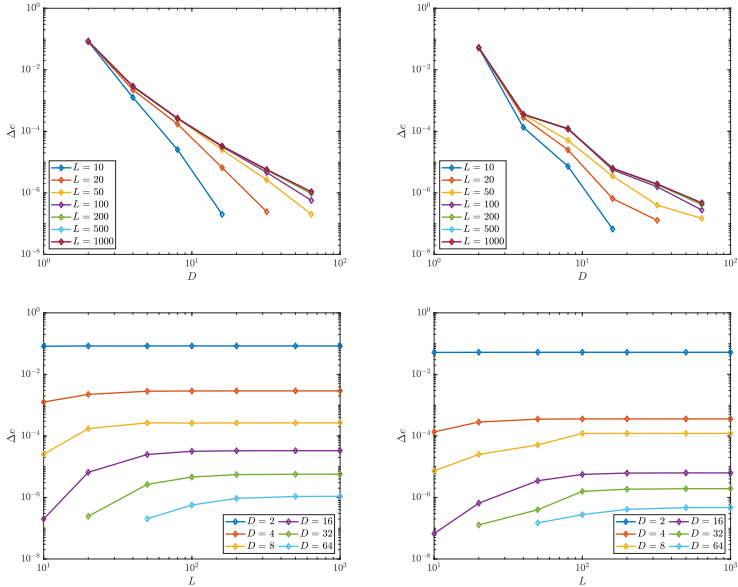


FIG. 3. Energy density error of optimized GfPEPS for a critical Chern insulator on a 2d square lattice with two Dirac cones ($\Delta = 0$, left) and one Dirac cone ($\Delta = 2$, right) as a function of both the bond dimension $D = \sqrt{2}^{\chi_1} = \sqrt{2}^{\chi_2}$ (top) and the linear system size L (bottom). The thermodynamic limit was clearly probed for all bond dimensions when $L = 1000$ and the onset of a power law can be discerned in the top panels.

5.4.2 Finite entanglement scaling in 2D metals

A second research project involving GfTNS extends the concept of finite-entanglement scaling for 1D critical models to 2D models with a Fermi surface. This resulted in a paper that is currently published as a preprint. The author performed all SU(2)-symmetric simulations with GfTNS in the Kraus-Schuch formalism while co-author Ming-Hao Li focused on the GVW formalism and its application to spinless fermions. Both these authors contributed equally to the manuscript under the supervision of Jutho Haegeman and Nick Bultinck.

Finite-entanglement scaling of 2D metals

Quinten Mortier*,¹ Ming-Hao Li*,² Jutho Haegeman,¹ and Nick Bultinck^{1,2}

¹*Department of Physics, Ghent University, Krijgslaan 281, 9000 Gent, Belgium*

²*Rudolf Peierls Centre for Theoretical Physics, Parks Road, Oxford, OX1 3PU, UK*

We extend the study of finite-entanglement scaling from one-dimensional gapless models to two-dimensional systems with a Fermi surface. In particular, we show that the entanglement entropy of a contractible spatial region with linear size L scales as $S \sim L \log(\xi f(L/\xi))$ in the optimal tensor-network, and hence area-law entangled, state approximation to a metallic state, where $f(x)$ is a scaling function which depends on the shape of the Fermi surface and ξ is a finite correlation length induced by the restricted entanglement. Crucially, the scaling regime can be realized with numerically tractable bond dimensions. We also discuss the implications of the Lieb-Schultz-Mattis theorem at fractional filling for tensor network state approximations of metallic states.

Introduction. — In the last two decades it has become increasingly clear that ground states of local lattice Hamiltonians have an interesting and rich entanglement structure. For example, generic ground states of *gapped* local Hamiltonians are observed to satisfy the so-called ‘area law’ for the entanglement entropy of a subregion, meaning that the leading term in the entanglement entropy scales with the area of the boundary separating the subregion from the rest of the system (in 1D, the area law has been proven Ref. [1]). Furthermore, subleading corrections to the area law contain universal information about the topological phase of the system [2, 3]. Related quantities, such as the entanglement spectrum [4] and multipartite entanglement measures [5–11] have also been shown to reveal topological information.

In the case of gapless local Hamiltonians, the area law is frequently violated. Two notable examples are gapless 1D systems with long-wavelength properties that can be described by conformal field theory (CFT), and systems in higher dimensions with a Fermi surface. In the former case, the entanglement of a subregion with linear size L scales as $S \sim c/3 \log L$, with c the central charge of the CFT [12–14], whereas $S \sim L^{d-1} \log L$ in a d -dimensional system exhibiting a codimension 1 Fermi surface [15–18].

The entanglement structure of ground states has direct practical consequences for classical simulations of quantum systems. The existence of an area law is both a necessary condition as well as a strong motivation to represent the ground state as a Tensor Network State (TNS) [19–22]. TNS are compressed representations of quantum states in terms of local tensors which contain a number of parameters that scales only polynomially in the system size. Since TNS can be stored and manipulated efficiently by classical computers, they form an extremely useful variational space for the study of lattice Hamiltonians. For systems violating the area law, the theory of ‘finite-entanglement scaling’ [23–28] describes how an area-law state (i.e. a TNS) best approximates the

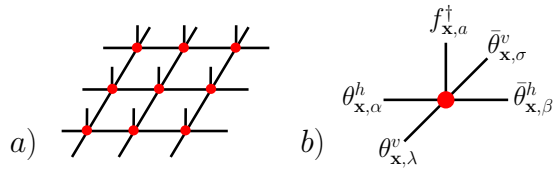


FIG. 1. (a) A 2D tensor network on a 3×3 square lattice. (b) The assignment of physical creation operators f_x^\dagger to the physical index, and virtual Grassmann variables $\theta_x, \bar{\theta}_x$ to the virtual indices, of a Gaussian fermionic tensor.

non-area-law ground state in the thermodynamic limit. A remarkable result from finite-entanglement scaling is that for 1D critical ground states described by a CFT, the finite entanglement induced by the finite TNS bond dimension D (i.e. the dimension of the virtual, contracted indices of the tensors) results in a finite correlation length $\xi \propto D^\kappa$, where κ is a universal number determined by the central charge of the CFT [23, 24]. As a result, the entanglement entropy of a region of length L can be expressed in terms of a scaling function which depends only on the ratio L/D^κ [23, 24, 29].

In this work we extend the finite-entanglement scaling analysis to two dimensions and show that a similar scaling collapse is possible for the entanglement entropy of metals, i.e. states with a Fermi surface, despite the fact that there is no underlying CFT describing the long wavelength physics. Our results show that moderate bond dimensions are sufficient to obtain information about the Fermi surface through ‘entanglement spectroscopy’. We note that some interesting previous works have studied finite-correlation-length scaling for 2D TNS [30–33], but these works did not consider area-law-violating ground states and finite-entanglement scaling.

Gaussian fermionic TNS. — For concreteness we will perform our analysis on a square lattice. Since we are interested in 2D states with a Fermi surface we use fermionic Projected Entangled-Pair States (PEPS) [34–39]. In particular, we will be working with *Gaussian* fermionic tensors, which produce either a Slater determinant or a Bardeen-Cooper-Schrieffer (BCS) pairing (or

* These authors contributed equally to this work.

pfaffian) state after contraction of the virtual indices. To define the Gaussian tensors, we assign fermion creation operators $f_{\mathbf{x},a}^\dagger$ ($a \in \{1, \dots, N\}$) to the physical index of the tensor at site \mathbf{x} , and Grassmann variables $\theta_{\mathbf{x},\alpha}^h, \bar{\theta}_{\mathbf{x},\beta}^h, \theta_{\mathbf{x},\lambda}^v, \bar{\theta}_{\mathbf{x},\sigma}^v$ ($\alpha, \beta, \lambda, \sigma \in \{1, \dots, M\}$) to the virtual indices, as in Fig. 1. The Grassmann variables square to zero, are mutually anti-commuting, and also anti-commute with the creation operators $f_{\mathbf{x},a}^\dagger$. The Gaussian tensor at site \mathbf{x} is defined as

$$\hat{T}_\mathbf{x} = \exp\left(\frac{1}{2}\chi_\mathbf{x}^T A \chi_\mathbf{x}\right), \quad (1)$$

where the column vector $\chi_\mathbf{x} \equiv (f_{\mathbf{x}}^\dagger, \theta_{\mathbf{x}}^h, \bar{\theta}_{\mathbf{x}}^h, \theta_{\mathbf{x}}^v, \bar{\theta}_{\mathbf{x}}^v)$ collects the N creation operators and $4M$ Grassmann variables assigned to site \mathbf{x} and the antisymmetric matrix $A \in \mathbb{C}^{(N+4M) \times (N+4M)}$ contains the variational parameters. Note that in Eq. (1) we have taken A to be independent of \mathbf{x} , which means that we are restricting ourselves to translation-invariant (TI) states. With the definition of the tensors in place, we can now define the (unnormalized) contracted Gaussian fermionic TNS (GfTNS) via the Berezin integral [40]

$$|\psi\rangle = \int [D\theta] \int [D\bar{\theta}] \prod_{\mathbf{x}} e^{\bar{\theta}_\mathbf{x}^h T \theta_{\mathbf{x}+\mathbf{e}_x}^h} e^{\bar{\theta}_\mathbf{x}^v T \theta_{\mathbf{x}+\mathbf{e}_y}^v} \hat{T}_\mathbf{x} |0\rangle, \quad (2)$$

where $|0\rangle$ is the physical Fock vacuum and $\mathbf{e}_{x/y}$ are unit vectors along the x/y -direction. Every Grassmann variable spans a two-dimensional super vector space, so the bond dimension of the GfTNS is $D = 2^M$.

Because we are considering TI states, the Gaussian Grassmann integral in Eq.(2) can be further simplified by going to momentum space. Working with a finite system containing $N_s = N_x N_y$ sites, and defining $\chi_\mathbf{k} = \frac{1}{\sqrt{N_s}} \sum_{\mathbf{x}} e^{i\mathbf{k}\cdot\mathbf{x}} \chi_\mathbf{x}$, we can write

$$|\psi\rangle = \int [D\theta] \int [D\bar{\theta}] \exp\left(\frac{1}{2} \sum_{\mathbf{k}} \chi_{-\mathbf{k}}^T [A + M(\mathbf{k})] \chi_\mathbf{k}\right) |0\rangle.$$

Here, $M(\mathbf{k})$ is defined as $M(\mathbf{k}) = \mathbf{0}_N \oplus \tilde{M}(\mathbf{k})$, with $\mathbf{0}_N$ a $N \times N$ zero matrix, and

$$\tilde{M}(\mathbf{k}) = \begin{pmatrix} \mathbf{0}_M & -e^{ik_x} \mathbb{1}_M \\ e^{-ik_x} \mathbb{1}_M & \mathbf{0}_M \end{pmatrix} \oplus \begin{pmatrix} \mathbf{0}_M & -e^{ik_y} \mathbb{1}_M \\ e^{-ik_y} \mathbb{1}_M & \mathbf{0}_M \end{pmatrix}. \quad (3)$$

Writing $A = \begin{pmatrix} B & -C^T \\ C & D \end{pmatrix}$, with $N \times N$ submatrix B , $4M \times N$ submatrix C , and $4M \times 4M$ submatrix D , we finally obtain

$$|\psi\rangle \propto e^{\frac{1}{2} \sum_{\mathbf{k}} f_{-\mathbf{k}}^\dagger (B + C^T [D + \tilde{M}(\mathbf{k})]^{-1} C) f_\mathbf{k}^\dagger} |0\rangle. \quad (4)$$

Here, we have assumed that $D + \tilde{M}(\mathbf{k})$ is non-degenerate at every \mathbf{k} and refer to Ref. [41] for the degenerate case.

The construction of GfTNS as presented here was introduced in Ref. [37], and has been used in numerous

previous studies [38, 42–44]. There also exists an alternative formulation in terms of density matrices [45]. For our numerical results presented below we have used both formalisms, each of which has different practical advantages. However, the two formalisms are ultimately equivalent and can be translated into each other [41].

The state in Eq. (4) takes the form of a general BCS pairing state. Given that we set out to study states with a Fermi surface, the reader might worry that we are using TNS which contract to pairing states. The reason for this is simply that a finite-D Gaussian fTNS with explicit charge conservation symmetry always has an integer particle number at every momentum which is constant throughout the Brillouin zone, and therefore cannot represent or even closely approximate a state with a Fermi surface. This is not an embarrassing shortcoming of GfTNS, but a direct consequence of the Lieb-Schultz-Mattis theorem, which states that one cannot have a trivial insulator at non-integer fillings [46–49]. In particular, in Ref. [50], it was shown that if a general, explicitly TI and U(1)-symmetric fTNS is forced to have a filling $\nu = p/q$, with p and $q > 1$ coprime integers, then the tensors necessarily have a purely virtual \mathbb{Z}_2 symmetry. The Entanglement Entropy (EE) in a generic tensor network state with such virtual symmetry scales as $S = \alpha L - \ln 2q + \mathcal{O}(L^{-1})$, which implies that the fTNS has non-trivial topological order [51–54]. So the incompatibility of Gaussianity and explicit U(1) symmetry at fractional filling $\nu = p/q$ for fTNS is a manifestation of the simple fact that Slater determinants cannot represent states with non-trivial topological order. The only way for a TI GfTNS to introduce finite entanglement in a metallic state is therefore to open a small superconducting gap at the Fermi surface.

Spinless fermions. — We first consider the case with $N = 1$, i.e. spinless fermions with a single orbital per site. To obtain the GfTNS, we minimise the energy of the following simple hopping Hamiltonian

$$H = -t \sum_{\langle ij \rangle} f_i^\dagger f_j - t' \sum_{\langle\langle ij \rangle\rangle} f_i^\dagger f_j + h.c. - \mu \sum_i f_i^\dagger f_i, \quad (5)$$

where the first (second) sum is over nearest (next-nearest) neighbours. We choose the chemical potential μ such that there is a single electron pocket centered at the Γ point. With periodic boundary conditions, the total number of electrons in the spinless Fermi sea is odd for every system size. If a state at momentum \mathbf{k} is occupied, then so is the state at $-\mathbf{k}$. So the electrons appear in pairs, except at the time-reversal invariant momenta (TRIM). Here, the only TRIM which is occupied is the center of Brillouin zone $\mathbf{k} = 0$, hence the overall fermion parity is odd. The tensors defined in Eq. (1) have even fermion parity, and therefore the GfTNS also necessarily has even parity (for every system size). This is reflected in the fact that the wavefunction in Eq. (4) with $N = 1$ always leaves the states at the TRIM empty. It

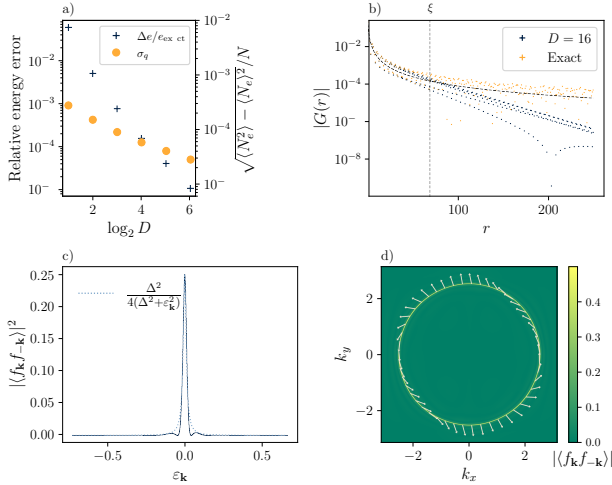


FIG. 2. Results for spinless fermions with $t'/t = 0.353$ at half filling of $N_s = 999^2$ sites. (a) Relative difference in energy per site (denoted as $\Delta e/e_{\text{exact}}$) between the exact ground state and the optimised GfTNS as a function of bond dimension D ; and the standard deviation σ_q of the particle number per site of the optimised GfTNS. (b) $|\langle f_r f_0 \rangle|$ for $D = 16$ GfTNS vs the exact ground state. Near ξ , which is extracted from the EE, $|G(r)|$ for GfTNS starts to decay much faster than the power law behaviour for that of the exact ground state. (c) $|\langle f_{\mathbf{k}} f_{-\mathbf{k}} \rangle|^2$ at $D = 32$ along a radial direction in the Brillouin zone as a function of the single-particle energy $\varepsilon_{\mathbf{k}}$ of H (Eq. (5)). (d) $\langle f_{\mathbf{k}} f_{-\mathbf{k}} \rangle$ at $D = 32$ throughout the Brillouin zone. The color map denotes the magnitude, the arrows the complex phase.

is possible to fix this discrepancy by inserting an additional Grassmann variable ‘on the virtual level’ in Eq. (2), which makes the fTNS have odd parity [41] (this Grassmann variable is identical to the string operators that have appeared in fTNS constructions [55] of the $p_x + ip_y$ superconductor [56]). Here, however, we will use a simpler way to sidestep this issue and work with anti-periodic boundary conditions such that the spinless Fermi surface state has even fermion parity for every system size.

We choose μ to fix the total particle number N_e at half filling, i.e. $\nu = N_e/N_s = 1/2$, and use $t'/t = 0.353$ to realise an almost circular Fermi surface. For these parameter values we optimised the GfTNS to minimise its energy $\langle H \rangle$, at different bond dimensions D (see Ref. [41] for details of the numerical simulations). Fig. 2(a) depicts the difference in energy of the optimal GfTNS compared the exact result, as well as the standard deviation of the total particle number per site, i.e. $\sigma_q \equiv \sqrt{\langle N_e^2 \rangle - \langle N_e \rangle^2}/N_s$. The latter is a quantifier for the charge conservation symmetry breaking in the GfTNS. We see that both the energy error and the particle number fluctuation decrease as a function of D , indicating –similarly as Ref. [57]– that the optimised GfTNS provides an approximation to the exact metallic ground state which improves systemati-

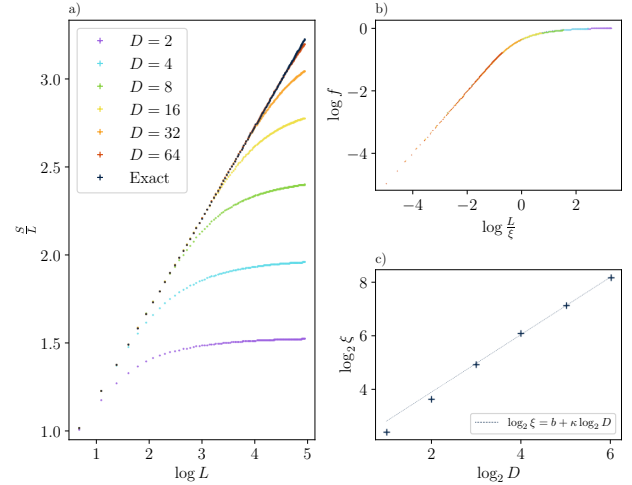


FIG. 3. (a) Scaling collapse of the entanglement entropy S of a $L \times L$ region in the optimised GfTNS for spinless fermions at half filling with $t'/t = 0.353$ and $N_s = 999^2$, obtained at different bond dimensions D . We have fixed $\alpha = 2k_F/3\pi$. (b) Linear fit of the correlation length ξ as a function of D obtained from the scaling collapse of S .

cally with bond dimension. Fig. 2(b) shows the correlation function $G(\mathbf{r}) = \langle f_{\mathbf{r}+\mathbf{r}'}^\dagger f_{\mathbf{r}'} \rangle$ of the $D = 16$ GfTNS, which agrees with the exact result for $|\mathbf{r}| \lesssim \xi \approx 70$. In Fig. 2(c) and 2(d) we plot the pairing function $\langle f_{\mathbf{k}} f_{-\mathbf{k}} \rangle$ for $D = 32$, both along a radial cut, and throughout the entire Brillouin zone. We observe that $|\langle f_{\mathbf{k}} f_{-\mathbf{k}} \rangle|^2$ is peaked at the Fermi surface and can be approximated by the BCS expression $\Delta^2/4(\Delta^2 + \varepsilon_{\mathbf{k}}^2)$, where $\varepsilon_{\mathbf{k}}$ is the single-particle dispersion of H . Fig. 2(d) illustrates that the phase of $\langle f_{\mathbf{k}} f_{-\mathbf{k}} \rangle$ winds by 2π along the Fermi surface, i.e. it is a $p_x + ip_y$ gap. We explain how the GfTNS deals with the chiral topology of the weak-pairing $p_x + ip_y$ superconductor [43, 56, 58] in the supplement [41].

The leading term in the EE of a square $L \times L$ spatial region R in a 2D state with a single spinless Fermi surface is given by

$$S = \frac{\log(\Lambda L)}{24\pi} \oint_{\partial R} \oint_{FS} |\mathrm{d}S_{\mathbf{x}} \cdot \mathrm{d}S_{\mathbf{k}}|, \quad (6)$$

where Λ is a non-universal inverse length scale, and the integrals are over the boundary of R and over the Fermi surface, and $\mathrm{d}S_{\mathbf{x}}$ ($\mathrm{d}S_{\mathbf{k}}$) is a surface element of ∂R (the Fermi surface) [16]. For the special case of a circular Fermi surface with radius k_F , this general expression evaluates to $S_{\text{circ}} = \frac{2k_F L}{3\pi} \log L$.

In Fig. 3(a), we plot the EE S as a function of L , calculated from the optimised GfTNS at different D . This plot shows our main result, which is that the leading contribution to the EE at finite D can be written as

$$S_{\text{fTNS}} = \log(\Lambda \xi f(L/\xi)) \times \frac{1}{24\pi} \oint_{\partial R} \oint_{FS} |\mathrm{d}S_{\mathbf{x}} \cdot \mathrm{d}S_{\mathbf{k}}|, \quad (7)$$

where ξ is the finite-bond-dimension-induced correlation length, and $f(x)$ is a scaling function which satisfies $f(x \ll 1) \sim x$ and $f(x \gg 1) = \text{constant}$. Fig. 3(a) shows how the optimised GfTNS at different D approximate the $L \log L$ scaling of the EE, while Fig. 3(b) directly plots the scaling function $f(x)$ onto which the numerical data obtained at different D can be collapsed. Note that to obtain the scaling collapse we have only one tuning parameter ξ if we require that the GfTNS results agree with the exact result at small L . The length scale ξ obtained from the EE of the $D = 16$ GfTNS [41] is indicated as the vertical dashed line in the plot of $G(\mathbf{r})$ in Fig. 2(b). This shows that ξ agrees with the physical correlation length, i.e. the length scale at which the exponential decay of correlations in the GfTNS sets in. Finally, Fig. 3(c) confirms that ξ increases monotonically as a function of D . For the moderate bond dimensions used in this work, ξ seems to follow a power law as a function of D . However, based on both analytical [59] and numerical [41] results in 1D, which show that Gaussian fermionic Matrix Product States (GfMPS) cannot reproduce the power-law scaling $\xi \propto D^\kappa$ of generic MPS, we anticipate that for GfTNS, deviations from the power-law relation between ξ and D could occur at higher D . For general (i.e. non-Gaussian) fTNS, we nevertheless conjecture that $\xi \propto D^\kappa$, similarly as in 1D.

Spinful fermions. — Next, we consider the same Hamiltonian as in Eq. (5), but now for spinful fermions ($N = 2$) created by $f_{\mathbf{x},\sigma}^\dagger$ with $\sigma = \uparrow, \downarrow$. An important difference between the spinless and spinful models lies in the nature of the superconducting gap of the optimal GfTNS approximation. In particular, as we explicitly impose SU(2) spin symmetry on the GfTNS, the superconducting gap will be spin-singlet and hence even under inversion.

We now verify whether the finite-entanglement scaling law (7) also holds for the spinful model. In doing so, we have used the density-matrix-based method of Kraus et al. [34, 41] for GfTNS, and a numerical optimisation which relies on minimising the Frobenius norm of the difference between the exact single-particle density matrix and the GfTNS density matrix (see Ref. [41] for details of the numerical simulations). Note that, as we impose exact SU(2) symmetry, the virtual fermion degrees of freedom are forced to carry spin-1/2, which means that the bond dimension D is restricted to occur in powers of 4.

As for the spinless model, we have computed the EE of a $L \times L$ region R for the spinful Fermi surface model and its GfTNS approximations. The spinful results displayed in Fig. 4 show a similar behavior as the spinless results in Fig. 3, with some minor differences. In particular, right before the EE reaches the area-law regime (signalled by the plateau in Fig. 4), we discern a small ‘bump’ where S_{FTNS} rises slightly above the exact value for S (indicated by the arrow in Fig. 4). We attribute this to the correlations between the different spin flavors induced by the singlet pairing. Another difference with the spinless case

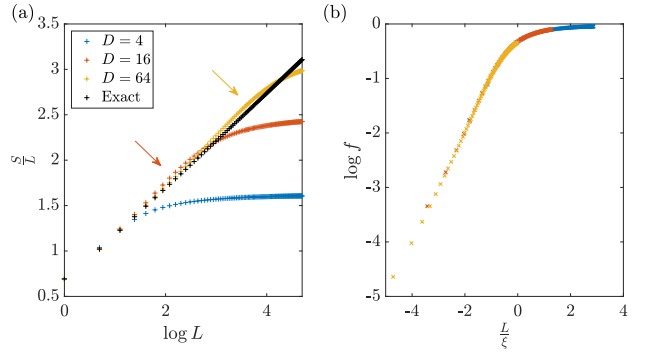


FIG. 4. (a) Entanglement entropies for a $L \times L$ square subsystem in the exact ground state and its GfTNS approximations with the indicated bond dimensions. Up to a bulk correlation length ξ the exact profile is reproduced. After the transition region with a characteristic ‘bump’ (marked by the arrows), the GfTNS profiles saturate. (b) Collapse of the GfTNS entanglement entropies using the scaling law of Eq. (7).

are the generally lower ξ values for the same bond dimension. This is a natural consequence of the increased local Hilbert space dimension. Also, the rate at which ξ increases with D is lower than in the spinless case, which is reminiscent of what happens in general 1D MPS simulations, where an increase in the central charge lowers the exponent κ in $\xi \propto D^\kappa$. Besides these minor differences, Fig. 4(b) confirms our main result, which is that the EE at different D can be collapsed using the scaling law in Eq. (7).

Properties of the scaling function. — Similarly to the scaling functions of gapless systems with conformal symmetry in the IR, $f(x)$ is expected to be insensitive to lattice-scale details. We also expect that $f(x)$ will depend on the shape of the Fermi surface, in analogy to the finite-temperature EE scaling functions for Fermi liquids [60]. To verify the first expectation we have performed numerical data collapses of the EE obtained at different fillings, while keeping the FS approximately circular. These results [41], confirm that the EE at different fillings can indeed be collapsed on the same curve. By tuning away from $t'/t = 0.353$ in either direction, which changes the FS to being either more diamond-like or more square-like, we observe that the results collapse on different scaling functions, thus confirming the dependence of $f(x)$ on the FS geometry [41].

Conclusions. — We have shown that the theory of finite-entanglement scaling can be generalized from 1D gapless systems to 2D states with a Fermi surface. Our main result is that $S_{\text{FTNS}}(L, D)$, the EE of a $L \times L$ spatial region in the optimal bond-dimension- D fTNS approximation of a metallic state, can be written as $S_{\text{FTNS}}(L, D) \sim L \log(\xi_D f(L/\xi_D))$, where ξ_D is a finite infrared length scale which results from the area-law structure (and thus the finite bond dimension D) of the tensor

network state, and $f(x)$ is a scaling function which depends on the shape of the Fermi surface, but not on the length scale k_F^{-1} , with k_F the Fermi momentum.

Fermionic tensor networks are being used in a variety of different ways, e.g. for numerical studies of lattice gauge theories [61–63], as numerically tractable Gutzwiller-projected states [64–70], as a tool for large-scale mean-field calculations with reduced computational cost [71, 72], as trial states for non-trivial topological phases [43, 52, 58, 73–76], and as a general class of variational states for numerical simulations of strongly interacting systems [36, 77–79]. The results presented in this work show how these applications of fTNS can be systematically extended to metallic states, and how information about the Fermi surface can be obtained from the scaling behaviour of the entanglement entropy.

Acknowledgments. — We acknowledge useful discussions with Hong-Hao Tu, Mike Zaletel, Roger Mong, Ignacio Cirac, Siddharth Parameswaran and Steven R. White. We also thank Siddharth Parameswaran for helpful feedback on an earlier version of the manuscript. QM and JH have received support from the European Research Council (ERC) under the European Union’s Horizon 2020 program [Grant Agreement No. 715861 (ERQUAF)] and from the Research Foundation Flanders. NB was supported by a University Research Fellowship of the Royal Society. ML has received support from the European Research Council under the European Union Horizon 2020 Research and Innovation Programme, through Starting Grant [Agreement No. 804213-TMCS], and from a Buckee Scholarship at Merton College.

-
- [1] M. B. Hastings, An area law for one-dimensional quantum systems, *Journal of Statistical Mechanics: Theory and Experiment* **2007**, P08024 (2007).
 - [2] A. Kitaev and J. Preskill, Topological entanglement entropy, *Phys. Rev. Lett.* **96**, 110404 (2006).
 - [3] M. Levin and X.-G. Wen, Detecting topological order in a ground state wave function, *Phys. Rev. Lett.* **96**, 110405 (2006).
 - [4] H. Li and F. D. M. Haldane, Entanglement spectrum as a generalization of entanglement entropy: Identification of topological order in non-abelian fractional quantum hall effect states, *Phys. Rev. Lett.* **101**, 010504 (2008).
 - [5] Y. Zou, K. Siva, T. Soejima, R. S. K. Mong, and M. P. Zaletel, Universal tripartite entanglement in one-dimensional many-body systems, *Phys. Rev. Lett.* **126**, 120501 (2021).
 - [6] K. Siva, Y. Zou, T. Soejima, R. S. K. Mong, and M. P. Zaletel, Universal tripartite entanglement signature of ungappable edge states, *Phys. Rev. B* **106**, L041107 (2022).
 - [7] Y. Liu, R. Sohal, J. Kudler-Flam, and S. Ryu, Multipartitioning topological phases by vertex states and quantum entanglement, *Phys. Rev. B* **105**, 115107 (2022).
 - [8] Y. Liu, Y. Kusuki, J. Kudler-Flam, R. Sohal, and S. Ryu,

Multipartite entanglement in two-dimensional chiral topological liquids, arXiv e-prints , arXiv:2301.07130 (2023), arXiv:2301.07130.

- [9] I. H. Kim, B. Shi, K. Kato, and V. V. Albert, Chiral central charge from a single bulk wave function, *Phys. Rev. Lett.* **128**, 176402 (2022).
- [10] P. M. Tam, M. Claassen, and C. L. Kane, Topological multipartite entanglement in a fermi liquid, *Phys. Rev. X* **12**, 031022 (2022).
- [11] R. Sohal and S. Ryu, Entanglement in tripartitions of topological orders: a diagrammatic approach, arXiv e-prints , arXiv:2301.07763 (2023), arXiv:2301.07763.
- [12] C. Holzhey, F. Larsen, and F. Wilczek, Geometric and renormalized entropy in conformal field theory, *Nuclear Physics B* **424**, 443 (1994).
- [13] G. Vidal, J. I. Latorre, E. Rico, and A. Kitaev, Entanglement in quantum critical phenomena, *Phys. Rev. Lett.* **90**, 227902 (2003).
- [14] P. Calabrese and J. Cardy, Entanglement entropy and quantum field theory, *Journal of Statistical Mechanics: Theory and Experiment* **2004**, P06002 (2004).
- [15] M. M. Wolf, Violation of the entropic area law for fermions, *Phys. Rev. Lett.* **96**, 010404 (2006).
- [16] D. Gioev and I. Klich, Entanglement entropy of fermions in any dimension and the widom conjecture, *Phys. Rev. Lett.* **96**, 100503 (2006).
- [17] B. Swingle, Entanglement entropy and the fermi surface, *Phys. Rev. Lett.* **105**, 050502 (2010).
- [18] W. Ding, A. Seidel, and K. Yang, Entanglement entropy of fermi liquids via multidimensional bosonization, *Phys. Rev. X* **2**, 011012 (2012).
- [19] M. Fannes, B. Nachtergael, and R. F. Werner, Finitely correlated states on quantum spin chains, *Communications in Mathematical Physics* **144**, 443 (1992).
- [20] F. Verstraete and J. I. Cirac, Valence-bond states for quantum computation, *Phys. Rev. A* **70**, 060302 (2004).
- [21] F. Verstraete and J. I. Cirac, Renormalization algorithms for Quantum-Many Body Systems in two and higher dimensions, arXiv e-prints , cond-mat/0407066 (2004), arXiv:cond-mat/0407066.
- [22] J. I. Cirac, D. Pérez-García, N. Schuch, and F. Verstraete, Matrix product states and projected entangled pair states: Concepts, symmetries, theorems, *Rev. Mod. Phys.* **93**, 045003 (2021).
- [23] L. Tagliacozzo, T. R. de Oliveira, S. Iblisdir, and J. I. Latorre, Scaling of entanglement support for matrix product states, *Phys. Rev. B* **78**, 024410 (2008).
- [24] F. Pollmann, S. Mukerjee, A. M. Turner, and J. E. Moore, Theory of finite-entanglement scaling at one-dimensional quantum critical points, *Phys. Rev. Lett.* **102**, 255701 (2009).
- [25] B. Pirvu, G. Vidal, F. Verstraete, and L. Tagliacozzo, Matrix product states for critical spin chains: Finite-size versus finite-entanglement scaling, *Phys. Rev. B* **86**, 075117 (2012).
- [26] V. Stojanovic, J. Haegeman, I. P. McCulloch, L. Tagliacozzo, and F. Verstraete, Conformal data from finite entanglement scaling, *Phys. Rev. B* **91**, 035120 (2015).
- [27] N. E. Sherman, A. Avdoshkin, and J. E. Moore, Universality of critical dynamics with finite entanglement, (2023), arXiv:2301.09681 [quant-ph].
- [28] A. Ueda and M. Oshikawa, Finite-size and finite bond dimension effects of tensor network renormalization, arXiv e-prints , arXiv:2302.06632 (2023), arXiv:2302.06632.

- [29] P. Calabrese and J. Cardy, Entanglement entropy and conformal field theory, *Journal of Physics A: Mathematical and Theoretical* **42**, 504005 (2009).
- [30] P. Corboz, P. Czarnik, G. Kapteijns, and L. Tagliacozzo, Finite correlation length scaling with infinite projected entangled-pair states, *Phys. Rev. X* **8**, 031031 (2018).
- [31] M. Rader and A. M. Läuchli, Finite correlation length scaling in lorentz-invariant gapless ipeps wave functions, *Phys. Rev. X* **8**, 031030 (2018).
- [32] P. Czarnik and P. Corboz, Finite correlation length scaling with infinite projected entangled pair states at finite temperature, *Phys. Rev. B* **99**, 245107 (2019).
- [33] B. Vanhecke, J. Hasik, F. Verstraete, and L. Vanderstraeten, Scaling hypothesis for projected entangled-pair states, *Phys. Rev. Lett.* **129**, 200601 (2022).
- [34] C. V. Kraus, N. Schuch, F. Verstraete, and J. I. Cirac, Fermionic projected entangled pair states, *Phys. Rev. A* **81**, 052338 (2010).
- [35] T. Barthel, C. Pineda, and J. Eisert, Contraction of fermionic operator circuits and the simulation of strongly correlated fermions, *Phys. Rev. A* **80**, 042333 (2009).
- [36] P. Corboz, R. Orús, B. Bauer, and G. Vidal, Simulation of strongly correlated fermions in two spatial dimensions with fermionic projected entangled-pair states, *Phys. Rev. B* **81**, 165104 (2010).
- [37] Z.-C. Gu, F. Verstraete, and X.-G. Wen, Grassmann tensor network states and its renormalization for strongly correlated fermionic and bosonic states, *arXiv e-prints* , arXiv:1004.2563 (2010), arXiv:1004.2563.
- [38] Z.-C. Gu, Efficient simulation of grassmann tensor product states, *Phys. Rev. B* **88**, 115139 (2013).
- [39] N. Bultinck, D. J. Williamson, J. Haegeman, and F. Verstraete, Fermionic projected entangled-pair states and topological phases, *Journal of Physics A: Mathematical and Theoretical* **51**, 025202 (2017).
- [40] F. Berezin, *The Method of Second Quantization*, Pure and applied physics : a series of monographs and textbooks. 24 (Academic Press, 1966).
- [41] See supplemental material to this article.
- [42] B. Béri and N. R. Cooper, Local tensor network for strongly correlated projective states, *Phys. Rev. Lett.* **106**, 156401 (2011).
- [43] J. Dubail and N. Read, Tensor network trial states for chiral topological phases in two dimensions and a no-go theorem in any dimension, *Phys. Rev. B* **92**, 205307 (2015).
- [44] S. Yin, N. R. Cooper, and B. Béri, Strictly local tensor networks for short-range topological insulators, *Phys. Rev. B* **99**, 195125 (2019).
- [45] N. Schuch, J. I. Cirac, and M. M. Wolf, Quantum states on harmonic lattices, *Communications in Mathematical Physics* **267**, 65 (2006).
- [46] E. Lieb, T. Schultz, and D. Mattis, Two soluble models of an antiferromagnetic chain, *Annals of Physics* **16**, 407 (1961).
- [47] I. Affleck, Spin gap and symmetry breaking in cuo₂ layers and other antiferromagnets, *Phys. Rev. B* **37**, 5186 (1988).
- [48] M. Oshikawa, Commensurability, excitation gap, and topology in quantum many-particle systems on a periodic lattice, *Phys. Rev. Lett.* **84**, 1535 (2000).
- [49] M. B. Hastings, Lieb-schultz-mattis in higher dimensions, *Phys. Rev. B* **69**, 104431 (2004).
- [50] N. Bultinck and M. Cheng, Filling constraints on fermionic topological order in zero magnetic field, *Phys. Rev. B* **98**, 161119 (2018).
- [51] N. Schuch, I. Cirac, and D. Pérez-García, Peps as ground states: Degeneracy and topology, *Annals of Physics* **325**, 2153 (2010).
- [52] N. Bultinck, M. Mariën, D. Williamson, M. Şahinoğlu, J. Haegeman, and F. Verstraete, Anyons and matrix product operator algebras, *Annals of Physics* **378**, 183 (2017).
- [53] A. Molnar, A. Ruiz de Alarcón, J. Garre-Rubio, N. Schuch, J. I. Cirac, and D. Pérez-García, Matrix product operator algebras I: representations of weak Hopf algebras and projected entangled pair states, *arXiv e-prints* , arXiv:2204.05940 (2022), arXiv:2204.05940.
- [54] A. Ruiz-de-Alarcon, J. Garre-Rubio, A. Molnar, and D. Perez-Garcia, Matrix Product Operator Algebras II: Phases of Matter for 1D Mixed States, *arXiv e-prints* , arXiv:2204.06295 (2022), arXiv:2204.06295.
- [55] T. B. Wahl, S. T. Haßler, H.-H. Tu, J. I. Cirac, and N. Schuch, Symmetries and boundary theories for chiral projected entangled pair states, *Phys. Rev. B* **90**, 115133 (2014).
- [56] N. Read and D. Green, Paired states of fermions in two dimensions with breaking of parity and time-reversal symmetries and the fractional quantum hall effect, *Phys. Rev. B* **61**, 10267 (2000).
- [57] Q. Mortier, N. Schuch, F. Verstraete, and J. Haegeman, Tensor networks can resolve fermi surfaces, *Phys. Rev. Lett.* **129**, 206401 (2022).
- [58] T. B. Wahl, H.-H. Tu, N. Schuch, and J. I. Cirac, Projected entangled-pair states can describe chiral topological states, *Phys. Rev. Lett.* **111**, 236805 (2013).
- [59] A. Franco-Rubio and J. I. Cirac, Gaussian matrix product states cannot efficiently describe critical systems, *Phys. Rev. B* **106**, 235136 (2022), arXiv:2204.02478.
- [60] B. Swingle and T. Senthil, Universal crossovers between entanglement entropy and thermal entropy, *Phys. Rev. B* **87**, 045123 (2013).
- [61] E. Zohar, M. Burrello, T. B. Wahl, and J. I. Cirac, Fermionic projected entangled pair states and local u(1) gauge theories, *Annals of Physics* **363**, 385 (2015).
- [62] P. Emonts and E. Zohar, Gauss law, minimal coupling and fermionic PEPS for lattice gauge theories, *SciPost Phys. Lect. Notes* , 12 (2020).
- [63] P. Emonts and E. Zohar, Fermionic Gaussian PEPS in 3 + 1d: Rotations and Relativistic Limits, *arXiv e-prints* , arXiv:2304.06744 (2023).
- [64] Y.-H. Wu, L. Wang, and H.-H. Tu, Tensor network representations of parton wave functions, *Phys. Rev. Lett.* **124**, 246401 (2020).
- [65] H.-K. Jin, H.-H. Tu, and Y. Zhou, Efficient tensor network representation for gutzwiller projected states of paired fermions, *Phys. Rev. B* **101**, 165135 (2020).
- [66] G. Petrica, B.-X. Zheng, G. K.-L. Chan, and B. K. Clark, Finite and infinite matrix product states for gutzwiller projected mean-field wave functions, *Phys. Rev. B* **103**, 125161 (2021).
- [67] H.-K. Jin, H.-H. Tu, and Y. Zhou, Density matrix renormalization group boosted by gutzwiller projected wave functions, *Phys. Rev. B* **104**, L020409 (2021).
- [68] J.-W. Li, J. von Delft, and H.-H. Tu, U(1)-symmetric Gaussian fermionic projected entangled paired states and their Gutzwiller projection, *arXiv e-prints* , arXiv:2208.04623 (2022), arXiv:2208.04623.

- [69] Q. Yang, X.-Y. Zhang, H.-J. Liao, H.-H. Tu, and L. Wang, Projected d-wave superconducting state: a fermionic projected entangled pair state study, *arXiv e-prints*, arXiv:2208.04566 (2022), arXiv:2208.04566.
- [70] H.-K. Jin, R.-Y. Sun, Y. Zhou, and H.-H. Tu, Matrix product states for hartree-fock-bogoliubov wave functions, *Phys. Rev. B* **105**, L081101 (2022).
- [71] M. T. Fishman and S. R. White, Compression of correlation matrices and an efficient method for forming matrix product states of fermionic gaussian states, *Phys. Rev. B* **92**, 075132 (2015).
- [72] N. Schuch and B. Bauer, Matrix product state algorithms for gaussian fermionic states, *Phys. Rev. B* **100**, 245121 (2019).
- [73] N. Bultinck, D. J. Williamson, J. Haegeman, and F. Verstraete, Fermionic matrix product states and one-dimensional topological phases, *Phys. Rev. B* **95**, 075108 (2017).
- [74] C. Wille, O. Buerschaper, and J. Eisert, Fermionic topological quantum states as tensor networks, *Phys. Rev. B* **95**, 245127 (2017).
- [75] A. Hackenbroich, B. A. Bernevig, N. Schuch, and N. Regnault, Fermionic tensor networks for higher-order topological insulators from charge pumping, *Phys. Rev. B* **101**, 115134 (2020).
- [76] S. K. Shukla, T. D. Ellison, and L. Fidkowski, Tensor network approach to two-dimensional bosonization, *Phys. Rev. B* **101**, 155105 (2020).
- [77] L. Wang, P. Corboz, and M. Troyer, Fermionic quantum critical point of spinless fermions on a honeycomb lattice, *New Journal of Physics* **16**, 103008 (2014).
- [78] B.-X. Zheng, C.-M. Chung, P. Corboz, G. Ehlers, M.-P. Qin, R. M. Noack, H. Shi, S. R. White, S. Zhang, and G. K.-L. Chan, Stripe order in the underdoped region of the two-dimensional hubbard model, *Science* **358**, 1155 (2017).
- [79] Z. Dai, Y. Wu, T. Wang, and M. P. Zaletel, Fermionic Isometric Tensor Network States in Two Dimensions, *arXiv e-prints*, arXiv:2211.00043 (2022), arXiv:2211.00043.
- [80] A. Y. Kitaev, Unpaired majorana fermions in quantum wires, *Physics-Uspekhi* **44**, 131 (2001).
- [81] H. Becker, On the transformation of a complex skew-symmetric matrix into a real normal form and its application to a direct proof of the bloch-messiah theorem, *Lettere al Nuovo Cimento (1971-1985)* **8**, 185 (1973).
- [82] P. K. Mogensen, J. M. White, A. N. Riseth, T. Holy, M. Lubin, C. Stocker, A. Noack, A. Levitt, C. Ortner, B. Johnson, D. Lin, K. Carlsson, Y. Yu, C. Rackauckas, J. Grawitter, A. Williams, A. Stukalov, B. Kuhn, B. Legat, J. Regier, J. F. de Cossio-Diaz, M. Creel, R. Rock, T. R. Covert, B. Pasquier, T. Arakaki, A. Clausen, and A. Strouwen, [Juliansolvers/optim.jl: v1.7.4](#) (2022).
- [83] S. Bravyi, Lagrangian representation for fermionic linear optics, *Quantum Info. Comput.* **5**, 216 (2005).
- [84] N. Boumal, B. Mishra, P.-A. Absil, and R. Sepulchre, Manopt, a Matlab toolbox for optimization on manifolds, *Journal of Machine Learning Research* **15**, 1455 (2014).
- [85] C.-K. Chiu, J. C. Y. Teo, A. P. Schnyder, and S. Ryu, Classification of topological quantum matter with symmetries, *Rev. Mod. Phys.* **88**, 035005 (2016).
- [86] J. Hasik, M. Van Damme, D. Poilblanc, and L. Vanderstraeten, Simulating chiral spin liquids with projected entangled-pair states, *Phys. Rev. Lett.* **129**, 177201 (2022).
- [87] A. Perelomov, “*Generalized Coherent States and their Applications*” (Springer-Verlag, Berlin, 1986).

— Supplemental Material — Finite-entanglement scaling of 2D metals

Quinten Mortier,¹ Ming-Hao Li,² Jutho Haegeman,¹ and Nick Bultinck^{1,2}

¹*Department of Physics, Ghent University, Krijgslaan 281, 9000 Gent, Belgium*

²*Rudolf Peierls Centre for Theoretical Physics, Parks Road, Oxford, OX1 3PU, UK*

We provide several appendices to support the main text while maintaining its readability.

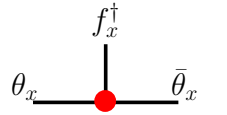
- Appendix A Degenerate GfTNS and odd parity states
- Appendix B Gu-Verstraete-Wen formalism for spinless fermions: optimisation method and additional results
- Appendix C Kraus-Schuch formalism for (symmetric) GfTNS
- Appendix D Kraus-Schuch formalism for spinful fermions: optimisation method and additional results
- Appendix E GfTNS in 1D: power law relation between precision and bond dimension cannot be sustained
- Appendix F Chirality of approximate GfTNS
- Appendix G Connection between GfTNS and general fTNS defined via super vector spaces
- Appendix H Connection between the Gu-Verstraete-Wen and Kraus-Schuch formalisms for GfTNS

Appendix A discusses how degenerate GfTNS realize odd parity states. Appendices B-D discuss the two Gaussian TNS *Ansätze* used in this work in detail and provide additional results. In Appendix E and F we describe some intricacies of these GfTNS. Finally, Appendices G and H relate both Gaussian formalisms to each other, and to generic fermionic tensor network states formulated in the super vector space formalism.

Appendix A – Degenerate GfTNS and odd parity states

In the main text we constructed GfTNS via a Berezin integral, and we mentioned two (related) subtleties that can arise in this construction: one when the matrix $D + \tilde{M}(\mathbf{k})$ as defined in Eq. (4) becomes degenerate, and the other when the state has odd fermion parity for every system size. To see how these two issues are related, we start by discussing the illuminating example of Kitaev’s Majorana chain [80]. With periodic boundary conditions, the non-trivial Majorana chain has odd fermion parity, and, as we will shortly see, the matrix $D + \tilde{M}(k)$ which appears in the Gaussian fermionic matrix-product state (GfMPS) representation of the Majorana chain is degenerate at $k = 0$.

For simplicity, we will consider the RG fixed point of the non-trivial Majorana chain (corresponding to decoupled Majorana dimers between neighbouring sites [80]), which is known to have an exact $D = 2$ fMPS representation [73]. Here we will write this exact fMPS as a GfMPS using the formalism introduced in the main text. As the fMPS has bond dimension two, we need to assign a single Grassmann number to the virtual indices of the tensors at the different sites labeled by x as follows



We also assign a single spinless electron creation operator f_x^\dagger to the physical index. Defining $\chi_x = (f_x^\dagger, \theta_x, \bar{\theta}_x)^T$, the Gaussian tensor at site x is given by

$$\hat{T}_x = \exp\left(\frac{1}{2}\chi_x^T A \chi_x\right) \quad \text{with} \quad A = \begin{pmatrix} 0 & 1 & 1 \\ -1 & 0 & 1 \\ -1 & -1 & 0 \end{pmatrix}. \quad (8)$$

Let us now proceed as in the main text and define the unnormalized GfMPS as

$$|\psi\rangle \propto \int [D\theta] \int [D\bar{\theta}] \prod_x e^{\bar{\theta}_x \theta_{x+1}} \hat{T}_x |0\rangle. \quad (9)$$

This state has even fermion parity so it cannot be the ground state of the non-trivial Majorana chain with periodic boundary conditions. But let us momentarily proceed with this state, as we will shortly see how to fix this issue.

In momentum space the GfMPS can be written as

$$|\psi\rangle \propto \int [D\theta] \int [D\bar{\theta}] \exp \left[\sum_k -(\theta_{-k} + \bar{\theta}_{-k}) f_k^\dagger + \frac{1}{2} (\theta_{-k} \bar{\theta}_{-k}) \begin{pmatrix} 0 & 1-e^{ik} \\ -1+e^{-ik} & 0 \end{pmatrix} (\bar{\theta}_k \theta_k) \right] |0\rangle. \quad (10)$$

Note that the 2D matrix appearing in the exponent becomes zero at $k = 0$. As a result, the momentum-space Grassmann variable $\frac{1}{\sqrt{2}}(\bar{\theta}_0 - \theta_0)$ does not appear in the exponent, and hence the Grassmann integral evaluates to zero. This is a manifestation of the fact that the ground state of the non-trivial Majorana chain needs to have odd fermion parity with periodic boundary conditions – in Ref. [73] it was found that when the generic fMPS representation of the Majorana chain is contracted with periodic boundary conditions it evaluates to zero, unless an additional odd matrix (the ‘ y matrix’ of Ref. [73]) is inserted on the virtual level of the fMPS. Here we also have to insert an additional odd object, i.e. the Grassmann number $\frac{1}{\sqrt{2}}(\bar{\theta}_0 - \theta_0)$, by hand into the Berezin integral in order to obtain a non-vanishing GfTNS. So the correct state is given by

$$|\psi\rangle \propto \int [D\theta] \int [D\bar{\theta}] (\bar{\theta}_0 - \theta_0) \exp \left[\sum_k -(\theta_{-k} + \bar{\theta}_{-k}) f_k^\dagger + \frac{1}{2} (\theta_{-k} \bar{\theta}_{-k}) \begin{pmatrix} 0 & 1-e^{ik} \\ -1+e^{-ik} & 0 \end{pmatrix} (\bar{\theta}_k \theta_k) \right] |0\rangle. \quad (11)$$

Performing the integral gives

$$|\psi\rangle \propto \exp \left[\frac{1}{2} \sum_{k \neq 0} (-1 \ -1) \begin{pmatrix} 0 & 1-e^{ik} \\ -1+e^{-ik} & 0 \end{pmatrix}^{-1} \begin{pmatrix} -1 \\ -1 \end{pmatrix} f_{-k}^\dagger f_k^\dagger \right] f_0^\dagger |0\rangle \quad (12)$$

$$= \exp \left[\frac{1}{2} \sum_{k \neq 0} -i \cotan \left(\frac{k}{2} \right) f_{-k}^\dagger f_k^\dagger \right] f_0^\dagger |0\rangle. \quad (13)$$

After normalizing the state, we finally arrive at

$$|\psi\rangle = \prod_{k>0} \frac{1}{\sqrt{1 + \cotan^2(k/2)}} \left(1 - i \cotan \left(\frac{k}{2} \right) f_{-k}^\dagger f_k^\dagger \right) f_0^\dagger |0\rangle, \quad (14)$$

which is indeed the ground state of the fixed-point Majorana chain Hamiltonian $H = -\sum_x f_x^\dagger f_{x+1} + i f_x^\dagger f_{x+1}^\dagger + h.c.$.

Going back to real space, the correct (i.e. non-zero and parity odd) GfMPS is given by

$$|\psi\rangle \propto \sum_{x'} \int [D\theta] \int [D\bar{\theta}] (\bar{\theta}_{x'} - \theta_{x'}) \prod_x e^{\bar{\theta}_x \theta_{x-1}} \hat{T}_x |0\rangle \quad (15)$$

$$= \sum_{x'} \int [D\theta] \int [D\bar{\theta}] (\bar{\theta}_{x'} - \theta_{x'+1}) \prod_x e^{\bar{\theta}_x \theta_{x+1}} \hat{T}_x |0\rangle. \quad (16)$$

This expression is equivalent to

$$|\psi\rangle \propto \int [D\theta] \int [D\bar{\theta}] (\bar{\theta}_{x'} - \theta_{x'+1}) \prod_x e^{\bar{\theta}_x \theta_{x+1}} \hat{T}_x |0\rangle, \quad (17)$$

i.e. we can insert $\bar{\theta}_{x'} - \theta_{x'+1}$ just once on the bond between sites $x'+1$ and x' , and the resulting expression is independent of the choice of x' . This shows that $\bar{\theta}_{x'} - \theta_{x'+1}$ is exactly the y matrix from Ref. [73], which commutes with the (G)fMPS tensors.

Having worked out the Majorana-chain example, we are now naturally lead to the following conclusions for general GfTNS:

- If the matrix $D + \tilde{M}(\mathbf{k})$ is not full rank at a particular momentum \mathbf{k} , then the state obtained by contracting the Gaussian tensors without additional Grassmann variables is zero, unless the rows of the matrix C (defined in Eq. (4)) span the kernel of $D + \tilde{M}(\mathbf{k})$.
- Assume that the rows of C do not span the kernel of $D + \tilde{M}(\mathbf{k})$, and define an arbitrary basis $|v_i\rangle$ for the part of the kernel not contained in the row space of C . In order to obtain a non-zero GfTNS, one has to insert the product of Grassmann variables $\prod_i \langle \Theta_\mathbf{k} | v_i \rangle$ ($\langle \Theta_\mathbf{k} | = (\bar{\theta}_{\mathbf{k},\alpha}, \theta_{\mathbf{k},\beta})$) in the Berezin integral which defines the GfTNS.

- If $D + \tilde{M}(\mathbf{k})$ at $\mathbf{k} = 0$ has a non-trivial kernel (which necessarily has even dimension), and the part of this kernel which is not in the row space of C has an odd dimension, then the corresponding GfTNS with periodic boundary conditions necessarily has odd fermion parity if it is non-vanishing.

In the Majorana-chain example, the kernel of $B + \tilde{M}(k)$ at $k = 0$ has dimension 2, and the part which is not spanned by the rows of C has dimension 1, hence the state necessarily has odd fermion parity. In 2D, the $p_x + ip_y$ superconductor in the weak-pairing phase also has odd parity on the torus with periodic boundary conditions along both cycles [56]. In Refs. [43, 55, 58], GfTNS representations of the weak-pairing $p_x + ip_y$ superconductor were studied, and it was found that an additional operator needs to be inserted on the virtual level in order to obtain a non-zero state [55]. In our formalism, this operator exactly corresponds to the Grassmann variable $\langle \Theta_{\mathbf{k}} | v \rangle$ at $\mathbf{k} = 0$, where $|v\rangle$ is the single vector in the kernel of $D + \tilde{M}(0)$ which is not in the row space of C . In Ref. [52], non-Gaussian fTNS were studied which represent states with non-trivial topological order, and which also have odd parity on the torus with periodic boundary conditions along both cycles. In this case, the proper generalization of the Grassmann numbers $\langle \Theta_{\mathbf{k}} | v \rangle$ are fermionic matrix-product operators [52].

Appendix B – Gu-Verstraete-Wen formalism for spinless fermions: optimisation method and additional results

In this section, we describe our numerical method to optimise GfTNS for 2D states with a Fermi surface composed of a single spinless fermion in detail. We apply the Gu-Verstraete-Wen (GVW) formalism for Gaussian tensor networks, as introduced in [37]. As $N = 1$, the B submatrix of A now reduces to zero so that

$$|\psi\rangle = \int D[\theta] D[\bar{\theta}] \prod_{\mathbf{x}} \exp\left(\bar{\theta}_{\mathbf{x}}^{h^T} \theta_{\mathbf{x}+\mathbf{e}_x}^h\right) \exp\left(\bar{\theta}_{\mathbf{x}}^{v^T} \theta_{\mathbf{x}+\mathbf{e}_y}^v\right) \exp\left(\frac{1}{2} \theta_{\mathbf{x}}^T D \theta_{\mathbf{x}}\right) \exp(\theta_{\mathbf{x}}^T C f_{\mathbf{x}}^\dagger) |0\rangle, \quad (18)$$

where $\theta_{\mathbf{x}} \equiv (\theta_{\mathbf{x}}^{h^T}, \bar{\theta}_{\mathbf{x}}^{h^T}, \theta_{\mathbf{x}}^{v^T}, \bar{\theta}_{\mathbf{x}}^{v^T})^T$ collects the virtual Grassmann numbers associated to site \mathbf{x} and $f_{\mathbf{x}}^\dagger$ creates the spinless fermion on site \mathbf{x} . Furthermore, D is a complex anti-symmetric $4M \times 4M$ matrix, whereas C is a complex vector of length $4M$. The number of (complex) variational parameters in this state thus seems to be $8M^2 + 2M$. However, the state has gauge redundancies which can be eliminated. The origin of the gauge redundancies can be discerned by examining a single term $\exp(\bar{\theta}_{\mathbf{x}}^{h^T} \theta_{\mathbf{x}+\mathbf{e}_x}^h)$, which is invariant under

$$\bar{\theta}_{\mathbf{x}}^{h^T} \mapsto \bar{\theta}_{\mathbf{x}}^{h^T} W^{-1}, \quad \theta_{\mathbf{x}+\mathbf{e}_x}^h \mapsto W \theta_{\mathbf{x}+\mathbf{e}_x}^h \quad \forall W \in GL(M, \mathbb{C}). \quad (19)$$

Similarly we can also transform θ^v and $\bar{\theta}^v$. To keep the translation invariance explicit, we can apply the same transformation to every bond. Since we are integrating the Grassmann variables out, we can check that the resulting Gaussian state is invariant under these transformations.

To make the discussions more transparent, let us write D and C in terms of blocks,

$$D \equiv \begin{bmatrix} D_{hh} & D_{h\bar{h}} & D_{hv} & D_{h\bar{v}} \\ D_{\bar{h}h} & D_{\bar{h}\bar{h}} & D_{\bar{h}v} & D_{\bar{h}\bar{v}} \\ D_{vh} & D_{v\bar{h}} & D_{vv} & D_{v\bar{v}} \\ D_{\bar{v}h} & D_{\bar{v}\bar{h}} & D_{\bar{v}v} & D_{\bar{v}\bar{v}} \end{bmatrix}, \quad C \equiv \begin{bmatrix} C_h \\ C_{\bar{h}} \\ C_v \\ C_{\bar{v}} \end{bmatrix}. \quad (20)$$

There are two independent gauge transformations, $W_{\mathbf{x}}$ and $W_{\mathbf{y}}$, transforming, for instance, the blocks D_{hh} and D_{vv} in the following way,

$$D_{hh} \mapsto W_{\mathbf{x}}^T D_{hh} W_{\mathbf{x}}, \quad D_{vv} \mapsto W_{\mathbf{y}}^T D_{vv} W_{\mathbf{y}}. \quad (21)$$

Because D_{hh} and D_{vv} are anti-symmetric, they admit real normal forms [81],

$$D_{hh} = U_h^T \left(\bigoplus_{i=1}^{\lfloor \frac{M}{2} \rfloor} \begin{bmatrix} 0 & \alpha_i \\ -\alpha_i & 0 \end{bmatrix} (\oplus[0]) \right) U_h, \quad D_{vv} = U_v^T \left(\bigoplus_{i=1}^{\lfloor \frac{M}{2} \rfloor} \begin{bmatrix} 0 & \beta_i \\ -\beta_i & 0 \end{bmatrix} (\oplus[0]) \right) U_v, \quad (22)$$

where U_h and U_v are unitary matrices, $\{\alpha_i, \beta_i\}$ are non-negative real numbers and the direct sums $\oplus[0]$ only appear when M is odd. Therefore, by choosing

$$W_{\mathbf{x}} \equiv U_h^\dagger \left(\bigoplus_{i=1}^{\lfloor \frac{M}{2} \rfloor} \begin{bmatrix} \frac{1}{\sqrt{\alpha_i}} & 0 \\ 0 & \frac{1}{\sqrt{\alpha_i}} \end{bmatrix} (\oplus[1]) \right), \quad W_{\mathbf{y}} \equiv U_v^\dagger \left(\bigoplus_{i=1}^{\lfloor \frac{M}{2} \rfloor} \begin{bmatrix} \frac{1}{\sqrt{\beta_i}} & 0 \\ 0 & \frac{1}{\sqrt{\beta_i}} \end{bmatrix} (\oplus[1]) \right), \quad (23)$$

we bring D_{hh} and D_{vv} into very simple form $J^{\oplus \lfloor \frac{M}{2} \rfloor} (\oplus [0])$ with $J = i\sigma_y$. Thus, the gauge degrees of freedom are eliminated by fixing D_{hh} and D_{vv} in our GfTNS, thereby reducing the number of complex variational parameters to $7M^2 + 3M$. We optimised GfTNS with and without fixed gauge and found matching energies, thus not only confirming the validity of the gauge fixing procedure but also providing confidence that the optimisation procedure (as described in the next paragraph) is not struggling with local minima. However, the optimisation with gauge degrees of freedom removed convergence significantly faster, which was crucial to obtain converged results for the larger bond dimensions D used in this study.

To evaluate the energy of the GfTNS, we go to momentum space,

$$|\psi\rangle = \int [D\theta] \int [D\bar{\theta}] \exp \left(\frac{1}{2} \sum_{\mathbf{k}} \theta_{-\mathbf{k}}^T [D + \tilde{M}(\mathbf{k})] \theta_{\mathbf{k}} + \theta_{-\mathbf{k}}^T C f_{\mathbf{k}}^\dagger \right) |0\rangle = \prod_{\mathbf{k}} \frac{1}{\sqrt{1 + |g_{\mathbf{k}}|^2}} \exp \left(\frac{1}{2} g_{\mathbf{k}} f_{-\mathbf{k}}^\dagger f_{\mathbf{k}}^\dagger \right) |0\rangle, \quad (24)$$

where $g_{\mathbf{k}} \equiv C^T [D + \tilde{M}(\mathbf{k})]^{-1} C = C^T S(\mathbf{k})^{-1} C$ and where $\tilde{M}(\mathbf{k})$ is defined as in Eq. (3) in the main text. Consequently, the modal occupation and pairing term expectation values are given by

$$n(\mathbf{k}) = \langle f_{\mathbf{k}}^\dagger f_{\mathbf{k}} \rangle = \frac{|g_{\mathbf{k}}|^2}{1 + |g_{\mathbf{k}}|^2}, \quad \text{and} \quad x(\mathbf{k}) = \langle f_{\mathbf{k}} f_{-\mathbf{k}} \rangle = \frac{g_{\mathbf{k}}}{1 + |g_{\mathbf{k}}|^2}. \quad (25)$$

Using this and the fact that we can rewrite the free-fermion Hamiltonian from Eq. (5) as $H = \sum_{\mathbf{k}} H(\mathbf{k}) f_{\mathbf{k}}^\dagger f_{\mathbf{k}}$ with $H(\mathbf{k}) = -2t(\cos k_x + \cos k_y) - 2t'(\cos(k_x + k_y) + \cos(k_x - k_y)) - \mu$, we obtain the energy density,

$$e = \frac{1}{N_s} \langle \psi | H | \psi \rangle = \frac{1}{N_s} \sum_{\mathbf{k}} H(\mathbf{k}) \frac{|g_{\mathbf{k}}|^2}{(1 + |g_{\mathbf{k}}|^2)}. \quad (26)$$

The above expression serves as our cost function $e \equiv e(z)$ with the variational parameters in z encoding D and C . More concretely, the first $7M^2 - M$ elements of this complex vector, denoted as z_D , encode the gauge independent entries of D . The last $4M$ entries, denoted as z_C , correspond directly to C . The gradient of the cost function w.r.t. (the complex conjugate of) z can hence be expressed as

$$2 \frac{\partial e}{\partial \bar{z}} = \frac{2}{N_s} \sum_{\mathbf{k}} H(\mathbf{k}) \frac{g_{\mathbf{k}}(z)}{(1 + |g_{\mathbf{k}}(z)|^2)^2} \frac{\partial \bar{g}_{\mathbf{k}}(\bar{z})}{\partial \bar{z}}, \quad (27)$$

where

$$\frac{\partial g_{\mathbf{k}}}{\partial z_D} = -C^T S^{-1}(\mathbf{k}) \frac{\partial S(\mathbf{k})}{\partial z_D} S^{-1}(\mathbf{k}) C, \quad \frac{\partial g_{\mathbf{k}}}{\partial z_C} = \frac{\partial C^T}{\partial z_C} S^{-1}(\mathbf{k}) C + C^T S^{-1}(\mathbf{k}) \frac{\partial C}{\partial z_C}. \quad (28)$$

It should be noted that $\partial S(\mathbf{k})/\partial z_D$ and $\partial C/\partial z_C$ are sparse matrices/vectors. Considering z_D as example, each entry in z_D is associated with an ordered pair (i, j) , such that $(\partial S(\mathbf{k})/\partial z_D)_{ij} = -(\partial S(\mathbf{k})/\partial z_D)_{ji} = 1$, and the rest of the matrix is 0. Having the analytical form of the cost function and the gradient, we use the quasi-Newton BFGS method, implemented in the `Optim.jl` package [82], to optimise the cost function. We observed that, for this problem, the BFGS method greatly outperforms alternative methods. We also remark that it is not difficult to work out the analytical expression of the Hessian of our cost function. While this enables the use of the second-order Newton's method, we found that it is too expensive in practice.

In addition to the result in the main text, we further optimised the GfTNS for Fermi surfaces with different fillings and shapes, the results for which are collected in Fig. 5. The four columns in the figure correspond to: 1) $t'/t = 0.353$, with $\mu = 0.754$ that enforces the filling to be 0.5; 2) $t'/t = 0.353$, with $\mu = 0.449$ that enforces the filling to be 0.45; 3) $t'/t = 0.353$, with $\mu = 1.00$ that enforces the filling to be 0.55; 4) $t'/t = 0.2$, with $\mu = 0.476$ that enforces the filling to be 0.5; 5) $t'/t = 0.5$, with $\mu = 0.963$ that enforces the filling to be 0.5. For all of these cases, we observe a similar scaling of energy error/correlation length with the bond dimension. Furthermore, we find that the scaling function is independent of the filling fraction (comparing cases 1, 2 and 3), but does show an (albeit weak) dependence on the shape of the Fermi surface (comparing case 1 with 4 and 5), as demonstrated in Fig. 6. While the scaling function for the different cases has the same asymptotic behavior for small and large x , there is a small deviation between the results for different Fermi surface shapes in the transition region. Drawing intuition from the finite temperature behavior of Fermi surface EE [60], it is not surprising that the scaling function is dependent on the Fermi surface shape. We leave a detailed analysis to a future study.

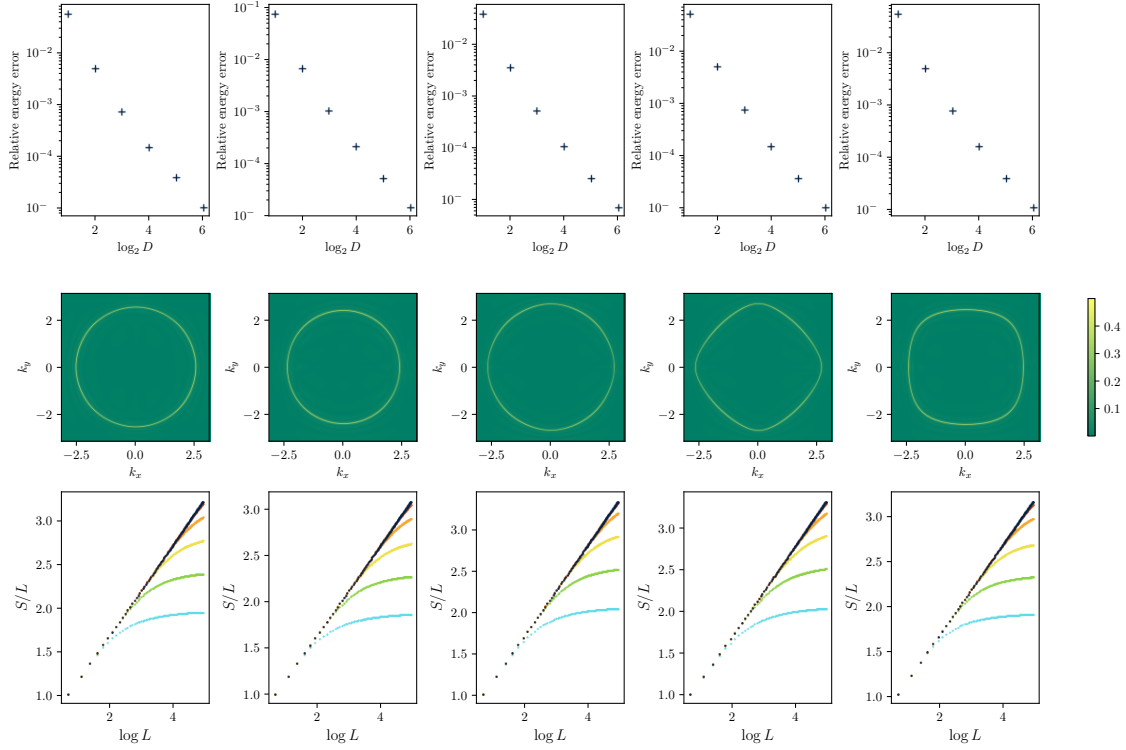


FIG. 5. Collection of additional GfTNS results for the spinless model. The columns correspond to different parameter choices for $(t, t', n_{\text{filling}})$, respectively $(1, 0.353, 0.5)$, $(1, 0.353, 0.45)$, $(1, 0.353, 0.55)$, $(1, 0.2, 0.5)$ and $(1, 0.5, 0.5)$. The system size for the optimisation of these GfTNS is $N_s = 1000^2$. The first row collects the relative energy errors for the GfTNS. The second row collects $\langle f_{\mathbf{k}} f_{-\mathbf{k}} \rangle$ at $D = 32$ throughout the Brillouin zone. The color map denotes the magnitude. The third row collects the EE of a $L \times L$ region. The color of the data is chosen to match that of Fig. 3 for bond dimensions $D = 4, 8, 16, 32, 64$, while the $D = 2$ results have been omitted because they offer a poor description of the Fermi surface.

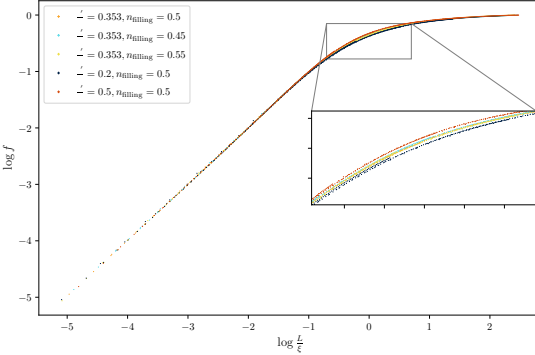


FIG. 6. The scaling collapse of EE data. We note that, in contrast with the spinful case, the scaling function for the spinless GfTNS is less sensitive to the change of Fermi surface shape. However, the fuzziness near the transition region indicates that the scaling function for the spinless case could be Fermi surface dependent after all.

We close this section by explaining how the scaling function and correlation lengths are extracted from the EE data. We recall the formula of the EE and, correspondingly, the definition of the scaling function,

$$S = \alpha L \log \left(\xi \Lambda f \left(\frac{L}{\xi} \right) \right) \iff f \left(\frac{L}{\xi} \right) = \frac{1}{\xi \Lambda} \exp \left(\frac{S}{\alpha L} \right), \quad (29)$$

where the prefactor α and UV length scale Λ are constants determined by the exact Fermi surface ground state, whereas the infrared length scale ξ depends on the bond dimension D of the GfTNS approximation. The value of ξ

as function of D should be such that the results collapse onto a single curve f . However, this leaves an overall scale undetermined, as setting $\tilde{\xi} = s\xi$ simply leads to a redefined scaling function $\tilde{f}(x) = \frac{1}{s}f(sx)$ with the same shape. This scale can be fixed by requiring that the asymptotic value $\lim_{x \rightarrow \infty} f(x) = 1$, so that $\lim_{L \rightarrow \infty} S(L) = \alpha L \log(\Lambda\xi)$. However, as the cost to compute $S(L)$ grows quite rapidly in L , namely as $\mathcal{O}(L^6)$, the calculations are restricted to moderate values of L . Hence, in practice, the scale is chosen schematically as demonstrated in Fig. 7, namely by setting $f(x) = 1$ for $x = L/\xi$ for the largest L and for the smallest D in our set, where the asymptotic regime is approximately reached. Once the correlation length for *one* bond dimension is fixed, the correlation lengths for the GfTNS at other values of D can be fixed by the collapse. The resulting values can be found in Table I.

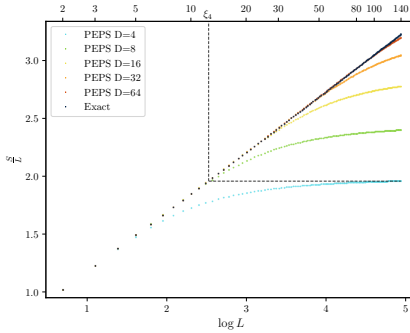


FIG. 7. The procedure to extract the correlation length from the EE data. For the GfTNS with bond dimension D , the crossover from the $\log L$ -Fermi surface regime to the area law regime is long. When the crossover is completed, S/L enters into a plateau with value $y_{\text{plateau},D} = S_D/L$. We identify the correlation length ξ_D to be the length scale at which the exact Fermi surface S_{exact}/L reaches the value $y_{\text{plateau},D}$.

t'/t	μ/t	n_{filling}	$D = 4$	$D = 8$	$D = 16$	$D = 32$	$D = 64$
0.353	0.754	0.50	12.4	30.2	68.9	141.8	287.5
0.353	0.449	0.45	11.8	28.1	63.4	132.1	265.0
0.353	1.000	0.55	13.3	33.4	77.6	163.6	321.1
0.200	0.476	0.50	13.5	34.4	80.9	170.1	322.8
0.500	0.963	0.50	11.6	27.3	60.1	127.6	244.8

TABLE I. The collection of correlation lengths, for the spinless case, obtained via the scaling collapse procedure.

Appendix C – Kraus-Schuch formalism for (symmetric) GfTNS

In Ref. [34], Kraus et al. introduced an alternative to the GVW formulation of fermionic TNS, including a restriction to the Gaussian submanifold based on [45]. This formalism was utilized here to optimise GfTNS (with a built-in SU(2) symmetry) for the spinful model. First, we introduce the basic version of this *Ansatz* without the additional symmetry. This is mostly a repetition of [57], which together with its Supplemental Material can be consulted for more details. Next, we discuss how symmetries can be added to the *Ansatz* with a focus on SU(2). Our discussion will be restricted to $d = 2$ spatial dimensions for simplicity, but the extension to general d is straightforward.

Consider again the 2D lattice built up by a periodic repetition of $N_x \times N_y = N_s$ unit cells, spanned by \mathbf{e}_x and \mathbf{e}_y . To each vertex we attribute N physical fermionic orbitals with creation (annihilation) operators $f_{\mathbf{x},j}^\dagger$ ($f_{\mathbf{x},j}$) where $j = 1, \dots, N$ is the orbital/flavor index. Corresponding Majorana operators are denoted by $c_{\mathbf{x},2j-1} = f_{\mathbf{x},j}^\dagger + f_{\mathbf{x},j}$ and $c_{\mathbf{x},2j} = -i(f_{\mathbf{x},j}^\dagger - f_{\mathbf{x},j})$. Within this framework, a PEPS *Ansatz* can be obtained by first introducing four sets of virtual Majoranas per site: $\{c_{\mathbf{x},i}^l\}$, $\{c_{\mathbf{x},i}^r\}$, $\{c_{\mathbf{x},i}^d\}$ and $\{c_{\mathbf{x},i}^u\}$, respectively in the left, right, down- and upward direction with $i = 1, \dots, \chi$. Next, a maximally correlated pure state $\rho_{\text{in}} = |\psi_{\text{in}}\rangle\langle\psi_{\text{in}}|$ is constructed on the virtual level by entangling neighbouring Majoranas in both directions. This is realised by placing the Majoranas in their joint vacuum, essentially creating χ virtual Majorana chains in each direction. Finally, the maximally correlated state is locally projected onto the physical level by a channel $\mathcal{E} = \bigotimes_{\mathbf{x}} \mathcal{E}_{\mathbf{x}}^{\text{loc}}$ encoding the fermionic PEPS tensor and

yielding the (possibly mixed) $\rho_{\text{out}} = \mathcal{E}(\rho_{\text{in}})$. By increasing the number of virtual Majoranas, the variational set can be enlarged. In the case of a pure state, it can be represented as a fTNS with an effective bond dimension $D = \sqrt{2}^{\chi}$.

Since ρ_{in} is a free-fermion state, Gaussianity of the resulting PEPS can be enforced by restricting the channel \mathcal{E} to be Gaussian as well [45, 83]. Both the input and the output state can then be fully described in terms of their real and antisymmetric correlation matrices, $\Gamma_{\mathbf{x}\mathbf{y}}^{ij} = \frac{i}{2} \text{Tr}(\rho [c_{\mathbf{x},i}, c_{\mathbf{y},j}])$, which are related in the form of a Schur complement, $\Gamma_{\text{out}} = A + B(D + \Gamma_{\text{in}}^{-1})^{-1}B^T$ where the matrices A , B and D parameterize the Gaussian channel \mathcal{E} . In fact, because of the local structure of \mathcal{E} , these matrices exhibit a decomposition $A = \bigoplus_{\mathbf{n}} A_{\mathbf{n}}^{\text{loc}}$ and similarly for B and D with $A_{\mathbf{x}}^{\text{loc}} \in \mathbb{R}^{2N \times 2N}$, $B_{\mathbf{x}}^{\text{loc}} \in \mathbb{R}^{2N \times 2d\chi}$ and $D_{\mathbf{x}}^{\text{loc}} \in \mathbb{R}^{2d\chi \times 2d\chi}$. Furthermore, $X = \begin{pmatrix} A & B \\ -B^T & D \end{pmatrix}$ is antisymmetric and $XX^T \leq \mathbb{1}$ with the equality holding for a pure state.

For TI Gaussian states, it is more convenient to work in Fourier space, where these states can be described completely in terms of the Fourier transformed correlation matrix, $G_{\mathbf{k}\mathbf{q}}^{ij} = \frac{i}{2} \text{Tr}(\rho [d_{\mathbf{k},i}, d_{\mathbf{q},j}^\dagger])$. Herein, $d_{\mathbf{k},i} = \frac{1}{\sqrt{N_s}} \sum_{\mathbf{x}} e^{-i\mathbf{k}\cdot\mathbf{x}} c_{\mathbf{x},i}$ with momentum modes \mathbf{k} . The Fourier transformed correlation matrix is anti-Hermitian, satisfies $GG^\dagger \leq \mathbb{1}$ (with the equality again holding for a pure state) and, for TI states, decomposes in diagonal blocks $G = \bigoplus_{\mathbf{k}} G(\mathbf{k})$ with, for instance,

$$G_{\text{in}}(\mathbf{k}) = \begin{pmatrix} 0 & e^{ik_x} \\ -e^{-ik_x} & 0 \end{pmatrix}^{\oplus \chi} \oplus \begin{pmatrix} 0 & e^{ik_y} \\ -e^{-ik_y} & 0 \end{pmatrix}^{\oplus \chi} \quad (30)$$

for the input state described before. Assuming translation invariance of the PEPS, so that $\mathcal{E}_{\mathbf{x}}^{\text{loc}}$ is independent of \mathbf{x} , the transition matrix X decomposes into identical blocks and yields $G_{\text{out}}(\mathbf{k}) = A^{\text{loc}} + B^{\text{loc}}(D^{\text{loc}} - G_{\text{in}}(\mathbf{k}))^{-1}B^{\text{loc}T}$ where the purity of the input state was used to replace $G_{\text{in}}^{-1}(\mathbf{k})$ by $-G_{\text{in}}(\mathbf{k})$.

To impose symmetries within this framework, we observe that in the current Gaussian context, we have to restrict to symmetries, i.e. a set of unitary transformations \mathcal{U}_g (for all $g \in G$ with G the symmetry group) commuting with the Hamiltonian ($\mathcal{U}_g H \mathcal{U}_g^\dagger = H$), that represent a canonical transformation, i.e. the operators \mathcal{U}_g map the creation and annihilation operators to a linear combination thereof that preserves the anticommutation relations. Collecting the creation and annihilation operators in the Nambu spinor, $\Upsilon_{\mathbf{x}} = (\{f_{\mathbf{x},i}\} \quad \{f_{\mathbf{x},i}^\dagger\})^T$, we must have

$$\mathcal{U} \Upsilon_{\mathbf{x},i} \mathcal{U}^\dagger = V_{\mathbf{x}\mathbf{y}}^{ji} \Upsilon_{\mathbf{y},j}, \quad (31)$$

where the $V_{\mathbf{x}\mathbf{y}}^{ji}$ factors are just numbers. We now focus on on-site symmetries where $\mathcal{U} = \bigotimes_{\mathbf{x}} \mathcal{U}_{\mathbf{x}}^{\text{loc}}$, with $\mathcal{U}_{\mathbf{x}}^{\text{loc}}$ independent of \mathbf{x} . Equivalently, we have $V_{\mathbf{x}\mathbf{y}}^{ji} = \delta_{\mathbf{x}\mathbf{y}} v^{ji}$ with v a $2N \times 2N$ matrix. In fact, for those symmetries that can be understood at the single particle level, the local matrix v further decomposes as $v = \bar{u} \oplus u$ where u is the local unitary transformation of the modes on a single site, i.e. the annihilation and creation operators transform as $\mathcal{U} f_{\mathbf{x},i} \mathcal{U}^\dagger = \bar{u}^{ji} f_{\mathbf{x},j}$ and $\mathcal{U} f_{\mathbf{x},i}^\dagger \mathcal{U}^\dagger = u^{ji} f_{\mathbf{x},j}^\dagger$ without mixing. This is true for most symmetries (particle hole transformations excluded) and in particular for the on-site SU(2) that we are targeting here. This requires that the N -dimensional mode space associated with each site decompose into a direct sum SU(2) multiplets. For the spinful Hamiltonian that we consider, $N = 2$ and the mode space corresponds exactly to a single copy of the spin- $\frac{1}{2}$ irreducible representation. For a spin rotation with angle ϕ around axis \mathbf{n} , we thus have $u = e^{i\frac{\phi}{2}\hat{\mathbf{n}}\cdot\boldsymbol{\sigma}}$ with $\boldsymbol{\sigma}$ collecting the Pauli matrices. This transformation is obtained by the many-body unitary operator

$$\mathcal{U}_{\mathbf{x}}^{\text{loc}} = \exp\left(i\frac{\phi}{2} f_{\mathbf{x}}^{\sigma\dagger} (\hat{\mathbf{n}} \cdot \boldsymbol{\sigma})_{\sigma\sigma'} f_{\mathbf{x}}^{\sigma'}\right) = \exp(i\phi \hat{\mathbf{n}} \cdot \mathbf{S}_{\mathbf{x}}) \quad (32)$$

with $\mathbf{S}_{\mathbf{x}} = f_{\mathbf{x}}^{\sigma\dagger} (\frac{\sigma}{2})_{\sigma\sigma'} f_{\mathbf{x}}^{\sigma'}$ the local spin operator.

Now consider a general free-fermion Hamiltonian

$$H = \frac{1}{2} \sum_{AB} \Upsilon_A^\dagger H_{\text{BdG}}^{AB} \Upsilon_B + \tilde{E}, \quad (33)$$

where Υ collects the Nambu spinors on all sites with the A, B labels discerning between its upper (annihilator) and lower (creator) half, \tilde{E} is an energy offset and H_{BdG}^{AB} is the Bogoliubov-de Gennes single-particle Hamiltonian, which takes the form

$$H_{\text{BdG}} = \begin{pmatrix} \Xi & \Delta \\ -\Delta & -\Xi^T \end{pmatrix}, \quad \Xi = \Xi^\dagger, \quad \Delta = -\Delta^T. \quad (34)$$

and thus satisfies $(\sigma_x \otimes \mathbb{1}_f) H_{\text{BdG}}^T (\sigma_x \otimes \mathbb{1}_f) = -H_{\text{BdG}}$. Further assuming translation invariance, $\Xi_{\mathbf{x}\mathbf{y}}^{ij} = \Xi_{\mathbf{x}-\mathbf{y}}^{ij}$ and $\Delta_{\mathbf{x}\mathbf{y}}^{ij} = \Delta_{\mathbf{x}-\mathbf{y}}^{ij}$, yields

$$H = \frac{1}{2} \sum_{\mathbf{k}} \Upsilon_{\mathbf{k}}^\dagger H_{\text{BdG}}(\mathbf{k}) \Upsilon_{\mathbf{k}} = \frac{1}{2} \sum_{\mathbf{k}} \Upsilon_{\mathbf{k}}^\dagger \begin{pmatrix} \Xi(\mathbf{k}) & \Delta(\mathbf{k}) \\ -\Delta(-\mathbf{k}) & -\Xi^T(-\mathbf{k}) \end{pmatrix} \Upsilon_{\mathbf{k}} \quad (35)$$

where $\Upsilon_{\mathbf{k}} = \left(\{f_{\mathbf{k},i}\}, \{f_{-\mathbf{k},i}^\dagger\} \right)^T$ with $f_{\mathbf{k},i} = \frac{1}{\sqrt{N}} \sum_{\mathbf{x}} e^{-i\mathbf{k}\cdot\mathbf{x}} f_{\mathbf{x},i}$, $\Xi^{ij}(\mathbf{k}) = \sum_{\mathbf{x}} e^{-i\mathbf{k}\cdot\mathbf{x}} \Xi_{\mathbf{x}}^{ij}$ and $\Delta^{ij}(\mathbf{k}) = \sum_{\mathbf{x}} e^{-i\mathbf{k}\cdot\mathbf{x}} \Delta_{\mathbf{x}}^{ij}$. As a result, $\Xi^\dagger(\mathbf{k}) = \Xi(\mathbf{k})$ and $\Delta(\mathbf{k}) = -\Delta^T(-\mathbf{k})$ so that $(\sigma_x \otimes \mathbb{1}_N) H_{\text{BdG}}^T(-\mathbf{k}) (\sigma_x \otimes \mathbb{1}_N) = -H_{\text{BdG}}(\mathbf{k})$. Invariance of such a Hamiltonian under an on-site single particle transformation u then amounts to

$$\begin{pmatrix} u & \bar{u} \end{pmatrix} H_{\text{BdG}}(\mathbf{k}) \begin{pmatrix} u^\dagger & \bar{u}^\dagger \end{pmatrix} = H_{\text{BdG}}(\mathbf{k}) \quad (36)$$

and thus requires $u\Xi(\mathbf{k})u^\dagger = \Xi(\mathbf{k})$ and $u\Delta(\mathbf{k})\bar{u}^\dagger = u\Delta(\mathbf{k})u^T = \Delta(\mathbf{k})$. For our case of interest, where $N = 2$ and u is an arbitrary SU(2) matrix, this amounts to $\Xi(\mathbf{k}) = \xi(\mathbf{k}) \otimes \mathbb{1}$ and $\Delta(\mathbf{k}) = \delta(\mathbf{k}) \otimes J$. This shows that pairing terms, opening a superconducting gap in the GfTNS approximation of the ground state of the spinful Hamiltonian, will necessarily entangle both spins as discussed in the main text.

Having discussed symmetric Hamiltonians, we now have to consider symmetric states. A state $|\psi\rangle$ is symmetric when $\mathcal{U}_g |\psi\rangle = \lambda_g |\psi\rangle$ for all $g \in G$, with λ_g a possible phase factor, which forms a one-dimensional representation of G . Expectation values of symmetric operators O ($\mathcal{U}O\mathcal{U}^\dagger = O$) then remain unchanged when performing a symmetry transformation. We can utilize this characterization to work out what the symmetry entails for the correlation matrix of a Gaussian symmetric state. For later purposes, we now generalise to the case where we have $N/2$ spinful fermion modes associated to every site or momentum, the creation operator of which is denoted by $(f_{\mathbf{k},i}^\sigma)^\dagger$ with $i = 1, \dots, N/2$. Imposing SU(2) symmetry, where we can ignore the phase factor as SU(2) does not have non-trivial one-dimensional representations, we then find

$$\begin{aligned} n_{ij}^{\sigma\sigma'}(\mathbf{k}) &= \langle f_{\mathbf{k},i}^\sigma f_{\mathbf{k},j}^{\sigma'} \rangle = \langle \psi | \mathcal{U}^\dagger \mathcal{U} f_{\mathbf{k},i}^\sigma \mathcal{U}^\dagger \mathcal{U} f_{\mathbf{k},j}^{\sigma'} \mathcal{U}^\dagger \mathcal{U} | \psi \rangle = \langle \psi | u^{\tau\sigma} f_{\mathbf{k},i}^\tau \bar{u}^{\tau'\sigma'} f_{\mathbf{k},j}^{\tau'} | \psi \rangle = (u^T)^{\sigma\tau} n_{ij}^{\tau\tau'}(\mathbf{k}) \bar{u}^{\tau'\sigma'} \\ x_{ij}^{\sigma\sigma'}(\mathbf{k}) &= \langle f_{\mathbf{k},i}^\sigma f_{-\mathbf{k},j}^{\sigma'} \rangle = \langle \psi | \mathcal{U}^\dagger \mathcal{U} f_{\mathbf{k},i}^\sigma \mathcal{U}^\dagger \mathcal{U} f_{-\mathbf{k},j}^{\sigma'} \mathcal{U}^\dagger \mathcal{U} | \psi \rangle = \langle \psi | \bar{u}^{\tau\sigma} f_{\mathbf{k},i}^\tau \bar{u}^{\tau'\sigma'} f_{-\mathbf{k},j}^{\tau'} | \psi \rangle = (u^\dagger)^{\sigma\tau} x_{ij}^{\tau\tau'}(\mathbf{k}) \bar{u}^{\tau'\sigma'} \end{aligned} \quad (37)$$

for the Fourier space hopping and pairing term expectation values and this $\forall u \in \text{SU}(2)$. As a result, $n(\mathbf{k}) = \bar{u}n(\mathbf{k})u^T$ and $x(\mathbf{k}) = ux(\mathbf{k})u^T$ implying that $n(\mathbf{k}) = n_1(\mathbf{k}) \otimes \mathbb{1}$ and $x(\mathbf{k}) = x_2(\mathbf{k}) \otimes J$, mimicking their corresponding Hamiltonian terms. Noting that $\begin{pmatrix} d_{\mathbf{k},2j-1} \\ d_{\mathbf{k},2j} \end{pmatrix} = \begin{pmatrix} +1 & +1 \\ +i & -i \end{pmatrix} \begin{pmatrix} f_{\mathbf{k},j} \\ f_{-\mathbf{k},j}^\dagger \end{pmatrix}$ the correlation matrix can be expressed as

$$G(\mathbf{k}) = J^{\oplus N} + i \left[-Wn^T(\mathbf{k})W^\dagger + \bar{W}n(-\mathbf{k})W^T + Wx(\mathbf{k})W^T + \bar{W}x^\dagger(\mathbf{k})W^\dagger \right], \quad (38)$$

where $W = \mathbb{1}_N \otimes \begin{pmatrix} 1 \\ i \end{pmatrix}$. Consequently, the terms containing $n(\mathbf{k})$ will yield contributions of the form $\dots \otimes \mathbb{1} \otimes \mathbb{1}$ and $\dots \otimes \mathbb{1} \otimes J$ while those with $x(\mathbf{k})$ give $\dots \otimes J \otimes \sigma_x$ and $\dots \otimes J \otimes \sigma_z$. Therefore, a Gaussian TI state is SU(2) symmetric with spin $\frac{1}{2}$ when

$$G(\mathbf{k}) = G_0(\mathbf{k}) \otimes \mathbb{1} \otimes \mathbb{1} + G_1(\mathbf{k}) \otimes \mathbb{1} \otimes J + G_2(\mathbf{k}) \otimes J \otimes \sigma_x + G_3(\mathbf{k}) \otimes J \otimes \sigma_z. \quad (39)$$

Together, $\mathbb{1} \otimes \mathbb{1}$, $\mathbb{1} \otimes J$, $J \otimes \sigma_x$ and $J \otimes \sigma_z$ span a real representation of the quaternions so that the correlation matrix of a symmetric state can equivalently be formulated in quaternion form $G^{\mathbb{H}}(\mathbf{k}) = G_0(\mathbf{k}) + iG_1(\mathbf{k}) + jG_2(\mathbf{k}) + kG_3(\mathbf{k})$ where $G^{\mathbb{H}\dagger}(\mathbf{k}) = -G^{\mathbb{H}}(\mathbf{k})$ and $G^{\mathbb{H}\dagger}(\mathbf{k})G^{\mathbb{H}}(\mathbf{k}) \leq \mathbb{1}$.

Knowing how symmetries and in particular SU(2) symmetry are realised in Gaussian models and states, we ask the question of how to build these into the GfTNS *Ansatz*. A natural way to do so is by starting with symmetric input states and projecting these in a symmetric way to the physical level. As we want our fPEPS to be Gaussian, operators on the physical and virtual level are only coupled quadratically, implying that operators transforming according to different irreducible representations cannot couple in a symmetric way. Hence, also the input state should be constructed out of SU(2) multiplets, and its correlation matrix should also decompose in the quaternionic, spin- $\frac{1}{2}$ manner of Eq. (39). As two Majorana operators cannot transform under the spin-1/2 representation of SU(2) (as this representation is not real, whereas a canonical transformation of Majorana operators is real orthogonal), we

need at least $\chi = 4$ Majorana operators, or thus a full spinful fermion, as elementary building block for the input state. Taking χ an integer multiple of four, a symmetric input state can be constructed with

$$G_{\text{in}}(\mathbf{k}) = \left(\begin{pmatrix} e^{-ik_x} & \\ e^{ik_x} & \end{pmatrix} \otimes J \otimes \sigma_x \right)^{\oplus \frac{\chi}{4}} \oplus \left(\begin{pmatrix} e^{-ik_y} & \\ e^{ik_y} & \end{pmatrix} \otimes J \otimes \sigma_x \right)^{\oplus \frac{\chi}{4}}. \quad (40)$$

The GfTNS can be made symmetric by requiring the channel correlation matrix to be quaternionic as well, i.e. $X \cong X^{\mathbb{H}} = X^0 + iX^1 + jX^2 + kX^3$ with $X^{\mathbb{H}} = -X^{\mathbb{H}\dagger}$ and $X^{\mathbb{H}}X^{\mathbb{H}\dagger} \leq \mathbb{1}$.

Appendix D – Kraus-Schuch formalism for spinful fermions: optimisation method and additional results

In this work, the results for spinful fermions were obtained by approximating the ground state of the spinful model by SU(2) symmetric GfTNS as introduced in Appendix C. In this case, the optimal GfTNS is found by minimising the difference between its correlation matrix $G_{\text{out}}(\mathbf{k})$ with that of the exact ground state, $G_{\text{ex}}(\mathbf{k})$. This procedure has been applied for different bond dimensions ($D = 4, 16, 64$) and for increasing system sizes. To probe the thermodynamic limit, a procedure similar to [57] was followed where optimised results for smaller system sizes were used as initial guesses for larger systems reaching up to a 1000×1000 square lattice. As the model contains both spin up and down fermions, the exact parity is even throughout the full Brillouin zone, allowing to use periodic boundary conditions and even system lengths without parity obstructions.

For the successive optimisations, a Riemannian limited-memory, quasi-Newton (L-BFGS) procedure, based on [84], was applied to find the minimum of the cost function,

$$C_F = \frac{1}{N_s} \sum_{\mathbf{k}} \left(\frac{1}{\sqrt{2N}} \|G_{\text{out}}(\mathbf{k}) - G_{\text{ex}}(\mathbf{k})\|_F \right)^2 = \frac{1}{2NN_s} \sum_{\mathbf{k}} \|\Delta G(\mathbf{k})\|_F^2, \quad (41)$$

where $\|\cdot\|_F$ denotes the Frobenius norm. Its Euclidean gradient w.r.t. the variational parameters in X^{loc} (we will drop the superscript) is easily computed,

$$\frac{\partial C_F}{\partial X_{ab}} = \frac{1}{NN_s} \sum_{\mathbf{k}} \left(\overline{\Delta G^{ij}(\mathbf{k})} \frac{\partial G_{\text{out}}^{ij}(\mathbf{k})}{\partial X_{ab}} + \Delta G^{ij}(\mathbf{k}) \frac{\partial \overline{G_{\text{out}}^{ij}}(\mathbf{k})}{\partial X_{ab}} \right), \quad (42)$$

where one can use the Schur complement formula to obtain

$$\begin{aligned} \frac{\partial G_{\text{out}}^{ij}}{\partial A_{ab}}(\mathbf{k}) &= \delta_{ia}\delta_{jb} & \frac{\partial G_{\text{out}}^{ij}}{\partial C_{ab}}(\mathbf{k}) &= -\delta_{jb}B_{iu}K_{ua}(\mathbf{k}) \\ \frac{\partial G_{\text{out}}^{ij}}{\partial B_{ab}}(\mathbf{k}) &= -\delta_{ia}K_{bv}(\mathbf{k})C_{vj} & \frac{\partial G_{\text{out}}^{ij}}{\partial D_{ab}}(\mathbf{k}) &= (BK)_{ia}(\mathbf{k})(KC)_{bj}(\mathbf{k}) \end{aligned} \quad (43)$$

with $K(\mathbf{k}) = (D - G_{\text{in}}(\mathbf{k}))^{-1}$. The parametric X matrix is not fully arbitrary since $X = -X^\dagger$, $XX^\dagger \leq \mathbb{1}$ in addition to $X \cong X^{\mathbb{H}}$ for SU(2) symmetry. Assuming purity and without any additional symmetry, we therefore parametrize X as $X = QEQT$ with Q orthogonal and E containing $\pm J$ blocks. All can be set to $+J$ via an orthogonal transformation that can be absorbed in Q . As we intend Riemannian optimisation over a manifold of variational parameters, we would like Q to live on a connected Riemannian manifold and thus restrict it to $\text{SO}(2(N+2\chi))$. The parity of the number of $-J$ blocks in E does matter now as it cannot be changed by a special orthogonal Q . Both parity choices in E should thus be considered. Similarly, SU(2) symmetry can be imposed by parameterizing X as $X = QEQT$ where all blocks now have to be (equivalent to) quaternions. For E , this implies that only $\pm J$ blocks with pairwise equal signs can appear, corresponding to $\pm \mathbb{1} \otimes J \cong \pm i$. The sign does not matter as $-i$ can always be transformed to $+i$ (e.g., via $k(-i)\bar{k} = i$). We thus choose $E^{\mathbb{H}} = \bigoplus_{n=1}^{\frac{N+2\chi}{2}} (+i)$. Q , on the other hand, has to be orthogonal so that $Q^{\mathbb{H}}Q^{\mathbb{H}\dagger} = \mathbb{1}$. Consequently, the parametric manifold is given by $\text{U}^{\mathbb{H}}(\frac{N+2\chi}{2})$, the unitary quaternion matrices with linear dimension $\frac{N+2\chi}{2}$. For SU(2), there are no different subclasses in the *Ansatz* as the spin labeling the irreducible representations is fully imposed by the physical level and allows no further freedom. We conclude that X is parametrized via an orthogonal Q living on a specific, symmetry-dependent manifold. These manifolds are Riemannian submanifolds of $\mathbb{R}^{2(N+2\chi) \times 2(N+2\chi)}$ so that the Riemannian gradient of the cost function w.r.t. Q can be expressed as $\text{grad } C_F(Q) = \text{Proj}_Q (\text{grad } \overline{C_F}(Q))$ where $\overline{C_F}(Q)$ is the smooth extension of $C_F(Q)$ to $\mathbb{R}^{2(N+2\chi) \times 2(N+2\chi)}$ and Proj_Q

the orthogonal projector of ambient vectors in the Euclidean space to the tangent bundle of the embedded manifold at Q (see [84] for more details). Using antisymmetry and the chain rule, the Euclidean gradient can be expressed as $\text{grad } \overline{C_F}(Q) = \frac{\partial \overline{C_F}}{\partial Q} = \frac{\partial C_F}{\partial X}(-2QE)$. The orthogonal projector, on the other hand, can always be expressed as $\text{Proj}_Q(V) = V - Q \text{sym}(Q^T V)$ where $\text{sym}(X) = \frac{1}{2}(X + X^T)$ so that $\text{grad } C_F(Q) = -2\frac{\partial C_F}{\partial X}QE + 2Q \text{sym}(Q^T \frac{\partial C_F}{\partial X} QE)$. This gradient and projector were combined with a suitable (here, QR -based) retraction to build the L-BFGS solver.

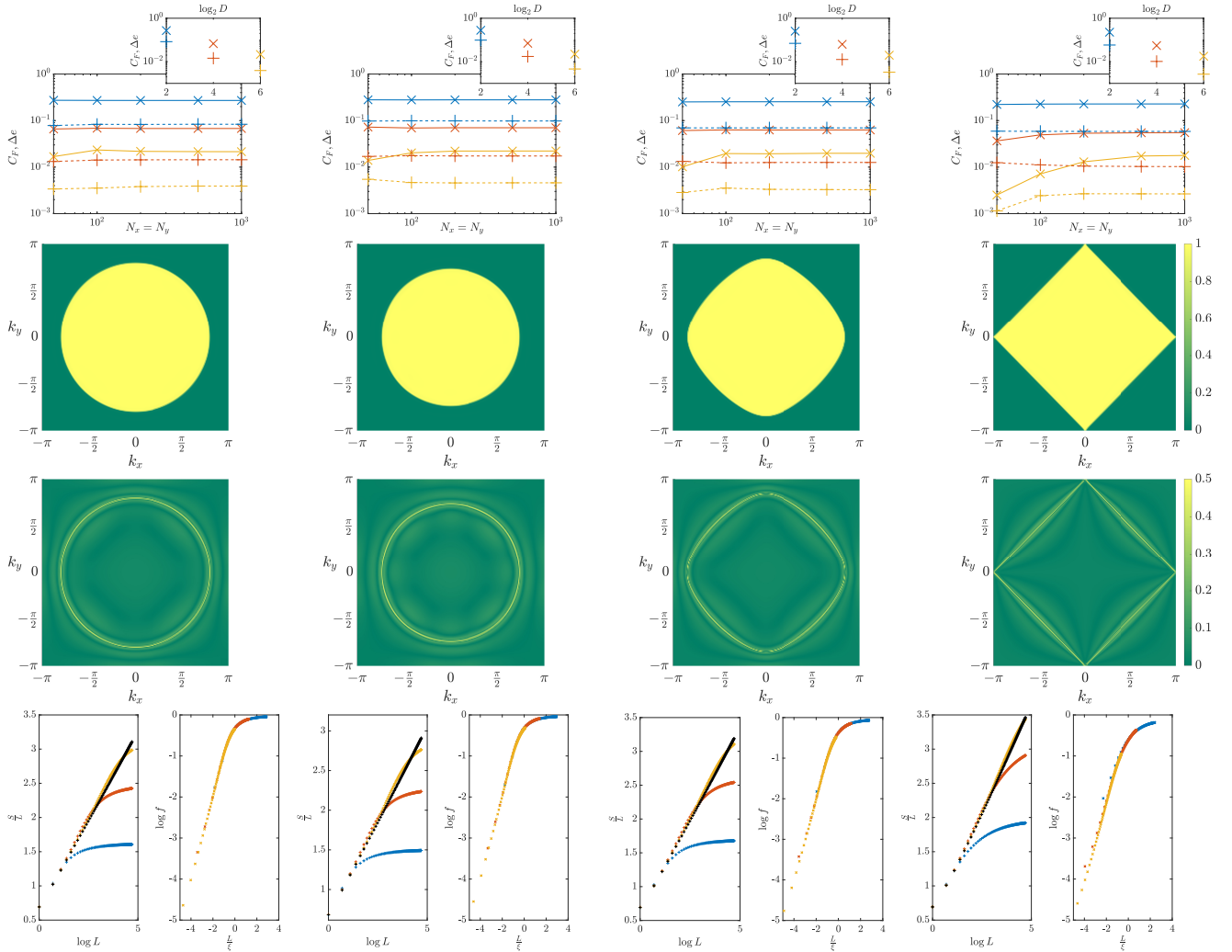


FIG. 8. Collection of GfTNS results for the spinful model. The columns correspond to different parameter choices for (t, t', μ) , respectively $(1, 0.353, 0.754)$, $(1, 0.353, 0.3)$, $(1, 0.2, 0.476)$ and $(1, 0, 0)$. The first row collects convergence results of the GfTNS optimisation for different linear system lengths $N_x = N_y$ with blue, red and yellow markers for $D = 4, 16, 64$. Cross (plus sign) markers correspond to the optimised values of the cost function C_F (energy density error Δe). The full, respectively dashed, lines were added as guide for the eye and indicate that the thermodynamic limit was probed for the largest system sizes. These results were also repeated in the inset and show a steady decrease as a function of the bond dimension. The second and third row display the modal occupation $n_1(\mathbf{k})$ and spin-coupled pairing $x_2(\mathbf{k})$ throughout the Brillouin zone for the $D = 64$ GfTNS at $N_x = 200$. While the former quantity shows that the TNS can reproduce a sharp transition from fully occupied to vacated at the Fermi surface, the latter quantity maximises its magnitude there as in Fig. 2(d). In the bottom row, the left panels display the exact EE of a $L \times L$ subregion in black and compare it to analogous GfTNS results for different bond dimensions using the color scheme of the first row. GfTNS results were collapsed according to Eq. (7) on the right panels.

In the main text, we introduced the finite-entanglement scaling law (Eq. (7)). Although the scaling function $f(x)$ is not identical for every model, some degree of universality is present. As in the spinless case, the scaling function does not seem to depend on the filling fraction. The shape of the Fermi surface on the other hand does have an influence. A more nested, square-like shape seems to widen the transition region between the asymptotic behaviors

$f(x) \approx x$ for small values of x (subject to subleading corrections to the entanglement entropy for small L and thus small x) and $f(x) \approx 1$ for large values of x . To verify this, we considered several cases, including the spinful equivalent of Eq. (5) with $(t, t', \mu) = (1, 0.353, 0.754)$, a non-half-filled version with filling fraction $n_{\text{filling}} = 0.429$ where $(t, t', \mu) = (1, 0.353, 0.3)$, a non-circular Fermi surface variant with $(t, t', \mu) = (1, 0.2, 0.476)$, and a model without next-nearest-neighbour hopping terms with $(t, t', \mu) = (1, 0, 0)$, leading to a highly nested, square Fermi surface. In all four cases, we confirmed the scaling law in Fig. 8. The entanglement entropies of the circular models with different filling fractions can be collapsed onto a single, *universal* scaling function, while this is not the case for the Fermi surfaces with different shapes, as shown in Fig. 9.

We used the SU(2) symmetric optimisation method for $D = 4, 16, 64$, gradually increasing the system size to obtain the results. The first row of Fig. 8 shows the cost function C_F , based on the correlation matrix, and the energy density error Δe for the optimised states at linear system length $N_x = N_y$. These results indicate that for the largest system sizes, N_x no longer affects the outcome, suggesting that the thermodynamic limit is being properly probed. In the insets, we compare the limit values for the different bond dimensions and find a consistent decrease. Comparing these plots with those in Fig. 2 (a), we observe that the larger magnitude in the former can be attributed to the model having twice as many physical degrees of freedom. Additionally, optimising C_F instead of e allows Δe to be slightly higher than its minimum minimorum. Finally, the enforced symmetry results in a significantly smaller number of parameters at the same bond dimension. In the second and third row of Fig. 8, the Fourier space occupation $n_1(\mathbf{k})$, respectively, pairing $x_2(\mathbf{k})$ (with $n(\mathbf{k}) = n_1(\mathbf{k}) \otimes \mathbb{1}$ and $x(\mathbf{k}) = x_2(\mathbf{k}) \otimes J$) are displayed for the largest bond dimension and for $N_x = 200$. The sharp transition in the modal occupation at the Fermi surface is clearly reproduced by the GfTNS with the same circle at $k_F = \sqrt{2\pi}$ as in Fig. 2(d) appearing for the half-filled model. For $\mu = 0.3$, on the other hand, one obtains a smaller circle at $k_F = 2.314$ while the third column with $t' = 0.2$ transitions to the square Fermi surface in the fourth column. Similar to Fig. 2, the magnitude of the pairing terms maximises at the Fermi surface to facilitate the transition from filled to empty in line with the Lieb-Schultz-Mattis theorem. However, it is spread out more than in the spinless case which can again be attributed to the double amount of physical flavors.

The left panels in the final row of Fig. 8 display a comparison between the exact and the GfTNS EE for linear subsystem lengths, L , varying from 1 to 110 and at different D . The exact $\sim L \log L$ profile is followed up to a certain correlation length ξ , after which the finite entanglement results in a saturation of the curves. In the right panels these data are collapsed using the scaling law of Eq. (7). For the circular Fermi surface, $\alpha = \frac{2k_F}{3\pi}$ while for the square Fermi surface Eq. (6) yields $\alpha = \frac{2}{3}$. When $t'/t = 0.2$, this Widom factor has to be calculated numerically, yielding $\alpha = 0.563$. The utilized correlation lengths were determined in the same way as in Appendix B and all collapsed results were combined in Fig. 9, confirming the scaling function depends on the Fermi surface morphology but not on the filling fraction.

t'/t	μ/t	n_{filling}	$ D = 4 $	$ D = 16 $	$ D = 64 $
0.353	0.754	0.500	6.255	30.63	111.8
0.353	0.300	0.429	5.797	27.58	101.1
0.200	0.476	0.500	7.032	35.16	134.0
0.000	0.000	0.500	9.868	52.06	206.2

TABLE II. Bulk correlation lengths ξ determined from the bottom row of Fig. 8 as described in Appendix B.

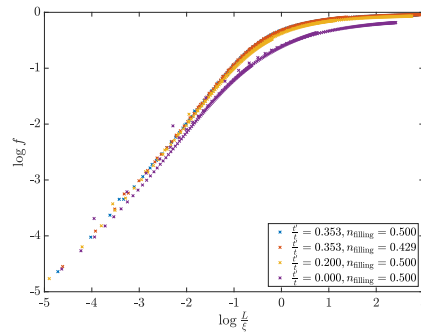


FIG. 9. Scaling function for the different parameter choices. While the scaling function depends on the Fermi surface geometry with the $f(x)$ shifting to lower values for the nested case, it is independent of the filling fraction.

Appendix E – GfTNS in 1D cannot reproduce the power law relation between correlation length and bond dimension

In Ref. [59], the authors showed that GfMPS approximate critical states significantly less efficiently than generic MPS. Here we back this claim from another perspective, namely by showing that GfMPS cannot reproduce the power-law relation $\Delta e \sim D^{-\omega}$ (recall that Δe is the error in the energy density), which is known to hold for generic MPS approximations to one-dimensional critical ground states [23–25].

Here we study a one-dimensional fermion system, with anti-periodic boundary condition, described by the following hopping Hamiltonian,

$$H = - \sum_{\langle ij \rangle} (f_i^\dagger f_j + f_j^\dagger f_i). \quad (44)$$

We work with system size $N_s = 100\,000$, and $\mu = 0$ to ensure half-filling. Using the GVW formalism, we optimised GfMPS of $D = 4, \dots, 4096$. For the optimised GfMPS, the energy density errors are plotted in Fig. 10. A closer examination of the data shows a clear deviation from the power-law behavior. Since our bond dimensions satisfy $D \equiv 2^M$, $\frac{\Delta e(M+1)}{\Delta e(M)}$ would be a constant if the power law relation is satisfied. However, as we can see in Table. III, this is clearly not the case. Moreover, in the generic MPS case, $\frac{\Delta e(M+1)}{\Delta e(M)} = 5.28$ for the model we wrote down. Thus the data presented in Table. III shows that GfMPS are not able to approximate critical states as nearly as well as generic MPS with comparable bond dimension.

M	2	3	4	5	6	7	8	9	10	11
$\frac{\Delta e(M+1)}{\Delta e(M)}$	6.6962	4.9788	4.1240	3.6087	3.2619	3.0111	2.8206	2.6707	2.5500	2.4519

TABLE III. The energy density error ratios between adjacent GfMPS.

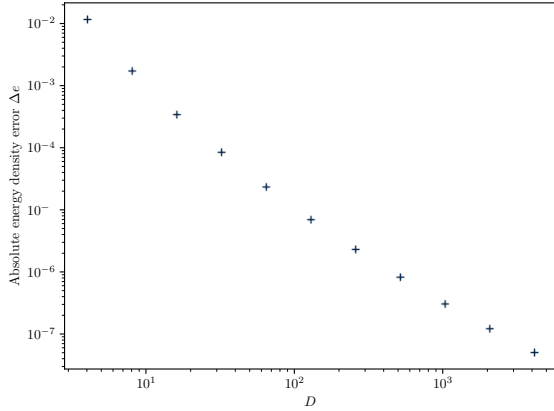


FIG. 10. The energy density error of optimised GfMPS.

This behaviour is quite well understood for GfMPS. For a bipartition of the ground state (with open boundary conditions) into a left and right half, the reduced density matrix is also Gaussian, and can be diagonalised to take the form $\exp(-\sum_m \nu_m b_m^\dagger b_m)$. For the Hamiltonian in Eq. (44) in particular, the values ν_m are proportional to the nonnegative integers in the thermodynamic limit, i.e. $\nu_m \sim m$. The entanglement spectrum (logarithm of the spectrum of Schmidt coefficients) can then be scaled to also correspond to the integers (now including zero), where each value n has a degeneracy given by the number of strict partitions $q(n)$ of that integer. A GfMPS approximation of the true ground state with M virtual fermions (or Grassmann numbers) corresponds to an MPS with bond dimension 2^M , but can only capture the values $\nu_m \sim m$ for $m = 1, \dots, M$. As a consequence, the distribution of the entanglement spectrum of the GfMPS captures the right degeneracy only up to the value $n = M$, even though it contains values all the way up to $n = M(M+1)/2$. Hence, only the first $\sum_{n=1}^M q(n) \ll 2^M$ Schmidt coefficients are correct, with in particular $\lim_{M \rightarrow 0} 2^{-M} \sum_{n=1}^M q(n) = 0$, i.e. the relative fraction of correct Schmidt coefficients decreases for increasing M .

M . A generic MPS of bond dimension 2^M is not bound by this free-fermion structure of the entanglement spectrum and can capture all Schmidt coefficients up to its full bond dimension correctly.

Whether this behaviour extends to the GfPEPS case is unclear. As there is no clear entanglement interpretation to a single PEPS bond, it is impossible to make an informed prediction about the role of the free-fermion structure in the PEPS truncation.

Appendix F – Chirality of approximate GfTNS

In the main text and Appendix A, we discussed that the even parity of the local tensors in a GfTNS induces an equal filling of all TRIMs. As a result, any (non-degenerate) GfTNS will leave the $\mathbf{k} = 0$ mode empty, thus yielding a fixed energy error. These errors tend to render the numerical optimisation less stable. Therefore, we worked with anti-periodic boundary conditions, avoiding the problematic TRIMs and the corresponding stability issues. While this easily solves the numerical problem, the conceptual one remains. Indeed, directly using a parameter matrix A , optimised for a large but finite system size N_s , in the thermodynamic limit, the $\mathbf{k} = 0$ mode will be sampled again and yield an erroneous occupation. While this will have a vanishing influence on the energy density as the corresponding energy error will be suppressed by dividing it by the diverging N_s factor (therefore not contradicting the claims made in Appendix B and D about energy densities ‘probing the thermodynamic limit’), conceptual issues also arise in the assessment of the chiral features of GfTNS. Indeed, these are characterized by the Chern number, C , a topological invariant that can be computed for all 2D TI BdG Hamiltonians (Eq. (35)) as

$$C = \frac{i}{2\pi} \int_{\text{BZ}} \text{tr } \mathcal{F}. \quad (45)$$

One thus has to integrate over the Brillouin zone and is therefore obliged to work with a \mathbf{k} continuum, i.e. to work in the thermodynamic limit. We first expand on the integrand where \mathcal{F} is the Berry curvature, a differential form defined as $\mathcal{F} = dA + A \wedge A$ [85]. Herein is $A^{\alpha\beta} = A_i^{\alpha\beta}(\mathbf{k}) dk_i$ the non-Abelian Berry connection with

$$A_i^{\alpha\beta}(\mathbf{k}) = \langle u_-^\alpha(\mathbf{k}) | \frac{\partial}{\partial k_i} | u_-^\beta(\mathbf{k}) \rangle. \quad (46)$$

where $\{|u_-^\alpha(\mathbf{k})\rangle\}$ are the N eigenvectors of $H_{\text{BdG}}(\mathbf{k})$ with a negative energy. The trace of the Berry curvature can be expressed as

$$\begin{aligned} \text{tr } \mathcal{F} &= \sum_{\alpha,\beta=1}^N dA^{\alpha\alpha} + A^{\alpha\beta} \wedge A^{\beta\alpha} \\ &= \sum_{\alpha,\beta=1}^N \left(\frac{\partial}{\partial k_i} A_j^{\alpha\alpha}(\mathbf{k}) + A_i^{\alpha\beta}(\mathbf{k}) A_j^{\beta\alpha}(\mathbf{k}) \right) dk_i \wedge dk_j = \left(\frac{\partial}{\partial k_x} \text{tr}(A_y(\mathbf{k})) - \frac{\partial}{\partial k_y} \text{tr}(A_x(\mathbf{k})) \right) dk_x dk_y. \end{aligned} \quad (47)$$

Note that there is some freedom in the eigenvectors as they can always be altered by a phase, $|v^\alpha(\mathbf{k})\rangle = e^{i\theta^\alpha(\mathbf{k})} |u^\alpha(\mathbf{k})\rangle$, resulting in gauge dependence for the Berry connection

$$A'_i^{\alpha\alpha}(\mathbf{k}) = \langle v^\alpha(\mathbf{k}) | \frac{\partial}{\partial k_i} | v^\alpha(\mathbf{k}) \rangle = A_i^{\alpha\alpha}(\mathbf{k}) + i \frac{\partial \theta^\alpha}{\partial k_i}(\mathbf{k}) \quad (48)$$

and thus also for its trace, derivatives etc. One could also collect the occupied eigenvectors in a $2N \times N$ matrix, $U_-(\mathbf{k}) = (|u_-^1(\mathbf{k})\rangle | \dots | |u_-^N(\mathbf{k})\rangle)$ so that $\text{tr}(A_i) = \text{tr}(U_-^\dagger(\mathbf{k}) \frac{\partial}{\partial k_i} U_-(\mathbf{k}))$, showing that gauge independent properties like the Chern number will not depend on the exact form of the $\{|u_-^\alpha(\mathbf{k})\rangle\}$ but rather on the occupied space spanned by these vectors and how this space behaves throughout the Brillouin zone. Therefore, an even more general gauge transformation is allowed, $V_-(\mathbf{k}) = U_-(\mathbf{k})g(\mathbf{k})$ where $g(\mathbf{k})$ is an $N \times N$ unitary matrix. For the corresponding change in the Berry connection and curvature, one obtains $A' = g^{-1}A g + g^{-1}dg$ and $\mathcal{F}' = g^{-1}\mathcal{F}g$, manifestly showing that the Chern number is indeed gauge independent. Another way to capture the occupied space is via the spectral projector

$$P(\mathbf{k}) = \sum_{\alpha \text{ occ.}} |u^\alpha(\mathbf{k})\rangle \langle u^\alpha(\mathbf{k})| = U_-(\mathbf{k}) U_-^\dagger(\mathbf{k}) \quad (49)$$

or equivalently $Q(\mathbf{k}) = 1 - 2P(\mathbf{k})$. Due to gauge independence, both belong to the Grassmannian manifold $\text{Gr}(N, 2N) = \text{U}(2N)/(\text{U}(N) \times \text{U}(N))$. Topologically distinct maps on this manifold are classified via their second homotopy group, $\pi_2(\text{Gr}(N, 2N))$, and are hence characterized by an integer topological invariant. This is again the Chern number which can be expressed as

$$C = -\frac{i}{16\pi} \int_{\text{BZ}} \text{tr} (Q \, dQ \wedge dQ) . \quad (50)$$

Now consider a pure, Gaussian and TI state, fully characterized by its Fourier transformed correlation matrix $G(\mathbf{k})$ as discussed in Appendix C. Purity implies that $G^2(\mathbf{k}) = -\mathbb{1}$ so that the eigenvalues of $G(\mathbf{k})$ are $\pm i$. Consequently, a flat-band TI BdG parent Hamiltonian can always be constructed with $H_{\text{BdG}}(\mathbf{k}) = -iV^\dagger G(\mathbf{k})V$ and $V = \mathbb{1}_N \otimes \begin{pmatrix} +1 & +1 \\ +i & -i \end{pmatrix}$ the constant matrix transforming the Fourier space Nambu spinor in the $\{d_{\mathbf{k},i}\}$ operators (with $V^{-1} = \frac{1}{2}V^\dagger$). Indeed, when

$$H = \frac{1}{2} \sum_{\mathbf{k}} \Upsilon_{\mathbf{k}}^\dagger H_{\text{BdG}}(\mathbf{k}) \Upsilon_{\mathbf{k}} = \frac{1}{8} \sum_{\mathbf{k}} d_{\mathbf{k}}^\dagger V H_{\text{BdG}}(\mathbf{k}) V^\dagger d_{\mathbf{k}} , \quad (51)$$

the energy of a Gaussian state characterized by $\tilde{G}(\mathbf{k})$ can be evaluated as

$$E \left[\tilde{G}(\mathbf{k}) \right] = \frac{i}{8} \sum_{\mathbf{k}} \text{Tr} \left(V H_{\text{BdG}}(\mathbf{k}) V^\dagger \tilde{G}(\mathbf{k}) \right) = \frac{1}{2} \sum_{\mathbf{k}} \text{Tr} \left(G(\mathbf{k}) \tilde{G}(\mathbf{k}) \right) \quad (52)$$

which is minimal for $\tilde{G}(\mathbf{k}) = G(\mathbf{k})$ with $E = -NN_s$. Denoting the orthonormal eigenvectors of $G(\mathbf{k})$ with eigenvalue $\pm i$ as $|w_{\pm}^{\alpha}(\mathbf{k})\rangle$ we have $H_{\text{BdG}}(\mathbf{k}) \frac{1}{\sqrt{2}} V^\dagger |w_{\pm}^{\alpha}(\mathbf{k})\rangle = (\pm 2) \frac{1}{\sqrt{2}} V^\dagger |w_{\pm}^{\alpha}(\mathbf{k})\rangle$, showing that the single particle energy bands are indeed flat and that $|u_{\pm}^{\alpha}(\mathbf{k})\rangle = \frac{1}{\sqrt{2}} V^\dagger |w_{\pm}^{\alpha}(\mathbf{k})\rangle$. We thus get access to the occupied space and find $G(\mathbf{k}) = i \left(W_+(\mathbf{k}) W_+^\dagger(\mathbf{k}) - W_-(\mathbf{k}) W_-^\dagger(\mathbf{k}) \right) = \frac{i}{2} V Q(\mathbf{k}) V^\dagger$. The Chern number can hence be evaluated directly from the Fourier transformed correlation matrix as

$$C = \frac{1}{16\pi} \int_{\text{BZ}} \text{Tr} \left(G(\mathbf{k}) \left[\frac{\partial G}{\partial k_x}(\mathbf{k}), \frac{\partial G}{\partial k_y}(\mathbf{k}) \right] \right) dk_x dk_y . \quad (53)$$

We conclude that to mathematically assess the topological features of optimised GfTNS, we have to go to the thermodynamic limit in order to compute this integral. Here, we will be confronted again with the conceptual issues near the zone center. Indeed, take a GfTNS with $D = 16$, optimised for the spinless model (Eq. (5)) on a finite lattice with antiperiodic boundary conditions and $N_s = 50^2$. Fig. 11 (c) displays the integrand in Eq. (53) for this state when evaluated on a finer mesh ($N_s = 100^2$) with periodic boundary conditions (for instance in an attempt to numerically approximate the integral in Eq. (53)). We observe that the Berry curvature generated at the Fermi surface is compensated near the zone center to yield a topologically trivial state. Indeed, the no-go theorem of Read and Duval [43] requires a degenerate state to realise chirality. We observe that the numerically optimised GfTNS never becomes truly degenerate, i.e. the quantity $d(\mathbf{k}) = \det(D - G_{\text{in}}(\mathbf{k}))$ depicted in Fig. 11(b) becomes small ($\sim 10^{-7}$) but never reaches zero. Hence, our numerically optimised GfTNS realises $C = 0$ and an equal occupation on all TRIMs (see Fig. 11(a)). In the strict mathematical sense, GfTNS optimised on a finite lattice are therefore not chiral.

In Fig. 11 we show that the region at the zone center, compensating the Berry curvature generated near the Fermi surface, is very small in \mathbf{k} space. Optimising the GfTNS at increasingly larger system sizes shows that this region steadily shrinks. Indeed, from a numerical perspective, we understand that when more small \mathbf{k} modes are sampled and optimised towards complete occupation, the size of the region around $\mathbf{k} = 0$ where $n(\mathbf{k}) \neq 1$ decreases. This is confirmed in Fig. 12, where we compare the average occupation for a zoomed-in region around the zone center for GfTNS optimised at different N_s . Not only is the dip in the occupation smeared out in one spatial direction (i.e. the k_x direction here, as could already be observed in Fig. 11) to avoid as many sampled \mathbf{k} points as possible, it also becomes smaller when the GfTNS optimisation is performed at higher N_s . Repeating this process for increasing N_s values, the central panel of Fig. 12 shows that the characteristic radius $k_r = \sqrt{\sigma_x \sigma_y}$ of the underoccupation region (obtained by a Gaussian fit to the peak with standard deviations σ_x and σ_y) steadily decreases. If this process were continued for even higher N_s , one would eventually end up with a state where k_r decreases to zero in the thermodynamic limit, or thus, the underoccupation region reduces to a single point. Of course, to accommodate these smaller underoccupation regions, the determinant $d(\mathbf{k})$ will become smaller as well (see again the central panel of Fig. 12) to eventually yield

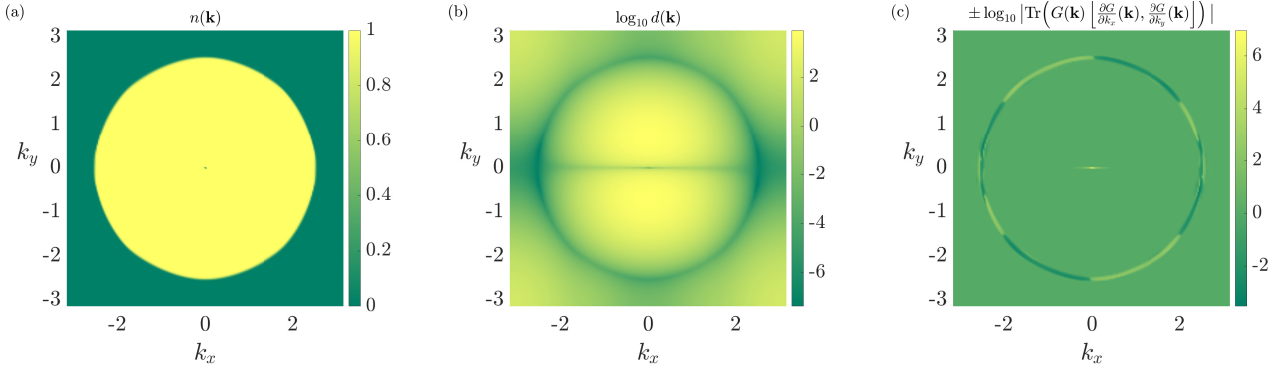


FIG. 11. A GfTNS optimised for the spinless model (Eq.(5)) on a finite lattice ($N_s = 50^2$) with antiperiodic boundary conditions is examined on a finer mesh in \mathbf{k} space ($N_s = 100^2$) with periodic boundary conditions. Panel (a) shows that the average occupation in the zone center is not reproduced correctly due to the well-known parity obstructions for non-degenerate GfTNS. Panel (b) displaying $\log_{10} d(\mathbf{k})$ confirms that this state is indeed non-degenerate and thus non-chiral. In (c) the latter is made visible by displaying the integrand in Eq. (53) throughout the Brillouin zone (i.e. the trace of the Berry curvature up to a prefactor). The (mostly negative) Berry curvature generated near the Fermi surface is compensated near the zone center by a positive peak. Note that we took the logarithm of the integrand due to the large absolute values. Signs were added again afterwards and the color axis should be read accordingly.

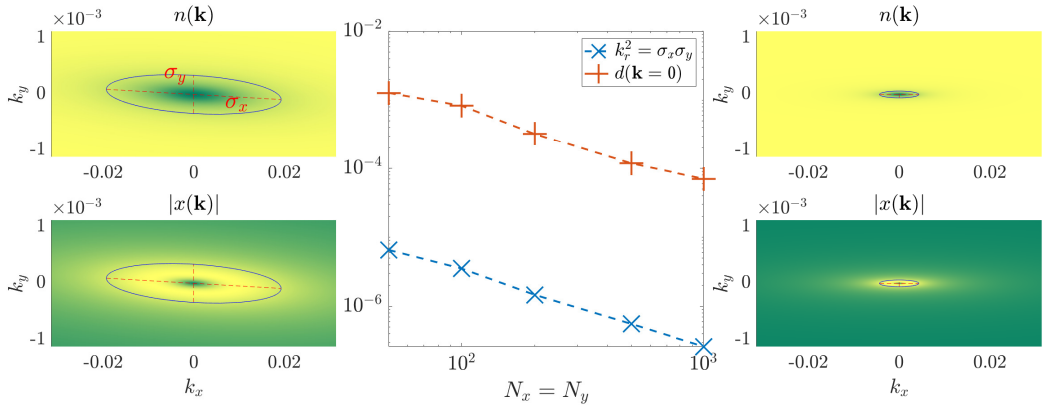


FIG. 12. Comparison of the near-zone-center behavior between GfTNS optimised for the spinless model (Eq.(5)) on finite lattices with antiperiodic boundary conditions and increasing system sizes. The left panels display the average occupation $n(\mathbf{k})$ and pairing term expectation values $|x(\mathbf{k})|$ for optimisation on the smallest lattice ($N_s = 50^2$). The right panels show the same but for $N_s = 1000^2$. The underoccupation regions are strongly anisotropic and spread out in one spatial direction (notice the different scales on both axes). Furthermore, they clearly become smaller when the optimisation lattice is increased in size. To quantify this, a Gaussian profile with standard deviations σ_x, σ_y was fitted to the underoccupation peaks with $k_r = \sqrt{\sigma_x \sigma_y}$ as a relevant momentum scale. As $N_x = N_y$ increases, k_r^2 (proportional to the area of the ellipses spanned by σ_x and σ_y) decreases $\sim N_x^{-1}$. A similar power law can be observed in the determinant $d(\mathbf{k})$ in the zone center. We conclude that by increasing N_s the GfTNS decreases the size of the erroneous region, simultaneously making the state more degenerate.

a degenerate state with a nonzero Chern number $C \neq 0$. Finally, note that the pairing terms in the neighbourhood of the zone center are again maximised where the occupation changes.

As our optimised GfTNS are not exactly degenerate, we do not expect power-law tails in real space correlations as in [58]. However, three regimes can still be discerned (see Fig. 13). For the smallest distances, the algebraic decay of correlations of the exact metallic ground state is reproduced up to the bulk correlation length ξ , corresponding to the superconducting gap near the Fermi surface. Fig. 13 confirms that this bond dimension induced length scale is the same as in the EE scaling law and thus the most relevant for this work. After ξ , the state realises an exponential decay of correlations, characteristic to TNS with a finite bond dimension and similar to the situation for MPS approximations of one-dimensional critical states. In these two regimes (Friedel) oscillations are present (consistent with wavelength $\frac{2\pi}{k_F}$). Indeed, the correlations are dominated by what happens near the Fermi surface (i.e. at the

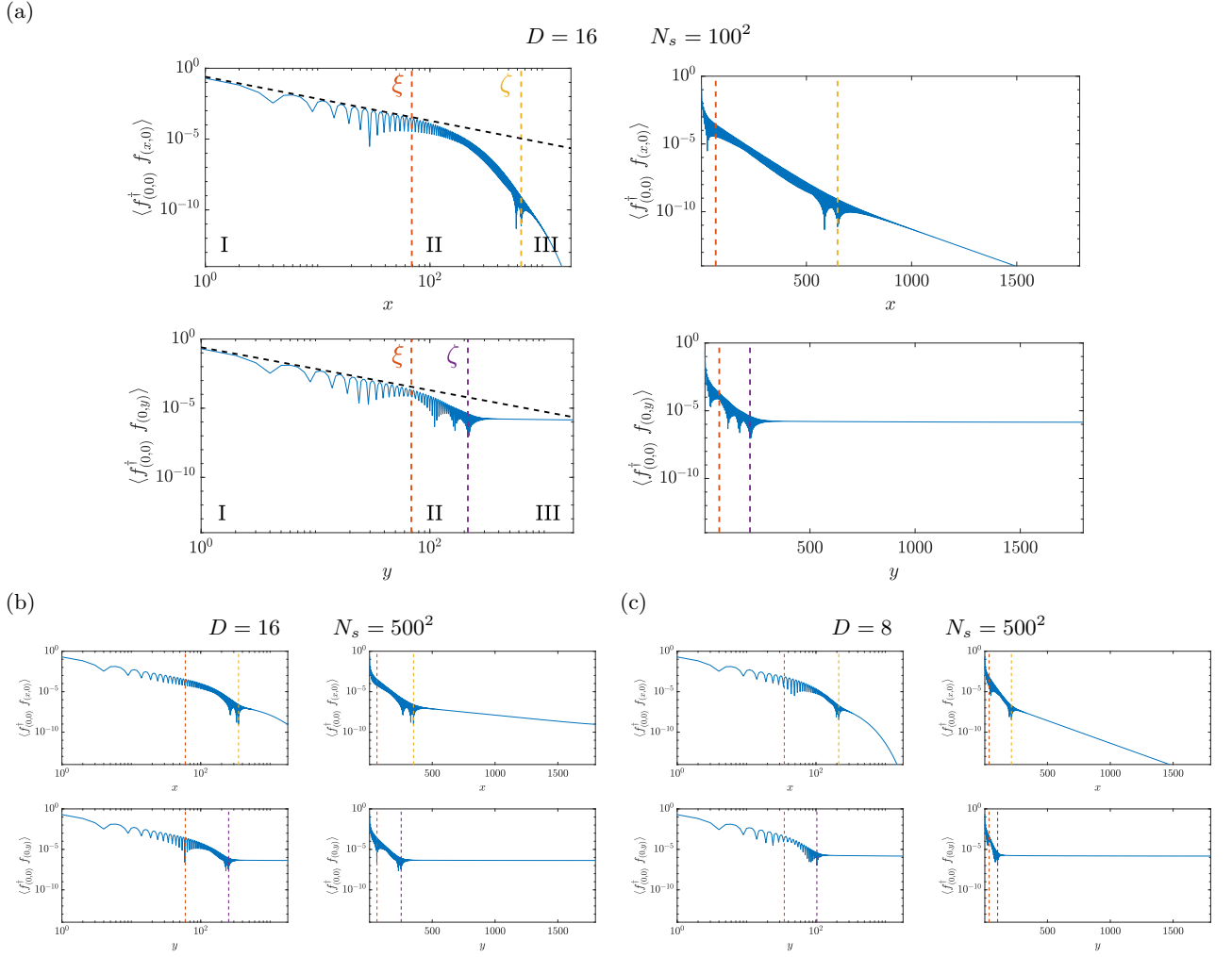


FIG. 13. Real-space correlations $\langle f_{\mathbf{0}}^\dagger f_{\mathbf{x}} \rangle$ for GfTNS with the indicated bond dimension, D , optimised on a lattice with N_s sites. Panel (a) displays the basic case with $D = 16$ and $N_s = 100^2$. In panel (b) the optimisation lattice is increased in size. Additionally, the bond dimension is decreased in panel (c). On each panel, the left (right) graphs have a log-log (lin-log) scale to discern between regions with algebraic and exponential decay of correlations. The bottom (top) graphs display the correlations in the x (y) direction. The (envelope of the) exact power law (indicated with the dashed black line) is reproduced up to the bulk correlation length ξ taken from Table II (region I). After that the decay becomes exponential with a fixed exponent up to ζ (region II). Note that this length scale is different in the x and y direction, approaching each other when N_s increases. For distances well above ζ , a second exponential region sets in (region III) where the decay becomes flatter when N_s increases. A higher bond dimension shifts ξ and ζ to higher values and flattens out the tails as well.

Fermi momentum k_F). Finally, a third regime takes over at a very large length scale, ζ . The decay in this regime is exponential as well but displays no oscillations. We understand this regime as originating from what happens near the zone center (hence the absence of oscillations). Indeed, the near-degenerate/chiral, sharply peaked behavior at $\mathbf{k} = 0$ requires long-range tails in the real-space correlations. This is reminiscent of the long-range tails observed in [86] for generic PEPS approximations of chiral states. We also obtained some qualitative insight in how these tails behave as function of the bond dimension D and N_s , the system size used for the optimisation. For increasing N_s , GfTNS become more singular with a sharper peak near the zone center. As a result, the exponent in the long-range tails decreases, yielding a more flat profile in the third region. This effect can also be observed when examining the correlations in the y -direction. Indeed, the underoccupation region is already more squeezed in this direction for the smallest N_s , resulting in even more flat profiles setting in at smaller ζ . Increasing N_s , it thus seems that the real-space correlations in both directions become more alike with an almost flat long-range tail setting in at ζ values that grow closer in both directions. The bond dimension plays a more involved role. As we know from the

EE scaling, increasing D increases ξ . This is reflected in a lower ξ in Fig. 13(c) compared to (a) due to the smaller D . Furthermore, the smaller number of variational degrees of freedom, results in a smoother peak at $\mathbf{k} = 0$ when compared to panel (b). As a result, correlations in the third region decay faster and the ζ values in both directions differ more. However, they are both smaller than the ζ values observed for $D = 16$. Therefore, we expect that the transition between the second and third region also shifts to higher distances when the bond dimension is increased. We reserve a more rigorous study of the real-space correlations for a follow-up work.

To summarize, optimised GfTNS are not strictly chiral as they are not degenerate and therefore do not have power-law tails in their real-space correlations. However, increasing the system size used during optimisation, they approach degeneracy/chirality increasingly well so that a minor change in the variational parameters can convert the states from non-chiral to chiral. Moreover, the long-range tails have no influence whatsoever on expectation values of local operators and the optimised states thus behave as their fully chiral counterparts for all practical purposes on finite lattices. That is why we classify the optimised GfTNS in the main text as approximate $p_x + ip_y$ -superconductors. Alternatively, one could impose degeneracy (and thus chirality) as an extra constraint on the parametric manifold. However, this constraint is more involved (Appendix A) to combine with the utilized optimisation schemes. Therefore, this manifestly chiral construction was not pursued here.

Appendix G – Connection between GfTNS and general fTNS defined via super vector spaces

The most commonly used TNS represent spin wave functions, and hence are bosonic, i.e. the constituent tensors are simply arrays of complex numbers. To every index of the bosonic tensors we can associate a vector space with a particular choice of basis, and the arrays of complex numbers represent the components of the tensors in these basis.

Fermionic TNS are defined as a natural extension of conventional bosonic TNS. In particular, to every index of a fermionic tensor one associates a *super* vector space V [73]. A super vector space is a \mathbb{Z}_2 graded vector space, which means that it comes with an operator Z which squares to the identity (the fermion parity operator), and partly induces a canonical choice of basis such that basis vectors are eigenstates of Z . States which are eigenstates of Z are called homogeneous states, and the parity of a homogeneous state $|i\rangle$ is denoted as

$$Z|i\rangle = (-1)^{|i|}|i\rangle, |i| \in \{0, 1\}. \quad (54)$$

The subspace of V spanned by the vectors which are even under Z is denoted as V^0 , and is called the even subspace. The odd subspace is denoted as V^1 . The properties of a super vector space V naturally carry over to its dual space V^* , which is also graded. The natural action of dual vectors on vectors gives rise to the evaluation map \mathcal{C} , and we can choose a canonical dual basis $\langle i|$ such that

$$\mathcal{C} : V^* \otimes V \rightarrow \mathbb{C} : \langle i| \otimes |j\rangle \rightarrow \delta_{ij}. \quad (55)$$

It then also follows that $\langle i|Z = (-1)^{|i|}\langle i|$ so that $|i\rangle$ and $\langle i|$ have the same parity. The \mathbb{Z}_2 grading induced by Z becomes important when vectors are ‘reordered’. More precisely, when working with tensor products of super vector spaces, one always uses the following canonical isomorphism,

$$\mathcal{F} : V \otimes W \rightarrow W \otimes V : |i\rangle \otimes |j\rangle \rightarrow (1)^{|i||j|}|j\rangle \otimes |i\rangle, \quad (56)$$

which encodes the fermionic anti-commutation relations. The same reordering rule is used when one or two of the vectors involved are dual vectors. *Tensor contraction* is then defined as the following sequence of steps: (1) take the tensor product of the tensors to be contracted, (2) use \mathcal{F} to bring the vectors and dual vectors corresponding to the legs which are to be contracted next to each other, and (3) use the evaluation \mathcal{C} as defined in Eq. (55) to contract the legs. This procedure is unambiguous up to an innocuous overall minus sign as long as the tensors respect the superselection rule which comes with super vector spaces: all tensors need to have a well-defined fermion parity. For more details we refer to Ref. [73].

The GfTNS introduced in the main text are a special case of the general fTNS defined in terms of super vector spaces. To unveil the connection, we have to translate the Gaussian formalism based on Grassmann numbers to the language of super vector spaces. This translation is based on an isomorphism between polynomials of M Grassmann numbers and a super vector space of dimension 2^M . To illustrate how this isomorphism works, consider the case of a single Grassmann number θ . To every monomial we associate a basis state of the super vector space as follows,

$$\theta^n \cong |n\rangle, \quad n \in \{0, 1\}. \quad (57)$$

The dual space is isomorphic to polynomials of another Grassmann number $\bar{\theta}$,

$$\bar{\theta}^n \cong \langle n |, \quad n \in \{0, 1\}. \quad (58)$$

The evaluation map is then given by the following Berezin integral,

$$\mathcal{C} : \langle n | \otimes | m \rangle \cong \bar{\theta}^n \theta^m \rightarrow \int d\theta \int d\bar{\theta} e^{\bar{\theta}\theta} \bar{\theta}^n \theta^m = \langle n | m \rangle = \delta_{nm}. \quad (59)$$

This explains the presence of the factors $e^{\bar{\theta}_x \theta_x + \epsilon_{x/y}}$ in the definition of the GfTNS in Eq. (2): they ensure that the Berezin integral implements the tensor contraction according to the conventional evaluation map of the super vector spaces associated with the legs of the fermionic tensors. The canonical isomorphism \mathcal{F} defined in Eq. (56) is implemented automatically via the anti-commutation relations of Grassmann numbers. The mapping of monomials of Grassmann numbers to basis states of a super vector space generalizes straightforwardly to the case with more than one Grassmann number.

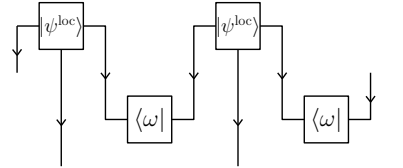
Appendix H – Connection between the Gu-Verstraete-Wen and Kraus-Schuch formalisms for GfTNS

In this work, two different Gaussian *Ansätze* were applied to approximate critical fermion states with a Fermi surface. Here, we establish a connection between both in the 1D setting. To do so, it is important to reflect on the conceptual differences between a GVW state $|\psi\rangle$ (Eq. (2) in the main text) and the Kraus-Schuch *Ansatz* $\rho_{\text{out}} = \mathcal{E}(\rho_{\text{in}})$ (as defined in Appendix C). An immediate observation is that the latter allows for mixed states (when $XX^T < \mathbb{1}$) while the former is a pure state by construction. As a result, we only intend to establish a connection in the pure case, i.e. when $\rho_{\text{out}} = |\psi_{\text{out}}\rangle\langle\psi_{\text{out}}|$. Another direct observation is that the GVW *Ansatz* always contains a vacuum contribution in its local tensors due to the exponential in \hat{T}_x (Eq. (1) in the main text). As a result, $|\psi\rangle$ will also contain the vacuum, precluding a $|\psi_{\text{out}}\rangle \perp |0\rangle$ (e.g. an odd-parity $|\psi_{\text{out}}\rangle$). This can be solved by the addition of virtual Grassmann numbers to the exponential in the local tensor or to the overall contraction (e.g. as discussed in Appendix A). Here, we will only focus on cases where $|\psi_{\text{out}}\rangle \not\perp |0\rangle$ and is thus an even state. A final, more high-level difference between both formalisms lies in their general architecture. While the Kraus-Schuch formalism starts from an input state to which a local Gaussian projection is applied to realise the output state, the GVW *Ansatz* starts from local entities and contracts these in a conventional way with the Berezin integral. Schematically, they can be contrasted as



where $A_x \cong \hat{T}_x$ in the sense of Appendix G. In these diagrams, the outward (inward) arrows differentiate between (co)vectors. Furthermore, we assumed purity of ρ_{out} so that T_E is the single Kraus operator of the local channel \mathcal{E}^{loc} . To establish a connection, we rephrase the Kraus-Schuch formalism as in Ref. [72], where one starts from a local Gaussian state, ρ^{loc} , defined on both the virtual and physical level. Due to Gaussianity, this state can be characterized by a correlation matrix $\gamma^{ij} = \frac{i}{2} \text{tr}(\rho^{\text{loc}} [c^i, c^j])$ with $\{c^i\}$ the local Majorana operators. Discerning between physical (placed first) and virtual (placed last) Majorana operators, we rewrite this real anti-symmetric matrix as $\gamma = \begin{pmatrix} A & B \\ C & D \end{pmatrix}$ with $\gamma\gamma^T = \mathbb{1}$ (again assuming purity). Next, we make ρ_ω , a simple Gaussian state on two fermions with correlation matrix $\gamma_\omega = \begin{pmatrix} 0 & -\sigma_x \\ \sigma_x & 0 \end{pmatrix}$. This state is pure and $\rho_\omega = |\omega\rangle\langle\omega|$ with $|\omega\rangle = \frac{1}{\sqrt{2}}(|0\rangle|0\rangle + |1\rangle|1\rangle)$. N_s copies of ρ^{loc} placed on a line can be described in Fourier space by $G_\rho = \bigoplus_k \gamma$. Identifying the spaces of $|\omega\rangle$ with two neighbouring virtual spaces in $(\rho^{\text{loc}})^{\otimes N_s}$ and doing this for each neighbouring pair, $\rho_\omega^{\otimes (\frac{N_s}{2})}$ is described by $G_\omega = \bigoplus_k \begin{pmatrix} 0 & -e^{-ik}\sigma_x \\ e^{ik}\sigma_x & 0 \end{pmatrix}^{\oplus \frac{N_s}{2}}$. One can then construct the partial trace over the virtual spaces of the composition of these two density operators,

$\text{tr}_{\text{virt}}((\rho^{\text{loc}})^{\otimes N_s} \rho_{\omega}^{\otimes (\frac{\chi}{2} N_s)}) = |\langle \omega^{\otimes (\frac{\chi}{2} N_s)} | (\psi^{\text{loc}})^{\otimes N_s} \rangle_{\text{virt}}|^2$, yielding



where the purity of $\rho^{\text{loc}} = |\psi^{\text{loc}}\rangle \langle \psi^{\text{loc}}|$ was used to only consider the ket layer. Essentially, we use $\langle \omega|$ to glue the local tensors together like the Berezin integral. Expressing $(\rho^{\text{loc}})^{\otimes N}$ and $\rho_{\omega}^{\otimes (\frac{\chi}{2} N)}$ in Grassmann numbers as in [83], this partial trace can be rewritten as a Gaussian integral, yielding

$$G(\mathbf{k}) = A - B(D + G_{\omega}(\mathbf{k}))^{-1}C \quad (60)$$

for the resulting Gaussian state. Both formulations of the Kraus-Schuch *Ansatz* thus result in a very similar Schur complement formula and can be converted into each other by requiring $G_{\omega}(\mathbf{k}) = -G_{\text{in}}(\mathbf{k})$. Some minor remarks are in order. While we discussed this reinterpretation in 1D, it can be readily extended to a general spatial dimension d . An odd number of virtual Majorana pairs per bond (i.e. an odd χ_i) constitutes an important exception. In this case, one cannot simply define $|\psi^{\text{loc}}\rangle$ with full ($D = 2$) virtual orbitals and combine these with a conventional $\langle \omega|$ as this would immediately lead to a doubling of the entangled Majorana pairs.

We conclude that a direct conversion of the Kraus-Schuch into the GVW *Ansatz* is only possible for pure states, non-orthogonal to the vacuum and for bond dimensions that are powers of 2. Under these conditions, we can reinterpret the Kraus-Schuch *Ansatz* and equate

$$\xleftarrow{\quad \leftarrow |\psi^{\text{loc}}\rangle \rightarrow \langle \omega| \leftarrow \quad} = \xleftarrow{\quad \leftarrow A_x \leftarrow \quad} \quad \text{or equivalently} \quad \xleftarrow{\quad \leftarrow |\psi^{\text{loc}}\rangle \rightarrow \quad} = \xleftarrow{\quad \leftarrow A_x \leftarrow \langle \omega| \rightarrow \quad} = \frac{1}{Z} \exp\left(\frac{1}{2}(f^{\dagger})^T A f^{\dagger}\right) |0\rangle$$

where Z is a normalization constant and where f^{\dagger} collects the creators (e.g. $f^{\dagger} = (f_p^{\dagger T} \quad f_l^{\dagger T} \quad f_r^{\dagger T})^T$) in case we order the operators as in Eq. (1), i.e. physical, left,right). Relating both GfTNS constructions thus boils down to relating the pure (all ket) $|\psi^{\text{loc}}\rangle$ with correlation matrix γ to the exponential creator parametrized by A which is exactly the same A as in Eq. (1) when the operator order is chosen accordingly. This final step can be taken relatively easily as states of the latter kind have been studied extensively [87], where for the hopping and pairing expectation values it is derived that

$$n_{ij} = \langle f_i^{\dagger} f_j \rangle = (A(1 + A^{\dagger} A)^{-1} A^{\dagger})_{ji} \quad x_{ij} = \langle f_i f_j \rangle = - (A(1 + A^{\dagger} A)^{-1})_{ij} \quad (61)$$

while $Z = \det(1 + AA^{\dagger})^{-\frac{1}{4}}$. Note that $n^T x = xn$ and $(n^T - \frac{1}{2})^2 - x\bar{x} = \frac{1}{4}$ while $n^T = -xA^{\dagger}$. The inverse is also true. When n and x satisfy these equations, the matrix A can be obtained from the latter such that n and x can be expressed as a function of this A or, equivalently, such that there exists a GVW parametrization for these states. It is straightforward to check that the former two equations for n and x just express purity while the latter can always be solved with the (pseudo)inverse of x as long as the Gaussian state described by n and x is not orthogonal to the vacuum. Note that relating the states in this way, the main computational effort is the solution of the linear system. Hence, there is no exponential scaling in χ_i , which would happen if the tensor entries would have been evaluated as in Appendix G.

We conclude this Appendix by summarizing the recipe to convert a pure Kraus-Schuch state, non-orthogonal to vacuum and with bond dimension $D = 2^M$, to a GVW GfTNS (or vice-versa) and apply it to an example.

- ρ_{out} is built from \mathcal{E} and ρ_{in} , respectively characterized by X^{loc} and $G_{\text{in}}(\mathbf{k})$. Reinterpret this state as a contraction of local tensors, i.e. in terms of a local γ and $|\omega\rangle$.
- Extract from γ the hopping and pairing expectation values n and x .
- Solve $n^T = -xA^{\dagger}$ to find A and hence \hat{T}_x from Eq. (1).

As an example, consider a $D = 2$ GfMPS, ρ_{out} , in the Kraus-Schuch formalism with

$$X^{\text{loc}} = \left(\begin{array}{cc|ccc} 0 & 0 & -1 & 0 & 0 & 0 \\ 0 & 0 & 0 & 1 & 0 & 0 \\ \hline 1 & 0 & 0 & 0 & 0 & 0 \\ 0 & -1 & 0 & 0 & 0 & 0 \\ 0 & 0 & 0 & 0 & 0 & 1 \\ 0 & 0 & 0 & 0 & -1 & 0 \end{array} \right) = \left(\begin{array}{c|c} A^{\text{loc}} & B^{\text{loc}} \\ \hline -B^{\text{loc}}{}^T & D^{\text{loc}} \end{array} \right) \quad (62)$$

where we order the operators as physical, left, right and with $G_{\text{in}}(k)$ as in Eq. (30) where $\chi = 2$. Note that the state is pure as $X^{\text{loc}} X^{\text{loc}}{}^\dagger = \mathbb{1}$. Its output correlation matrix is given by the Schur complement formula,

$$G_{\text{out}}(k) = A^{\text{loc}} + B^{\text{loc}} (D^{\text{loc}} - G_{\text{in}}(k))^{-1} B^{\text{loc}}{}^T = \begin{pmatrix} 0 & e^{ik} \\ -e^{-ik} & 0 \end{pmatrix}. \quad (63)$$

Using that $G_{\text{in}}(k) = -P^T G_\omega(k) P$ with

$$G_\omega(k) = \begin{pmatrix} 0 & -e^{-ik} \sigma_x \\ e^{ik} \sigma_x & 0 \end{pmatrix} \quad \text{and} \quad P = \begin{pmatrix} 0 & 1 & 0 & 0 \\ 0 & 0 & 0 & 1 \\ 0 & 0 & -1 & 0 \\ -1 & 0 & 0 & 0 \end{pmatrix} \quad (64)$$

we can rewrite this formula as

$$G_{\text{out}}(k) = A^{\text{loc}} + B^{\text{loc}} P^T (P D^{\text{loc}} P^T + G_\omega(k))^{-1} P B^{\text{loc}}{}^T \quad (65)$$

and thus reinterpret the *Ansatz* as a contraction of local Gaussian tensors with correlation matrix

$$\gamma = \begin{pmatrix} A^{\text{loc}} & B^{\text{loc}} P^T \\ P B^{\text{loc}}{}^T & P D^{\text{loc}} P^T \end{pmatrix} \quad (66)$$

by means of the conventional $|\omega\rangle$. From this γ we obtain

$$n = \frac{1}{2} \begin{pmatrix} 1 & \frac{1}{2} & -\frac{1}{2} \\ \frac{1}{2} & 1 & \frac{1}{2} \\ -\frac{1}{2} & \frac{1}{2} & 1 \end{pmatrix} \quad \text{and} \quad x = \frac{1}{4} \begin{pmatrix} 0 & -1 & -1 \\ 1 & 0 & -1 \\ 1 & 1 & 0 \end{pmatrix} \quad (67)$$

allowing to solve for the GVW matrix A from $n^T = -xA^\dagger$. While x is not invertible, application of its pseudoinverse yields $A = -4x$, solving the system and signaling that the original state was non-orthogonal to the vacuum. Note that this parameter matrix is the same as in Eq. (8) so that for the GVW state we immediately obtain,

$$\begin{aligned} n(k) &= \frac{|g_k|^2}{1 + |g_k|^2} = \frac{\sin^2 k}{2(1 - \cos k)} & \text{since} & \quad g_k = -i \frac{\sin k}{1 - \cos k} = -i \cotan\left(\frac{k}{2}\right). \\ x(k) &= \frac{g_k}{1 + |g_k|^2} = -\frac{i}{2} \sin k \end{aligned} \quad (68)$$

Compare these to their Kraus-Schuch analogues,

$$\begin{aligned} n(k) &= \frac{1}{2} + \frac{i}{4} W^T G_{\text{out}}^T(k) \bar{W} = \frac{1}{2}(1 + \cos k) \\ x(k) &= -\frac{i}{4} W^\dagger G_{\text{out}}(k) \bar{W} = -\frac{i}{2} \sin k \end{aligned} \quad (69)$$

Indeed, both Gaussian *Ansätze* yield exactly the same correlation matrices and are hence equivalent.

5.4.3 PEPS encoding Fermi surface spin liquids

Quantum spin liquids were introduced in Chapter 2 as peculiar topological phases expected to contain the ground states of geometrically frustrated Mott insulators. Furthermore, the parton construction was put forward as one of the conventional tools to study these spin liquids. Herein the spin degrees of freedom are embedded in either fermionic or bosonic operators (thus enlarging the Hilbert space) and the resulting Hamiltonian is studied in a mean-field approximation. The correct parton occupation on each site, namely one particle per site amounting to half-filling in the case of spin- $\frac{1}{2}$ fermions, is enforced by coupling the model to a gauge field, thus gauging the corresponding emergent \mathbb{Z}_2 or U(1) symmetry of the parton model. The spin liquid phases can then be classified in terms of the different deconfined phases of the resulting gauge theories. However, neither correct energy expectation values nor an idea about which particular spin liquid phase is realized by a given microscopic Hamiltonian can be determined via this method. What the mean-field Hamiltonian in the parton construction, H_0 , does provide are trial states which can be used to calculate variational energies. Indeed, we could simply solve H_0 , yielding a Gaussian state, $|\psi_0\rangle$. Of course, this state does not satisfy the occupational constraints but rather than imposing these *a priori* by gauging H_0 we do this *post hoc* and project out all the erroneous (non-half-filled) parts of the wavefunction. *I.e.* we apply a so-called Gutzwiller projection,

$$P_G = \prod_{\mathbf{x}} n_{\mathbf{x}}(2 - n_{\mathbf{x}}), \quad (5.50)$$

with $n_{\mathbf{x}} = \sum_{\sigma} a_{\mathbf{x},\sigma}^{\dagger} a_{\mathbf{x},\sigma}$ the local number operator (here for spinful fermions), projecting $|\psi_0\rangle$ down to $|\psi_P\rangle$ with single occupancy on each site and hence only a spin degree of freedom. The projected state should then, at least qualitatively, describe the spin liquid ground state. In this way, one could build a set of parton trial states (e.g. incorporating different types of spin liquids) for a certain physical Hamiltonian and energetically compare these to gain insight in if and which spin liquid is realized. However, to perform this comparative analysis, one needs to calculate energies and as $|\psi_P\rangle$ is a strongly-correlated, interacting state, this is far from trivial. Yet, a variational Monte Carlo procedure has been devised to extract expectation values from the resulting non-Gaussian states. For certain gapped \mathbb{Z}_2 spin liquids, it was shown that the Gutzwiller approach indeed yields a state describing the same physics as obtained from lattice gauge theory [232, 159]. Although the story is more complicated for gapless spin liquids, recent works claim to have found both numerical [233] and experimental [234, 235, 236] evidence for Fermi surface spin liquids (typically on the triangular lattice and possibly “aided” by ring exchanges). As a fingerprint for these spin liquids, one can examine real-space spin-spin correlations functions that should display Friedel oscillations consistent with the Fermi momentum. In Fourier space, this requires non-analyticities for the spin structure factor. While these appear as discontinuous second derivatives in the mean-field parton model, the non-analyticities become stronger upon Gutzwiller projection and yield discontinuities in the structure factor itself [237].

The goal of this research project was to verify if a similar approach would also be possible by means of TNS. Note that the Gutzwiller projection is local and identical on all sites so that it can easily be represented as a (fermionic) tensor. Also the relevant

Gaussian parton states can be represented by tensor networks. Indeed, even in the case of critical H_0 with Fermi surfaces, we showed that GfTNS allow for a precise and scalable tensor network approximation of $|\psi_0\rangle$. Therefore we expect that translating this GfTNS to generic fTNS by means of the methods outlined in Sec. 5.3, it should also be possible to generate spin liquid PEPS. The most daunting trial wavefunctions to construct will be those with corrections to the area law of entanglement scaling, *i.e.* Dirac spin liquids (with subleading corrections) and Fermi surface spin liquids (with multiplicative, logarithmic corrections). For the former it has already been shown that a PEPS approximation exist exactly by applying the outlined method [238]. Therefore, the objective is to do the same for Fermi surface spin liquids. Below we discuss the consecutive steps in more detail together with intermediate results.

An important remark is that we *approximate* the spin liquid states with a PEPS. Indeed, already on the free parton level, the area law precludes an exact PEPS representation of $|\psi_0\rangle$. As discussed in the previous Sections we will rather approximate it with a superconducting state whose gap is regulated by the bond dimension. As a result, this entanglement cut-off is also expected to be present in the spin liquid state. *I.e.* rather than reproducing a polynomially decaying and oscillatory spin-spin correlation function for arbitrary large length scales, we expect to do this up to a certain correlation length after which exponential decay without oscillations sets in. Correspondingly, we do not expect diverging spin structure factors in Fourier space but rather a peaked behavior, intensifying when increasing the bond dimension.

Step 1: GfTNS for the parton model

For the mean-field parton model we again consider the spinful (next-)nearest-neighbor hopping model on a square lattice as introduced in Sec. 5.4.2. We will work with $t'/t = 0.353$ and $\mu/t = 0.7535$ so that the Fermi surface is circular and characterized by a single isotropic Fermi momentum $k_F \approx \sqrt{2\pi}$. For this model we already optimized SU(2)-symmetric GfTNS in Sec. 5.4.2. We will reuse these results here. However, before proceeding to their reformulation as generic TNS, we first examine the Fermi surface characteristics that may persist (to some degree) upon Gutzwiller projecting, *i.e.* the aforementioned real-space spin-spin correlation functions or, equivalently, the spin static structure factors, defined by

$$s(\mathbf{k}) = \sum_{\mathbf{x}} e^{i\mathbf{k}\cdot\mathbf{x}} \langle \mathbf{S}_{\mathbf{x}} \cdot \mathbf{S}_0 \rangle \quad (5.51)$$

with $\mathbf{S}_{\mathbf{x}} = \frac{1}{2} a_{\mathbf{x}}^{\alpha\dagger} \boldsymbol{\sigma}_{\alpha\beta} a_{\mathbf{x}}^{\beta}$ the spin operator at site \mathbf{x} . Considering these properties on the Gaussian level we will already have a sense of the bond dimensions required to resolve typical Fermi surface characteristics. Fig. 5.1, for instance, compares several real-space connected correlation functions for the analytic solution of the problem (obtained by working in the TD limit and setting $x(\mathbf{k}) = 0$ and $n(\mathbf{k}) = 1$ for $|\mathbf{k}| \leq k$ and zero for all other \mathbf{k} , which can be Fourier transformed to give Bessel functions with period $\frac{2\pi}{k_F}$ for the real-space $a^\dagger a$ correlations), the exact solution (obtained by exactly solving the finite-size quadratic model with its slightly imperfect circular Fermi surface) and GfTNS approximations hereof for $D = 4, 16, 64$. The analytic and exact solution clearly contain the polynomially decaying correlations with k_F -consistent oscillations. For higher D , the

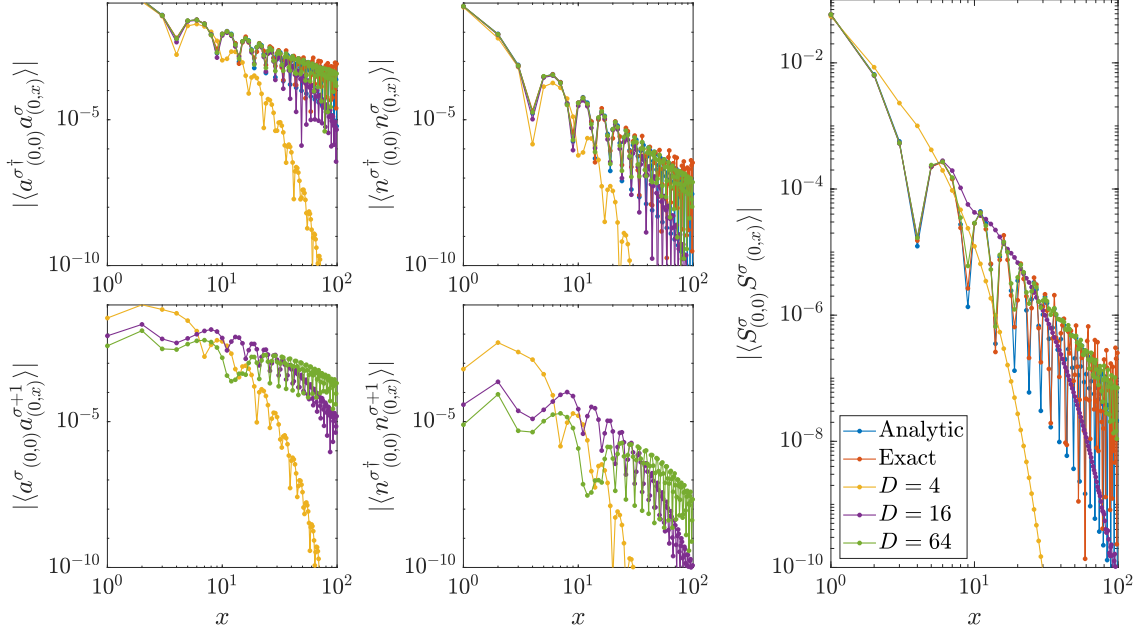


Figure 5.1: Real-space connected correlation functions along the x -axis for a diagonal combination of $a^\dagger a$ operators, an off-diagonal combination of aa operators, both a diagonal and an off-diagonal combination of nn (density-density) operators, and the inner product of spin-spin operators. Results were compared for the analytic solution, the exact solution and variationally optimized SU(2)-symmetric GfTNS with $D = 4, 16, 64$.

GfTNS reproduce these increasingly well. Indeed, considering the $a^\dagger a$ correlations, $D = 4$ only gets a single period right before decaying exponentially while $D = 16$ and $D = 64$ can follow the exact profile much longer. For the aa correlations there is no exact or analytic curve as these are exactly zero due to particle number conservation. However, the GfTNS must break this symmetry due to the LSMOH theorem and thus yield erroneous non-zero aa correlations, though these become smaller for increasing D . For the diagonal and off-diagonal terms in the connected real-space density-density correlations, the picture is relatively similar. However, the off-diagonal part has a decisive influence on the spin-spin correlations. Indeed, while the latter contain clear oscillations for the analytic and exact solutions, these are completely absent in the $D = 4$ GfTNS, exactly due to the erroneous off-diagonal part of the density-density correlations. The fact that U(1) is broken thus destroys the oscillations. Luckily, they can be recovered by increasing D as the $D = 16$ and $D = 64$ results show. Still, it is important to note that necessary charge fluctuations tend to tamper with the oscillations we would like to see. Therefore, one expects at least $D = 16$ to be necessary to see fingerprints of Fermi surfaces after Gutzwiller projection. In this regard, P_G could possibly help us as it removes exactly those fluctuations that were the problem for the oscillations.

As the spin-spin correlation function for $D = 16$ only shows a weak single-period oscillation, we turned to its Fourier transform, the spin static structure factor in order to

obtain a more pronounced signature of the spinon Fermi surface. As Fig. 5.2 shows this is indeed the case. The analytic solution contains a conic profile around the zone center and discontinuous second derivatives on circles with $|\mathbf{k}| = 2k_F$. Therefore, each second line in Fig. 5.2 shows the absolute value of $\nabla^2 s(\mathbf{k})$, calculated analytically for the analytical solution and by finite differencing in all other cases. The positions of the (periodically shifted) $2k_F$ circles for the exact solution are highlighted by the dashed lines. Clearly the analytical solution is peaked around these circles. The same is true for the exact solution but the image is more pixelated due to the finite differences. For the GfTNS, the general shape of the structure factor is reproduced for all D but resolving details like the conic point at the zone center require $D \geq 16$. Indeed, the colorplot of the second derivatives obtained from the $D = 16$ GfTNS already reproduces many of the features of the exact solution. In particular, the $2k_F$ circles can clearly be identified. We conclude that by working in Fourier space, $D = 16$ might also suffice to see Fermi surface features in the spin liquid wavefunction after Gutzwiller projection.

Step 2: fTNS for the Gutzwiller-projected state

Utilizing the $SU(2)$ symmetric variant of the bottom-up method outlined in Sec. 5.3, we were able to reformulate the optimized GfTNS as \mathbb{Z}_2 -graded, $SU(2)$ -symmetric PEPS tensors with $D = 4, 16, 64$. Gutzwiller projection is performed by contracting the physical legs of these tensors with $P = |1, \frac{1}{2}\rangle \langle 1, \frac{1}{2}|$ (where the numbers respectively denote the fermionic superselection sector and $SU(2)$ irrep). Indeed, in this way one orthogonally projects down to the subspace with single occupation.

Step 3: extracting the Fermi surface signature from the projected state

To successfully carry out this step, we need to compute correlation functions and spin structure factors for a critical, interacting PEPS with at least $D = 16$. Needless to say, this task is challenging, and the required boundary MPS calculations are currently in progress. However, we are hopeful about their convergence, and once this most demanding step is completed, we can proceed relatively smoothly with the computation of correlation functions in 1D. For the spin structure factors, we can utilize the window MPS method, as described in [199].

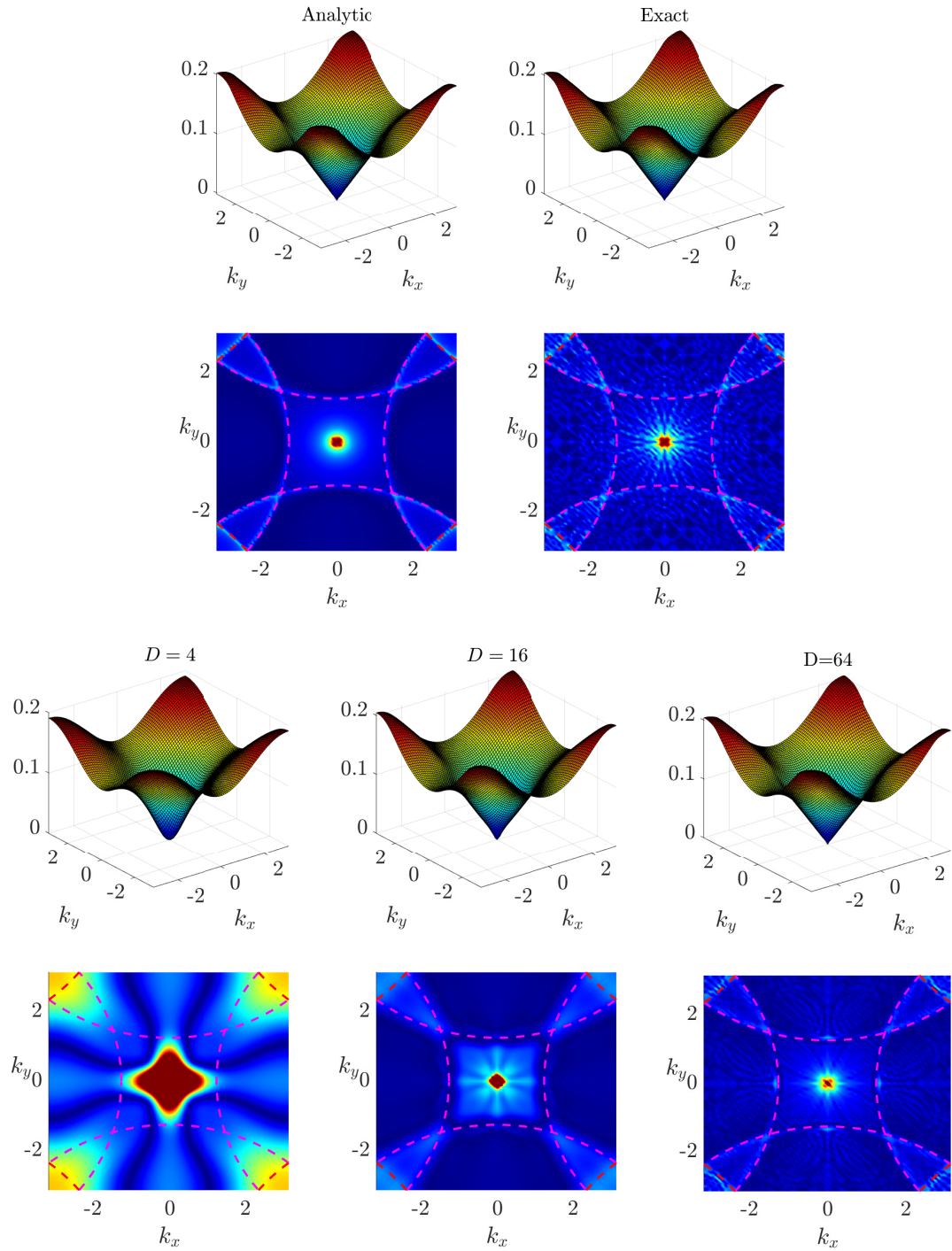


Figure 5.2: Spin static structure factors $s(\mathbf{k})$ (upper panels) as well as the absolute value of their Laplacian, $|\nabla^2 s(\mathbf{k})|$, (lower panels) for the analytic solution, the exact solution and variationally optimized, SU(2)-symmetric GfTNS with $D = 4, 16, 64$.

Chapter 6

Conclusions and outlook

We began this work by describing the quantum many body problem and its challenging exponential scaling. In response, tensor network states were put forward. These *Ansätze* represent quantum states in a compressed way via local tensors and hence possess an inherent area law of entanglement scaling that allows them to capture the essential physics of quantum many-body systems. However, critical models, in particular those with a Fermi surface, can violate this area law, thus endangering the applicability of TNS. By variationally optimizing Gaussian fermionic TNS for these systems, we demonstrated that a systematic improvement in precision can still be achieved. *A fortiori*, the same should hold for generic fermionic TNS. Yet, the restriction to the Gaussian submanifold was necessary due to the high degree of criticality and in order to reach sufficiently large bond dimensions. However, it also confronted us with parity obstructions that were understood as specific manifestations of a broader no-go theorem.

By systematically examining the optimized GfTNS for metallic systems, particularly focusing on their entanglement properties, we discovered that the entanglement entropy of a contractible spatial region with linear size L scales as $S \sim L \log(\xi f(L/\xi))$. Here $f(x)$ is a scaling function which depends on the shape of the Fermi surface and ξ is a finite correlation length induced by the restricted entanglement. The notion of finite-entanglement scaling in 1D thus also exists for 2D metallic states. More generally we expect that PEPS applications can be systematically extended to critical systems.

Expanding our view beyond Gaussian states, we also ventured into generic TNS algorithms for fermionic degrees of freedom. More specifically, we further developed the formalism of \mathbb{Z}_2 -graded tensor network states with a focus on their integration in standard TNS algorithms like VUMPS, TDVP, the excitation *Ansatz*, etc. After demonstrating that the typical tensor network diagrams still apply up to the addition of a limited number of parity tensors, these fTNS methods were benchmarked both in 1D and 2D by application to the Kitaev chain, to the 1D Hubbard model (where we observed spin-charge separation) and to chiral superconductors (where we reproduced typical long-range tails in the correlation functions). The latter application required the reformulation of GfTNS as generic fTNS. This method was also applied in the context of a final research project where the parton construction for spin liquids was implemented on the level of TNS with the aim to realize a Fermi surface spin liquid. While not yet finished the success of this project would be the culmination of our research as it combines all methodological con-

tributions and applies them to a interesting but complex, strongly-interacting system.

Looking to the future, the fermionic TNS methods we developed, both Gaussian and non-Gaussian, can be applied to a myriad of interesting fermionic problems, gapped and critical alike. As an example we mention the quest for high- T_c superconductivity in realistic materials like the cuprates. There, downfolding procedures typically yield extended Hubbard models, thus requiring a fermionic method for their solution. As quantum Monte Carlo cannot be applied due to the sign problem, TNS represent the go-to alternative. The GfTNS can also serve in this context as physically motivated initial guesses. Another future application could be the extension of the TNS parton construction to other geometries (e.g. the triangular or kagome lattice). A comparative energy analysis of realistic microscopic Hamiltonians by means of the spin liquid TNS could be an interesting addition to the field as well.

On the conceptual side, many open questions were already touched upon throughout this work. To name a few: Does the inefficient use of bond dimension in GfTNS also lead to a sub-polynomial increase of energy precision in 2D critical models and how does this compare to the generic *Ansatz*? Can we understand how the geometry of Fermi surfaces influences the finite-entanglement scaling function? Can the purely virtual symmetries in topologically non-trivial GfTNS be understood as an MPO symmetry? We conclude that like the violation of the area law in systems with a Fermi surface, the number of interesting directions for future research only increases in size.

Appendix A

Fermionic tangent space methods

A.1 Tangent-space projector for fermionic MPS

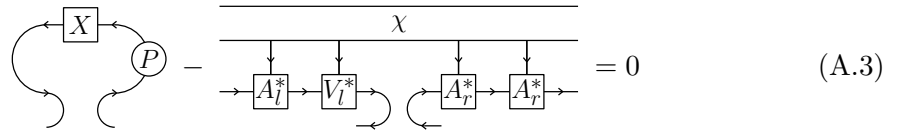
We derive an expression for $P_{|\Psi(A)\rangle}$, the tangent space projector in (and orthogonal to) a point $|\Psi(A)\rangle$ on the uniform fMPS manifold. Therefore, consider an arbitrary translation-invariant state $|\chi\rangle$. Its projection onto the tangent space, $|\Phi(B(X); A)\rangle = P_{|\Psi(A)\rangle} |\chi\rangle$, can be parametrized by a tensor X as in Eq. (4.97) where

$$\begin{aligned} X &= \min_X \| |\chi\rangle - |\Phi(B(X); A)\rangle \|^2 \\ &= \min_X (\langle \Phi(B(X); A) | \Phi(B(X); A) \rangle - \langle \Phi(B(X); A) | \chi \rangle - \langle \chi | \Phi(B(X); A) \rangle). \end{aligned} \quad (\text{A.1})$$

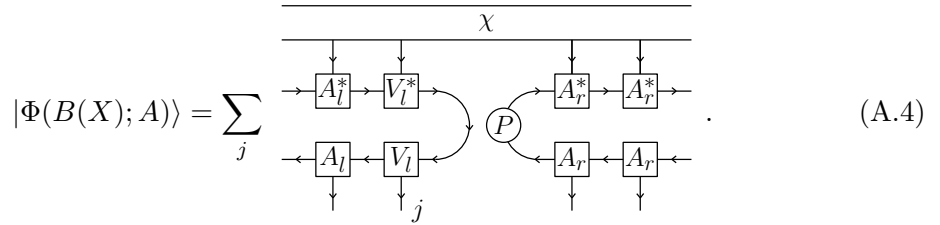
Differentiating w.r.t. the complex conjugate of the entries of X , this minimum is characterized by

$$0 = \frac{\partial}{\partial \bar{X}} \| |\chi\rangle - |\Phi(B(X); A)\rangle \|^2, \quad (\text{A.2})$$

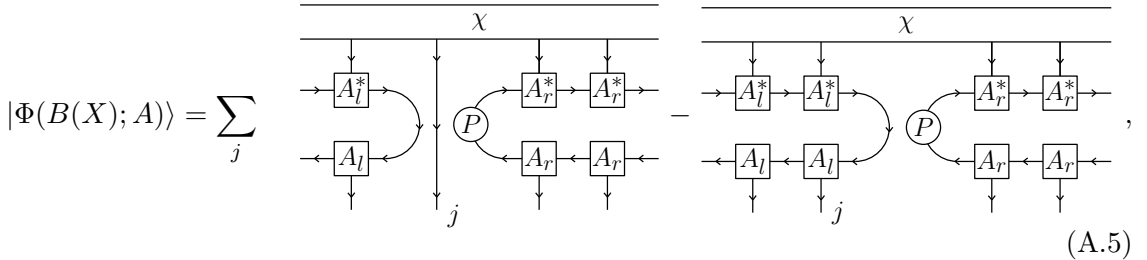
i.e.



so that



Using the completeness relation from Eq. (4.98), we can rewrite this as



yielding the final result for the tangent space projector

$$P_{|\Psi(A)\rangle} = \sum_j \left[\begin{array}{c} \text{Diagram showing } P_{|\Psi(A)\rangle} \text{ as a sum of two terms involving } A_l^*, A_r^*, A_l, A_r \text{ and a projector } P. \\ \text{The first term has } A_l^* \rightarrow A_r^* \text{ and } A_r \rightarrow A_l^*. \\ \text{The second term has } A_l^* \rightarrow A_l \text{ and } A_r \rightarrow A_r^*. \\ \text{A vertical line labeled } j \text{ connects the two terms.} \end{array} \right] - \left[\begin{array}{c} \text{Diagram showing } P_{|\Psi(A)\rangle} \text{ as a sum of two terms involving } A_l^*, A_r^*, A_l, A_r \text{ and a projector } P. \\ \text{The first term has } A_l^* \rightarrow A_r^* \text{ and } A_r \rightarrow A_l^*. \\ \text{The second term has } A_l^* \rightarrow A_l \text{ and } A_r \rightarrow A_r^*. \\ \text{A vertical line labeled } j \text{ connects the two terms.} \end{array} \right] . \quad (\text{A.6})$$

A.2 Vumps for fermionic MPOs

Consider a 1D fermionic, Hamiltonian formulated as a Matrix Product Operator (MPO),

$$H = T(O) = \begin{array}{c} \text{Diagram showing } H = T(O) \text{ as a chain of five boxes labeled } O. \\ \text{Arrows indicate left-to-right flow.} \end{array} . \quad (\text{A.7})$$

Its ground state minimizes the real-valued Rayleigh quotient,

$$\frac{\langle \Psi | H | \Psi \rangle}{\langle \Psi | \Psi \rangle}, \quad (\text{A.8})$$

and so does its optimal MPS approximation $|\Psi(\tilde{A})\rangle$ when restricting $|\Psi\rangle$ to the MPS manifold. Put differently, the derivative of Eq. (A.8) w.r.t. to the (complex conjugate of) the MPS parameters equals zero, *i.e.*

$$\frac{\partial}{\partial \tilde{A}} (\langle \Psi(A) |) \left(H - \frac{\langle \Psi(A) | H | \Psi(A) \rangle}{\langle \Psi(A) | \Psi(A) \rangle} \right) |\Psi(A)\rangle = 0 \quad (\text{A.9})$$

when $A = \tilde{A}$. This expresses that the tangent space projection of the original eigenvalue equation equals zero in the optimal MPS, *i.e.*

$$P_{|\Psi(\tilde{A})\rangle} (H - E) |\Psi(\tilde{A})\rangle = 0. \quad (\text{A.10})$$

As discussed in Sec. 4.2.4 and Appendix A.1, this yields the fixed-point equations, $A'_c \propto A_c$ and $C' \propto C$, where we dropped the tilde and

$$\begin{array}{c} \text{Diagram showing } A'_c \text{ as a sum of two terms involving } A_l, A_c, A_r \text{ and a projector } P. \\ \text{The first term has } A_l \rightarrow A_c \rightarrow A_r. \\ \text{The second term has } A_l^* \rightarrow A_r^* \text{ and a circular arrow around } A_c. \\ \text{A horizontal line labeled } T \text{ connects the two terms.} \end{array} , \quad (\text{A.11})$$

$$\begin{array}{c} \text{Diagram showing } C' \text{ as a sum of two terms involving } A_l, C, A_r \text{ and a projector } P. \\ \text{The first term has } A_l \rightarrow C \rightarrow A_r. \\ \text{The second term has } A_l^* \rightarrow A_r^* \text{ and a circular arrow around } C. \\ \text{A horizontal line labeled } T \text{ connects the two terms.} \end{array} . \quad (\text{A.12})$$

The proportionality factor in the fixed-point equations is equal to the (infinite) eigenvalue E . In order to solve the eigenvalue problems for A_c and C , we invoke the MPO structure of H to define the environments G_l and G_r as

$$\begin{array}{c} \text{---} \\ | \\ \text{---} \end{array} \xrightarrow{\quad A_l \quad} \xleftarrow{\quad O \quad} \xrightarrow{\quad A_l^* \quad} = \lambda \begin{array}{c} \text{---} \\ | \\ \text{---} \end{array} \xleftarrow{\quad G_l \quad} \quad \text{and} \quad \begin{array}{c} \text{---} \\ | \\ \text{---} \end{array} \xleftarrow{\quad A_r \quad} \xleftarrow{\quad O \quad} \xleftarrow{\quad G_r \quad} = \lambda \begin{array}{c} \text{---} \\ | \\ \text{---} \end{array} \xleftarrow{\quad G_r \quad}, \quad (\text{A.13})$$

i.e. the dominant left and right eigenvectors of the transfer matrices

$$\begin{array}{c} \text{---} \\ | \\ \text{---} \end{array} \xleftarrow{\quad E_l^l \quad} = \begin{array}{c} \text{---} \\ | \\ \text{---} \end{array} \xleftarrow{\quad A_l \quad} \xleftarrow{\quad O \quad} \xleftarrow{\quad A_l^* \quad} \quad \text{and} \quad \begin{array}{c} \text{---} \\ | \\ \text{---} \end{array} \xleftarrow{\quad E_r^r \quad} = \begin{array}{c} \text{---} \\ | \\ \text{---} \end{array} \xleftarrow{\quad A_r \quad} \xleftarrow{\quad O \quad} \xleftarrow{\quad A_r^* \quad}. \quad (\text{A.14})$$

Note that the eigenvalues have to be identical due to the canonicalization constraints. Although the determination of the environments is generally an eigenvalue problem, it is simplified to a linear problem when H is (quasi-)local and can be reformulated as an MPO in Schur form [239, 240, 198]. With the environments, the fixed-point equations become

$$\begin{array}{c} \text{---} \\ | \\ \text{---} \end{array} \xleftarrow{\quad A_c' \quad} = \lambda^{N_l+N_r-1} \begin{array}{c} \text{---} \\ | \\ \text{---} \end{array} \xleftarrow{\quad G_l \quad} \xleftarrow{\quad O \quad} \xleftarrow{\quad G_r \quad} = E \begin{array}{c} \text{---} \\ | \\ \text{---} \end{array} \xleftarrow{\quad A_c \quad} \quad (\text{A.15})$$

and

$$\begin{array}{c} \text{---} \\ | \\ \text{---} \end{array} \xleftarrow{\quad C' \quad} = \lambda^{N_l+N_r} \begin{array}{c} \text{---} \\ | \\ \text{---} \end{array} \xleftarrow{\quad G_l \quad} \xleftarrow{\quad C \quad} \xleftarrow{\quad G_r \quad} = E \begin{array}{c} \text{---} \\ | \\ \text{---} \end{array} \xleftarrow{\quad C \quad} \quad (\text{A.16})$$

where N_l (N_r) is the number of sites where A was left- (right-)canonicalized. Of course, both are infinite here but this shows that normalizing the environments as

$$\begin{array}{c} \text{---} \\ | \\ \text{---} \end{array} \xleftarrow{\quad C \quad} \xleftarrow{\quad G_l \quad} \xleftarrow{\quad G_r \quad} = 1, \quad (\text{A.17})$$

$E = \lambda^{N_l+N_r} = \lambda^{|Z|}$ so that E is either infinite when $\lambda > 1$, zero when $\lambda < 1$ or 1 when $\lambda = 1$. Furthermore, the dominant eigenvalue of the A_c eigenvalue problem equals λ while for the C eigenvalue problem we find eigenvalue 1. In case of a (quasi-)local Hamiltonian, the finite energy density can also be extracted from the linear problem for the

environments by taking into account the Schur form of O [198]. Important is that this calculation requires the left and right fixed-points of the MPS transfer matrix (without MPO in between). Using the center-site gauge, these are I and P as opposed to only I in the bosonic case.

In our derivation of the VUMPS algorithm we used that H was Hermitian. However, all of the techniques involved (based on the determination of dominant eigenvalues (typically involving Krylov methods)) also apply when searching the dominant eigenvector for a more general, non-Hermitian MPO. However, the method is no longer variational then. In this regard, one could wonder if there exists a local way to express that a fermionic MPO is Hermitian. *I.e.* is there a condition on O under which we know that T is Hermitian? Building on Sec. 4.1.4, we know that Hermiticity of such an operator comes down to

$$T = \begin{array}{c} \xleftarrow{\quad\downarrow\quad} \\ \square O \end{array} \xleftarrow{\quad\downarrow\quad} \begin{array}{c} \xleftarrow{\quad\downarrow\quad} \\ \square O \end{array} = \begin{array}{c} \xleftarrow{\quad\downarrow\quad} \\ \square O^* \end{array} \xleftarrow{\quad\downarrow\quad} \begin{array}{c} \xleftarrow{\quad\downarrow\quad} \\ \square O^* \end{array} \xleftarrow{\quad\downarrow\quad} \begin{array}{c} \xleftarrow{\quad\downarrow\quad} \\ \square O^* \end{array} = T^\dagger. \quad (\text{A.18})$$

Hence, one could infer a sufficient condition by relating the local tensors on both sides of the equality. However, as the virtual arrows point in opposite directions, we need to flip them. Furthermore, both MPOs might be related via a gauge transform. Hence, if there exists some arbitrary flipper satisfying

$$\rightarrow \triangle f \xleftarrow{\quad} \circ P \xleftarrow{\quad} \triangle f^{-1} \rightarrow = \rightarrow \circ I \rightarrow \quad (\text{A.19})$$

such that the relation

$$\begin{array}{c} \xleftarrow{\quad\downarrow\quad} \\ \square O \end{array} = \begin{array}{c} \xleftarrow{\quad\downarrow\quad} \\ \triangle f^{-1} \end{array} \rightarrow \begin{array}{c} \xleftarrow{\quad\downarrow\quad} \\ \square O^* \end{array} \xleftarrow{\quad\downarrow\quad} \begin{array}{c} \xleftarrow{\quad\downarrow\quad} \\ \triangle f \end{array} \leftarrow \circ P \xleftarrow{\quad\downarrow\quad} \begin{array}{c} \xleftarrow{\quad\downarrow\quad} \\ \square O \end{array}, \quad (\text{A.20})$$

is satisfied, then $T(O)$ will be Hermitian.

A.3 Vumps for a double-layer transfer matrix

This type of VUMPS algorithm is typically encountered when computing PEPS expectation values as the contraction of a 2D bra and ket layer with possibly a local operator in between. Hence, we will determine the leading eigenvector of the transfer operator

$$T(O) = \begin{array}{c} \xleftarrow{\quad\downarrow\quad} \\ \square O \end{array} \xleftarrow{\quad\downarrow\quad} \begin{array}{c} \xleftarrow{\quad\downarrow\quad} \\ \square O \end{array} \xleftarrow{\quad\downarrow\quad} \begin{array}{c} \xleftarrow{\quad\downarrow\quad} \\ \square O \end{array} \quad (\text{A.21})$$

where O is a double-layer tensor as in Eq. (4.129). For the fixed-point, we propose an MPS *Ansatz*,

$$|\Psi(M)\rangle = \begin{array}{c} \xleftarrow{\quad\downarrow\quad} \\ \square M \end{array} \xleftarrow{\quad\downarrow\quad} \begin{array}{c} \xleftarrow{\quad\downarrow\quad} \\ \square M \end{array} \xleftarrow{\quad\downarrow\quad} \begin{array}{c} \xleftarrow{\quad\downarrow\quad} \\ \square M \end{array} \xleftarrow{\quad\downarrow\quad} \quad (\text{A.22})$$

The optimal M tensors are then determined by projecting the eigenvalue equation for $T(O)$ onto the MPS tangent space, yielding

$$P_{|\Psi(M)\rangle} (T(O) - \Lambda) |\Psi(M)\rangle = 0. \quad (\text{A.23})$$

To do so, we have to determine the tangent space projector $P_{|\Psi(M)\rangle}$ in and orthogonal to a MPS with two physical legs. Note therefore that all the concepts mentioned in Appendix A.1 can readily be extended to multiple physical legs, with P tensors on the upward physical legs as the only exception. In particular, we can bring the MPS in the mixed gauge

$$|\Psi(M)\rangle = \begin{array}{c} \leftarrow \boxed{M_l} \leftarrow \boxed{M_c} \leftarrow \boxed{M_r} \leftarrow \\ \downarrow \uparrow \quad \downarrow \uparrow \quad \downarrow \uparrow \end{array} \quad (\text{A.24})$$

where

$$\begin{array}{c} \leftarrow \boxed{M_l} \leftarrow \circlearrowleft \boxed{C} \leftarrow \\ \downarrow \uparrow \end{array} = \begin{array}{c} \leftarrow \boxed{M_c} \leftarrow \\ \downarrow \uparrow \end{array} = \begin{array}{c} \leftarrow \circlearrowleft \boxed{C} \leftarrow \boxed{M_r} \leftarrow \\ \downarrow \uparrow \end{array} \quad (\text{A.25})$$

with

$$\begin{array}{c} \leftarrow \boxed{M_l} \leftarrow \\ \downarrow \uparrow \end{array} = \begin{array}{c} \curvearrowright \\ \curvearrowleft \end{array} \quad \text{and} \quad \begin{array}{c} \leftarrow \boxed{M_r} \leftarrow \\ \downarrow \uparrow \end{array} = \begin{array}{c} \curvearrowleft \\ \curvearrowright \end{array}. \quad (\text{A.26})$$

Here, the circular tensors in the physical contractions again indicate a parity tensor. A tangent vector for the $|\Psi(M)\rangle$ states can always be expressed as

$$|\Phi(B; M)\rangle = \sum_j \begin{array}{c} \leftarrow \boxed{M_l} \leftarrow \boxed{B} \leftarrow \boxed{M_r} \leftarrow \\ \downarrow \uparrow \quad \downarrow \uparrow \quad \downarrow \uparrow \\ j \end{array}. \quad (\text{A.27})$$

When orthogonal to the MPS, we can parametrize the B tensor herein as

$$\begin{array}{c} \leftarrow \boxed{V_l} \leftarrow \circlearrowleft \boxed{X} \leftarrow \\ \downarrow \uparrow \end{array} \quad \text{or} \quad \begin{array}{c} \leftarrow \circlearrowleft \boxed{X} \leftarrow \boxed{V_r} \leftarrow \\ \downarrow \uparrow \end{array}, \quad (\text{A.28})$$

i.e. the left-, respectively, right-canonical form where V_l spans the right null-space of M_l^* while V_r describes the left null-space of M_r^* so that

$$\begin{array}{c} \leftarrow \boxed{B} \leftarrow \\ \downarrow \uparrow \end{array} = 0, \quad \text{respectively,} \quad \begin{array}{c} \leftarrow \boxed{B} \leftarrow \\ \downarrow \uparrow \end{array} = 0 \quad (\text{A.29})$$

and the X tensor thus essentially contains all the parametric freedom in $|\Phi(B; M)\rangle$. Furthermore, both V_l and V_r are normalized in the same way as their corresponding MPS tensor such that

$$\begin{array}{c} \rightarrow \boxed{V_l^*} \rightarrow \\ \downarrow \uparrow \end{array} + \begin{array}{c} \rightarrow \boxed{M_l^*} \rightarrow \\ \downarrow \uparrow \end{array} = \begin{array}{c} \curvearrowright \\ \curvearrowleft \end{array} \quad \begin{array}{c} \rightarrow \boxed{V_l} \rightarrow \\ \downarrow \uparrow \end{array} + \begin{array}{c} \rightarrow \boxed{M_l} \rightarrow \\ \downarrow \uparrow \end{array} = \begin{array}{c} \curvearrowleft \\ \curvearrowright \end{array} \quad (\text{A.30})$$

and

$$\begin{array}{c} \downarrow \uparrow \\ \square V_r^* \rightarrow \\ \square V_r \leftarrow \\ \downarrow \uparrow \end{array} + \begin{array}{c} \downarrow \uparrow \\ \square M_r^* \rightarrow \\ \square M_r \leftarrow \\ \downarrow \uparrow \end{array} = \begin{array}{c} \downarrow \uparrow \\ \square \circ \\ \square P \rightarrow \\ \downarrow \uparrow \end{array} \quad (\text{A.31})$$

due to completeness. In both gauges the overlap between two tangent vectors thus reduces to

$$\langle \Phi(B_2; M) | \Phi(B_1; M) \rangle = |\mathbb{Z}| \begin{array}{c} \square B_1 \\ \downarrow \circ \\ \square P \end{array} = |\mathbb{Z}| \begin{array}{c} \square X_1 \\ \leftarrow \square X_2 \rightarrow \\ \square P \end{array}. \quad (\text{A.32})$$

The tangent space projection in and orthogonal to $|\Psi(M)\rangle$ of a general translation-invariant state $|\chi\rangle$ is the tangent vector parametrized by X for which

$$X = \min_X \| |\chi\rangle - |\Phi(B(X); M)\rangle \|^2. \quad (\text{A.33})$$

Again differentiating with respect to the complex conjugate of the entries of X , this minimum is characterized by

$$\begin{array}{c} \square X \\ \leftarrow \square P \end{array} - \begin{array}{c} \overbrace{\hspace{10em}}^{\chi} \\ \square M_l^* \rightarrow \square V_l^* \rightarrow \\ \square M_r^* \rightarrow \end{array} = 0. \quad (\text{A.34})$$

so that

$$|\Phi(B(X); M)\rangle = P_{|\Psi(M)\rangle} |\chi\rangle = \sum_j \begin{array}{c} \overbrace{\hspace{10em}}^{\chi} \\ \square M_l^* \rightarrow \square V_l^* \rightarrow \\ \square M_r^* \rightarrow \\ j \end{array} \quad (\text{A.35})$$

Using the aforementioned completeness relations we thus obtain

$$P_{|\Psi(M)\rangle} = \sum_j \begin{array}{c} \square M_l^* \rightarrow \\ \square M_l \leftarrow \\ \downarrow \uparrow \end{array} \Bigg|_j \begin{array}{c} \square M_r^* \rightarrow \\ \square M_r \leftarrow \\ \downarrow \uparrow \end{array} - \begin{array}{c} \square M_l^* \rightarrow \square V_l^* \rightarrow \\ \square M_l \leftarrow \square V_l \leftarrow \\ \downarrow \uparrow \end{array} \Bigg|_j \begin{array}{c} \square M_r^* \rightarrow \\ \square M_r \leftarrow \\ \downarrow \uparrow \end{array}. \quad (\text{A.36})$$

for the “two-leg” tangent space projector as the P tensors appear due to the operator application. The MPS approximation for the fixed-point of $T(O)$ thus satisfies the typical

VUMPS fixed-point equations, $M'_c \propto M_c$ and $C' \propto C$, where now

$$\begin{array}{c} \text{---} \\ \text{---} \end{array} \begin{array}{c} M_l \\ \downarrow \\ O \\ \uparrow \\ M_l^* \end{array} = \begin{array}{c} M_l \\ \leftarrow \quad \leftarrow \\ \downarrow \quad \uparrow \\ O \quad O \quad O \\ \uparrow \quad \downarrow \quad \uparrow \\ M_r^* \quad M_r \quad M_l^* \\ \leftarrow \quad \leftarrow \quad \leftarrow \\ \text{---} \quad \text{---} \quad \text{---} \end{array} \quad (A.37)$$

and

$$\begin{array}{c} \text{---} \\ \text{---} \end{array} \begin{array}{c} M_l \\ \leftarrow \quad \leftarrow \\ \downarrow \quad \uparrow \\ O \quad O \\ \uparrow \quad \downarrow \\ M_r^* \quad M_r \\ \leftarrow \quad \leftarrow \\ \text{---} \quad \text{---} \end{array} = \begin{array}{c} M_l \\ \leftarrow \quad \leftarrow \\ \downarrow \quad \uparrow \\ (C) \\ \uparrow \quad \downarrow \\ M_r^* \quad M_r \\ \leftarrow \quad \leftarrow \\ \text{---} \quad \text{---} \end{array} . \quad (A.38)$$

I.e. M_c and C are the solutions to an eigenvalue problem which we can solve by determining the environments G_l and G_r , defined by

$$\begin{array}{c} \text{---} \\ \text{---} \end{array} \begin{array}{c} G_l \\ \leftarrow \quad \leftarrow \\ \downarrow \quad \uparrow \\ M_l \\ \downarrow \\ O \\ \uparrow \\ M_l^* \\ \leftarrow \quad \leftarrow \\ \text{---} \end{array} = \lambda \begin{array}{c} \text{---} \\ \text{---} \end{array} \begin{array}{c} G_l \\ \leftarrow \quad \leftarrow \\ \text{---} \end{array} \quad \text{and} \quad \begin{array}{c} \text{---} \\ \text{---} \end{array} \begin{array}{c} G_r \\ \leftarrow \quad \leftarrow \\ \downarrow \quad \uparrow \\ M_r \\ \downarrow \\ O \\ \uparrow \\ M_r^* \\ \leftarrow \quad \leftarrow \\ \text{---} \end{array} = \lambda \begin{array}{c} \text{---} \\ \text{---} \end{array} \begin{array}{c} G_r \\ \leftarrow \quad \leftarrow \\ \text{---} \end{array} . \quad (A.39)$$

The VUMPS fixed-point equations then reduce to

$$\begin{array}{c} \text{---} \\ \text{---} \end{array} \begin{array}{c} M'_c \\ \downarrow \uparrow \\ \text{---} \end{array} = \begin{array}{c} \text{---} \\ \text{---} \end{array} \begin{array}{c} G_l \\ \leftarrow \quad \leftarrow \\ \downarrow \quad \uparrow \\ M_c \\ \downarrow \\ O \\ \uparrow \\ G_r \\ \leftarrow \quad \leftarrow \\ \text{---} \end{array} = \lambda \begin{array}{c} \text{---} \\ \text{---} \end{array} \begin{array}{c} M_c \\ \downarrow \uparrow \\ \text{---} \end{array} \quad (A.40)$$

and

$$\begin{array}{c} \text{---} \\ \text{---} \end{array} \begin{array}{c} (C)' \\ \leftarrow \quad \leftarrow \\ \text{---} \end{array} = \begin{array}{c} \text{---} \\ \text{---} \end{array} \begin{array}{c} G_l \\ \leftarrow \quad \leftarrow \\ \downarrow \quad \uparrow \\ (C) \\ \uparrow \quad \downarrow \\ G_r \\ \leftarrow \quad \leftarrow \\ \text{---} \end{array} = \begin{array}{c} \text{---} \\ \text{---} \end{array} \begin{array}{c} (C) \\ \leftarrow \quad \leftarrow \\ \text{---} \end{array} . \quad (A.41)$$

when the environments are normalized as

$$\begin{array}{c} \text{---} \\ \text{---} \end{array} \begin{array}{c} G_l \\ \leftarrow \quad \leftarrow \\ \downarrow \quad \uparrow \\ (C) \\ \uparrow \quad \downarrow \\ G_r \\ \leftarrow \quad \leftarrow \\ \text{---} \end{array} = 1 . \quad (A.42)$$

Appendix B

Parity obstructions: a proof

In Sec. 5.2 the reasoning for the (restricted) virtual parity configurations to be lifted to the physical level was rather hand-waving. Here, we present a rigorous, inductive proof. Therefore, we first consider the a GfTNS in 1D with $f = \chi = 1$ so that $A = \lambda J$ with

$$X = \begin{pmatrix} A & B \\ -B^T & D \end{pmatrix} \quad (\text{B.1})$$

the real and anti-symmetric local channel correlation matrix in the Kraus-Schuch formalism. As the state is pure, $XX^T = \mathbb{1}$ such that $AA^T + BB^T = 1$, implying that there exists a matrix $O \in O(2)$ with $B = \sqrt{1 - \lambda^2}O$. Furthermore, $AB + BD = 0$ so that $D = -\lambda O^T JO = -\lambda \det(O)J$. Consequently, the Fourier transformed correlation matrix of the GfTNS in the TRIMs is given by

$$G_{\text{out}} = \lambda J + (1 - \lambda^2) (-\lambda J - O(\pm J)O^T)^{-1} \quad (\text{B.2})$$

with the plus sign in the zone center and the minus sign at $k = \pi$ as G_{in} respectively equals J and $-J$ there. Simplifying this further, one obtains

$$\begin{aligned} G_{\text{out}} &= \lambda J + (1 - \lambda^2) (-\lambda \mp \det(O))^{-1} J^{-1} \\ &= \lambda J + (1 - \lambda^2) (\lambda \pm \det(O))^{-1} J \\ &= \pm \det(O)J. \end{aligned} \quad (\text{B.3})$$

Making a π jump in Fourier space hence corresponds to an extra minus sign for the parity in line with the odd number of virtual Majorana modes. Furthermore, the parity changing/conserving nature of the projection is determined by $\det O$. Writing X as $\tilde{O}^T J_{f+\chi} \tilde{O}$, it is straightforward to see that

$$\tilde{O} = \begin{pmatrix} 1 & & & \\ & \lambda & \sqrt{1 - \lambda^2} & \\ & \sqrt{1 - \lambda^2} & -\lambda & \\ & & & 1 \end{pmatrix} \begin{pmatrix} 1 & O \\ & \end{pmatrix} \quad (\text{B.4})$$

and thus $\text{Pf}(G_{\text{out}}) = (-1)^\chi \det \tilde{O} \text{Pf}(G_{\text{in}}) = (\mp 1)^\chi \det \tilde{O}$. This can be generalized to all integer χ by induction. Again starting from the purity of X and the fact that $A = \lambda J$,

one obtains (e.g. utilizing the SVD of B) that there exists an $O \in O(2\chi)$ so that

$$X = \begin{pmatrix} 1 & \\ & O^T \end{pmatrix} \begin{pmatrix} \lambda J & \sqrt{1-\lambda^2} \\ -\sqrt{1-\lambda^2} & -\lambda J \\ & J_{\chi-f} \end{pmatrix} \begin{pmatrix} 1 & \\ & O \end{pmatrix} \quad (\text{B.5})$$

and thus $X = \tilde{O}^T J_{f+\chi} \tilde{O}$ with $\det \tilde{O} = -\det O$. Using this orthogonal transformation, the correlation matrix of the output state can be rewritten as

$$G_{\text{out}} = \lambda J + (1 - \lambda^2) \begin{pmatrix} 1 \\ 0 \end{pmatrix}^T \left(\begin{pmatrix} -\lambda J & \\ & J_{\chi-f} \end{pmatrix} \mp X' \right)^{-1} \begin{pmatrix} 1 \\ 0 \end{pmatrix} \quad (\text{B.6})$$

where $X' = O J_\chi O^T = \begin{pmatrix} A' & B' \\ -B'^T & D' \end{pmatrix}$ ($J_n = J^{\oplus n}$) can be interpreted as a new but lower-dimensional GfTNS parameter matrix with $X' X'^T = 1$. Using the definition of Schur complements this can be simplified further to

$$G_{\text{out}} = \lambda J \mp (1 - \lambda^2)(\pm \lambda J + G')^{-1} \quad (\text{B.7})$$

with $G' = A' + B'(D' \mp J_{\chi-f})^{-1} B'^T$. Assuming validity of the fixed parity configuration for $\chi - 1$, $G' = (\mp 1)^{\chi-1} \det O J$ yielding

$$\begin{aligned} G_{\text{out}} &= \lambda J + (1 - \lambda^2) J (\lambda - (\mp 1)^\chi \det O)^{-1} \\ &= \lambda J - J (\lambda - (\mp 1)^\chi \det \tilde{O}) \\ &= (\mp 1)^\chi \det \tilde{O}. \end{aligned} \quad (\text{B.8})$$

Extending the proof to higher dimensions proceeds along similar lines but with G_{in} now existing of J blocks with possibly different signs (let ϕ denote the number of $-J$ blocks). For the output correlation matrix, one then obtains

$$G_{\text{out}} = \lambda J - (1 - \lambda^2) \begin{pmatrix} 1 \\ 0 \end{pmatrix}^T \left(\begin{pmatrix} \lambda J & \\ & -J_{\chi-f} \end{pmatrix} + X' \right)^{-1} \begin{pmatrix} 1 \\ 0 \end{pmatrix} \quad (\text{B.9})$$

but now with $\chi = \sum_i \chi_i$ and $X' = O G_{\text{in}} O^T = O' J_\chi O'^T$ so that $\det O = \det O' (-1)^\phi$. Again simplifying this further yields

$$G_{\text{out}} = \lambda J - (1 - \lambda^2)(\lambda J - G')^{-1} \quad (\text{B.10})$$

where validity of the proposition for $\chi - 1$ can again be used to rewrite G' as $(-1)^{\chi-1} \det O' J$ so that

$$\begin{aligned} G_{\text{out}} &= \lambda J + (1 - \lambda^2) J (\lambda - (-1)^{\chi-1} (-\det \tilde{O} (-1)^\phi))^{-1} \\ &= \lambda J - J (\lambda - (-1)^{\chi-\phi} \det \tilde{O}) \\ &= (-1)^{\chi-\phi} \det \tilde{O}. \end{aligned} \quad (\text{B.11})$$

Indeed, this result corresponds to the expected extra factor $(-1)^{\chi_i}$ for a $\frac{\mathbf{b}_i}{2}$ jump in Fourier space, thus completing the proof.

Finally, the proof can be extended to multiple physical fermions by first transforming A to $\bigoplus_{j=1}^f \lambda_j J$ with $O_1 \in O(2f)$. Purity of X in combination with the SVD of B can then again be used to construct $O_2 \in O(2\chi)$ with

$$X = O^T \begin{pmatrix} (\lambda_j J)^\oplus & \sqrt{1 - \lambda_j^2}^\oplus \\ -\sqrt{1 - \lambda_j^2}^\oplus & -(\lambda_j J)^\oplus \end{pmatrix} O \quad (\text{B.12})$$

and $O = \begin{pmatrix} O_1 & \\ & O_2 \end{pmatrix}$. For the output parity this gives

$$\text{Pf}(G_{\text{out}}) = \det O_1 \text{ Pf} \left[(\lambda_j J)^\oplus - \sqrt{1 - \lambda_j^2}^\oplus ((\lambda_j J_j)^\oplus - G')^{-1} \sqrt{1 - \lambda_j^2}^\oplus \right] \quad (\text{B.13})$$

with again $G' = A' + B'(D' - J_{\chi-f})^{-1}B'^T$ and $X' = O_2 G_{\text{in}} O_2^T$. As the calculation of the inner inverse is no longer analytically possible since $f > 1$, we rewrite the Pfaffian, using its Schur complement properties

$$\text{Pf}(G_{\text{out}}) = \det O_1 \text{ Pf}^{-1} ((\lambda_j J_j)^\oplus - G') \text{ Pf} \begin{pmatrix} (\lambda_j J_j)^\oplus & \sqrt{1 - \lambda_j^2}^\oplus \\ -\sqrt{1 - \lambda_j^2}^\oplus & (\lambda_j J_j)^\oplus - G' \end{pmatrix} \quad (\text{B.14})$$

where the Pfaffian of the large matrix can be calculated via its minors and making use of the validity of the proposition for lower χ .

Bibliography

- [1] E. M. Lifshitz L. D. Landau. *Quantum Mechanics*. Pergamon, Oxford, 1965.
- [2] J. J. Sakurai. *Modern Quantum Mechanics*. Addison-Wesley, Reading, 1994.
- [3] C. J. Joachain B. H. Bransden. *Quantum Mechanics*. Prentice Hall, Oxford, 2000.
- [4] W. Pauli. The Connection Between Spin and Statistics. *Physical Review*, 58(8):716–722, oct 1940.
- [5] Scott Aaronson and Alex Arkhipov. Bosonsampling is far from uniform, 2013.
- [6] Alexander Altland and Ben D. Simons. *Condensed Matter Field Theory*. Cambridge University Press, Cambridge, 2 edition, 2010.
- [7] V. Fock. Konfigurationsraum und zweite quantelung. *Zeitschrift für Physik*, 75(9):622–647, 1932.
- [8] G. G. Emch. *Algebraic methods in statistical mechanics and quantum field theory*. Wiley-Interscience, 1972.
- [9] M.A. Naimark I. Gelfand. On the imbedding of normed rings into the ring of operators in hilbert space. *Matematicheskii Sbornik*, 54(2):197–217, 1943.
- [10] I. E. Segal. Postulates for general quantum mechanics. *Annals of Mathematics*, 48(4):930–948, 1947.
- [11] P. W. Anderson. Infrared catastrophe in fermi gases with local scattering potentials. *Phys. Rev. Lett.*, 18:1049–1051, Jun 1967.
- [12] R. Haag. On quantum field theories. *Matematisk-fysiske Meddelelser*, 29:1–37, 1955.
- [13] A. Einstein. Quantentheorie des einatomigen idealen gases. *Königliche Preussische Akademie der Wissenschaften. Sitzungsberichte:*, pages 261–267, 1924.
- [14] S. N. Bose. Plancks gesetz und lichtquantenhypothese. *Zeitschrift für Physik*, pages 178–181, 1924.
- [15] Frank Verstraete and Henri Verschelde. On quantum channels, 2003.
- [16] K. Kraus. *States, Effects and Operations: Fundamental Notions of Quantum Theory*. Springer Verlag, 1983.

- [17] E. Schrödinger. Die gegenwärtige situation in der quantenmechanik. *Naturwissenschaften*, 23:807, 1935.
- [18] N. Rosen A. Einstein, B. Podolsky. Can quantum-mechanical description of physical reality be considered complete? *Physical Review*, 47:777, 1935.
- [19] D. J. Bohm. *Quantum Theory*. Dover Publications, 1951.
- [20] J. S. Bell. On the problem of hidden variables in quantum mechanics. *Reviews of Modern Physics*, 38:477, 1966.
- [21] Stuart J. Freedman and John F. Clauser. Experimental test of local hidden-variable theories. *Phys. Rev. Lett.*, 28:938–941, Apr 1972.
- [22] Alain Aspect, Jean Dalibard, and Gérard Roger. Experimental test of bell’s inequalities using time-varying analyzers. *Phys. Rev. Lett.*, 49:1804–1807, Dec 1982.
- [23] A. Shimony J. F. Clauser, M. A. Horne and R. A. Holt. Proposed experiment to test local hidden-variable theories. *Physical Review Letters*, 23:880, 1969.
- [24] C. E. Shannon. A mathematical theory of communication. *The Bell System Technical Journal*, 27(3):379–423, 1948.
- [25] B. S. Cirel’son. Quantum generalizations of bell’s inequality. *Letters in Mathematical Physics*, 4:93–100, 1980.
- [26] Valerie Coffman, Joydip Kundu, and William K. Wootters. Distributed entanglement. *Physical Review A*, 61(5), apr 2000.
- [27] Masato Koashi and Andreas Winter. Monogamy of quantum entanglement and other correlations. *Physical Review A*, 69(2), feb 2004.
- [28] Tobias J. Osborne and Frank Verstraete. General monogamy inequality for bipartite qubit entanglement. *Physical Review Letters*, 96(22), jun 2006.
- [29] Elliott H. Lieb and Mary Beth Ruskai. A fundamental property of quantum-mechanical entropy. *Phys. Rev. Lett.*, 30:434–436, Mar 1973.
- [30] Michael M. Wolf, Frank Verstraete, Matthew B. Hastings, and J. Ignacio Cirac. Area laws in quantum systems: Mutual information and correlations. *Phys. Rev. Lett.*, 100:070502, Feb 2008.
- [31] M. B. Hastings. Locality in quantum and markov dynamics on lattices and networks. *Phys. Rev. Lett.*, 93:140402, Sep 2004.
- [32] Matthew B. Hastings and Tohru Koma. Spectral gap and exponential decay of correlations. *Communications in Mathematical Physics*, 265(3):781–804, apr 2006.
- [33] G. C. Wick. The evaluation of the collision matrix. *Phys. Rev.*, 80:268–272, Oct 1950.
- [34] M. C. Arnesen, S. Bose, and V. Vedral. Natural thermal and magnetic entanglement in the 1d heisenberg model. *Physical Review Letters*, 87(1), jun 2001.

- [35] D. Gunlycke, V. M. Kendon, V. Vedral, and S. Bose. Thermal concurrence mixing in a one-dimensional ising model. *Physical Review A*, 64(4), sep 2001.
- [36] M B Hastings. An area law for one-dimensional quantum systems. *Journal of Statistical Mechanics: Theory and Experiment*, 2007(08):P08024–P08024, aug 2007.
- [37] Mark Srednicki. Entropy and area. *Phys. Rev. Lett.*, 71:666–669, Aug 1993.
- [38] M. Cramer, J. Eisert, M. B. Plenio, and J. Dreißig. Entanglement-area law for general bosonic harmonic lattice systems. *Physical Review A*, 73(1), jan 2006.
- [39] Boris Ponsioen, Sangwoo S. Chung, and Philippe Corboz. Period 4 stripe in the extended two-dimensional hubbard model. *Physical Review B*, 100(19), nov 2019.
- [40] Laurens Vanderstraeten, Bram Vanhecke, and Frank Verstraete. Residual entropies for three-dimensional frustrated spin systems with tensor networks. *Physical Review E*, 98(4), oct 2018.
- [41] Yuhang Liu, Ramanjit Sohal, Jonah Kudler-Flam, and Shinsei Ryu. Multipartitioning topological phases by vertex states and quantum entanglement. *Phys. Rev. B*, 105:115107, Mar 2022.
- [42] Yuhang Liu, Yuya Kusuki, Jonah Kudler-Flam, Ramanjit Sohal, and Shinsei Ryu. Multipartite entanglement in two-dimensional chiral topological liquids. *arXiv e-prints*, page arXiv:2301.07130, January 2023.
- [43] Isaac H. Kim, Bowen Shi, Kohtaro Kato, and Victor V. Albert. Chiral central charge from a single bulk wave function. *Phys. Rev. Lett.*, 128:176402, Apr 2022.
- [44] Karthik Siva, Yijian Zou, Tomohiro Soejima, Roger S. K. Mong, and Michael P. Zaletel. Universal tripartite entanglement signature of ungappable edge states. *Phys. Rev. B*, 106:L041107, Jul 2022.
- [45] Ramanjit Sohal and Shinsei Ryu. Entanglement in tripartitions of topological orders: a diagrammatic approach. *arXiv e-prints*, page arXiv:2301.07763, January 2023.
- [46] Christoph Holzhey, Finn Larsen, and Frank Wilczek. Geometric and renormalized entropy in conformal field theory. *Nuclear Physics B*, 424(3):443–467, 1994.
- [47] G. Vidal, J. I. Latorre, E. Rico, and A. Kitaev. Entanglement in quantum critical phenomena. *Phys. Rev. Lett.*, 90:227902, Jun 2003.
- [48] Pasquale Calabrese and John Cardy. Entanglement entropy and quantum field theory. *Journal of Statistical Mechanics: Theory and Experiment*, 2004(06):P06002, jun 2004.
- [49] Michael M. Wolf. Violation of the entropic area law for fermions. *Phys. Rev. Lett.*, 96:010404, Jan 2006.
- [50] Dimitri Gioev and Israel Klich. Entanglement entropy of fermions in any dimension and the widom conjecture. *Phys. Rev. Lett.*, 96:100503, Mar 2006.

- [51] Brian Swingle. Entanglement entropy and the fermi surface. *Phys. Rev. Lett.*, 105:050502, Jul 2010.
- [52] Wenzin Ding, Alexander Seidel, and Kun Yang. Entanglement entropy of fermi liquids via multidimensional bosonization. *Phys. Rev. X*, 2:011012, Mar 2012.
- [53] L. Tagliacozzo, Thiago. R. de Oliveira, S. Iblisdir, and J. I. Latorre. Scaling of entanglement support for matrix product states. *Phys. Rev. B*, 78:024410, Jul 2008.
- [54] Frank Pollmann, Subroto Mukerjee, Ari M. Turner, and Joel E. Moore. Theory of finite-entanglement scaling at one-dimensional quantum critical points. *Phys. Rev. Lett.*, 102:255701, Jun 2009.
- [55] Bram Vanhecke, Jutho Haegeman, Karel Van Acleyen, Laurens Vanderstraeten, and Frank Verstraete. Scaling hypothesis for matrix product states. *Physical Review Letters*, 123(25), dec 2019.
- [56] Philippe Corboz, Piotr Czarnik, Geert Kapteijns, and Luca Tagliacozzo. Finite correlation length scaling with infinite projected entangled-pair states. *Phys. Rev. X*, 8:031031, Jul 2018.
- [57] Michael Rader and Andreas M. Läuchli. Finite correlation length scaling in lorentz-invariant gapless ipeps wave functions. *Phys. Rev. X*, 8:031030, Jul 2018.
- [58] Piotr Czarnik and Philippe Corboz. Finite correlation length scaling with infinite projected entangled pair states at finite temperature. *Phys. Rev. B*, 99:245107, Jun 2019.
- [59] Bram Vanhecke, Juraj Hasik, Frank Verstraete, and Laurens Vanderstraeten. Scaling hypothesis for projected entangled-pair states. *Phys. Rev. Lett.*, 129:200601, Nov 2022.
- [60] Eugene Paul Wigner. *Gruppentheorie und ihre Anwendung auf die Quantenmechanik der Atomspektren*. Friedrich Vieweg und Sohn, 1931.
- [61] Franco Strocchi. *Symmetry breaking*, volume 643. Springer, 2005.
- [62] L. D. Landau. Theory of phase transformations. i. *Physikalische Zeitschrift der Sowjetunion*, 11:26, 1937.
- [63] L. D. Landau. Theory of phase transformations. ii. *Physikalische Zeitschrift der Sowjetunion*, 11:545, 1937.
- [64] V. L. Ginzburg and L. D. Landau. Concerning the theory of superconductivity. *Journal of Experimental and Theoretical Physics*, 20:1064, 1950.
- [65] K. G. Wilson and J. Kogut. The renormalization group and the epsilon expansion. *Physics Reports*, 12:75, 1974.
- [66] Jeffrey Goldstone, Abdus Salam, and Steven Weinberg. Broken symmetries. *Phys. Rev.*, 127:965–970, Aug 1962.

- [67] Robert V. Lange. Nonrelativistic theorem analogous to the goldstone theorem. *Phys. Rev.*, 146:301–303, Jun 1966.
- [68] Yoichiro Nambu. Quasi-particles and gauge invariance in the theory of superconductivity. *Phys. Rev.*, 117:648–663, Feb 1960.
- [69] S. R. Coleman. There are no goldstone bosons in two dimensions. *Communications in Mathematical Physics*, 31:259–264, 1973.
- [70] N. D. Mermin and H. Wagner. Absence of ferromagnetism or antiferromagnetism in one- or two-dimensional isotropic heisenberg models. *Phys. Rev. Lett.*, 17:1133–1136, Nov 1966.
- [71] P. C. Hohenberg. Existence of long-range order in one and two dimensions. *Phys. Rev.*, 158:383–386, Jun 1967.
- [72] F. J. Wegner. Duality in generalized ising models and phase transitions without local order parameters. *J. Math. Phys.*, 12:2259–2272, 1971.
- [73] J M Kosterlitz and D J Thouless. Ordering, metastability and phase transitions in two-dimensional systems. *Journal of Physics C: Solid State Physics*, 6(7):1181, apr 1973.
- [74] K. v. Klitzing, G. Dorda, and M. Pepper. New method for high-accuracy determination of the fine-structure constant based on quantized hall resistance. *Phys. Rev. Lett.*, 45:494–497, Aug 1980.
- [75] X. G. Wen. Gapless boundary excitations in the quantum hall states and in the chiral spin states. *Phys. Rev. B*, 43:11025–11036, May 1991.
- [76] D. C. Tsui, H. L. Stormer, and A. C. Gossard. Two-dimensional magnetotransport in the extreme quantum limit. *Phys. Rev. Lett.*, 48:1559–1562, May 1982.
- [77] Frank Wilczek. Quantum mechanics of fractional-spin particles. *Phys. Rev. Lett.*, 49:957–959, Oct 1982.
- [78] P.W. Anderson. Resonating valence bonds: A new kind of insulator? *Materials Research Bulletin*, 8(2):153–160, 1973.
- [79] X.G. Wen. *Quantum Field Theory of Many-body Systems: From the Origin of Sound to an Origin of Light and Electrons*. Oxford graduate texts. Oxford University Press, 2004.
- [80] C. L. Kane and E. J. Mele. Quantum spin hall effect in graphene. *Phys. Rev. Lett.*, 95:226801, Nov 2005.
- [81] N. Read and Dmitry Green. Paired states of fermions in two dimensions with breaking of parity and time-reversal symmetries and the fractional quantum hall effect. *Phys. Rev. B*, 61:10267–10297, Apr 2000.
- [82] Andreas P. Schnyder, Shinsei Ryu, Akira Furusaki, and Andreas W. W. Ludwig. Classification of topological insulators and superconductors in three spatial dimensions. *Phys. Rev. B*, 78:195125, Nov 2008.

- [83] Alexei Kitaev, Vladimir Lebedev, and Mikhail Feigel'man. Periodic table for topological insulators and superconductors. In *AIP Conference Proceedings*. AIP, 2009.
- [84] D. J. Thouless, M. Kohmoto, M. P. Nightingale, and M. den Nijs. Quantized hall conductance in a two-dimensional periodic potential. *Phys. Rev. Lett.*, 49:405–408, Aug 1982.
- [85] Matthew F. Lapa, Jeffrey C. Y. Teo, and Taylor L. Hughes. Interaction-enabled topological crystalline phases. *Phys. Rev. B*, 93:115131, Mar 2016.
- [86] Lukasz Fidkowski and Alexei Kitaev. Effects of interactions on the topological classification of free fermion systems. *Phys. Rev. B*, 81:134509, Apr 2010.
- [87] Lukasz Fidkowski and Alexei Kitaev. Topological phases of fermions in one dimension. *Phys. Rev. B*, 83:075103, Feb 2011.
- [88] D. Pérez-García, M. M. Wolf, M. Sanz, F. Verstraete, and J. I. Cirac. String order and symmetries in quantum spin lattices. *Phys. Rev. Lett.*, 100:167202, Apr 2008.
- [89] Nick Bultinck, Dominic J. Williamson, Jutho Haegeman, and Frank Verstraete. Fermionic matrix product states and one-dimensional topological phases. *Phys. Rev. B*, 95:075108, Feb 2017.
- [90] A.Yu. Kitaev. Fault-tolerant quantum computation by anyons. *Annals of Physics*, 303(1):2–30, jan 2003.
- [91] Paul Adrien Maurice Dirac. The quantum theory of the electron. *Proceedings of The Royal Society A: Mathematical, Physical and Engineering Sciences*, 117:610–624, 1928.
- [92] P. Pyykko. Relativistic effects in structural chemistry. *Chemical Reviews*, 88(3):563–594, 1988.
- [93] M. Born and R. Oppenheimer. Zur quantentheorie der moleküle. *Annalen der Physik*, 389(20):457–484, 1927.
- [94] E. Schrödinger. Quantisierung als eigenwertproblem. *Annalen der Physik*, 384(4):361–376, 1926.
- [95] D. R. Hartree. The wave mechanics of an atom with a non-coulomb central field. part i. theory and methods. *Mathematical Proceedings of the Cambridge Philosophical Society*, 24(1):89–110, 1928.
- [96] D. R. Hartree. The wave mechanics of an atom with a non-coulomb central field. part ii. some results and discussion. *Mathematical Proceedings of the Cambridge Philosophical Society*, 24(1):111–132, 1928.
- [97] J. C. Slater. The self consistent field and the structure of atoms. *Phys. Rev.*, 32:339–348, Sep 1928.
- [98] V. Fock. Näherungsmethode zur lösung des quantenmechanischen mehrkörperproblems. *Zeitschrift für Physik*, 61:126–148, 1930.

- [99] J. C. Slater. Atomic shielding constants. *Phys. Rev.*, 36:57–64, Jul 1930.
- [100] S. F. Boys and Alfred Charles Egerton. Electronic wave functions - i. a general method of calculation for the stationary states of any molecular system. *Proceedings of the Royal Society of London. Series A. Mathematical and Physical Sciences*, 200(1063):542–554, 1950.
- [101] John A Pople and Warren J Hehre. Computation of electron repulsion integrals involving contracted gaussian basis functions. *Journal of Computational Physics*, 27(2):161–168, 1978.
- [102] J. C. Slater. The theory of complex spectra. *Phys. Rev.*, 34:1293–1322, Nov 1929.
- [103] Rodney J. Bartlett and Monika Musiał. Coupled-cluster theory in quantum chemistry. *Rev. Mod. Phys.*, 79:291–352, Feb 2007.
- [104] Steven R. White. Density matrix formulation for quantum renormalization groups. *Phys. Rev. Lett.*, 69:2863–2866, Nov 1992.
- [105] P. Hohenberg and W. Kohn. Inhomogeneous electron gas. *Phys. Rev.*, 136:B864–B871, Nov 1964.
- [106] Pedro Borlido, Thorsten Aull, Ahmad W. Huran, Fabien Tran, Miguel A. L. Marques, and Silvana Botti. Large-scale benchmark of exchange–correlation functionals for the determination of electronic band gaps of solids. *Journal of Chemical Theory and Computation*, 15(9):5069–5079, 2019. PMID: 31306006.
- [107] W. Kohn and L. J. Sham. Self-consistent equations including exchange and correlation effects. *Phys. Rev.*, 140:A1133–A1138, Nov 1965.
- [108] Assa Auerbach. *Interacting electrons and quantum magnetism*. Springer Science and Business Media, 2012.
- [109] F. Bloch. Über die quantenmechanik der elektronen in kristallgittern. *Zeitschrift für Physik*, 52(7):555–600, 1929. PMID: 31306006.
- [110] E. Wigner and F. Seitz. On the constitution of metallic sodium. *Physical Review*, 43(10):804–810, may 1933.
- [111] J. Zak. Dynamics of electrons in solids in external fields. *Phys. Rev.*, 168:686–695, Apr 1968.
- [112] Nicola Marzari and David Vanderbilt. Maximally localized generalized wannier functions for composite energy bands. *Phys. Rev. B*, 56:12847–12865, Nov 1997.
- [113] Christian Brouder, Gianluca Panati, Matteo Calandra, Christophe Mourougane, and Nicola Marzari. Exponential localization of wannier functions in insulators. *Phys. Rev. Lett.*, 98:046402, Jan 2007.
- [114] J. C. Slater and G. F. Koster. Simplified lcao method for the periodic potential problem. *Phys. Rev.*, 94:1498–1524, Jun 1954.
- [115] P. R. Wallace. The band theory of graphite. *Phys. Rev.*, 71:622–634, May 1947.

- [116] L. D. Landau. The theory of a fermi liquid. *Sov. Phys. JETP*, 3(6):920, 1957.
- [117] L. D. Landau. On the theory of a fermi liquid. *Sov. Phys. JETP*, 8(1):70, 1959.
- [118] A A Abrikosov, I Dzyaloshinskii, L P Gorkov, and Richard A Silverman. *Methods Of Quantum Field Theory In Statistical Physics*. Dover, New York, 1975.
- [119] R. Shankar. Renormalization-group approach to interacting fermions. *Rev. Mod. Phys.*, 66:129–192, Jan 1994.
- [120] Sin-itiro Tomonaga. Remarks on bloch's method of sound waves applied to many-fermion problems. *Progress of Theoretical Physics*, 5(4):544–569, 07 1950.
- [121] J. M. Luttinger. An exactly soluble model of a many-fermion system. *Journal of Mathematical Physics*, 4(9):1154–1162, 12 2004.
- [122] Daniel C. Mattis and Elliott H. Lieb. Exact solution of a many-fermion system and its associated boson field. *Journal of Mathematical Physics*, 6(2):304–312, 12 2004.
- [123] Jean-Baptiste Morée, Motoaki Hirayama, Michael Thobias Schmid, Youhei Yamaji, and Masatoshi Imada. Ab initio low-energy effective hamiltonians for the high-temperature superconducting cuprates $\text{bi}_2\text{sr}_2\text{cu}_6$, $\text{bi}_2\text{sr}_2\text{cacu}_2\text{o}_8$, hgba_2cu_4 and cacu_2 . *Physical Review B*, 106(23), dec 2022.
- [124] Francesco Ferrari, Federico Becca, and Roser Valentí. Charge density waves in kagome-lattice extended hubbard models at the van hove filling. *Phys. Rev. B*, 106:L081107, Aug 2022.
- [125] Hubbard J. Electron correlations in narrow energy bands. *Proc. R. Soc. Lond.*, A276(238), 1963.
- [126] Martin C. Gutzwiller. Effect of correlation on the ferromagnetism of transition metals. *Phys. Rev. Lett.*, 10:159–162, Mar 1963.
- [127] J. Kanamori. Electron correlation and ferromagnetism of transition metals. *Progress of Theoretical Physics*, 30(3):275–289, September 1963.
- [128] H. Bethe. Zur theorie der metalle. *Zeitschrift für Physik*, 71(3):205–226, 1931.
- [129] Fabian H. L. Essler, Holger Frahm, Frank Göhmann, Andreas Klümper, and Vladimir E. Korepin. *The One-Dimensional Hubbard Model*. Cambridge University Press, Cambridge, 2005.
- [130] E. Y. Loh, J. E. Gubernatis, R. T. Scalettar, S. R. White, D. J. Scalapino, and R. L. Sugar. Sign problem in the numerical simulation of many-electron systems. *Phys. Rev. B*, 41:9301–9307, May 1990.
- [131] Steven R. White and D. J. Scalapino. Stripes on a 6-leg hubbard ladder. *Phys. Rev. Lett.*, 91:136403, Sep 2003.
- [132] Andrew S. Darmawan, Yusuke Nomura, Youhei Yamaji, and Masatoshi Imada. Stripe and superconducting order competing in the hubbard model on a square lattice studied by a combined variational monte carlo and tensor network method. *Phys. Rev. B*, 98:205132, Nov 2018.

- [133] T. Giamarchi and C. Lhuillier. Phase diagrams of the two-dimensional hubbard and t-j models by a variational monte carlo method. *Phys. Rev. B*, 43:12943–12951, Jun 1991.
- [134] Luca F. Tocchio, Federico Becca, and Sandro Sorella. Hidden mott transition and large- u superconductivity in the two-dimensional hubbard model. *Phys. Rev. B*, 94:195126, Nov 2016.
- [135] J. P. F. LeBlanc, Andrey E. Antipov, Federico Becca, Ireneusz W. Bulik, Garnet Kin-Lic Chan, Chia-Min Chung, Youjin Deng, Michel Ferrero, Thomas M. Henderson, Carlos A. Jiménez-Hoyos, E. Kozik, Xuan-Wen Liu, Andrew J. Millis, N. V. Prokof'ev, Mingpu Qin, Gustavo E. Scuseria, Hao Shi, B. V. Svistunov, Luca F. Tocchio, I. S. Tupitsyn, Steven R. White, Shiwei Zhang, Bo-Xiao Zheng, Zhenyue Zhu, and Emanuel Gull. Solutions of the two-dimensional hubbard model: Benchmarks and results from a wide range of numerical algorithms. *Phys. Rev. X*, 5:041041, Dec 2015.
- [136] J. M. Tranquada, B. J. Sternlieb, J. D. Axe, Y. Nakamura, and S. Uchida. Evidence for stripe correlations of spins and holes in copper oxide superconductors. *Nature*, 375(6532):561–563, 1995.
- [137] Andrej Mesaros, Kazuhiro Fujita, Stephen D. Edkins, Mohammad H. Hamidian, Hiroshi Eisaki, Shin ichi Uchida, J. C. Séamus Davis, Michael J. Lawler, and Eun-Ah Kim. Commensurate 4a0-period charge density modulations throughout the $\text{bi}_2\text{sr}_2\text{cacu}_2\text{o}_8+\text{x}$ pseudogap regime. *Proceedings of the National Academy of Sciences*, 113(45):12661–12666, 2016.
- [138] J. M. Tranquada, J. D. Axe, N. Ichikawa, A. R. Moodenbaugh, Y. Nakamura, and S. Uchida. Coexistence of, and competition between, superconductivity and charge-stripe order in $\text{la}_{1.6-\text{x}}\text{nd}_{0.4}\text{sr}_{\text{x}}\text{cu}_4$. *Phys. Rev. Lett.*, 78:338–341, Jan 1997.
- [139] K. A. Chao, J. Spalek, and A. M. Oleś. Canonical perturbation expansion of the hubbard model. *Phys. Rev. B*, 18:3453–3464, Oct 1978.
- [140] J. Bardeen, L. N. Cooper, and J. R. Schrieffer. Microscopic theory of superconductivity. *Phys. Rev.*, 106:162–164, Apr 1957.
- [141] J. Bardeen, L. N. Cooper, and J. R. Schrieffer. Theory of superconductivity. *Phys. Rev.*, 108:1175–1204, Dec 1957.
- [142] Leon N. Cooper. Bound electron pairs in a degenerate fermi gas. *Phys. Rev.*, 104:1189–1190, Nov 1956.
- [143] J. Bardeen. Theory of the meissner effect in superconductors. *Phys. Rev.*, 97:1724–1725, Mar 1955.
- [144] F. London. On the problem of the molecular theory of superconductivity. *Phys. Rev.*, 74:562–573, Sep 1948.
- [145] A Yu Kitaev. Unpaired majorana fermions in quantum wires. *Physics-Uspekhi*, 44(10S):131, oct 2001.

- [146] P. W. Anderson. An approximate quantum theory of the antiferromagnetic ground state. *Phys. Rev.*, 86:694–701, Jun 1952.
- [147] Ryogo Kubo. The spin-wave theory of antiferromagnetics. *Phys. Rev.*, 87:568–580, Aug 1952.
- [148] Takehiko Oguchi. Theory of spin-wave interactions in ferro- and antiferromagnetism. *Phys. Rev.*, 117:117–123, Jan 1960.
- [149] Runze Chi, Yang Liu, Yuan Wan, Hai-Jun Liao, and T. Xiang. Spin excitation spectra of anisotropic spin-1/2 triangular lattice heisenberg antiferromagnets. *Physical Review Letters*, 129(22), nov 2022.
- [150] Qian Li, Hong Li, Jize Zhao, Hong-Gang Luo, and Z. Y. Xie. Magnetization of the spin-1/2 heisenberg antiferromagnet on the triangular lattice. *Phys. Rev. B*, 105:184418, May 2022.
- [151] Elliott Lieb, Theodore Schultz, and Daniel Mattis. Two soluble models of an anti-ferromagnetic chain. *Annals of Physics*, 16(3):407–466, 1961.
- [152] Masaki Oshikawa. Commensurability, excitation gap, and topology in quantum many-particle systems on a periodic lattice. *Phys. Rev. Lett.*, 84:1535–1538, Feb 2000.
- [153] M. B. Hastings. Lieb-schultz-mattis in higher dimensions. *Phys. Rev. B*, 69:104431, Mar 2004.
- [154] T. Holstein and H. Primakoff. Field dependence of the intrinsic domain magnetization of a ferromagnet. *Phys. Rev.*, 58:1098–1113, Dec 1940.
- [155] Chanchal K. Majumdar and Dipan K. Ghosh. On Next-Nearest-Neighbor Interaction in Linear Chain. I. *Journal of Mathematical Physics*, 10(8):1388–1398, 11 2003.
- [156] P. W. Anderson. The resonating valence bond state in $\text{La}_{2-x}\text{Cu}_x\text{O}_4$ and superconductivity. *Science*, 235(4793):1196–1198, 1987.
- [157] G. Baskaran, Z. Zou, and P.W. Anderson. The resonating valence bond state and high-tc superconductivity — a mean field theory. *Solid State Communications*, 63(11):973–976, 1987.
- [158] Alexei Kitaev. Anyons in an exactly solved model and beyond. *Annals of Physics*, 321(1):2–111, 2006. January Special Issue.
- [159] Lucile Savary and Leon Balents. Quantum spin liquids: a review. *Reports on Progress in Physics*, 80(1):016502, nov 2016.
- [160] Michael Hermele, T. Senthil, Matthew P. A. Fisher, Patrick A. Lee, Naoto Nagaosa, and Xiao-Gang Wen. Stability of $u(1)$ spin liquids in two dimensions. *Phys. Rev. B*, 70:214437, Dec 2004.

- [161] Walter Rantner and Xiao-Gang Wen. Electron spectral function and algebraic spin liquid for the normal state of underdoped high t_c superconductors. *Phys. Rev. Lett.*, 86:3871–3874, Apr 2001.
- [162] Naoto Nagaosa and Patrick A. Lee. Normal-state properties of the uniform resonating-valence-bond state. *Phys. Rev. Lett.*, 64:2450–2453, May 1990.
- [163] Max A. Metlitski and Subir Sachdev. Quantum phase transitions of metals in two spatial dimensions. i. ising-nematic order. *Phys. Rev. B*, 82:075127, Aug 2010.
- [164] J. Ignacio Cirac, David Pérez-García, Norbert Schuch, and Frank Verstraete. Matrix product states and projected entangled pair states: Concepts, symmetries, theorems. *Reviews of Modern Physics*, 93(4), dec 2021.
- [165] M. Fannes, B. Nachtergaae, and R. F. Werner. Finitely correlated states on quantum spin chains. *Communications in Mathematical Physics*, 144:443, Mar 1992.
- [166] I. Affleck, T. Kennedy, E. H. Lieb, and H. Tasaki. Valence bond ground states in isotropic quantum antiferromagnets. *Communications in Mathematical Physics*, 115:477, Mar 1988.
- [167] J. Dukelsky, M. A. Martín-Delgado, T. Nishino, and G. Sierra. Equivalence of the variational matrix product method and the density matrix renormalization group applied to spin chains. *Europhysics Letters*, 43(4):457, aug 1998.
- [168] Stellan Östlund and Stefan Rommer. Thermodynamic limit of density matrix renormalization. *Phys. Rev. Lett.*, 75:3537–3540, Nov 1995.
- [169] Jacob Biamonte. Lectures on quantum tensor networks, 2020.
- [170] Jacob C Bridgeman and Christopher T Chubb. Hand-waving and interpretive dance: an introductory course on tensor networks. *Journal of Physics A: Mathematical and Theoretical*, 50(22):223001, may 2017.
- [171] J Ignacio Cirac and Frank Verstraete. Renormalization and tensor product states in spin chains and lattices. *Journal of Physics A: Mathematical and Theoretical*, 42(50):504004, dec 2009.
- [172] F. Verstraete and J. I. Cirac. Matrix product states represent ground states faithfully. *Phys. Rev. B*, 73:094423, Mar 2006.
- [173] J.I. Cirac, D. Pérez-García, N. Schuch, and F. Verstraete. Matrix product density operators: Renormalization fixed points and boundary theories. *Annals of Physics*, 378:100–149, mar 2017.
- [174] F. Verstraete and J. I. Cirac. Valence-bond states for quantum computation. *Phys. Rev. A*, 70:060302, Dec 2004.
- [175] F. Verstraete and J. I. Cirac. Renormalization algorithms for Quantum-Many Body Systems in two and higher dimensions. *arXiv e-prints*, pages cond-mat/0407066, July 2004.

- [176] T. B. Wahl, H.-H. Tu, N. Schuch, and J. I. Cirac. Projected entangled-pair states can describe chiral topological states. *Phys. Rev. Lett.*, 111:236805, Dec 2013.
- [177] Thorsten B. Wahl, Stefan T. Haßler, Hong-Hao Tu, J. Ignacio Cirac, and Norbert Schuch. Symmetries and boundary theories for chiral projected entangled pair states. *Phys. Rev. B*, 90:115133, Sep 2014.
- [178] G. Scarpa, A. Molnár, Y. Ge, J. J. García-Ripoll, N. Schuch, D. Pérez-García, and S. Iblisdir. Projected entangled pair states: Fundamental analytical and numerical limitations. *Physical Review Letters*, 125(21), nov 2020.
- [179] G. Vidal. Entanglement renormalization. *Phys. Rev. Lett.*, 99:220405, Nov 2007.
- [180] Xiang-Bin Wang, Tohya Hiroshima, Akihisa Tomita, and Masahito Hayashi. Quantum information with gaussian states. *Physics Reports*, 448(1):1–111, 2007.
- [181] Peter Woit. *Quantum Theory, Groups and Representations An Introduction*. Springer, 2017.
- [182] Maurice de Gosson. *Symplectic Geometry and Quantum Mechanics*. Springer, 2006.
- [183] Lucas Hackl and Eugenio Bianchi. Bosonic and fermionic gaussian states from kähler structures. *SciPost Physics Core*, 4(3), sep 2021.
- [184] Sergey Bravyi. Lagrangian representation for fermionic linear optics. *Quantum Info. Comput.*, 5(3):216–238, May 2005.
- [185] A Perelomov. *Generalized Coherent States and their Applications*. Springer-Verlag, Berlin, 1986.
- [186] John Williamson. On the algebraic problem concerning the normal forms of linear dynamical systems. *American Journal of Mathematics*, 58(1):141–163, 1936.
- [187] Martin R. Zirnbauer. Riemannian symmetric superspaces and their origin in random-matrix theory. *Journal of Mathematical Physics*, 37(10):4986–5018, 10 1996.
- [188] Alexander Altland and Martin R. Zirnbauer. Nonstandard symmetry classes in mesoscopic normal-superconducting hybrid structures. *Phys. Rev. B*, 55:1142–1161, Jan 1997.
- [189] M.F. Atiyah, R. Bott, and A. Shapiro. Clifford modules. *Topology*, 3:3–38, 1964.
- [190] Ching-Kai Chiu, Jeffrey C. Y. Teo, Andreas P. Schnyder, and Shinsei Ryu. Classification of topological quantum matter with symmetries. *Rev. Mod. Phys.*, 88:035005, Aug 2016.
- [191] Andrew M. Essin and Victor Gurarie. Bulk-boundary correspondence of topological insulators from their respective green’s functions. *Phys. Rev. B*, 84:125132, Sep 2011.
- [192] Gian Michele Graf and Marcello Porta. Bulk-edge correspondence for two-dimensional topological insulators. *Communications in Mathematical Physics*, 324:851–895, 2013.

- [193] Xiao-Liang Qi, Taylor L. Hughes, and Shou-Cheng Zhang. Topological field theory of time-reversal invariant insulators. *Phys. Rev. B*, 78:195424, Nov 2008.
- [194] Jeffrey C. Y. Teo and C. L. Kane. Topological defects and gapless modes in insulators and superconductors. *Phys. Rev. B*, 82:115120, Sep 2010.
- [195] B. Pirvu, G. Vidal, F. Verstraete, and L. Tagliacozzo. Matrix product states for critical spin chains: Finite-size versus finite-entanglement scaling. *Phys. Rev. B*, 86:075117, Aug 2012.
- [196] Vid Stojovic, Jutho Haegeman, I. P. McCulloch, Luca Tagliacozzo, and Frank Verstraete. Conformal data from finite entanglement scaling. *Phys. Rev. B*, 91:035120, Jan 2015.
- [197] Jutho Haegeman and Frank Verstraete. Diagonalizing transfer matrices and matrix product operators: A medley of exact and computational methods. *Annual Review of Condensed Matter Physics*, 8(1):355–406, 2017.
- [198] V. Zauner-Stauber, L. Vanderstraeten, M. T. Fishman, F. Verstraete, and J. Haegeman. Variational optimization algorithms for uniform matrix product states. *Physical Review B*, 97(4), jan 2018.
- [199] Laurens Vanderstraeten, Jutho Haegeman, and Frank Verstraete. Tangent-space methods for uniform matrix product states. *SciPost Phys. Lect. Notes*, page 7, 2019.
- [200] Tomotoshi Nishino and Kouichi Okunishi. Corner transfer matrix renormalization group method. *Journal of the Physical Society of Japan*, 65(4):891–894, 1996.
- [201] Tomotoshi Nishino and Kouichi Okunishi. Corner transfer matrix algorithm for classical renormalization group. *Journal of the Physical Society of Japan*, 66(10):3040–3047, 1997.
- [202] Román Orús and Guifré Vidal. Simulation of two-dimensional quantum systems on an infinite lattice revisited: Corner transfer matrix for tensor contraction. *Phys. Rev. B*, 80:094403, Sep 2009.
- [203] Laurens Vanderstraeten, Jutho Haegeman, Philippe Corboz, and Frank Verstraete. Gradient methods for variational optimization of projected entangled-pair states. *Physical Review B*, 94(15), oct 2016.
- [204] Hai-Jun Liao, Jin-Guo Liu, Lei Wang, and Tao Xiang. Differentiable programming tensor networks. *Phys. Rev. X*, 9:031041, Sep 2019.
- [205] Juraj Hasik, Didier Poilblanc, and Federico Becca. Investigation of the Néel phase of the frustrated Heisenberg antiferromagnet by differentiable symmetric tensor networks. *SciPost Phys.*, 10:012, 2021.
- [206] Boris Ponsioen, Fakher Assaad, and Philippe Corboz. Automatic differentiation applied to excitations with projected entangled pair states. *SciPost Physics*, 12(1), jan 2022.

- [207] Guifré Vidal. Efficient classical simulation of slightly entangled quantum computations. *Phys. Rev. Lett.*, 91:147902, Oct 2003.
- [208] G. Vidal. Classical simulation of infinite-size quantum lattice systems in one spatial dimension. *Phys. Rev. Lett.*, 98:070201, Feb 2007.
- [209] H. C. Jiang, Z. Y. Weng, and T. Xiang. Accurate determination of tensor network state of quantum lattice models in two dimensions. *Phys. Rev. Lett.*, 101:090603, Aug 2008.
- [210] J. Jordan, R. Orús, G. Vidal, F. Verstraete, and J. I. Cirac. Classical simulation of infinite-size quantum lattice systems in two spatial dimensions. *Phys. Rev. Lett.*, 101:250602, Dec 2008.
- [211] Jutho Haegeman, J. Ignacio Cirac, Tobias J. Osborne, Iztok Pižorn, Henri Verschelde, and Frank Verstraete. Time-dependent variational principle for quantum lattices. *Phys. Rev. Lett.*, 107:070601, Aug 2011.
- [212] Jutho Haegeman, Bogdan Pirvu, David J. Weir, J. Ignacio Cirac, Tobias J. Osborne, Henri Verschelde, and Frank Verstraete. Variational matrix product ansatz for dispersion relations. *Phys. Rev. B*, 85:100408, Mar 2012.
- [213] Laurens Vanderstraeten, Michaël Mariën, Frank Verstraete, and Jutho Haegeman. Excitations and the tangent space of projected entangled-pair states. *Phys. Rev. B*, 92:201111, Nov 2015.
- [214] P. Jordan and E. Wigner. Über das paulische Äquivalenzverbot. *Zeitschrift für Physik*, 47:631, 1928.
- [215] Zheng-Cheng Gu, Frank Verstraete, and Xiao-Gang Wen. Grassmann tensor network states and its renormalization for strongly correlated fermionic and bosonic states. *arXiv e-prints*, page arXiv:1004.2563, April 2010.
- [216] Zheng-Cheng Gu. Efficient simulation of grassmann tensor product states. *Phys. Rev. B*, 88:115139, Sep 2013.
- [217] J. Dubail and N. Read. Tensor network trial states for chiral topological phases in two dimensions and a no-go theorem in any dimension. *Phys. Rev. B*, 92:205307, Nov 2015.
- [218] B. Béri and N. R. Cooper. Local tensor network for strongly correlated projective states. *Physical Review Letters*, 106(15), apr 2011.
- [219] Philippe Corboz and Guifré Vidal. Fermionic multiscale entanglement renormalization ansatz. *Phys. Rev. B*, 80:165129, Oct 2009.
- [220] Christina V. Kraus, Norbert Schuch, Frank Verstraete, and J. Ignacio Cirac. Fermionic projected entangled pair states. *Phys. Rev. A*, 81:052338, May 2010.
- [221] Carlos Pineda, Thomas Barthel, and Jens Eisert. Unitary circuits for strongly correlated fermions. *Physical Review A*, 81(5), may 2010.

- [222] Nick Bultinck, Dominic J Williamson, Jutho Haegeman, and Frank Verstraete. Fermionic projected entangled-pair states and topological phases. *Journal of Physics A: Mathematical and Theoretical*, 51(2):025202, dec 2017.
- [223] Lukas Devos, Lander Burgelman, Bram Vanhecke, Jutho Haegeman, Frank Verstraete, and Laurens Vanderstraeten. TensorTrack, June 2022.
- [224] Robert N. C. Pfeifer, Glen Evenbly, Sukhwinder Singh, and Guifre Vidal. Ncon: A tensor network contractor for matlab, 2015.
- [225] Philipp Schmoll, Sukhbinder Singh, Matteo Rizzi, and Román Orús. A programming guide for tensor networks with global su2 symmetry. *Annals of Physics*, 419:168232, aug 2020.
- [226] A. Nietner, B. Vanhecke, F. Verstraete, J. Eisert, and L. Vanderstraeten. Efficient variational contraction of two-dimensional tensor networks with a non-trivial unit cell. *Quantum*, 4:328, sep 2020.
- [227] V. Zauner-Stauber, L. Vanderstraeten, J. Haegeman, I. P. McCulloch, and F. Verstraete. Topological nature of spinons and holons: Elementary excitations from matrix product states with conserved symmetries. *Physical Review B*, 97(23), jun 2018.
- [228] Juraj Hasik, Maarten Van Damme, Didier Poilblanc, and Laurens Vanderstraeten. Simulating chiral spin liquids with projected entangled-pair states. *Phys. Rev. Lett.*, 129:177201, Oct 2022.
- [229] Adrian Franco-Rubio and J. Ignacio Cirac. Gaussian matrix product states cannot efficiently describe critical systems. *Physical Review B*, 106(23):235136, December 2022.
- [230] Qi Yang, Xing-Yu Zhang, Hai-Jun Liao, Hong-Hao Tu, and Lei Wang. Projected d-wave superconducting state: a fermionic projected entangled pair state study. *arXiv e-prints*, page arXiv:2208.04566, August 2022.
- [231] Claude Bloch and Albert Messiah. The canonical form of an antisymmetric tensor and its application to the theory of superconductivity. *Nuclear Physics*, 39:95–106, 1962.
- [232] D. A. Ivanov and T. Senthil. Projected wave functions for fractionalized phases of quantum spin systems. *Phys. Rev. B*, 66:115111, Sep 2002.
- [233] Olexei I. Motrunich. Variational study of triangular lattice spin-1/2 model with ring exchanges and spin liquid state in $k - (et)_2cu_2(cn)_3$. *Physical Review B*, 72(4), jul 2005.
- [234] Yao Shen, Yao-Dong Li, Hongliang Wo, Yuesheng Li, Shoudong Shen, Bingying Pan, Qisi Wang, H. C. Walker, P. Steffens, M. Boehm, Yiqing Hao, D. L. Quintero-Castro, L. W. Harriger, M. D. Frontzek, Lijie Hao, Siqin Meng, Qingming Zhang, Gang Chen, and Jun Zhao. Evidence for a spinon fermi surface in a triangular-lattice quantum-spin-liquid candidate. *Nature*, 540(7634):559–562, 2016.

- [235] Yao Shen, Yao-Dong Li, Hongliang Wo, Yuesheng Li, Shoudong Shen, Bingying Pan, Qisi Wang, H. C. Walker, P. Steffens, M. Boehm, Yiqing Hao, D. L. Quintero-Castro, L. W. Harriger, M. D. Frontzek, Lijie Hao, Siqin Meng, Qingming Zhang, Gang Chen, and Jun Zhao. Evidence for a spinon fermi surface in a triangular-lattice quantum-spin-liquid candidate. *Nature (London)*, 540, 12 2016.
- [236] Wei Ruan, Yi Chen, Shujie Tang, Jinwoong Hwang, Hsin-Zon Tsai, Ryan L. Lee, Meng Wu, Hyejin Ryu, Salman Kahn, Franklin Liou, Caihong Jia, Andrew Aikawa, Choongyu Hwang, Feng Wang, Yongseong Choi, Steven G. Louie, Patrick A. Lee, Zhi-Xun Shen, Sung-Kwan Mo, and Michael F. Crommie. Evidence for quantum spin liquid behaviour in single-layer 1t-TaSe₂ from scanning tunnelling microscopy. *Nature Physics*, 17(10):1154–1161, aug 2021.
- [237] D. N. Sheng, Olexei I. Motrunich, and Matthew P. A. Fisher. Spin bose-metal phase in a spin-1/2 model with ring exchange on a two-leg triangular strip. *Physical Review B*, 79(20), may 2009.
- [238] Jheng-Wei Li, Jan von Delft, and Hong-Hao Tu. U(1)-symmetric gaussian fermionic projected entangled paired states and their gutzwiller projection. *Physical Review B*, 107(8), feb 2023.
- [239] L. Michel and I. P. McCulloch. Schur forms of matrix product operators in the infinite limit, 2010.
- [240] C. Hubig, I. P. McCulloch, and U. Schollwöck. Generic construction of efficient matrix product operators. *Phys. Rev. B*, 95:035129, Jan 2017.